UNIVERSITÀ DEGLI STUDI DI MILANO

FACOLTÀ DI SCIENZE MATEMATICHE FISICHE E NATURALI

DOCTORATE SCHOOL IN PHYSICS,

ASTROPHYSICS AND APPLIED PHYSICS

Commissioning of the tracking system in the ATLAS detector

Scientific Area Code (S.S.D.): FIS/04

Coordinator: Prof. Marco Bersanelli

Tutor: Prof. Francesco Ragusa

PhD DISSERTATION

Simone Montesano

XXII° CYCLE (2006–2009)

Academic Year 2008–2009

Contents

“The true origin of the university lies in the thirst for knowledge that is proper to man. The human being wants to know what everything around him is. He wants truth.”
— Benedict XVI

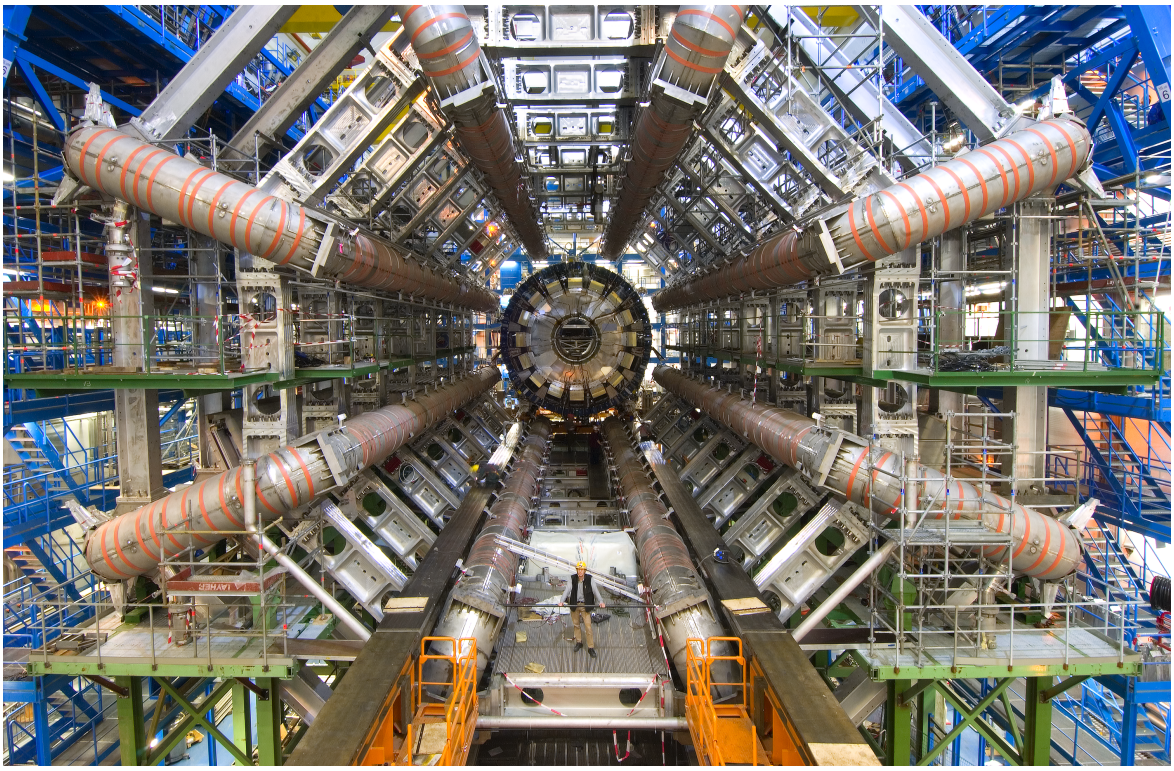

Introduction

The Large Hadron Collider Project [1] was approved by CERN Council in December 1994. The project was motivated by the need of testing and proving the electroweak symmetry breaking of the Standard Model. After the consolidation of the Standard Model knowledge, the data provided by the LHC will eventually be the basis to discover phenomena that characterize previously unexplored energies. Although fifteen years has passed since LHC approval, no experiment has been able to prove (or deny) the existence of the Higgs boson or the validity of the Supersymmetry theory, that are still among the main objectives of the project.

In order to record and analyze the different phenomena hidden in the data provided by the LHC, four detectors are placed in proximity of the beam collision points. ALICE [2] and LHCb [3] are focused on a single aspect of the Standard Model physics, i.e. the study of quark-gluon plasma in heavy ion interaction and the precise measurements of CP-violation through rare b-hadrons decay. ATLAS [4] and CMS [5], instead, aim at being *general purpose* experiments that can collect a huge amount of data, in order to sort out virtually every possible phenomena, either described or not by the Standard Model.

Many years of work have been necessary to build the 27-kilometers accelerator that is equipped with superconducting magnets and is designed to provide p-p collision at a center of mass energy of 14 TeV, as well as the surrounding detectors. Finally, on September 10^{th}, 2008, the first beam was circulated in the machine. Unfortunately, on September 19^{th}, a serious fault developed, damaging a number of superconducting magnets. The repair required a long technical intervention which has retarded the starting of the operations to November 2009.

The ATLAS detector was commissioned during 2008 and was perfecting its training by registering cosmic ray data, when the LHC incident happened. It was thus decided by the ATLAS collaboration to continue the cosmic ray data taking campaign and to fully profit from these data during 2009. The goal was to calibrate as much as possible the detector on real data, in order to be able to start physics analysis since the very first collisions in late 2009.

The sub-system that could mostly benefit from this activity was the tracking system, that could be tested by using single cosmic ray tracks that traversed all the detector. The tracking system is essential in all physics analysis, but its precision gains particular importance when the interaction region must be studied. A well calibrated inner tracker, in fact, is able to select tracks associated to particles that originate at few hundred microns from the primary interaction point. This knowledge can be applied to discriminate b-hadrons, τ leptons and other short-living particles that characterize rare physics events.

The activity described in this thesis is thus related to the commissioning of the ATLAS Inner Detector tracking system. Chapter 1 describes the ATLAS experiment, pointing out its physics programme and the requirements that it imposes, as well as some common definitions that are widely used in this thesis. Chapter 2 details the devices that compose the Inner Detector. Particular emphasis is given to the Pixel Detector, the innermost component of the tracking system. The Pixel Detector performance is essential to reach the desired resolution on the track impact parameter that, in turn, is used to discriminate particles originating in secondary vertexes. In this chapter the study of the tracking performance is motivated by presenting the importance of the *b*-tagging when selecting a pure set of top pair events.

The description of cosmic rays data sample is reported in Chapter 3. Chapter 4 and 5 contain the outcome of the commissioning activity. In particular, Chapter 4 describes the optimization of the Pixel Detector resolution. A position algorithm based on charge sharing among hit pixels has been studied, allowing to improve the resolution up to 50% in the azimuthal direction, depending on the particle incident angle. The effect of this algorithm has been evaluated by using cosmic ray tracks and its implementation has been integrated into the official reconstruction software. Chapter 5, instead, is devoted to the measurement of the global performance of the tracking system. A selection of cosmic ray tracks have been chosen, in order to consider tracks that could resemble trajectories originating from the nominal interaction point. These tracks have been split in two halves, that have been used to measure the resolution achievable on all track parameters. These have been studied as a function of the track direction, momentum and distance from the nominal interaction point. Results have been compared to design values and, after the commissioning activity, residual discrepancies have been measured. By the comparison with simulated data, an important contribution to resolution has been estimated to originate from the non-pointing geometry of the cosmic ray tracks. The remaining discrepancy with respect to design performance is mostly due to known systematic effects arising from misalignments of the detector elements. These deformations will be be solved only by using very high statistics of pointing tracks.

Chapter 1

The ATLAS detector: description and goals

"ATLAS is a particle physics experiment at the Large Hadron Collider at CERN. Starting in late 2009/2010, the ATLAS detector will search for new discoveries in the head-on collisions of protons of extraordinarily high energy. ATLAS will learn about the basic forces that have shaped our Universe since the beginning of time and that will determine its fate. Among the possible unknowns are the origin of mass, extra dimensions of space, unification of fundamental forces, and evidence for dark matter candidates in the Universe."

— The official outreach page for the ATLAS Experiment at CERN [6].

1.1 The Large Hadron Collider

The Large Hadron Collider (LHC) [1] is a two-ring-superconducting-hadron accelerator and collider installed in a 26.7 km tunnel in proximity of the CERN research center [7], near Geneva. Data provided by the LHC will extend the frontiers of particle physics with unprecedented high energy and luminosity. Inside the LHC, at full performances, bunches of up to 10^{11} protons will collide 40 million times per second to provide 14 TeV proton-proton collisions at a design luminosity of 10^{34} cm^{-2}s^{-1}. The LHC will also collide heavy ions, in particular lead nuclei, at 5.5 TeV per nucleon pair, at a design luminosity of 10^{27} cm^{-2}s^{-1}. The high interaction rates, radiation doses, particle multiplicities and energies, as well as the requirements for precision measurements, have set new standards for the design of particle detectors. Two general purpose detectors, ATLAS (A Toroidal LHC ApparatuS) [4] and CMS (Compact Muon Solenoid) [5] have been built for probing p-p and ion-ion collisions. Two more detectors, ALICE [2] and LHCb [3], are devoted to more focused studies: the study of quark-gluon plasma in heavy ion interaction and the precise measurements of CP-violation through rare b-hadrons decay, respectively.

At present time, the LHC is closing its commissioning phase. It has been able to provide proton-proton collisions at 450 GeV and at 1.18 TeV per beam during November and December 2009. After

a short technical stop in the first weeks of 2010, the main objective will be a physics run through to late 2010, starting at an initial beam energy of 3.5 TeV. Eventually the center of mass energy should be increase to 10 TeV, as well as the luminosity, that should reach 5×10^{32} cm^{-2}s^{-1} [8]. The final energy and luminosity will be only possible after testing the machine for at least one year and after an accurate training of the superconducting magnets.

1.2 The ATLAS experiment scientific program

LHC will provide a rich physics potential, ranging from more precise measurements of Standard Model parameters to the search for new physics phenomena. Recently, the details about the physics analyses that are foreseen in the first years of activity of the ATLAS detector have been collected in [9]. In this section, an overview of the experimental program is given.

1.2.1 Standard Model

Figure 1.1 shows the cross-section for the production of many Standard Model particles during collisions, as a function of the energy in the center of mass ($\sqrt{s}$). The high luminosity and increased cross-sections available at ATLAS, with respect to the Tevatron experiment [10], enable many high-precision tests of QCD, electroweak interactions, and flavour physics. Two examples, Higgs boson searches and top quark physics, are discussed in the following.

Higgs boson searches

While the Standard Model of electroweak and strong interactions is in excellent agreement with the numerous experimental measurements, the dynamics responsible for electroweak symmetry breaking is still unknown. Within the Standard Model, the Higgs mechanism is invoked to break the electroweak symmetry. A doublet of complex scalar fields is introduced, of which a single neutral scalar physical particle, the Higgs boson, remains after symmetry breaking. Many extensions of this minimal version of the Higgs sector have been proposed, mostly discussing a scenario with two complex Higgs doublets as realized in the Minimal Supersymmetric Standard Model (MSSM).

Within the Standard Model, the Higgs boson is the only particle that has not been discovered so far. The direct search at the e^+e^- collider LEP has led to a lower bound on its mass of 114.4 GeV [12]. Indirectly, high-precision electroweak data constrain the mass of the Higgs boson via their sensitivity to loop corrections. Assuming the overall validity of the Standard Model, a global fit [13] to all electroweak data leads to the 95% confidence level $m_H < 114$ GeV. The 95% confidence level lower limit obtained from LEP is not used in the determination of this limit. Including it increases the limit to 182 GeV [13].

On the basis of the present theoretical knowledge, the Higgs sector in the Standard Model remains largely unconstrained. While there is no direct prediction for the mass of the Higgs boson, an upper limit of ~ 1 TeV can be inferred from unitarity arguments. Further constraints can be derived under

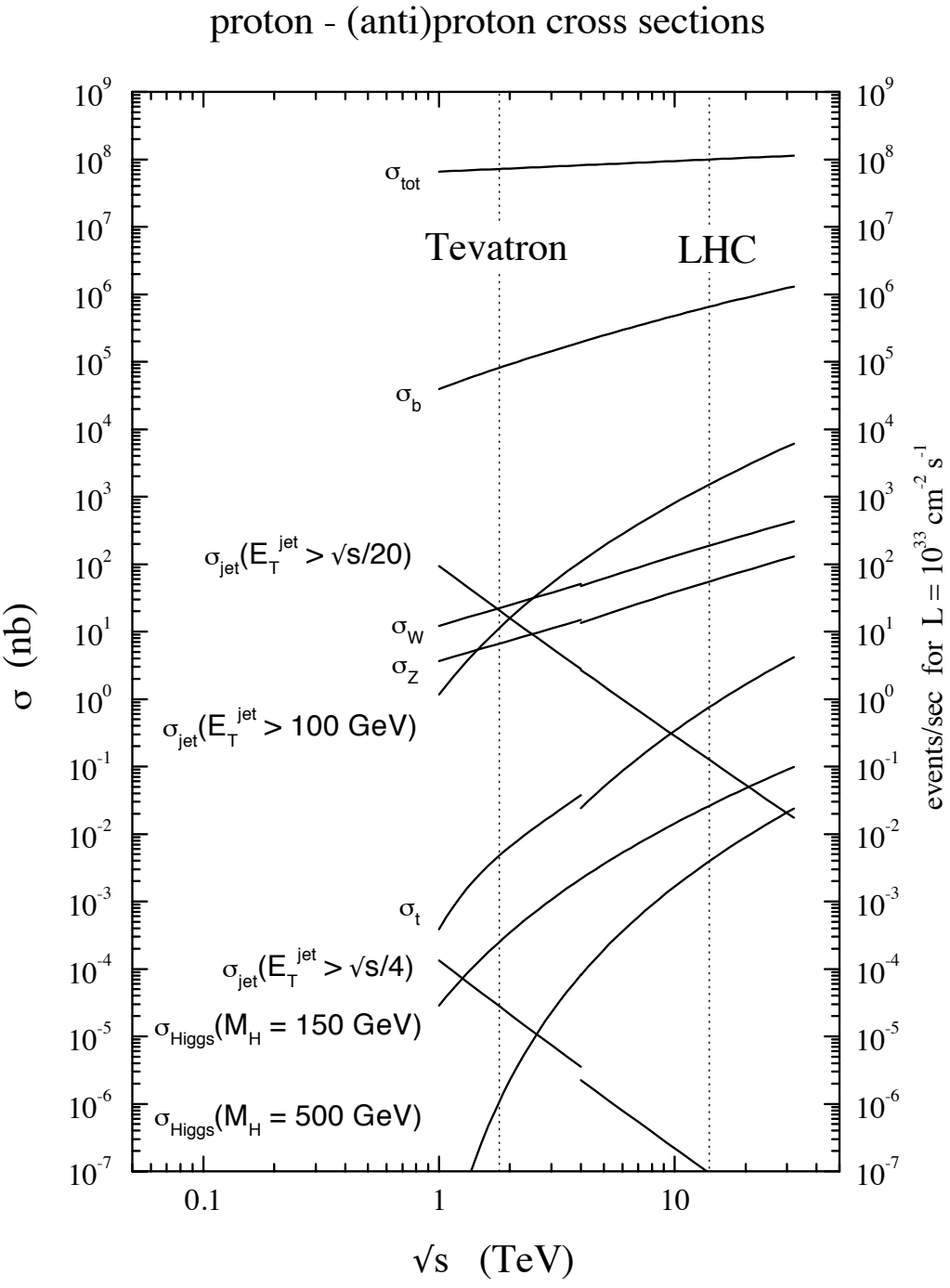

Figure 1.1: Cross section of the main Standard Model processes. Figure taken from [11]

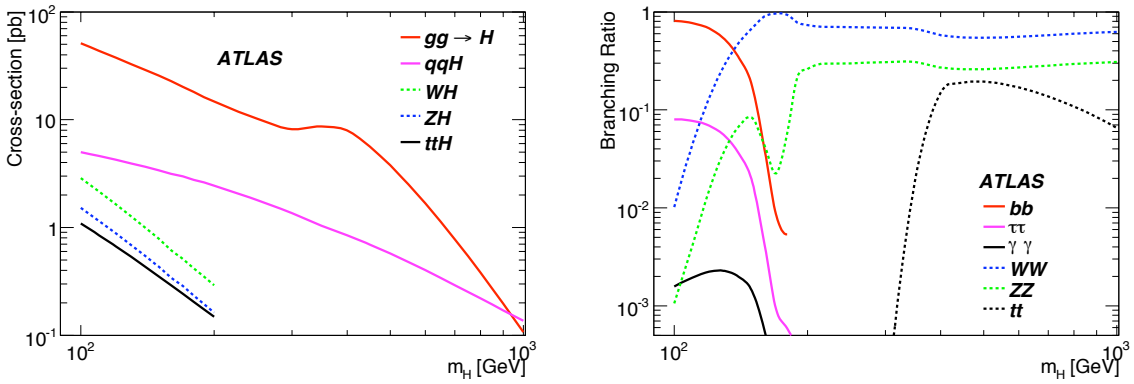

(a) (b)

Figure 1.2: 1.2(a): cross-sections for the five production channels of the Standard Model Higgs boson at the LHC at 14 TeV. 1.2(b): branching ratios for the relevant decay modes of the Standard Model Higgs boson as a function of its mass. Figures taken from [9].

the assumption that the Standard Model is valid only up to a cutoff energy scale Λ, beyond which new physics becomes relevant. Requiring that the electroweak vacuum is stable and that the Standard Model remains perturbative allows to set upper and lower bounds on the Higgs boson mass [14–24]. For a cutoff scale of the order of the Planck mass, the Higgs boson mass is required to be in the range $130 < m_H < 180$ GeV. If new physics appears at lower mass scales, the bound becomes weaker, e.g. for $\Lambda = 1$ TeV the Higgs boson mass is constrained to be in the range $50 < m_H < 800$ GeV.

Direct searches for the Standard Model Higgs boson at the Tevatron include looking for its production via gluon fusion and subsequent decay to $WW^{(*)}$. Searches at low mass, instead, are done by studying Higgs bosons produced in association with the W and Z, and looking for $H \to b\bar{b}$ with leptonic W and Z decays (e, μ). Preliminary results on the combination of the analyses from both experiments at Tevatron (i.e. CDF and DØ) lead to a 95% confidence level limit on the Higgs boson production cross-section to about $5.1 \times \sigma_{\mathrm{SM}}$ for $m_H = 115$ GeV and $1.1 \times \sigma_{\mathrm{SM}}$ for $m_H = 160$ GeV [25, 26], where σ_{SM} represent the cross-section predicted by the Standard Model.

The cross-section for the main Higgs production channels is displayed in Figure 1.2(a) as a function of its mass for 14 TeV collision energy, while the branching ratio for the relevant decay channels is shown in Figure 1.2(b). The high-energy collisions provided by the LHC will allow the search for Higgs bosons to be extended into unexplored mass regions. The experiments have a large discovery potential for Higgs bosons in both the Standard Model and in the MSSM over the full parameter range.

The search for the Standard Model Higgs boson has been used as a benchmark to establish the performance of important sub-systems of ATLAS. This process is particularly demanding in term of detector performances since there is a range of production and decay mechanisms, depending on the mass of the Higgs boson. At low masses ($m_H < 2m_Z$), the natural width would only be a few MeV, and so the observed width would be defined by the instrumental resolution. The predominant decay mode

into hadrons would be difficult to detect due to QCD backgrounds, and the two-photon decay channel would be an important one. Other promising channels could be, for example, associated production of H such as $t\bar{t}H$, WH and ZH with $H \to b\bar{b}$, using a lepton from the decay of one of the top quarks or of the vector boson for triggering and background rejection. For masses above 130 GeV, Higgs boson decays $H \to ZZ$, where each Z decays to a pair of oppositely charged leptons, would provide the experimentally cleanest channel to study the properties of the Higgs boson. For masses above approximately 600 GeV, WW and ZZ decays into jets or involving neutrinos would be needed to extract a signal. Searches for the Higgs boson beyond the Standard Model, for such particles as the A and $H^{\pm}$ of the Minimal Supersymmetric extension of the Standard Model (MSSM), require sensitivity to processes involving τ leptons and good b-tagging performance. If the Higgs boson will be discovered, it would need to be studied in several modes, regardless of its mass, in order to fully disentangle its properties and establish its credentials as belonging to the Standard Model or an extension thereof.

Top quark physics

The top quark will be produced at the LHC at a rate of a few Hz, when design energy will be met. This quark has been discovered only in 1995 at Tevatron [27–30], where the rate of production is two order of magnitude lower. Produced predominantly, in hadron-hadron collisions, through strong interactions, the top quark decays rapidly without forming hadrons, and almost exclusively through the mode $t \to Wb$. The relevant CKM coupling is already determined by the (three-generation) unitarity of the CKM matrix. The top quark is distinguished by its large mass, about 35 times larger than the mass of the next heavy quark, and close to the electroweak symmetry breaking scale.

This unique property raises a number of interesting questions. For example if the top quark mass is generated by the Higgs mechanism as the Standard Model predicts and if its mass is related to the top-Higgs-Yukawa coupling, or if it does play an even more fundamental role in the electroweak symmetry breaking mechanism. Non Standard Model physics could first manifest itself in non-standard couplings of the top quark which show up as anomalies in top quark production and decays. By studying the top quark, some of these questions may be answered. Further insight in top quark properties will come from measurements done with the high-statistics sample of $t\bar{t}$ pairs such as top quark and W polarization studies sensitive to anomalous W_{tb} couplings, searches for rare top quark decays indicating the presence of new physics, or for new resonances decaying to $t\bar{t}$ pairs.

Furthermore, the understanding of the experimental signatures for top quark events involves most parts of the ATLAS detector and is essential for claiming potential discoveries of new physics. Recent studies [31, 32] have confirmed the possibility to measure top cross-section even before the design energy of LHC is met. These activities will allow to measure top cross-section with higher precision with respect to Tevatron already during the first year of detector operation.

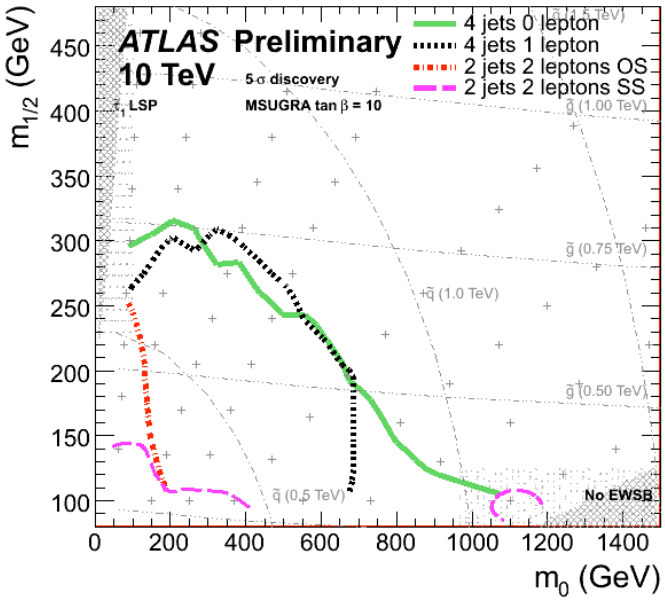

Figure 1.3: 5σ discovery reach of mSUGRA models as a function of m_0 and $m_{1/2}$ for $\tan\beta = 10$. The result of the scan is reported for channels with 0, 1 and 2 leptons with opposite charge (OS) and with same charge (SS). Only the channels with the largest discovery reach are shown for each lepton multiplicity. Figure taken from [33].

1.2.2 Supersymmetry

Supersymmetry (SUSY) is one of the theoretically favoured candidates for physics beyond the Standard Model. The main motivation is to protect the Higgs boson mass from quadratically diverging radiative corrections, in a theory where the Standard Model is valid only up to a high scale Λ. The proposed solution postulates the invariance of the theory under a symmetry which transforms fermions into bosons and vice-versa. The basic prediction of SUSY is thus the existence, for each Standard Model particle degree of freedom, of a corresponding *s-particle*, with spin different by half a unit. The SUSY generators commute with the $SU(2) \times U(1) \times SU(3)$ symmetries of the Standard Model, and with the Poincaré group. It follows that, with unbroken SUSY, the s-particles would have the same quantum numbers and masses as the Standard Model particles. Since no super-partner has been observed to date, SUSY must be broken. A common approach to the phenomenological study of SUSY is to assume the minimal possible particle content, and to parametrise the SUSY-breaking Lagrangian as the sum of all the terms which do not reintroduce quadratic divergences into the theory. The model thus obtained is called Minimal Supersymmetric Standard Model (MSSM) and is characterized by a large number of parameters (~ 100).

It is not possible to explore in full the 100-dimensional parameter space of the MSSM. It is therefore necessary to adopt some specific assumptions for the SUSY breaking, resulting in models defined by a small number of parameters at the SUSY breaking scale. The two main models are mSUGRA,

where SUSY breaking is mediated by gravitational interaction; and GMSB, where SUSY breaking is mediated by a gauge interaction through messenger gauge fields. These two models give quite different phenomenologies, due to the different nature of the lightest SUSY particle, which is the lightest neutralino for the mSUGRA case and the gravitino for the GMSB case.

In order to warrant the conservation of baryonic and leptonic quantum numbers, a new multiplicative quantum number, R-parity, is introduced, which is 1 for particles and -1 for the SUSY partners. Models where R-parity is violated can be formulated, but the majority of the studies refers to models with R-parity conservation. The consequences of R-parity conservation are that s-particles must be produced in pairs, and that each will decay to the lightest SUSY particle (LSP) which must be stable. Cosmological arguments suggest that stable LSPs should be weakly interacting and so would escape direct detection at ATLAS, resulting in the characteristic feature expected for SUSY events — an imbalance of the transverse energy measured in the detector. Other associated signatures will provide sensitivity to a large class of models.

These models explore a large variety of possible signals, e.g. different jet (2, 3, 4) and lepton (0, 1, 2, 3) multiplicities as well as channels with taus and photons. Figure 1.3, for example, shows the 5σ discovery reach for mSUGRA models. These models are described by only five parameters: m_0, $m_{1/2}$, $\tan\beta$, A_0 and μ. In fact they assume that bosons and fermions have a common mass at energy above the Supersymmetry breaking scale (i.e. m_0 and $m_{1/2}$, respectively). In this case, $\tan\beta$ is the ratio between the mass associated to the two components of the neutral Higgs section, while μ is the mass of the SM Higgs boson. Finally A_0 is the tri-linear coupling constants for scalar particles. The discovery reach is studied as a function of m_0 and $m_{1/2}$ for a fixed value of $\tan\beta = 10$.

Many studies are on-going, in order to be able to separate genuine SUSY signals from many background sources [33, 34]. At the same time, analyses have been developed to measure properties of SUSY particles, once they have been discovered, or to distinguish the fenomenology relative to different models [35, 36].

1.2.3 Other studies

Many other studies are foreseen taking advantage of the ATLAS detector. Several models, for examples, propose the existence of extra dimensions leading to a characteristic energy scale of quantum gravity in the TeV region. In terms of experimental signatures, this could lead to the emission of gravitons which escape into extra dimensions and therefore generate $E_{\mathrm{T}}^{\mathrm{miss}}$, or of Kaluza-Klein excitations which manifest themselves as Z-like resonances with a separations in mass of order of TeV [37, 38]. Other experimental signatures could be anomalous high-mass di-jet production [39], and miniature black-hole production with spectacular decays involving democratic production of fundamental final states such as jets, leptons, photons, neutrinos, W and Z [40]. Finally, heavy ions will be studied in dedicated LHC runs [41].

1.3 The ATLAS detector

The formidable LHC luminosity and resulting interaction rate are needed because of the small cross-sections expected for many of the processes that the experiment is expected to study. However, with an inelastic proton-proton cross-section of 80 mb, the LHC will produce a total rate of 109 inelastic events for every second at design luminosity. This presents a serious experimental difficulty as it implies that every candidate event for new physics will on the average be accompanied by 23 inelastic events per bunch crossing. The nature of proton-proton collisions imposes another difficulty. QCD jet production cross-sections dominate over the rare processes of interest, requiring the identification of experimental signatures characteristic of the physics processes in question, such as missing transverse energy or secondary vertexes. Identifying such final states for these rare processes imposes further demands on the integrated luminosity needed, and on the particle-identification capabilities of the detector. Viewed in this context, these benchmark physics goals can be turned into a set of general requirements for the LHC detectors:

- Due to the experimental conditions at the LHC, the detectors require fast, radiation-hard electronics and sensor elements. In addition, high detector granularity is needed to handle the particle fluxes and to reduce the influence of overlapping events.
- Large acceptance in pseudorapidity and almost full azimuthal angle coverage is required.
- Good charged-particle momentum resolution and reconstruction efficiency in the inner tracker are essential. For offline tagging of τ leptons and b-jets, vertex detectors close to the interaction region are required to observe secondary vertexes.
- Very good electromagnetic calorimetry for electron and photon identification and measurements, complemented by full-coverage hadronic calorimetry for accurate jet and missing transverse energy measurements, are important requirements, as these measurements form the basis of many of the studies mentioned above.
- Good muon identification and momentum resolution over a wide range of momenta and the ability to determine unambiguously the charge of high-momentum muons are fundamental requirements.
- Highly efficient triggering on low transverse-momentum objects with sufficient background rejection, is a prerequisite to achieve an acceptable trigger rate for most physics processes of interest.

1.3.1 Structure of the detector

The overall ATLAS detector layout is shown in Figure 1.4 and its main performance goals are listed in Table 1.1. The global reference frame adopted by ATLAS is centered on the nominal interaction point, which is defined as the origin of the coordinate system. The beam direction defines the z-axis and the x-y plane is transverse to the beam direction. The positive x-axis is defined as pointing from the interaction point to the centre of the LHC ring and the positive y-axis is defined as pointing upwards. The side-A of the detector is defined as that with positive z and side-C is that with negative z. Given

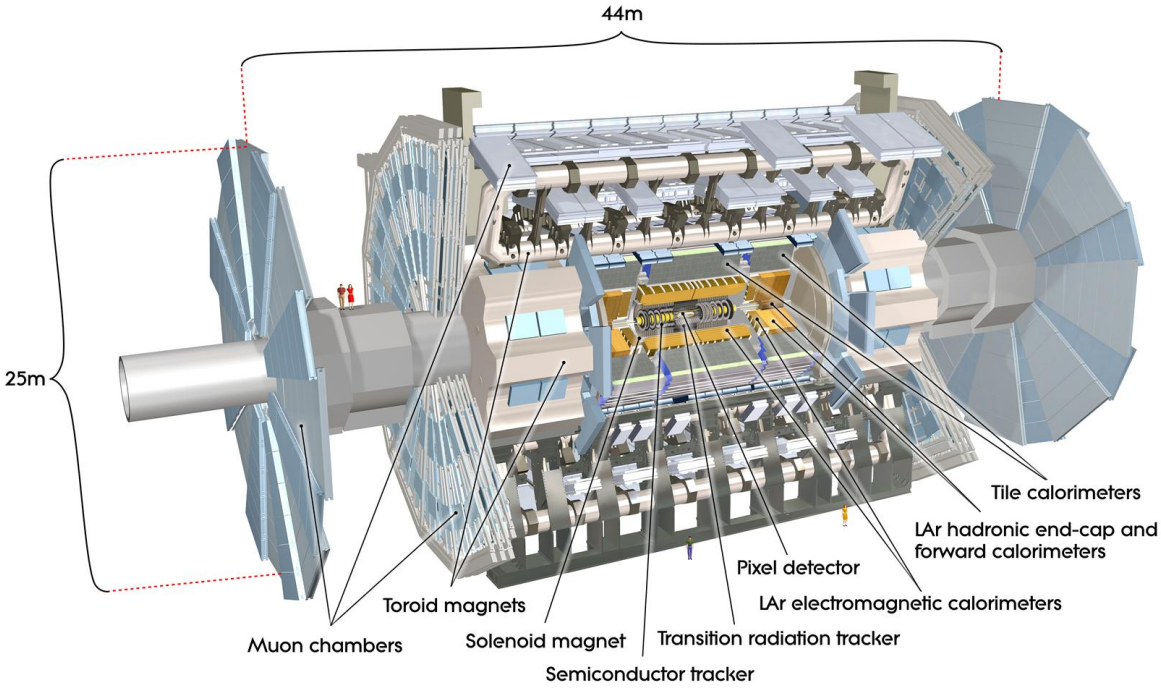

Figure 1.4: Cut-away view of the ATLAS detector structure.

the symmetry of the system, a cylindrical coordinate system is often used: the azimuthal angle Φ is measured as usual around the beam axis, and the polar angle Θ is the angle from the beam axis. The distance R is hence defined in the transverse (x-y) plane. The variable $\eta = -\log[\tan(\Theta/2)]$ is often used in place of Θ.

The magnet configuration comprises a thin superconducting solenoid surrounding the Inner Detector, and three large superconducting toroids (one barrel and two end-caps) arranged with an eight-fold azimuthal symmetry around the calorimeters. This fundamental choice drove the design of the rest of the detector.

Pattern recognition, momentum and vertex measurements, and electron identification are achieved with a combination of discrete, high-resolution semiconductor pixel and strip detectors in the inner part of the tracking volume, and straw-tube tracking detectors with the capability to generate and detect transition radiation in its outer part.

High-granularity liquid-argon (LAr) electromagnetic sampling calorimeters, with excellent performance in terms of energy and position resolution, cover the pseudorapidity range $|\eta| < 3.2$. The hadronic calorimetry in the range $|\eta| < 1.7$ is provided by a scintillator-tile calorimeter, which is separated into a large barrel and two smaller extended barrel cylinders, one on either side of the central barrel. In the end-caps ($|\eta| > 1.5$), LAr technology is also used for the hadronic calorimeters, matching the outer $|\eta|$ limits of end-cap electromagnetic calorimeters. The LAr forward calorimeters provide

Detector component	Required resolution	η coverage	
		Measurement	Trigger
Tracking	$\sigma_{p_T}/p_T = 0.05\%\ p_T \oplus 1\%$	± 2.5	
EM calorimetry	$\sigma_E/E = 10\%/\sqrt{E} \oplus 0.7\%$	± 3.2	± 2.5
Hadronic calorimetry (jets)			
barrel and end-cap	$\sigma_E/E = 50\%/\sqrt{E} \oplus 3\%$	± 3.2	± 3.2
forward	$\sigma_E/E = 100\%/\sqrt{E} \oplus 10\%$	$3.1 < \lvert\eta\rvert < 4.9$	$3.1 < \lvert\eta\rvert < 4.9$
Muon spectrometer	σ_{p_T}/p_T=10% at p_T = 1 TeV	± 2.7	± 2.4

Table 1.1: General performance goals of the ATLAS detector. For high-p_{T} muons, the muon-spectrometer performance is independent of the Inner Detector system. Table taken from [4].

both electromagnetic and hadronic energy measurements, and extend the pseudorapidity coverage to $|\eta| = 4.9$.

The calorimeter is surrounded by the muon spectrometer. The air-core toroid system, with a long barrel and two inserted end-cap magnets, generates strong bending power in a large volume within a light and open structure. Multiple-scattering effects are therefore minimised, and excellent muon momentum resolution is achieved with three layers of high-precision tracking chambers. The muon instrumentation includes, as a key component, trigger chambers with timing resolution of the range of 1.5–4 ns. The muon spectrometer defines the overall dimensions of the ATLAS detector.

The proton-proton interaction rate at the luminosity of 10^{34} cm^{-2} s^{-1} is approximately 1 GHz, while the event data recording, based on technology and resource limitations, is limited to about 200 Hz. This requires an overall rejection factor of 5×10^6 against minimum-bias processes while maintaining maximum efficiency for the new physics. The Level-1 trigger system uses a subset of the total detector information to make a decision on whether or not to continue processing an event, reducing the data rate to approximately 75 kHz (limited by the bandwidth of the read-out system, which is upgradeable to 100 kHz). The subsequent two levels, collectively known as the high-level trigger, are the Level-2 trigger and the event filter. They provide the reduction to a final data-taking rate of approximately 200 Hz. The initial input capacity will be limited to a Level-1 trigger rate of about 40 kHz. This capacity will be increased as needed to deal with the LHC luminosity profile during the first years. The ultimate goal is to be able to handle 100 kHz if needed.

1.3.2 Magnetic system

ATLAS features a unique hybrid system of four large superconducting magnets. This magnetic system is 22 m in diameter and 26 m in length, with a stored energy of 1.6 GJ. The four magnets provide the magnetic field over a volume of approximately 12 000 m^3 (defined as the region in which the field exceeds 50 mT). The structure of the ATLAS detector itself is determined by the layout of the magnetic system (see Figure 1.4). The spatial arrangement of the coil windings is shown in Figure 1.5.

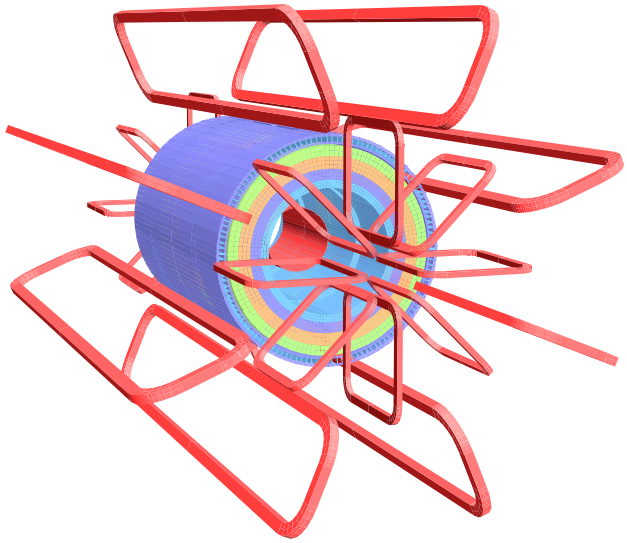

Figure 1.5: View of the coil windings forming the ATLAS magnetic system.

The central solenoid is designed to provide a 2 T axial field. To achieve the desired calorimeter performance, the layout is carefully optimised to keep the material thickness in front of the calorimeter as low as possible, resulting in the solenoid assembly contributing a total of ~ 0.66 radiation lengths at normal incidence. The inner and outer diameters of the solenoid are 2.46 m and 2.56 m and its axial length is 5.8 m. The flux is returned by the steel of the ATLAS hadronic calorimeter and its girder structure.

The system that generates the magnetic field for the muon spectrometer is composed of three large air-core toroids. The field is hence centered on the beam axis, perpendicular to the solenoidal field that serves the Inner Detector. The two end-cap toroids (inner diameter 1.65 m, outed diameter 10.7 m, length 5.0 m) are inserted in the barrel toroid (inner diameter 9.4 m, outed diameter 20.1 m, length 25.3 m) at each end and line up with the central solenoid. Each of the three toroids consists of eight coils assembled radially and symmetrically around the beam axis. The end-cap toroid coil system is rotated by 22.5° with respect to the barrel toroid coil system in order to provide radial overlap and to optimise the bending power at the interface between the two coil systems. The barrel toroid coils are housed in eight individual cryostats, with the linking elements between them providing the overall mechanical stability. Each end-cap toroid consists of eight racetrack-like coils in an aluminium alloy housing. Each coil has two double-pancake type windings. They are cold-linked and assembled as a single cold mass, housed in one large cryostat. Therefore the internal forces in the end-cap toroids are taken by the cold supporting structure between the coils, a different design solution than in the barrel toroid.

The performance of the toroids in terms of bending power is characterized by the field integral $\int B\mathrm{d}l$, where B is the field component normal to the muon direction and the integral is computed along an infinite momentum muon trajectory, between the innermost and outermost muon-chamber planes.

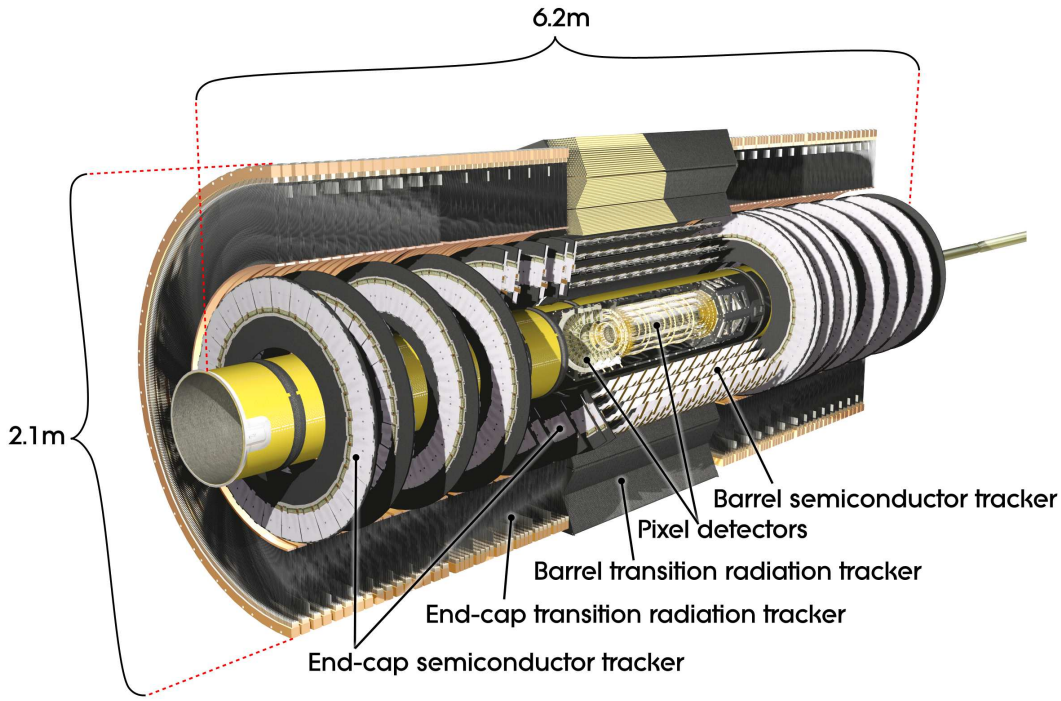

Figure 1.6: View of the Inner Detector structure.

The barrel toroid provides 1.5 to 5.5 Tm of bending power in the pseudorapidity range $0 < |\eta| < 1.4$, and the end-cap toroids approximately 1 to 7.5 Tm in the region $1.6 < |\eta| < 2.7$. The bending power is lower in the transition regions where the two magnets overlap ($1.4 < |\eta| < 1.6$).

1.3.3 Inner Detector

The ATLAS Inner Detector is described in detail in Chapter 2, where the characteristics of every subsystem will be detailed. Here only the main features are reported. The Inner Detector layout is illustrated in Figure 1.6: it is composed of pixel and silicon micro-strip (SCT) trackers in the internal region, used in conjunction with the straw tubes of the Transition Radiation Tracker (TRT) for the external layers and it is immersed in the 2 T magnetic field generated by the central solenoid

The precision tracking detectors (Pixel Detector and SCT) cover the region $|\eta| < 2.5$. In the barrel region, they are arranged on concentric cylinders around the beam axis while in the end-cap regions they are located on disks perpendicular to the beam axis. The highest granularity is achieved around the vertex region using silicon pixel detectors. All pixel sensors are identical and have a typical pixel size of 50×400 μm, allowing a resolution of 10 μm in R-Φ direction and 115 μm in z (R) direction for the barrel (disks). The Pixel Detector has approximately 80.4 million read-out channels and should provide three measurements for each track.

For the SCT, eight silicon strip detectors are crossed by each track. They are coupled in pairs with 40 mrad stereo angles to provide a total of four space points. In the barrel region each layer parallel to

the beam direction, measuring R-Φ. It consist of two 6.4 cm long daisy-chained sensors with a strip pitch of 80 μm. In the end-cap region, the detectors have a set of strips running radially. The mean pitch of the strips is also approximately 80 μm. The intrinsic accuracies per module are 17 μm (R-Φ) and 580 μm (z or R). The total number of read-out channels in the SCT is approximately 6.3 million.

A large number of hits (typically 36 per track) is provided by the 4 mm diameter straw tubes of the TRT, which enables track-following up to $|\eta| < 2.5$. The TRT only provides R-Φ information, for which it has an intrinsic accuracy of 130 μm per straw. In the barrel region, the straws are parallel to the beam axis and are 144 cm long, with their wires divided into two halves, approximately at $|\eta| = 0$. In the end-cap region, the 37 cm long straws are arranged radially in wheels. The total number of TRT read-out channels is approximately 351 000.

The combination of precision trackers at small radii with the TRT at a larger radius gives very robust pattern recognition and high precision in both R-Φ and z coordinates. The straw hits at the outer radius contribute significantly to the momentum measurement, since the lower precision per point compared to the silicon is compensated by the large number of measurements and longer measured track length. The Inner Detector system provides tracking measurements in a range matched by the precision measurements of the Electromagnetic Calorimeter. The electron identification capabilities are enhanced by the detection of transition-radiation photons in the xenon-based gas mixture of the straw tubes. The semiconductor trackers also allow impact parameter measurements and vertex reconstruction for heavy-flavour and τ lepton tagging. The secondary vertex measurement performance is enhanced by the innermost layer of pixels, at a radius of about 5 cm.

1.3.4 Calorimeters

A view of the sampling calorimeters is presented in Figure 1.7. These calorimeters cover the range $|\eta| < 4.9$, using different techniques suited to the widely varying requirements of the physics processes of interest and of the radiation environment over this large η-range. Over the η region matched to the Inner Detector, the fine granularity of the Electro-Magnetic (EM) calorimeter is ideally suited for precision measurements of electrons and photons. The coarser granularity of the rest of the calorimeter is sufficient to satisfy the physics requirements for jet reconstruction and $E_{\mathrm{T}}^{\mathrm{miss}}$ measurements. Calorimeters must provide good containment for electromagnetic and hadronic showers, as well as limit punch-through into the muon system. Hence, calorimeter depth is an important consideration. The total thickness of the EM calorimeter is more than 22 radiation lengths (X_0) in the barrel and more than 24 X_0 in the end-caps. The approximate 9.7 interaction lengths (λ) of active calorimeter in the barrel (10 λ in the end-caps) are adequate to provide good resolution for high-energy jets (see Table 1.1). The total thickness, including 1.3 λ from the outer support, is 11 λ at $\eta = 0$ and has been shown both by measurements and simulations to be sufficient to reduce punch-through well below the irreducible level of prompt or decay muons. Together with the large η coverage, this thickness will also ensure a good $E_{\mathrm{T}}^{\mathrm{miss}}$ measurement, which is crucial for many physics signatures.

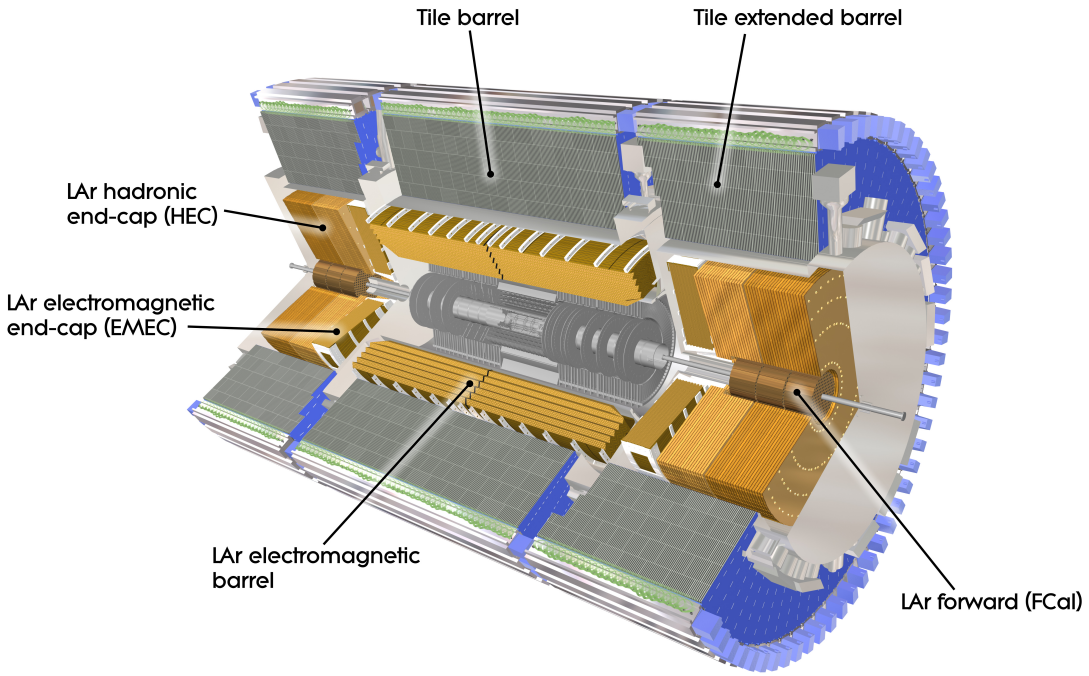

Figure 1.7: Cut-away view of the ATLAS calorimeter system.

The EM calorimeter is divided into a barrel part ($|\eta| < 1.475$) and two end-cap components ($1.375 < |\eta| < 3.2$), each one housed in its own cryostat. The position of the central solenoid in front of the EM calorimeter demands optimisation of the material in order to achieve the desired calorimeter performance. As a consequence, the central solenoid and the LAr calorimeter share a common vacuum vessel, thereby eliminating two vacuum walls. The barrel calorimeter consists of two identical half-barrels, separated by a small gap (4 mm) at $z = 0$. Each end-cap calorimeter is mechanically divided into two coaxial wheels: an outer wheel covering the region $1.375 < |\eta| < 2.5$, and an inner wheel covering the region $2.5 < |\eta| < 3.2$.

The EM calorimeter is a lead-LAr detector with accordion-shaped kapton electrodes and lead absorber plates over its full coverage. The accordion geometry provides complete Φ symmetry without azimuthal cracks. The lead thickness in the absorber plates has been optimised, as a function of η, in terms of EM calorimeter performance in energy resolution. Over the region devoted to precision physics ($|\eta| < 2.5$), the EM calorimeter is segmented into three longitudinal sections. For the end-cap inner wheel, the calorimeter is segmented in two longitudinal sections and has a coarser lateral granularity than for the rest of the acceptance. In the region of $|\eta| < 1.8$, a pre-sampler detector is used to correct for the energy lost by electrons and photons upstream of the calorimeter. The pre-sampler consists of an active LAr layer of thickness 1.1 cm (0.5 cm) in the barrel (end-cap) region.

The tile calorimeter is placed directly outside the EM calorimeter envelope. Its barrel covers the region $|\eta| < 1.0$, and its two extended barrels the range $0.8 < |\eta| < 1.7$. It is a sampling calorimeter

using steel as the absorber and scintillating tiles as the active material. The barrel and extended barrels are divided azimuthally into 64 modules. Radially, the tile calorimeter extends from an inner radius of 2.28 m to an outer radius of 4.25 m. It is longitudinally segmented in three layers approximately 1.5, 4.1 and 1.8 interaction lengths thick for the barrel and 1.5, 2.6, and 3.3 interaction length for the extended barrel. The total detector thickness at the outer edge of the tile-instrumented region is $9.7\,\lambda$ at $\eta = 0$. The tiles are 3 mm thick and the total thickness of the steel plates in one period is 14 mm. Two sides of the scintillating tiles are read out by wavelength shifting fibres into two separate photomultiplier tubes. In η, the read-out cells, built by grouping fibres into the photo-multipliers, are pseudo-projective towards the interaction region.

The Hadronic End-cap Calorimeter (HEC) consists of two independent wheels per end-cap, located directly behind the end-cap electromagnetic calorimeter and sharing the same LAr cryostats. To reduce the drop in material density at the transition between the end-cap and the forward calorimeter (around $|\eta| = 3.1$), the HEC extends out to $|\eta| = 3.2$, thereby overlapping with the forward calorimeter. Similarly, the HEC η range also slightly overlaps that of the tile calorimeter ($|\eta| < 1.7$) by extending to $|\eta| = 1.5$. Each wheel is built from 32 identical wedge-shaped modules, assembled with fixtures at the periphery and at the central bore. Each wheel is divided into two longitudinal segments, for a total of four layers per end-cap. The wheels closest to the interaction point are built from 25 mm parallel copper plates, while those further away use 50 mm copper plates (for all wheels the first plate is half-thickness). The outer radius of the copper plates is 2.03 m, while the inner radius is 0.475 m (except in the overlap region with the forward calorimeter where this radius becomes 0.372 m). The copper plates are interleaved with 8.5 mm LAr gaps, providing the active medium for this sampling calorimeter.

The Forward Calorimeter (FCal) is integrated into the end-cap cryostats, as this provides clear benefits in terms of uniformity of the calorimetric coverage as well as reduced radiation background levels in the muon spectrometer. In order to reduce the amount of neutron albedo in the Inner Detector cavity, the front face of the FCal is recessed by about 1.2 m with respect to the EM calorimeter front face. This severely limits longitudinal space and therefore calls for a high-density design. The FCal is approximately 10 interaction lengths deep, and consists of three modules in each end-cap: the first, made of copper, is optimised for electromagnetic measurements, while the other two, made of tungsten, measure predominantly the energy of hadronic interactions. Each module consists of a metal matrix, with regularly spaced longitudinal channels filled with the electrode structure consisting of concentric rods and tubes parallel to the beam axis. The LAr in the gap between the rod and the tube is the sensitive medium. This geometry allows for excellent control of the gaps, which are as small as 0.25 mm in the first section, in order to avoid problems due to ion buildup.

1.3.5 Muon spectrometer

The conceptual layout of the muon spectrometer is shown in Figure 1.8. It is based on the magnetic deflection of muon tracks in the large superconducting air-core toroid magnets, instrumented with separate trigger and high-precision tracking chambers. Over the range $|\eta| < 1.4$, magnetic bending is

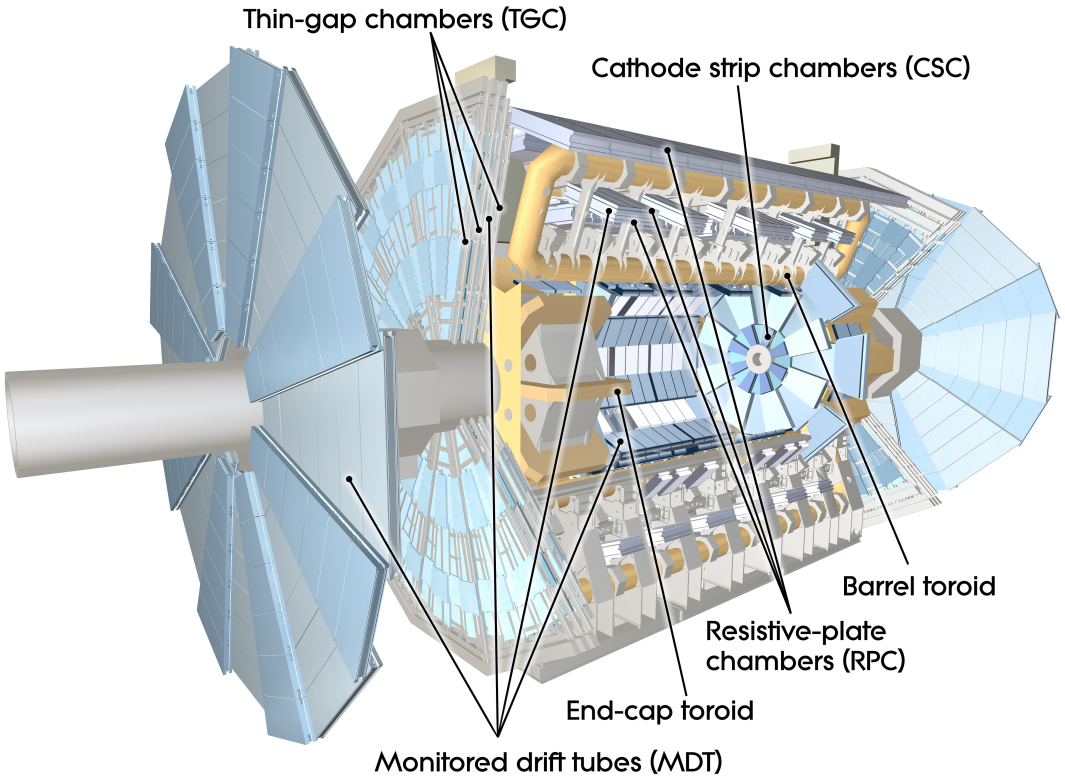

Figure 1.8: Cut-away view of the ATLAS muon spectrometers.

provided by the large barrel toroid. For $1.6 < |\eta| < 2.7$, muon tracks are bent by two smaller end-cap magnets inserted into both ends of the barrel toroid. Over $1.4 < |\eta| < 1.6$, usually referred to as the transition region, magnetic deflection is provided by a combination of barrel and end-cap fields. This magnet configuration provides a field which is mostly orthogonal to the muon trajectories, while minimising the degradation of resolution due to multiple scattering. The anticipated high level of particle flux has had a major impact on the choice and design of the spectrometer instrumentation, affecting performance parameters such as rate capability, granularity, ageing properties, and radiation hardness. In the barrel region, tracks are measured in chambers arranged in three cylindrical layers around the beam axis; in the transition and end-cap regions, the chambers are installed in planes perpendicular to the beam, also in three layers.

Over most of the η-range, a precision measurement of the track coordinates in the principal bending direction of the magnetic field is provided by Monitored Drift Tubes (MDT). The mechanical isolation in the drift tubes of each sense wire from its neighbours guarantees a robust and reliable operation. At large pseudorapidities, Cathode Strip Chambers (CSC, which are multi-wire proportional chambers with cathodes segmented into strips) with higher granularity are used in the innermost plane over $2 < |\eta| < 2.7$, to withstand the demanding rate and background conditions. The stringent requirements on the relative alignment of the muon chamber layers are met by the combination of precision mechanical-assembly techniques and optical alignment systems both within and between muon cham-

bers. The trigger system covers the pseudorapidity range $|\eta| < 2.4$. Resistive Plate Chambers (RPC) are used in the barrel and Thin Gap Chambers (TGC) in the end-cap regions. The trigger chambers for the muon spectrometer serve a three-fold purpose: provide bunch-crossing identification, provide well-defined transverse momentum thresholds, and measure the muon coordinate in the direction orthogonal to that determined by the precision-tracking chambers.

The overall performance over the large areas involved, particularly at the highest momenta, depends on the alignment of the muon chambers with respect to each other and with respect to the overall detector. The accuracy of the stand-alone muon momentum measurement necessitates a precision of 30 μm on the relative alignment of chambers both within each projective tower and between consecutive layers in immediately adjacent towers. The internal deformations and relative positions of the MDT chambers are monitored by approximately 12 000 precision-mounted alignment sensors, all based on the optical monitoring of deviations from straight lines. Because of geometrical constraints, the reconstruction and/or monitoring of the chamber positions rely on somewhat different strategies and sensor types in the end-cap and barrel regions, respectively. The accuracy required for the relative positioning of non-adjacent towers to obtain adequate mass resolution for multi-muon final states, lies in the few millimetre range. This initial positioning accuracy is approximately established during the installation of the chambers. Ultimately, the relative alignment of the barrel and forward regions of the muon spectrometer, of the calorimeters and of the Inner Detector will rely on high-momentum muon trajectories. For magnetic field reconstruction, the goal is to determine the bending power along the muon trajectory to a few parts in a thousand. The field is continuously monitored by a total of approximately 1800 Hall sensors distributed throughout the spectrometer volume. Their readings are compared with magnetic-field simulations and used for reconstructing the position of the toroid coils in space, as well as to account for magnetic perturbations induced by the tile calorimeter and other nearby metallic structures.

1.3.6 Forward detectors

Three smaller detector systems cover the ATLAS forward region. The main function of the first two systems is to determine the luminosity delivered to ATLAS. At $\pm$17 m from the interaction point lies LUCID (LUminosity measurement using Cerenkov Integrating Detector). It detects inelastic p-p scattering in the forward direction, and is the main online relative-luminosity monitor for ATLAS. The second detector is ALFA (Absolute Luminosity For ATLAS). Located at $\pm$240 m, it consists of scintillating fibre trackers located inside Roman pots which are designed to approach as close as 1 mm to the beam. The third system is the Zero-Degree Calorimeter (ZDC), which plays a key role in determining the centrality of heavy-ion collisions. It is located at $\pm$140 m from the interaction point, just beyond the point where the common straight-section vacuum-pipe divides back into two independent beam-pipes. The ZDC modules consist of layers of alternating quartz rods and tungsten plates which will measure neutral particles at pseudorapidities $|\eta| \geq 8.2$.

1.3.7 DAQ, trigger and control system

The Trigger and Data Acquisition (collectively TDAQ) systems, the timing- and trigger-control logic, and the Detector Control System (DCS) are partitioned into sub-systems, typically associated with sub-detectors, which have the same logical components and building blocks.

The trigger system has three distinct levels: Level-1 (L1), Level-2 (L2), and the Event Filter (EF). Each trigger level refines the decisions made at the previous level and, where necessary, applies additional selection criteria. The data acquisition system receives and buffers the event data from the detector-specific read-out electronics, at the L1 trigger accept rate, over 1600 point-to-point read-out links. The first level trigger uses a limited amount of the total detector information to make a decision in less than 2.5 μs, reducing the rate to about 75 kHz. The other two triggers, collectively known as High Level Trigger (HLT) [42], access more detector information for a final rate of up to 200 Hz with an event size of approximately 1.3 Mbyte.

The L1 trigger searches for high-p_{T} muons, electrons, photons, jets, and τ leptons decaying into hadrons, as well as large missing and total transverse energy. Its selection is based on information from a subset of detectors. High transverse-momentum muons are identified using trigger chambers in the barrel (RPC) and end-cap (TGC) regions of the spectrometer. Calorimeter selections are based on reduced-granularity information from all the calorimeters. Results from the L1 muon and calorimeter triggers are processed by the central trigger processor, which implements a trigger menu made up of combinations of trigger selections. Pre-scaling of trigger menu items is also available, allowing optimal use of the bandwidth as luminosity and background conditions change.

Events passing the L1 trigger selection are transferred to the next stages of the detector-specific electronics and subsequently to the data acquisition via point-to-point links. In each event, the L1 trigger also defines one or more Regions-of-Interest (RoIs), i.e. the geographical coordinates in η and Φ, of those regions within the detector where its selection process has identified interesting features. The RoI data include information on the type of feature identified and the criteria passed, e.g. a threshold. The L2 selection is seeded by the RoI information provided by the L1 trigger over a dedicated data path. L2 selections use, at full granularity and precision, all the available detector data within the RoIs (approximately 2% of the total event data). The L2 menus are designed to reduce the trigger rate to approximately 3.5 kHz, with an event processing time of about 40 ms, averaged over all events. The final stage of the event selection is carried out by the Event Filter, which reduces the event rate to roughly 200 Hz. Its selections are implemented using offline analysis procedures (see Section 1.4.2) within an average event processing time of the order of four seconds.

The Read Out Drivers (RODs) are detector-specific functional elements of the front-end systems, which achieve a higher level of data concentration and multiplexing by gathering information from several front-end data streams. Although each sub-detector uses specific front-end electronics and RODs, these components are built from standardised blocks and are subject to common requirements. The front-end electronics sub-system includes different functional components:

- the front-end analogue or analogue-to-digital processing;
- the L1 buffer in which the (analogue or digital) information is retained for a time long enough to accommodate the L1 trigger latency;
- the de-randomising buffer which stores the data corresponding to a L1 accept, in order to accommodate the maximum rate without introducing significant dead-time;
- the dedicated links or buses which are used to transmit the front-end data stream to the next stage.

After an event is accepted by the L1 trigger, the data from the pipe-lines are transferred off the detector to the RODs. Digitised signals are formatted as raw data prior to being transferred to the DAQ system. The RODs follow some general ATLAS rules, including the definition of the data format of the event, the error detection/recovery mechanisms to be implemented, and the physical interface for the data transmission to the DAQ system. The first stage of the DAQ, the read-out system, receives and temporarily stores the data in local buffers. It is subsequently solicited by the L2 trigger for the event data associated to RoIs. Those events selected by the L2 trigger are then transferred to the event-building system and subsequently to the event filter for final selection. Events selected by the event filter are moved to permanent storage at the CERN computer centre. In addition to the movement of data, the data acquisition also provides for the configuration, control and monitoring of the hardware and software components which together provide the data-taking functionality.

The DCS permits the coherent and safe operation of the ATLAS detector hardware, and serves as a homogeneous interface to all sub-detectors and to the technical infrastructure of the experiment. It controls, continuously monitors and archives the operational parameters, signals any abnormal behaviour to the operator, and allows automatic or manual corrective actions to be taken. Typical examples are high- and low-voltage systems for detector and electronics, gas and cooling systems, magnetic field, temperatures, and humidity. The DCS also enables bi-directional communication with the data acquisition system in order to synchronise the state of the detector with data-taking. It also handles the communication between the sub-detectors and other systems which are controlled independently, such as the LHC accelerator, the CERN technical services, the ATLAS magnets, and the detector safety system.

1.4 Software infrastructure

1.4.1 Geometry and conditions databases

Two databases are used to store informations about the detector status: one to store the detector description (the ATLAS geometry database), and one to store various conditions data (e.g. calibrations, dead channels, misalignments) for each specific data taking run (the ATLAS conditions database) [43]. Both the geometry and conditions databases support versioning of the data. The data are organized in a *tree* consisting of *branch* and *leaf* nodes. The nodes in this tree can be tagged, and one can create a

hierarchy of the tags. Such tag hierarchies are uniquely identified by the tag of the root node, which is usually referred to as top level geometry or conditions tag.

The geometry database stores all fundamental constants for detector construction. Volume dimensions, rotations, and positions, as well as element and material properties including density and radiation lenght, are all stored as database entries. Each sub-detector can update entries in the database and create a new detector-specific tag for inclusion in a global ATLAS geometry tag, where different tags generally correspond to different detector geometry revisions. When reconstruction or analysis of the events is done (see Section 1.4.2), the user can select a global geometry tag as well as detector-specific geometry tags to take advantage of the desired geometry. In addition to constants for detector construction, the geometry database contains links to external data files that may store, for example, magnetic field maps. By using links through the database, it is possible to select a magnetic field map based on the chosen geometry layout.

The conditions database stores detector conditions data which are indexed by intervals of validity and tags. During data collection, many calibration and alignment constants of the detector are recorded periodically in the central conditions database. The user can access calibrations and misalignment conditions for a specific run by selecting the required tag, by sub-detector if desired, at run time.

Simulation software (see Section 1.4.3) can access the geometry and conditions database to recreate a realistic description of the detector geometry, alignment and calibration. Other than accessing tags relative to data taking runs, the entire detector geometry may be optionally modified with ad-hoc global tags, for example to study the performance of the entire ATLAS detector with misalignments of the expected as-built magnitude. A variety of misalignments have been used in the lead-up to data taking in order to speed the process of global detector alignment and improve early physics searches.

1.4.2 Reconstruction software

The ATLAS Computing Model embraces the Grid paradigm and a high degree of decentralisation and sharing of computing resources [44]. The ATLAS detector, in fact, will produce approximately 3 Pbyte of raw data per year, a vast amount of information which prohibits the simple distribution to worldwide collaborators. The required level of computing resources means that off-site facilities will be vital to the operation of ATLAS in a way that was not the case for previous CERN-based experiments.

The primary event processing occurs at CERN in a Tier-0 Facility. The raw data collected by detectors are archived at CERN and copied (along with the primary processed data) to the Tier-1 facilities around the world. These facilities archive the raw data, provide the reprocessing capacity, provide access to the various processed versions, and allow scheduled analysis of the processed data by physics analysis groups. Derived datasets produced by the physics groups are copied to the Tier-2 facilities for further analysis. The Tier-2 facilities also provide the simulation capacity for the experiment, with the simulated data housed at Tier-1s. In addition, Tier-2 centres will provide analysis facilities, and some will provide the capacity to produce calibrations based on processing raw data. A CERN Analysis Fa-

cility provides an additional analysis capacity, with an important role in the calibration and algorithmic development work.

As a consequence of the Grid paradigm, the ATLAS software has been designed and optimize to be installed, configured and run on different computer facilities. The global framework, Athena [44], uses PYTHON as an object-oriented scripting and interpreter language to configure and load C++ algorithms and objects. Rather than develop an entirely new high-energy physics data processing infrastructure, ATLAS adopted the Gaudi framework [45], originally developed for LHCb and written in C++. Gaudi was created as a flexible framework to support a variety of applications through base classes and basic functionalities.

The high-level goals of Athena are to process the events delivered by the ATLAS trigger and data acquisition system, to deliver the processed results to physicists within the ATLAS Collaboration, and to provide tools for them to analyse the processed information in order to produce physics results. To enable physicists to analyse the data at remote sites, several different types of datasets, corresponding to different stages of reconstruction, are produced. Thus the following datasets are available:

- *Byte-stream Data* which is a persistent presentation of the event data flowing from the HLT.
- *Raw Data Object Data* (RDO) which is a C++ object representation of the byte-stream information.
- *Event Summary Data* (ESD) which contains the detailed output of the detector reconstruction and is produced from the raw data. It contains sufficient information to allow particle identification, track re-fitting, jet calibration, ..., thus allowing for the rapid tuning of reconstruction algorithms and calibrations.
- *Analysis Object Data* (AOD) which is a summary of the reconstructed event, and contains sufficient information for all common analyses.
- *Derived Physics Data* (DPD) which are tailor-made streams of AOD informations, optimized for the different needs of the physics community.

The reconstruction processing pipeline can be decomposed into several stages, from the reconstruction of the tracking and calorimetry detectors to the first steps in particle identification, until the reconstruction of complex objects, for example the b-tagging objects. The role of reconstruction is to derive from the stored raw data the relatively few particle parameters and auxiliary information necessary for physics analysis: photons, electrons, muons, τ leptons, K_0s, jets, missing transverse energy, primary vertex. Information from all detectors is combined so that the four-momentum reconstruction is optimal for the full momentum range, full rapidity range and any luminosity, and so that particles are identified with the least background, with the understanding that the optimum between efficiency and background rejection can be analysis dependent. A typical reconstruction algorithm takes one or more collections as input, calls a set of modular tools, and outputs typically one collection of reconstructed objects. Common tools are shared between tracking detectors on one side (Inner Detector and

Muon Spectrometer) and calorimeters on the other side. Reconstruction tools can share interfaces, for example for different types of calorimeter cluster corrections, or track extrapolation.

1.4.3 Simulation software

In order to study the detector response for a wide range of physics processes and scenarios, a detailed simulation has been implemented that carries events from the event generation through to output in a format which is identical to that of the true detector. The simulation program is integrated into the ATLAS software framework and uses the GEANT4 simulation toolkit [46, 47].

The simulation software chain is generally divided into three steps: generation of the event and immediate decays, simulation of the detector and physics interactions, and digitization of the energy deposited in the sensitive regions of the detector into voltages and currents for comparison to the read-out of the ATLAS detector. The output of the simulation chain can be presented in either an object-based format or in a format identical to the output of the ATLAS data acquisition system. Thus, both the simulated and real data from the detector can then be run through the same ATLAS trigger and reconstruction packages. Moreover, the ATLAS detector geometry used for simulation, digitization, and reconstruction is built from databases containing the information describing the physical construction and conditions data. The latter contains all the information needed to emulate a single data-taking run of the real detector (e.g. detector misalignments and temperatures).

Event generation

Event generation consists of the production of a set of particles which is then passed to detector simulation. Event generation runs within the Athena framework, but most of the generators themselves are written and maintained by authors external to ATLAS. The ATLAS-specific implementation, therefore, consists mostly of a set of interface packages.

Event production has been run with PYTHIA [48] (including an ATLAS variant, PythiaB [49, 50], used for production of events with b-hadrons), HERWIG [51–53], Sherpa [54], Hijing [55], Alpgen [56], MC@NLO [57], and AcerMC [58]. Tauola [59] and Photos [60] are used to handle τ decays and photon emission. EvtGen [61] is used for b-decays in cases where the physics is sensitive to details of the b-hadron decays. ISAJET [62] is used for generating SUSY particles in conjunction with HERWIG. The newer C++ generators PYTHIA 8 [63] and HERWIG++ [64] are being tested. Some production was also done with MadGraph [65], for vector boson scattering, and CHARYBDIS [66], for black-hole events generation. Single particle generators are also used to generate cosmic ray events and single particle events for performance studies and calibration of the detector.

Each generated event contains the particles from a single interaction with a vertex located at the geometric origin. Modifications to account for the beam properties are applied to the event before it is passed to GEANT4. Particles with a proper lifetime $c\tau > 10$ mm are considered stable by the event generator, since they can propagate far enough to interact with detector material before decaying. Any particles with $c\tau < 10$ mm, instead, are decayed by the event generator, and their interactions with

material or curving in the magnetic field of ATLAS are ignored. Because the generator only considers immediate decays, there is no need to consider detector geometry during the generation step, except in controlling what particles are considered stable. Events can be filtered at generation time so that only events with a certain property (e.g. leptonic decay or missing energy above a certain value) are kept.

Detector and interaction simulation

The generated events are then read into the simulation. A record of all particles produced by the generator is retained in the simulation output file, but cuts can be applied to select only certain particles to process in the simulation. Each particle is propagated through the full ATLAS detector by GEANT4. The configuration of the detector, including misalignments and distortions, is read from databases at this stage. The energies deposited in the sensitive portions of the detector are recorded as *hits*, containing the total energy deposition, position, and time.

In both event generation and detector simulation, *truth* information is recorded for each event. In the generation jobs, the truth is a history of the interactions from the generator, including incoming and outgoing particles. A record is kept for every particle, whether the particle is to be passed through the detector simulation or not. In the simulation jobs, truth tracks and decays for certain particles are stored. This truth contains, for example, the locations of the conversions of photons within the Inner Detector and the subsequent electron and positron tracks.

The interaction of particles that are considered include bremsstrahlung, ionization, hadronic interaction, decays and photon conversions. For each interaction a limit on the energy of the produced particles can be set, to decide whether it is propagated into the detector or it is accounted for together with the particle from which it originated. *Physics lists* include all numerical models that describe the particles interactions in the GEANT4 simulation.

Digitization

The ATLAS digitization software converts the hits produced by the core simulation into detector responses called *digits*. Typically, a digit is produced when the voltage or current on a particular read-out channel rises above a pre-configured threshold within a particular time-window. Some sub-detectors include the signal shape in detail over this time, while others simply record that the threshold has been exceeded within the relevant time window. The peculiarities of each sub-detector, including cross-talk, electronic noise and channel-dependent variations in detector response are modelled in sub-detector specific digitization software.

Simulating the detector read-out in response to a single interesting hard scattering interaction is unrealistic. In reality, for any given bunch crossing there may be multiple proton-proton interactions. In addition to the hard scattering which triggers the detector read-out, many inelastic, non-diffractive proton-proton interactions may appear. These interactions must be included in a realistic model of detector response. The effects of beam gas and beam halo interactions, as well as detector response to long-lived particles, must be incorporated. These interactions are treated separately at the event generation and simulation stages. Within a digitization job, hits from the hard scattering are overlaid

with those from the requested number of these additional interactions before the detector response is calculated. Because of long signal integration times, most sub-detector responses are affected by interactions from neighboring bunch crossings as well. Therefore, additional interactions offset in time are overlaid as necessary. The overlaying of these various types of events is known collectively as *pile-up*.

During the digitization, the first level trigger, that is installed in hardware on the real detector, is simulated in a "pass" mode. In fact no events are discarded but each trigger hypothesis is evaluated. Subsequently, the read-out functionality of the detector is emulated, and the output is registered. The High Level Trigger (see Section 1.3.7) and the reconstruction (see Section 1.4.2) can be run directly on this output.

Chapter 2

The ATLAS Inner Detector tracking system

The ATLAS Inner Detector (ID) is designed to provide hermetic and robust pattern recognition, excellent momentum resolution and both primary and secondary vertex measurements for charged tracks above a nominal p_{T} threshold of 0.5 GeV and within the pseudorapidity range $|\eta| < 2.5$. It also provides electron identification over $|\eta| < 2.0$ and a wide range of energies (i.e. between 0.5 GeV and 150 GeV) [67, 68].

The ID layout has been shown in Figure 1.6 and reflects the performance requirements. The ID is contained within a cylindrical envelope of length ± 3512 mm and of radius 1150 mm, within a solenoidal magnetic field of 2 T (see Section 1.3.2). Figures 2.1 and 2.2 show the sensors and structural elements traversed by 10 GeV tracks in respectively the barrel and end-cap regions.

The ID consists of three independent but complementary sub-detectors. At inner radii, high-resolution pattern recognition capabilities are available using discrete space-points from silicon pixel layers (Pixel Detector) and stereo pairs of silicon microstrip layers (SCT). At larger radii, the Transition Radiation Tracker (TRT) comprises many layers of gaseous straw tube elements interleaved with transition radiation material. With an average of 36 hits per track, it provides continuous tracking to enhance the pattern recognition and improve the momentum resolution over $|\eta| < 2.0$ and electron identification complementary to that of the calorimeter over a wide range of energies.

The high-radiation environment imposes stringent conditions on the Inner Detector sensors, on-detector electronics, mechanical structure and services. Over the ten-year design lifetime of the experiment, the pixel inner vertexing layer must be replaced after approximately three years of operation at design luminosity. The other pixel layers and the pixel disks must withstand a 1 MeV neutron equivalent fluence (F_{neq}) of up to 8×10^{14} cm^{-2}. The innermost parts of the SCT must withstand F_{neq} of up to 2×10^{14} cm^{-2}. To maintain an adequate noise performance after radiation damage, the silicon sensors must be kept at low temperature (approximately -5 to -10°C) implying coolant temperatures of -25°C. In contrast, the TRT is designed to operate at room temperature.

The operating specifications imply requirements on the alignment precision which are summarised in Table 2.1 and which serve as stringent upper limits on the silicon-module build precision, the TRT straw-tube position, and the measured module placement accuracy and stability. This leads to:

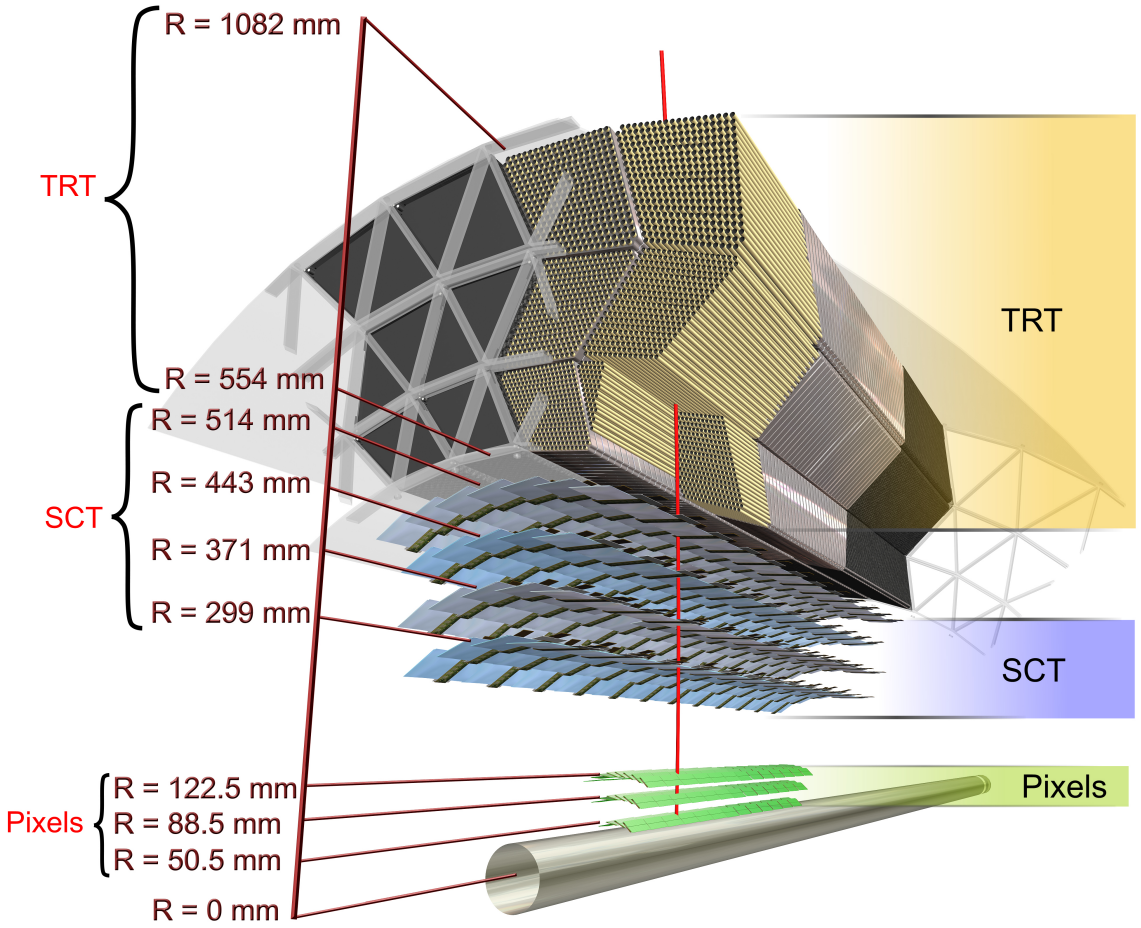

Figure 2.1: Scheme of the ATLAS inner detector barrel being crossed by one high-energy particle, labeled and with dimensions.

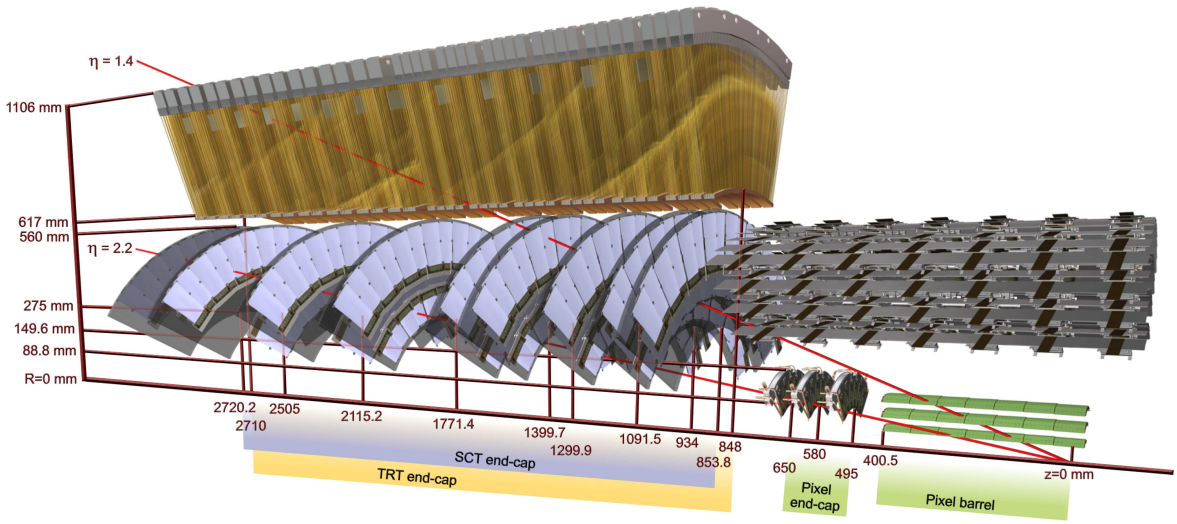

Figure 2.2: A partial view of the Inner Detector, crossed by particles coming from the interaction point

– a good build accuracy with radiation-tolerant materials having adequate detector stability and well understood position reproducibility following repeated cycling between temperatures of on the structure and module mechanics which minimises thermal distortions;

– an ability to monitor the position of the detector elements using charged tracks and, for the SCT, laser interferometric monitoring [69];

– a trade-off between the low material budget needed for optimal performance and the significant material budget needed to achieve a stable mechanical structure with the services of a highly granular detector.

The Inner Detector performance requirements imply the need for a stability between alignment periods which is high compared with the alignment precision. Quantitatively, the track precision should not deteriorate by more than 20% between alignment periods.

This chapter describes the characteristics of each of the Inner Detector constituents and reports an application of Inner Detector measurements to a physics analysis. In Section 2.1 the description of the Pixel Detector is reported. The SCT is described in Section 2.2, while the TRT is illustrated in Section 2.3. Finally, Section 2.4 introduces the issue of identifying b-hadrons (b-tagging). These particles are characterized by a short life-time that makes them to decay at a small but measurable distance from the primary interaction vertex. Algorithms that take advantage of the optimal vertex resolution given by the ID are presented. As a conclusion, the improvement given by b-hadrons identification in the selection of top quark pair ($t\bar{t}$) events is evaluated.

Item	Intrinsic accuracy (μm)	Alignment tolerances (μm)		
		Radial (R)	Axial (z)	Azimuth (R-ϕ)
Pixel				
Layer-0	10 (R-ϕ) 115 (z)	10	20	7
Layer-1 and -2	10 (R-ϕ) 115 (z)	20	20	7
Disks	10 (R-ϕ) 115 (R)	20	100	7
SCT				
Barrel	17 (R-ϕ) 580 (z)[1]	100	50	12
Disks	17 (R-ϕ) 580 (R)[1]	50	200	12
TRT	130			30[2]

[1] Arises from the 40 mrad stereo angle between back-to-back sensors on the SCT modules with axial (barrel) or radial (end-cap) alignment of one side of the structure. The result is pitch-dependent for end-cap SCT modules.

[2] The quoted alignment accuracy is related to the TRT drift-time accuracy.

Table 2.1: Intrinsic measurement accuracies and mechanical alignment tolerances for the Inner Detector subsystems, as defined by the performance requirements of the ATLAS experiment. The numbers in the table correspond to the single-module accuracy for the pixels, to the effective single-module accuracy for the SCT and to the drift-time accuracy of a single straw for the TRT. The table is taken from [4].

2.1 The Pixel Detector

The pixel tracker [70] is designed to provide at least three points on a charged track emanating from the collision region in ATLAS. The Pixel Detector, as the other elements of the Inner Detector, spans a pseudorapidity range $|\eta| < 2.5$.

The principal components of the pixel tracking system are the active region, the internal services (power, monitoring, optical input/output and cooling) and their associated mechanical support structures, the Pixel Support Tube into which the active part and the services are inserted and, finally, the external services that are connected to the internal services at the end of the Pixel Support Tube.

The active region of the pixel detector is shown in a schematic view in Figure 2.3. It consists of three barrel layers — *Layer 0* (so-called *b-Layer*), *Layer 1* and *Layer 2* — and two identical end-cap regions, each with three disk layers. The basic building block of the active part of the pixel detector is a module (Section 2.1.2) that is composed of silicon sensors (Section 2.1.1), front-end electronics and flex-hybrids with control circuits (Section 2.1.3). All modules are functionally identical at the sensor/integrated circuit level. The nominal pixel size is 50 microns in the Φ direction and 400 microns in z (barrel region) or R (disk region) for about 90% of pixels. The total number of pixels in the system is approximately 67 million in the barrel and 13 million in the end-caps, covering a total active area of about 1.7 m^2. In all cases for the barrel, the top of the module faces the beam-pipe, whereas the end-cap

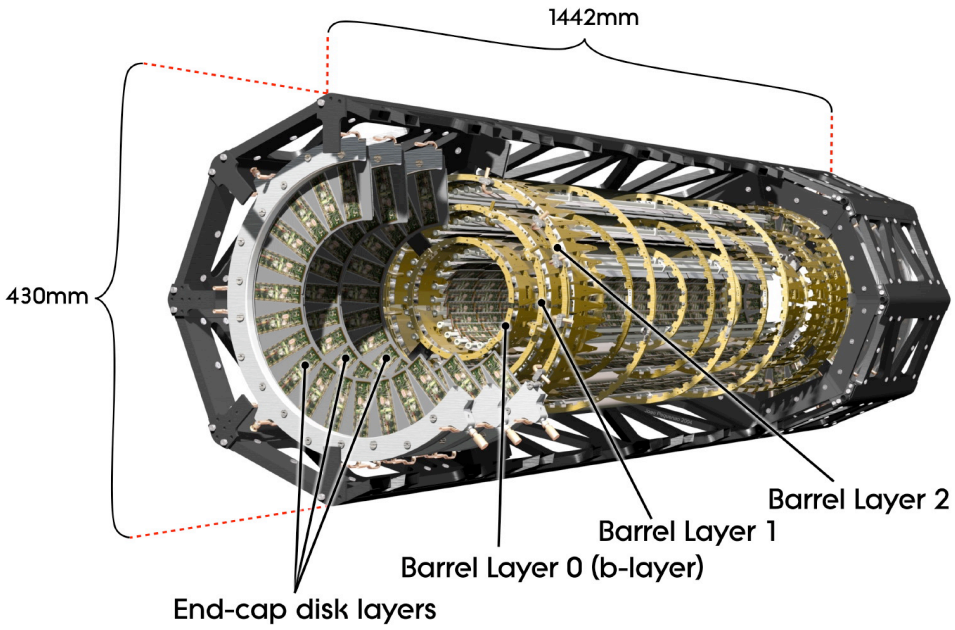

Figure 2.3: Structure of the ATLAS Pixel Detector with its overall dimensions.

disks have modules facing both ways. This means that the pixel sensors see in general the minimum amount of material in front of them, i.e. basically only the flex hybrid.

The essential parameters for the barrel region of the pixel detector system are summarized in Table 2.2. In this region, modules are mounted on mechanical supports, called *staves*. Thirteen modules are mounted on a stave and the stave layout is identical for all layers. The active length of each barrel stave is 801 mm. The staves are mounted in half-shells manufactured from a carbon-fiber composite material. Two half-shells are joined to form each barrel layer. The staves overlap and are mounted at a tilt angle (the tangent to the support cylinder surface in the plane perpendicular to the cylinder axis) of $-20°$, defined by geometrical constraints. The support structure of a stave consists of machined plates made of carbon-carbon laminate material and of an aluminium cooling tube. The tube is held in place by a carbon-fibre piece glued to the plate. The staves are joined to form bi-staves, which form the cooling unit in the barrel region. A custom-welded aluminium U-link is attached to one side of each bi-stave, in order to connect the aluminium tubes of each stave [71].

The two end-cap regions are identical. Each is composed of three disk layers, and each disk layer is identical. The basic parameters of the end-cap region are given in Table 2.3. In this case, modules are mounted on mechanical supports called disk sectors. There are eight identical sectors in each disk, comprising each six pixel modules. The sectors are composed of thin, carbon-carbon face-plates with a rectangular aluminium cooling tube and vitreous carbon foam between the face-plates. The cooling tube is bent into a W-like shape to fit within the sector and makes contact with the face-plates with a compliant, thermally conducting adhesive. Each cooling circuit in the disk region serves two sectors.

Layer Number	Mean Radius [mm]	Number of Staves	Number of Modules	Number of Channels	Active Area [m^2]
0	50.5	22	286	13,178,880	0.28
1	88.5	38	494	22,763,520	0.49
2	122.5	52	676	31,150,080	0.67
Total		112	1456	67,092,480	1.45

Table 2.2: Basic parameters for the barrel region of the ATLAS pixel detector system. Table taken from [70].

Disk Number	Mean z [mm]	Number of Sectors	Number of Modules	Number of Channels	Active Area [m^2]
0	495	8	48	2,211,840	0.0475
1	580	8	48	2,211,840	0.0475
2	650	8	48	2,211,840	0.0475
Total one endcap		24	144	6,635,520	0.14
Total both endcaps		48	288	13,271,040	0.28

Table 2.3: Basic parameters of the end-cap region of the ATLAS pixel detector system. Table taken from [70].

2.1.1 Pixel sensors

Sensors are the sensitive part of the Pixel Detector used for charged particle detection and function as a solid-state ionization chamber. The sensor must meet exacting geometrical constraints concerning thickness and granularity as well as have a high charge collection efficiency, while sustaining a massive amount of ionizing and non-ionizing particle radiation damage. On one hand, this is reflected in the selection of the bulk material and, on the other hand, it impacts the design of the pixel structure itself.

The ATLAS pixel sensor is an array of bipolar diodes placed on a high-resistivity n-type bulk close to the intrinsic charge concentration. The sensor is made by implanting high positive (p^+) and negative (n^+) dose regions on each side of a wafer. An depletion region at the p^+n junction operates in reverse bias and extends over the whole sensor bulk volume. Here, one is able to collect and detect charge carriers generated by ionizing particles passing through the active volume. The sensor design guarantees single pixel isolation, minimizes leakage current and makes the sensor testable as well as tolerant to radiation damage.

The pixel sensor consists of a 256 ± 3 μm thick n-bulk. The bulk contains n^+ implants on the read-out side and the pn junction on the back side. For each sensor tile, the 47 232 pixel implants are arranged in 144 *columns* and 328 *rows*. A *column* is made by pixels that share long sides, a *row* includes pixels with short sides adjacent. In 128 columns (41 984 or 88.9%) pixels have implant sizes of 382.5×30 μm^2 with a pitch corresponding to 400×50 μm^2, and in 16 columns (5 248 or 11.1%) pixels have implant sizes of 582.5×30 μm^2 corresponding to a pitch of 600×50 μm^2 (*long pixels*). In

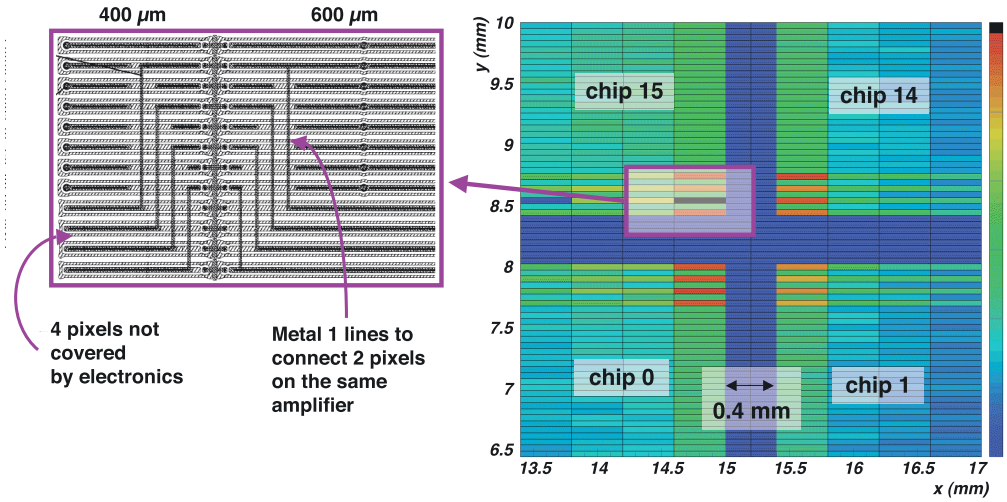

Figure 2.4: End-region of the Pixel Detector at the edge of four FE-chips. The area of the sensor covered by the chip edges is marked in grey. The pixels in between the chips (white rectangles) are connected through metal lines to another pixel underneath the chips. Figure taken from [70].

each column eight pairs of pixel implants, located near the center lines, are ganged to a common read-out (*ganged pixels*), resulting in 320 independent read-out rows or 46 080 pixel read-out channels (see Figure 2.4). This arrangement was chosen to allow for the connection of the sensor tile to 16 electronic front-end chips (see Section 2.1.3). When sensors are positioned inside ATLAS, the long side of the pixels defines the *local y* and results to be aligned with the beam axis (in the barrel) or with the radial direction (in the disks). The short side of pixels, instead, is always placed along the R-Φ directions and defines the *local x* coordinate.

Aside from increased leakage current, radiation damage will invert the sensor bulk and then gradually increase the depletion voltage. For non irradiated sensors, the depletion starts at the back (p^+) side, and the n^+ pixels are not insulated from each other until full depletion of the bulk. Irradiation of the bulk leads to a change in the effective doping concentration. First the doping concentration drops off and then runs through type inversion, after which the concentration increases [72]. At type inversion, the junction moves to the front (n^+) side, isolating the pixels and enabling operation even if the bulk cannot be fully depleted. Maximum achievable depletion is desirable to maximize the signal.

The positive and the negative implanted sensor wafer sides are both structured by mask processes for implantation, metalization and deposition of silicon-oxide and silicon-nitride. This double-sided processing demands precise mask steps and incorporates front-to-back mask alignment of a few microns, which makes the manufacturing process demanding. However, this allows for a segmented n^+ implantation used for the definition of pixel cells and a guard ring structure on the n^+ implanted wafer side, locating the main voltage drop on the sensor surface opposite to the bump connections. The sensors can be fully depleted before type inversion with bias voltages below 100 V. After type inversion the depletion zone grows primarily from the segmented n^+ implant when the region of highest electric field in the bulk now converts to p-type. On the sensor front side, pixel structures are arranged and

isolated by moderated p-spray implants [73], which have proven to be radiation tolerant with respect to surface damages induced by ionising charged particles for doses up to 500 kGy in silicon.

All 46 080 read-out channels of a sensor tile are connected to a common bias grid structure by employing a punch-through connection technique to each channel. The method biases the entire sensor without requiring individual connections, but still ensures isolation between pixels. An opening for each pixel in the passivation layer of the sensor allows for a connection to each channel using a bump-bond technique (see Section 2.1.2) to front-end electronics (see Section 2.1.3), which is DC-coupled and provides biasing for each individual pixel.

2.1.2 The Pixel module

The sensitive area of ~ 1.7 m^2 of the ATLAS pixel detector is covered with 1744 identical modules. Each module has an active surface of 6.08×1.64 cm^2. A module is assembled from the following parts:

- the sensor tile containing 47 232 pixels as described in Section 2.1.1;
- sixteen front-end electronics chips (FE) each containing 2880 pixel cells with amplifying circuitry, connected to the sensor by means of fine-pitch bump bonding;
- a fine-pitch, double-sided, flexible printed circuit (referred to as a flex-hybrid) with a thickness of about 100 mm to route signals and power;
- a module control chip (MCC) situated on the flex-hybrid;
- for the barrel modules, another flexible foil, called a pigtail, that provides the connection to electrical services via a low mass aluminium cable (*micro-cable*), whereas for the disk modules, the micro-cables were attached without the pigtail connection.

The concept of the ATLAS hybrid pixel module is illustrated in Figure 2.5. Sixteen front-end chips are connected to the sensor by means of bump bonding [74–77] and flip-chip technology. Each chip covers an area of 0.74×1.09 cm^2 and has been thinned before the flip-chip process to 195 ± 10 μm thickness by wafer-back-side grinding. A sizeable fraction ($\approx 25\%$) of the front-end chip is dedicated to the End-of-Column (EoC) logic. Once bonded, most of the EoC logic extends beyond the sensor area. Wire bonding pads at the output of the EoC logic are thus accessible to connect each front-end chip to the flex-hybrid by means of aluminum-wire wedge bonding.

The flex-hybrid is glued on the p^+ side of the sensor, opposed to the front-end. Copper traces on the flex-hybrid route the signals to the MCC. The MCC receives and transmits digital data out of the modules. The flex-hybrid is also used to distribute low-voltages to all the chips and the high-voltage for sensor depletion. The traces are dimensioned such that the voltage drop variation is limited to ≈ 50 mV in order to keep all the chips in the same operating range. The back-side of the flex-hybrid must be pinhole free, since it is glued to the high-voltage side of the sensor. A multiple solder mask layer was, therefore, used and all parts were tested up to 1000 V. Since all module components must

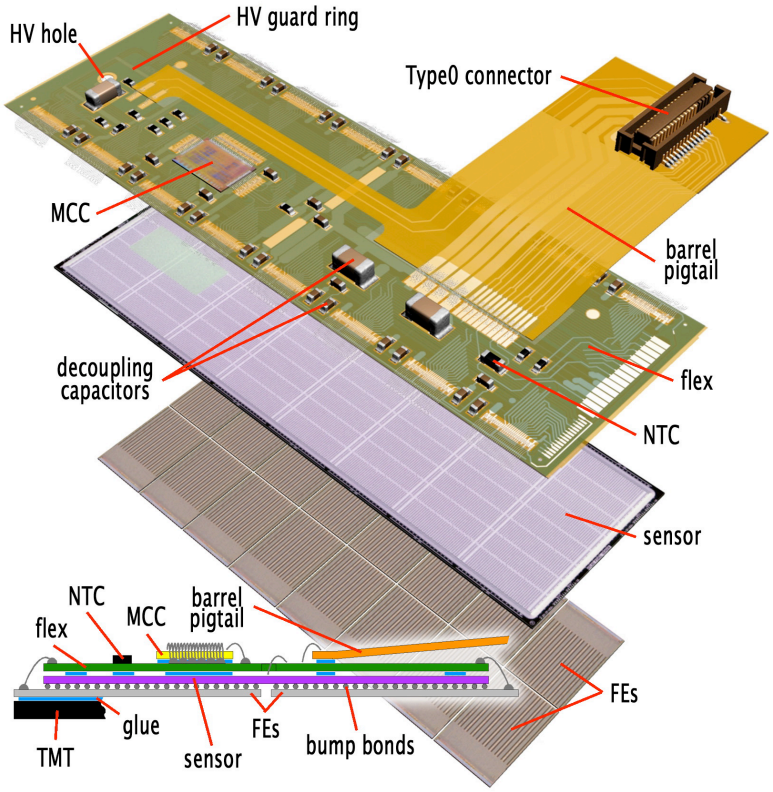

Figure 2.5: The elements of a pixel barrel module. Figure taken from [70].

withstand the lifetime radiation dose, polyimide was used as the base materials for the flex-hybrid with adhesiveless metalization. Passive components are added to the flex-hybrid for decoupling and filtering of the front-end chips. The module temperature is remotely monitored via a Negative Temperature Coefficient (NTC) thermistor loaded on the kapton circuit, and a fast interlock powers off a module when overheating occurs.

After a lifetime radiation dose, a module is expected to draw 1.3 A at 1.7 V from the analog supply and 0.9 A at 2.1 V from the digital supply. This includes the voltage drops from the pigtail (for barrel modules) and the flex-hybrid, but not the voltage drop from the micro-cables. In addition, the sensor bias draws 1 mA at 600 V, giving a total power of about 4.7 W. However, it is possible that the analog or digital supply voltages need to be increased in order to recover performance, which could result in a total power of up to about 6 W.

2.1.3 Electronics

A block diagram that illustrates the principal elements of the electronic system architecture is shown in Figure 2.6. There are 16 front-end chips (FE) in each pixel module and these are arranged in two rows of eight chips. The 16 FEs are read out by a Module Control Chip (MCC). Data are transmitted from the FE to the MCC using Low Voltage Differential Signalling (LVDS) serial links, configured in

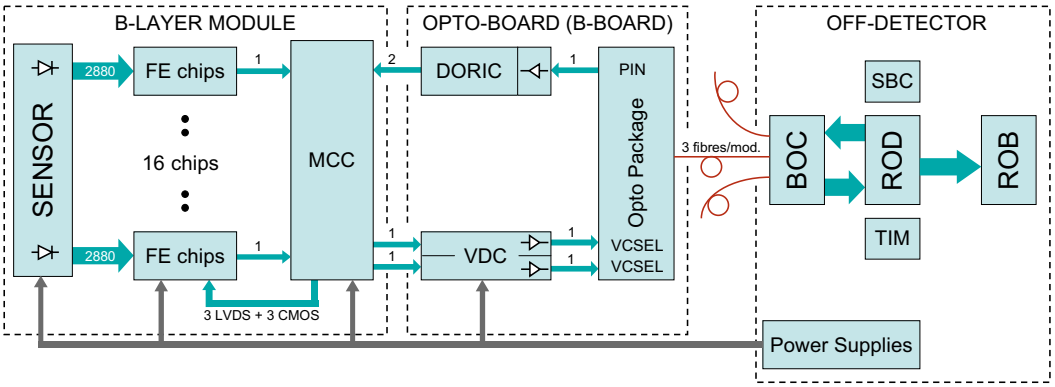

Figure 2.6: Block diagram of the pixel detector system architecture. Figure taken from [70].

a star topology. The serial protocol minimises the number of lines to be routed, while the star topology maximizes bandwidth and reliability. Each module is then connected to the off-detector Read-out Drivers (RODs) through optical-fiber links. One down link is used to transmit clock, trigger, commands and configuration data, while one or two up-links are used for event read-out. The b-Layer uses two up-links to increase the aggregate bandwidth needed for the higher average hit occupancy that occurs at the minimum radius. The read-out architecture is "data-push". This means that each component in the chain (FE, MCC) always transmits at the maximum rate, and there is no busy mechanism to stop transmission when buffers are full. Each upstream component in the read-out chain (MCC, ROD) constantly monitors the number of events received and compares the results with the number of triggers sent. If the difference of the two is bigger than a predefined value, triggers downstream are blocked and empty events are generated.

The power supply system uses a combination of customized-commercial components and fully-custom components for the low (electronics) and high (sensor bias) voltages. The use of deep sub-micron electronics, with an absolute maximum voltage rating of 4 V, required the use of low-voltage regulator boards, approximately 10 meters from the pixel detector. Signal communication between the detector and the RODs is performed over optical-links. These are custom made using commercial diode and laser array bare die with custom integrated circuits (DORIC and VDC) and packaging.

Each front-end read-out ASIC [78] of the pixel detector contains 2880 readout cells of 50×400 μm^2 size arranged in a 18×160 matrix. The ASICs are fabricated using commercial 0.25 μm CMOS technology. A high level of radiation tolerance is achieved by a combination of the process technology (thin gate oxide) and the use of special layout techniques (annular layout and guard rings for all NMOS transistors). The schematic and basic functionality of the pixel circuit is shown in Figure 2.7.

Each read-out cell contains an analogue block where the sensor charge signal is amplified and compared to a programmable discriminator threshold. The digital readout then transfers the hit pixel address, a hit time stamp and a digitised amplitude — the time over threshold (ToT) — to buffers at the chip periphery. These hit buffers monitor each stored hit by inspecting the associated time stamp.

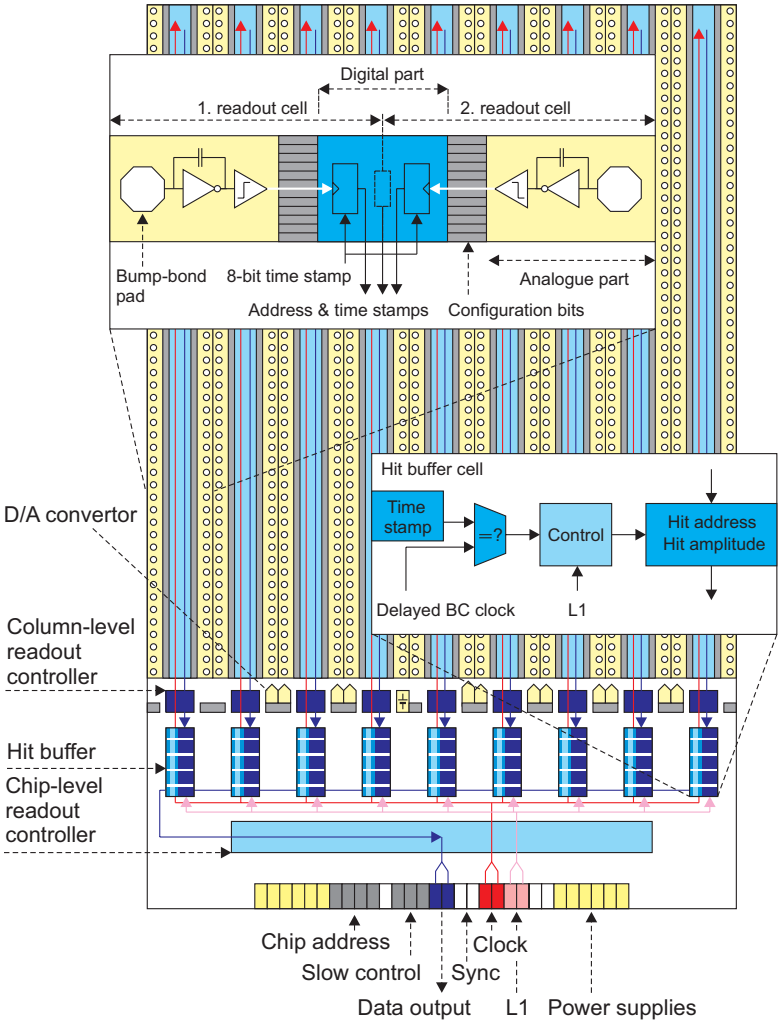

Figure 2.7: Schematic plan of the front-end chip with main functional elements, not to scale. Figure taken from [70].

The charge sensitive amplifier uses a single-ended folded-cascode topology optimised for a nominal capacitive load of 400 fF and designed for the negative signal expected from DC-coupled n^+-on-n sensors. Attention has been paid to the preamplifier design because, following the irradiation expected at the LHC, the sensor leakage current (50 nA) is two orders of magnitude larger than the signal, that is itself reduced due to carrier trapping inside the silicon. The pre-amplifier has an approximate 5 fF DC feedback capacitance with a 15 ns rise time. The total analogue front-end (pre-amplifier, second stage amplifier and discriminator) has a bias current of only 24 μA per pixel. To ensure the separation of contiguous bunch crossings, a front-end time-walk of < 25 ns is required.

To fulfill the requirements of sensor leakage current, a compensation circuit is implemented that drains the leakage current and prevents any influence on the bias current of the fast feedback circuit used to discharge the feedback capacitor. Each pixel can be configured individually to provide a high level of response uniformity and to mask defective channels. This configuration is stored in a 14-bit control

register which includes the feedback current (3 bits for tuning the ToT response) and the threshold (7 bits). A special MASK bit is reserved to switch off locally the pixel, while the SHUTDOWN can disable the charge amplifier. Finally, one bit is used to trigger the injection of a known charge in the pixel during ToT calibration, while the last one allows to decide if the leakage current from the preamplifier should be summed or not to the output signal.

The Module Control Chip (MCC) [79] is a digital chip running with the 40 MHz clock delivered by the LHC. It has three main system tasks: the loading of parameter and configuration data in the front-end chips and in the module-control chip itself, the distribution of timing signals such as bunch-crossing, L1 trigger and resets (TTC functions), and the front-end chip read-out and event building. The design of the module-control chip reflects the required pixel performance during LHC operation: the association of signals to a bunch-crossing, the expected bandwidths at the highest luminosity, the maximum L1 trigger rate of 100 kHz and the number of front-end chips, which are controlled in a module. Because of the high-radiation environment, particularly in the b-Layer modules, special attention has been given to ensure a single-event upset (SEU) tolerant design.

2.2 The Semi-Conductor Tracker

The Semi-Conductor Tracker (SCT) is required to reconstruct isolated leptons with a transverse momentum of $p_{\mathrm{T}} > 5$ GeV with 95% efficiency out to $|\eta| \leq 2.5$, to measure momentum up to $p_{\mathrm{T}} = 500$ GeV with better than 30% precision, to track back to the vertex z-coordinate with better than 1 mm accuracy, achieve two track resolution of better than 200 μm at 30 cm radius and represent no more than 20% X_0 in total [67, 68]. To achieve this, a design consisting of four barrel layers of 2112 silicon modules in total and two sets of nine disks (each set comprising 988 end-cap modules) was adopted by ATLAS. The resulting tracking detector has 63 m^2 of silicon micro-strip sensors with just under 40% in the two end-caps. Roughly speaking, the barrel region covers $|\eta| \leq 1$ on its own, while the disks are needed to extend the coverage to $|\eta| \leq 2.5$ minimising at the same time the material seen by the highly inclined tracks in these directions.

The four SCT cylinders in the barrel region have radii between 299 and 514 mm and a full length of 1492 mm (see Figures 2.1 and 2.2). Their surface areas are tiled with segmented detector elements, the SCT barrel modules, to provide complete four-layer digitization coverage for particles coming from a length of $\pm$76 mm about the nominal interaction point on the central axis, corresponding to $\pm$2 times the length of the beam interaction point. The barrel cylinder parameters and the numbers of modules are summarized in Table 2.4. While the barrel only requires one module type, the end-cap region is composed of disks made of three module types (see Section 2.2.2). The number of modules for each disk, as well as the nominal position of the disks are reported in Table 2.5.

Barrel cylinder	Radius (mm)	Length (full) (mm)	Tilt angle in ϕ(deg)	Number of modules
Barrel 3	299	1492	11	384
Barrel 4	371	1492	11	480
Barrel 5	443	1492	11.25	576
Barrel 6	514	1492	11.25	672
Total	—	—	—	2112

Table 2.4: SCT barrel cylinder parameters and the number of modules. *Tilt angle* is the angle of the modules relative to the local tangent to the surface of their supporting cylinder. Table taken from [80].

Disk	**1**	**2**	**3**	**4**	**5**	**6**	**7**	**8**	**9**
$\|z\|$ (mm)	853.8	934.0	1091.5	1299.9	1399.7	1771.4	2115.2	2505.0	2720.2
Outer	52								
Middle	40								None
Inner	None	40					None		

Table 2.5: The nominal z-position of the centre of each SCT end-cap disk and the number of modules on each disk (the total number of modules is 1976, summed over both end-caps). The modules are tiled in Φ by $\pm$2.75 mm about these nominal centres. Table taken from [4].

2.2.1 SCT sensors

The SCT sensors are realized in a construction procedure similar to the one of Pixel Detector [70, 81]. For reasons of cost and reliability, the 15 912 sensors of the SCT use a classic single-sided p^+n technology with AC-coupled read-out strips. The strip metal is grounded in operation. There is a reach-through protection structure for the coupling dielectric, with the strip implants extending to within 5–10 μm of the bias rail in order to limit the strip implant voltage in the case of beam splash. In conjunction with this protection, the coupling dielectric is required to withstand a potential difference of at least 100 V between the grounded strip metal and the substrate. The ground contact is the bias rail implant surrounding the strips and the high-voltage contact is a metallised, unpassivated, n-implant on the rear of the sensor. Apart from pads used for bonding and probing, the front sides of the sensors are fully passivated. The passivation, together with stringent requirements on the quality of the cut edge (the latter being at the backplane bias potential), is important to reduce the risk of creating accidental high voltage shorts during module construction or operation.

The sensors are to be operated at about 150 V bias voltage initially. After 10 years of LHC operation, they are expected to be operated at between 250 and 450 V bias voltage, depending on their positions in ATLAS relative to the beam. The sensor thickness of 285$\pm$15 μm is a compromise between the required operating voltage, the primary signal ionisation and the simplicity of fabrication.

Sensor type	Cut length (μm)	Outer width (μm)	Inner width (μm)
Barrel	63,960	63,560	63,560
Endcap W12	61,060	55,488	45,735
Endcap W21	65,085	66,130	55,734
Endcap W22	54,435	74,847	66,152
Endcap W31	65,540	64,635	56,475
Endcap W32	57,515	71,814	64,653

Sensor type	Readout strip pitch (μm)	Interstrip angle (μrad)
Barrel	80	0
Endcap W12	56.9–69.2	207
Endcap W21	69.9–83.0	207
Endcap W22	83.4–94.2	207
Endcap W31	70.9–81.1	161.5
Endcap W32	81.5–90.4	161.5

Table 2.6: External cut dimensions of the barrel and end-cap SCT sensors. The specified tolerance on all dimensions is ±25 mm. Table taken from [81].

The strip pitch was determined by the required digitising precision, granularity, particle occupancy and noise performance.

All sensors for the barrel region of the SCT have identical rectangular geometry, with 768 read-out strips at a constant 80 μm pitch. The metallisation mask for each sensor (both barrel and end-cap) incorporated a set of fiducial marks for use in the precision alignment of the sensor during the module assembly process. The geometry of the end-cap sensors is more complicated then for the barrel, because of their layout on discs. The objective was to provide end-cap coverage with the minimum number of different types of sensor. This number is five, with sensors given the names W12, W21, W22, W31 and W32. They are grouped to form modules (see Section 2.2.2): W12 for the short inner module type, W21 bonded to W22 in a middle module, and W31 to W32 in an outer module (the middle modules on one disc are short, without the W21 sensor, for geometrical reasons). Each sensor again has 768 readout strips, but these are not at a constant pitch because of the wedge-shaped geometry. The outer dimensions of each sensor type and the range of the strip read-out pitches are given in Table 2.6. The surface areas of the barrel and the different end-cap sensors are the same to within 6%, with the exception of the W12 sensor, which has only 76% of the surface area of a barrel sensor.

2.2.2 SCT modules

As already introduced, barrel modules and end-cap modules follow different designs for the SCT detector. The 2112 barrel SCT modules [80] use 80 μm pitch micro-strip sensors, which are described in Section 2.2.1. The sensors are connected to binary signal read-out chips, which are described in Sec-

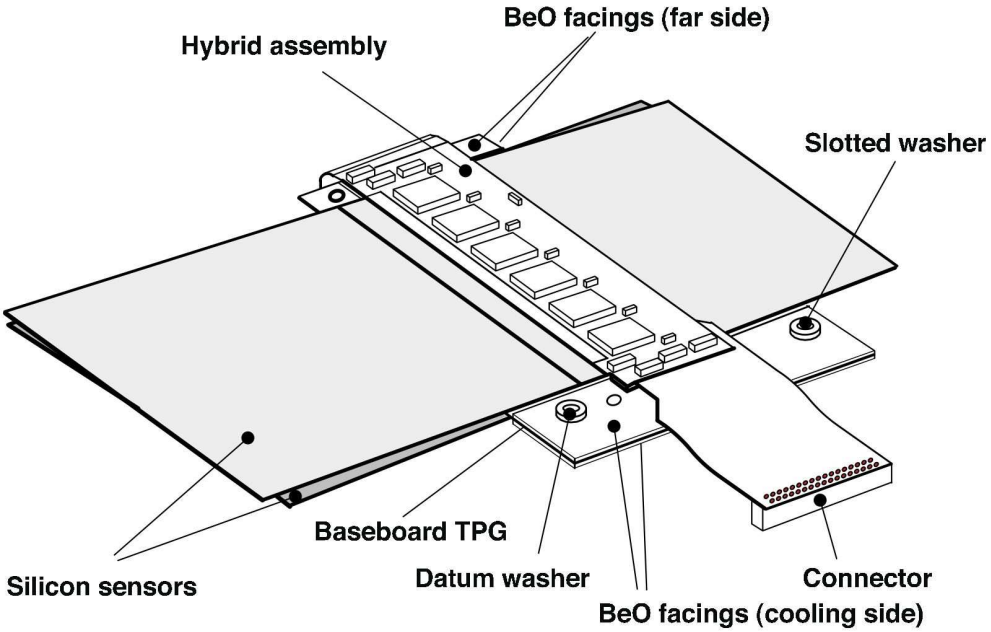

Figure 2.8: 3D view of the ATLAS SCT barrel module. Figure taken from [80].

tion 2.2.3. The barrel module is shown, with its components, in Figure 2.8. The four sensors, two each on the top and bottom side, are rotated with their hybrids by ± 20 mrad around the geometrical centre of the sensors. They are glued on a 380 mm-thick thermal pyrolitic graphite (TPG) base-board, which provides the thermal and mechanical structure. This extends sideways to include beryllia facings. A polyimide hybrid with a carbon-fibre substrate bridges the sensors on each side. The two 770-strip (768 active) sensors on each side form a 128 mm long unit (126 mm active with a 2 mm dead space). High voltage is applied to the sensors via the conducting base-board.

Figure 2.9 shows the construction of an end-cap module [82]. There are three module types, as shown in Table 2.5. Each of the 1976 modules has two sets of sensors glued back-to-back around a central TPG spine with a relative rotation of ± 20 mrad to give the required space-point resolution in R-Φ and R. The module thickness is defined by the individual components and variations are compensated by the glue thickness (nominally 90 μm). The TPG spine conducts heat from the sensors to cooling and mounting points at the module ends and serves as the bias contact to the sensors. Glass fan-ins attach one end of the spine to a carbon base-plate with the polyimide flex hybrid glued to it. The modules are arranged in tiled outer, middle and inner rings.

The spatial resolution of individual SCT modules has been measured in a test beam, for both non-irradiated and fully irradiated modules. At normal incidence, a combined spatial resolution of ~ 16 μm is measured in R-Φ; the resolution is consistent with the binary read-out of the two sensors with 80 μm strips, including a small fraction of multiple hits. The resolution is not significantly degraded after irradiation.

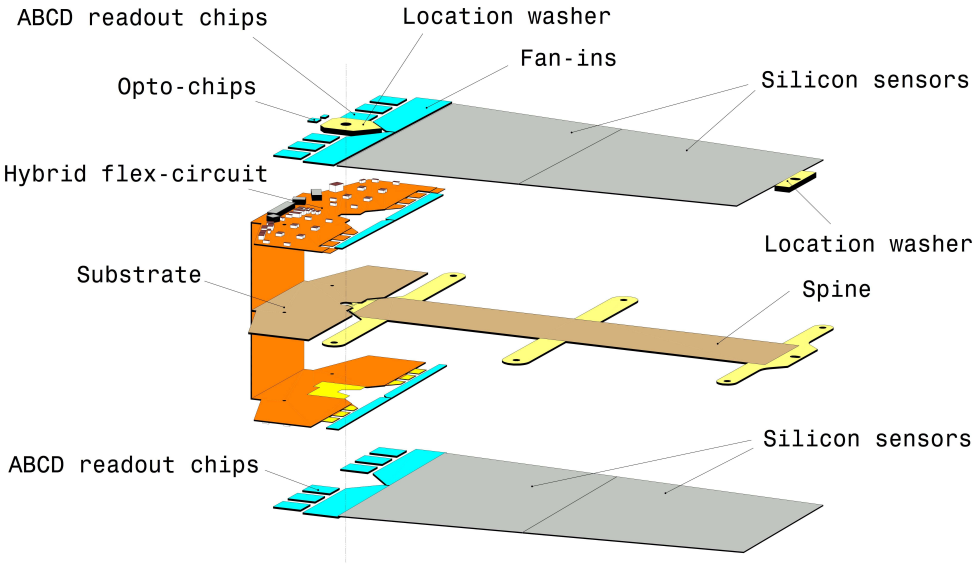

Figure 2.9: Exploded view of an SCT end-cap module showing the different components. Figure taken from [82].

The barrel and end-cap sensors are specified to operate at $-7°$C, with a maximum variation within and between modules of 5°C, to reduce the bulk leakage current after radiation damage. The hybrid power will be 5.5–7.5 W per module, and the sensor load will reach 1 W per module after ten years of operation. In addition, convective loads of 0.8 W per module plus 0.8 W per module at the top of the barrel cylinders and outer disks are expected. The heat is extracted by evaporating C_3F_8 at $-25°$C, circulating in cooling pipes attached to each module. For the barrel, the sensor and hybrid heat leaves via the base-board and the hybrid substrate to the large beryllia facing on the base-board, which is interfaced to an aluminium block with a 100 μm layer of thermal grease and a copper-polyimide capacitive shunt shield. At full load for irradiated modules, the hybrid and sensor temperatures are expected to be approximately 14°C and 12°C above the cooling-pipe temperature, respectively. The block is itself soldered to a 3.6 mm diameter Cu/Ni cooling pipe. Each cooling loop serves 48 barrel modules. For the end-cap, the sensor heat leaves via the spine, while the hybrid heat is transferred via the carbon-fibre hybrid substrate to a carbon-carbon cooling block, which is split to minimise heat transfer between the sensor and the hybrid. At full load, the ASIC and sensor temperatures are expected to be respectively 30°C and 10–15°C above the coolant temperature. A layer of thermal grease is applied between the modules and the cooling block. The blocks are soldered to a Cu/Ni cooling pipe that serves up to 33 modules.

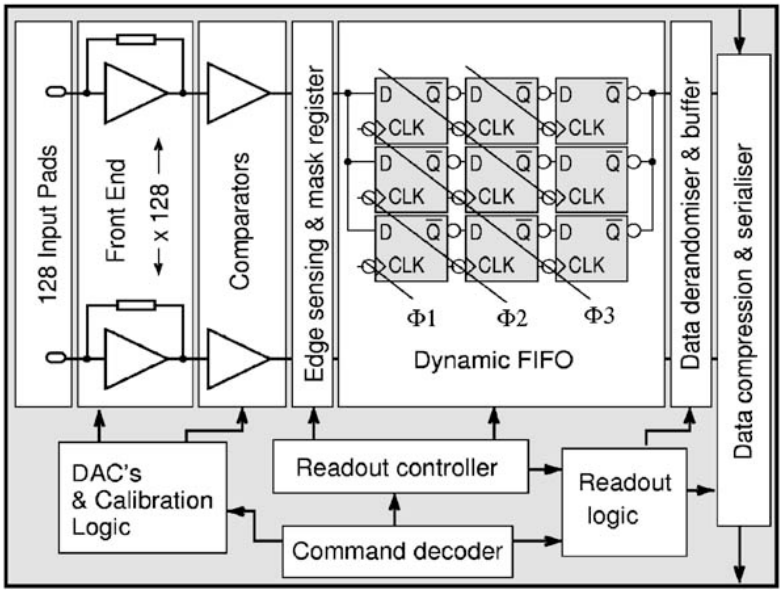

Figure 2.10: Block diagram of the ABCD3TA chip. Figure taken from [83].

2.2.3 SCT electronics

The read-out hybrid of each SCT module houses 12 identical 128-channel ABCD3TA ASICs [83] to read a total of 1536 sensor strips per module. The ASIC is fabricated in radiation tolerant bi-CMOS DMILL technology. Two critical performance specifications are the detection efficiency ($> 99\%$) and noise occupancy ($< 5 \times 10^{-4}$), for signals from the 12 cm long silicon strips with a capacitive load of 20 pF. These led to the choice of a front-end discriminator threshold of 1 fC.

The structural blocks of the ASIC are shown in the circuit schematic of Figure 2.10. A pre-amplifier, shaper and tunable discriminator exist for each channel. A 132-length binary pipeline stores the hit information for each channel associated to the beam crossing for a period of ~ 3.2 μs. Following a L1 trigger, the chip compresses the data pertinent to that beam crossing and serialises it for output. An 8-deep de-randomising buffer after the pipeline ensures that the dead-time is negligible for the expected data rates. Data must be identified with a particular LHC bunch crossing and first-level trigger. To achieve this, each front-end ASIC keeps a count of the number of triggers (4 bits) and the number of clocks (8 bits) it has received. The values of the counters form part of each ASICs event data header.

The principal connections to the front-end modules, to the ATLAS central DAQ and between SCT specific components are shown in Figure 2.11. The communication is made by optical links [84] operating at 40 Mbits/s with total lenght around 80 m. The data from each side of the module are read out serially via a *master* ABCD3TA and are elaborated by a custom ASIC, the VDC, which drives two GaAs Vertical Cavity Surface Emitting Lasers (VCSELs) channels. The VDC, developed specifically for the SCT project, translates the approximate LVDS signal produced by the ABCD3TA into the drive

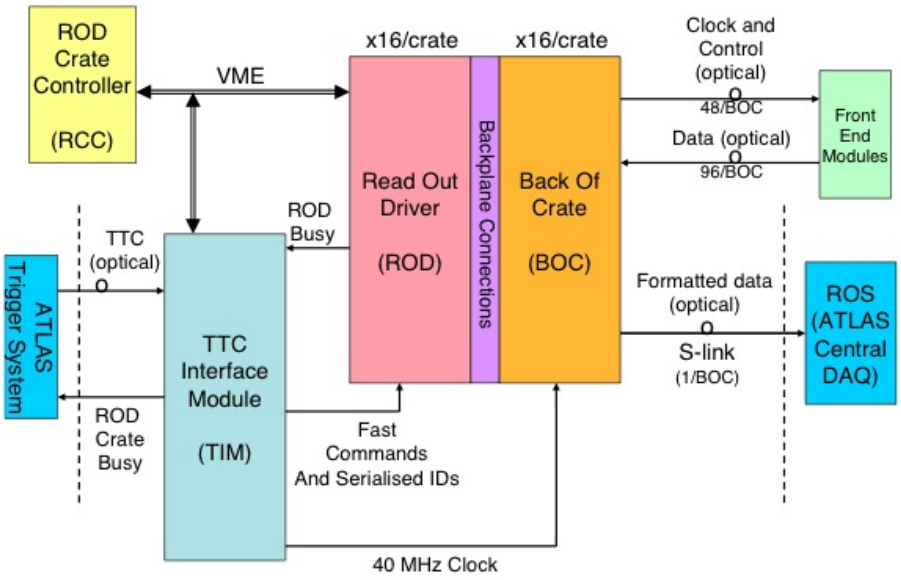

Figure 2.11: Block diagram of the SCT data acquisition hardware showing the main connections between components. Figure taken from [85].

signal required to operate the VCSEL. The data are sent to a Back of Crate (BOC) [85] card, which provides the interface between the optical signals and the off-detector electronics in the SCT Read Out Driver (ROD). Some redundancy is built into the data links in that two independent links are provided for each SCT module. In normal operation, each link reads out one of the sides of the module, but if one link fails then all the data can be read out via the working link. The redundancy mode reduces the available bandwidth, but this will not cause any loss of data at the expected rates.

Each ROD/BOC pair deals with the control and data for up to 48 front-end modules. Up to 16 RODs and BOCs are linked with a TTC Interface Module (TIM) which accepts the Timing, Trigger and Control (TTC) signals from ATLAS and distributes them to the RODs and BOCs. The ROD Crate Controller (RCC) is a commercial 6U Single Board Computer running Linux which acts as the VME master. The RCC configures the other components and provides overall control of the data acquisition functions within a crate. The highly modular design was motivated by considerations of ease of construction and testing. Redundancy is built into the TTC system by having electrical links from one module to its neighbour. If a module loses its TTC signal for any reason, an electrical control line can be set which will result in the neighbouring module sending a copy of its TTC data to the module with the failed signal. For the barrel part of the SCT, the redundancy system is configured as a loop of 12 modules, each connecting two adjacent barrel harnesses. For the end-cap, the redundancy loops join detectors in a ring on a disk and consist of 40 or 52 modules.

In physics data-taking mode, triggers pass from the ATLAS TTC to the TIM and are distributed to the RODs. Each ROD fans out the triggers via its BOC to the front-end modules. The resultant hit data from the front-end modules are received on the BOC, formatted on the ROD and then returned to the BOC to be passed on to the first module of the ATLAS central DAQ. The RODs can also be

set up to sample and histogram events and errors from the data stream for monitoring. For calibration purposes, the SCT DAQ can operate separately from the central ATLAS DAQ. In this mode the ATLAS global central trigger processor is not used. The TIM generates the clock and SCT-specific triggers are taken from other sources. For most tests they are generated internally on the RODs, but for tests which require synchronisation they can be sourced from the SCTs local trigger processor or from the TIM. The resultant data are not passed on to the ROS, but the ROD monitoring functions still sample and histogram the events.

2.3 The Transition Radiation Tracker

The TRT section of the tracker is formed from a central TRT barrel detector [86] with sensor layers parallel to the beam axis and two (forward and backward) TRT end-cap detectors [87] with their sensor layers radial to the beam axis. The TRT provide both continuous tracking in individual axial drift tubes (or straws) and electron identification using the straws to absorb and to detect transition radiation X-ray photons originating from fibers (in the barrel) or thin foils (in the end-caps) between the straw themselves.

The requirement for the momentum measurement is to contribute to the overall tracking performance by providing a measurement in the R-Φ plane to reach 30 μm at luminosity of $\mathscr{L} = 10^{33}$ cm^{2}s^{-1} and 50 μm at $\mathscr{L} = 10^{34}$ cm^{2}s^{-1}. The particle identification is designed to identify clean samples of electrons covering a wide range of particle momenta with a p_{T} between 20 GeV and 40 GeV reaching a rejection factor for charged pions of about 10. The expected number of transition radiation (TR) photons depends on the length of the track inside the TRT, e.g. for an electron with a momentum of 40 GeV about 11 TR photons are expected at $|\eta| \sim 1.7$ and 5 TR photons for an electron passing the detector at $|\eta| \sim 2.0$. On average about eight transition radiation photons are expected for an electron at 40 GeV.

The TRT Barrel is divided into 96 modules of three types, arranged in three cylinders of 32 modules of each type, as shown in Figure 2.12(a). It covers the radius range 56–108 cm and has a sensitive region of total length of 144 cm along the beam direction, corresponding to a pseudorapidity range of $|\eta| < 1$. The modules are supported at each end by the Barrel Support System (BSS). Each module consists of a carbon-fiber composite cover or shell, an internal array of drift tubes, which are the detector elements, and an internal matrix of polypropylene fibers - the transition radiation material. The drift tubes were constructed from two layers of conductively-coated polyimide film. They form an approximately uniform array parallel to the beam axis, with an average spacing of about 6.6 mm between centers radially and tangentially. The layout of the drift tubes was designed to optimize the probability of the detection of transition radiation as well as to maximize the number of hits along a track. Charged particle tracks with transverse momentum $p_{\mathrm{T}} > 0.5$ GeV and with pseudorapidity $|\eta| < 2.0$ should cross about 35 straws (except in the barrel/end-cap transition region). The three sizes of Barrel modules are sequentially mounted in 32 Φ sectors. Each module is a quadrilateral prism with

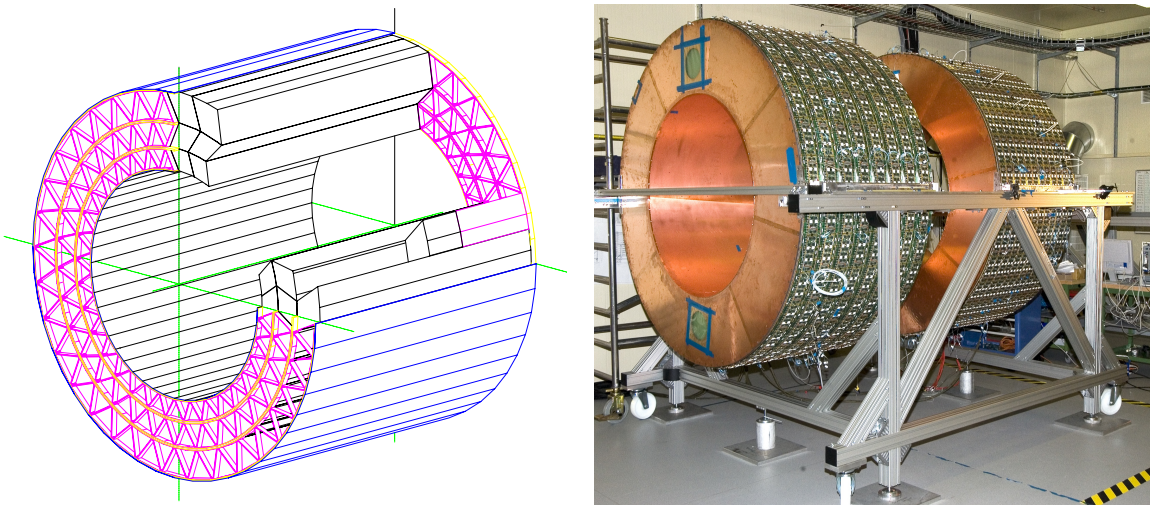

(a) (b)

Figure 2.12: 2.12(a): sketch of the TRT barrel assembly, showing the Barrel Support System, in pink. The Barrel Support System supports and locates the two ends of each module. Figure taken from [86]. 2.12(b): Photograph of the TRT end-caps. Figure taken from [87].

Module	Inner Radius (m)	$\|\eta\|$ at Rmin	Layers	# Straws	Mass (kg)
Type 1	0.56	1.06	19	329	2.97
Type 2	0.70	0.89	24	520	4.21
Type 3	0.86	0.75	30	793	6.53
Total for Barrel			73	52544	439

Table 2.7: TRT Barrel Module parameters. Table taken from [86].

front and back faces in a plane perpendicular to the local radial ray, and sides that follow the close packing array shape of straws, approximating a 30° deviation with respect to a radial line. This design was chosen to minimize the amount of dead tracking area for high-momentum particles. The resulting numbers of straws in each module are listed in Table 2.7. The mass listed in the table are for modules only, with no electronics or external services connected. The total number of straws for all 32 sectors, and the total mass of the 96 modules is indicated in the bottom line of the table.

Along the z-axis, in each TRT end-cap, there is a total of 160 layers of straws. The straws are arranged so that every charged particle with a transverse momentum $p_{\mathrm{T}} > 0.5$ GeV and with a pseudo-rapidity η between $1.0 < |\eta| < 2.0$ produces hits in 20 to 36 straws. The independent modules that make up the TRT end-caps are referred to as wheels because of their cylindrical form (see Figure 2.12(b)) and radial straws like spokes. There are two types of wheels, Type-A and Type-B. Each of them constitutes a mechanically independent unit, and contains eight planes of straws. In both cases each of these layers contains 768 radially oriented straws of ~ 37 cm length with uniform azimuthal

Wheel type	Number of eight plane wheels	Layers	Straws	$\lvert\eta_{min}\rvert$	$\lvert\eta_{max}\rvert$	z_{min} (mm)	z_{max} (mm)	Mass (kg)
A	12	96	73,728	0.77	1.7	848	1710	424
B	8	64	49,152	1.32	2.0	1740	2710	438
Total for end-cap	20	160	122,880					862

Table 2.8: TRT end-cap parameters. The minimum (maximum) pseudo-rapidity $|\eta_{min}|$ ($|\eta_{max}|$) corresponds to the maximum (minimum) end-cap radius $R_{max} = 1004$ mm ($R_{min} = 644$ mm) at minimum (maximum) position of the end-cap along z-axis z_{min} (z_{max}). Table taken from [87].

spacing but stepped, layer to layer, in Φ. The Type-A wheels make up the 96 straw layers closest to the interaction point and features adjacent straw planes with a clearance of 4 mm in the z-direction. The Type-B wheels which make up the remaining 64 layers have a clearance of 11 mm so that tracks at small θ angles cross approximately the same number of straws as tracks at larger angles. The space between successive straw layers in each wheel is filled with layers of 15 μm thick polypropylene radiator foils separated by a polypropylene net. The number of straws and the coverage in η and z for each set of wheels is listed in Table 2.8. The mass listed in the table is for wheels, with electronics but without external services connected.

2.3.1 TRT straw tubes

Polyimide drift tubes of 4 mm diameter are the basic TRT detector elements [88]. The straw tube wall, especially developed to have good electrical and mechanical properties with minimal wall thickness, is made of two 35 μm thick multi-layer films bonded back-to-back. The bare material, a 25 μm thick polyimide film, is coated on one side with a 0.2 μm Al layer which is protected by a 5–6 μm thick graphite-polyimide layer. The other side of the film is coated by a 5 μm polyurethane layer used to heat-seal the two films back-to-back. Mechanically, the straws are stabilised using carbon fibres. After fabrication, the straws were cut to length (144 cm for the barrel and 37 cm for the end-caps) and leak-tested at 1 bar over-pressure. The straw (cathode) resistance was required to be $< 300\ \Omega/\text{m}$.

For both the barrel and end-cap straws, the anodes are 31 μm diameter tungsten (99.95%) wires plated with 0.5–0.7 μm gold, supported at the straw end by an end-plug. They are directly connected to the front-end electronics (see Section 2.3.3) and kept at ground potential. The anode resistance is approximately 60 Ω/m and the assembled straw capacitance is < 10 pF. The signal attenuation length is 4 m and the signal propagation time is 4 ns/m. The cathodes are operated typically at -1530 V to give a gain of 2.5×10^4 for the chosen gas mixture of 70% Xe, 27% CO_2 and 3% O_2 with 5–10 mbar over-pressure. Under normal operating conditions, the maximum electron collection time is 47 ns and the operational drift-time accuracy is 130 μm [88]. Low energy TR photons are absorbed in the Xe-based gas mixture, and yield much larger signal amplitudes than minimum-ionising charged particles. The distinction between TR and tracking signals is obtained on a straw-by-straw basis using separate low and high thresholds in the front-end electronics.

For the barrel straws, the anode wires (active length $\pm$71.2 cm) are read out from each end. Near their centre, the wires are supported mechanically by a plastic insert glued to the inner wall of the straw and split electrically by a fused glass capillary of 6 mm length and 0.254 mm diameter to reduce the occupancy. Each long barrel straw is therefore inefficient near its centre over a length of 2 cm. In the inner nine layers of Type-1 barrel modules, the wires are subdivided into three segments keeping only the 31.2 cm long end-segments on each side active.

At LHC rates, significant heat is generated in the straws by the ionisation current in the gas. The heat dissipation is proportional to the single straw counting rate and is estimated to be 10 mW to 20 mW per straw for the highest-occupancy straws (inner barrel layers) at the LHC design luminosity. To preserve gas-gain uniformity, the temperature gradient along each straw is required to be $< 10^{\circ}$C. The heat is evacuated differently for the barrel modules and end-cap wheels (see Section 2.3.2).

2.3.2 TRT modules

Barrel modules

The barrel TRT is divided into three rings of 32 modules each, supported at each end by a space frame, which is the main component of the barrel support structure. Each module consists of a carbon-fibre laminate shell and an internal array of straws embedded in a matrix of 19 μm diameter polypropylene fibres serving as the transition radiation material. The straws form a uniform axial array with a mean spacing of $\sim$ 7 mm. The module shells are non-projective to reduce the dead region for high-p_{T} tracks.

The dimensional specifications are set by the intrinsic straw R-Φ resolution of 130 μm, implying that each wire position is constrained to within $\pm$50 μm. The module shell, made of 400 μm thick carbon fibre with high thermal conductivity and flat to within 250 μm, is measured to satisfy maximum distortions of < 40 μm under full load. The module shells also serve as a gas manifold for CO_2 which circulates outside the straws to prevent high-voltage discharges and the accumulation of xenon due to possible gas leaks which would absorb the transition radiation photons. The heat dissipated by the barrel straws is transferred to the module shell by conduction through the CO_2 gas envelope. Each module shell is cooled by two cooling tubes located in the acute corners. These tubes also serve as return pipes for the C_6F_{14} cooling circuits of the front-end electronics.

The barrel module end with its components is shown in Figure 2.13. The central element is the HV plate which has stringent requirements on flatness and cleanliness to prevent discharges and on the straw feed-through accuracy to ensure mechanical precision of the straw location. The HV plates were individually surveyed after machining. The tension plate of Figure 2.13 mounted on the HV plate is a printed-circuit board holding the wire ends (and ensuring the wire tension) and providing electrical connections. It also closes the active gas volume and serves as a Faraday cage for the active module elements.

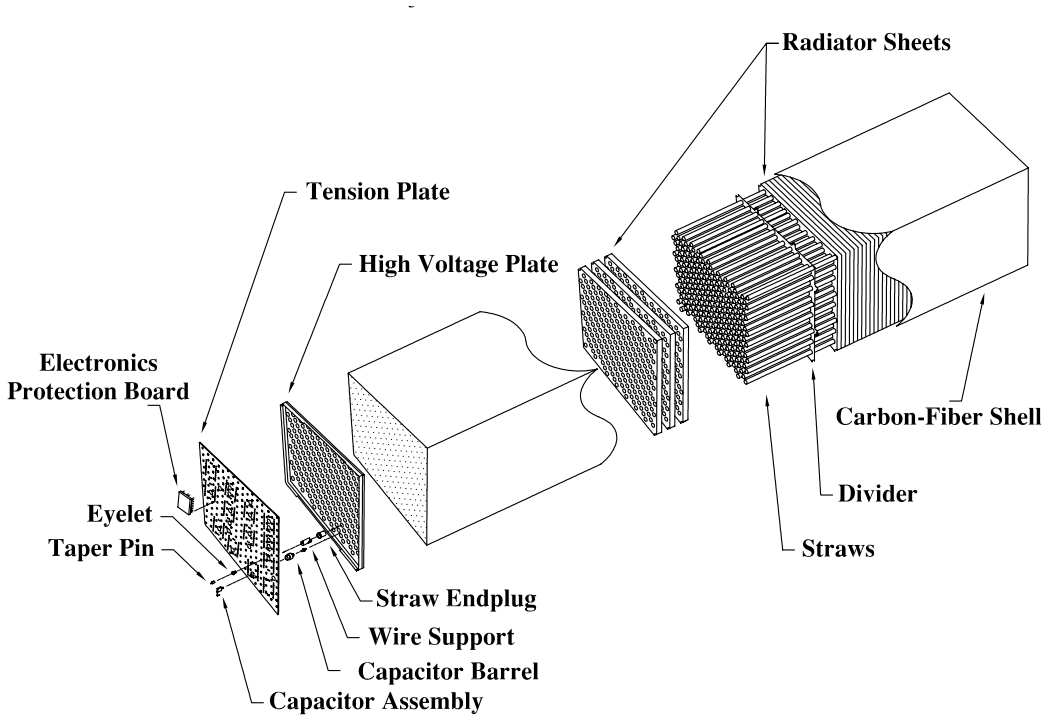

Figure 2.13: Isometric view of a barrel module with end plates, radiator, straws and shell. Figure taken from [86].

End-cap modules

The TRT end-caps consist of two sets of independent wheels (see Table 2.8), called Type-A and Type-B, containing each eight layers of straws. Each eight-plane wheel consists of two basic four-plane assembly units. To assemble a four-plane wheel, straws were inserted and glued into precisely drilled holes in grounded inner and outer carbon fibre rings. The rings and the straws constitute the main mechanical structure of the wheels. The successive straw layers, interleaved by the radiators, are rotated from one layer to the next by 3/8 of the azimuthal straw spacing in a given layer. For high-p_{T} prompt tracks, this ensures optimal uniformity in the number of crossed straws, which varies radially from six to four straws across an eight-plane wheel.

Flex-rigid printed-circuit boards provide high voltage and signal connections to the four-plane assemblies, as shown in Figure 2.14. Each of the flexible layers has conducting paths on one side which connect to the rigid part of the board. To provide a reliable electrical connection, flexible "petals" in the high-voltage layer are forced into contact with the inner straw wall through the insertion of a plastic plug. A press-fit between similar but smaller petals in the signal layer and a metallic crimping pin positions and fixes the anode wires. There are 32 such boards per four-plane wheel, each serving a Φ-sector of 96 straws. Each sector is further segmented into three groups of 32 read-out channels and 12 high-voltage groups of eight straws sharing a common fuse and blocking capacitor. The carbon-fibre ring holding the straws and flex-rigid boards, together with a third carbon-fibre ring and a simpler glass

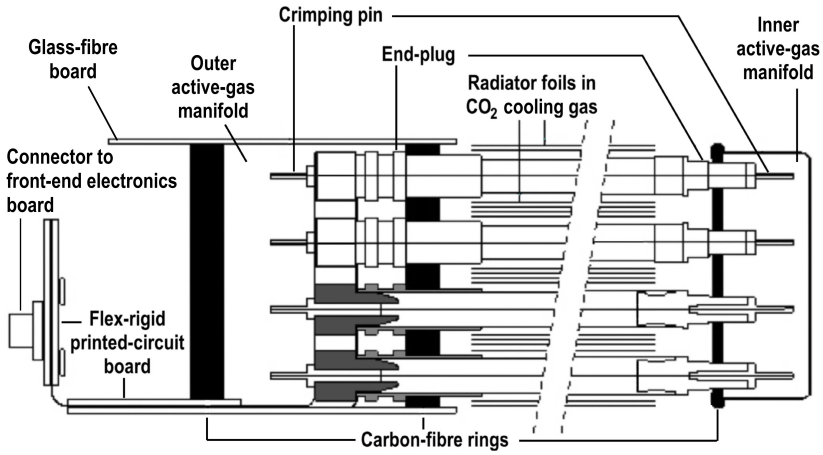

Figure 2.14: Schematic view of the TRT end-cap wheels, showing the plastic end plugs used to position and fix the straws in the inner (right side of this figure) and outer (left side of figure) C-fibre rings, the crimping pins holding and positioning the wires, the inner and outer active-gas manifolds, and the flex-rigid printed-circuit board on the left used to connect the straws to high voltage and the wires to the front-end electronics. Figure taken from [87].

fibre board provide a rigid structure around the outer wheel perimeter that also serves as a gas manifold (see Figure 2.14). The inner gas manifold is made from reinforced polyimide material.

The heat dissipated by the end-cap straws is evacuated through the CO_2 gas envelope which is forced to flow along the straws from the inner to the outer radius. Each group of wheels has its own CO_2 cooling circuit, passing the gas sequentially through all the wheels of the group. Heat exchangers cooled with C_6F_{14} extract heat from the gas between adjacent wheels. The high flow rates required, 50 m^3 per hour for Type-A and 25 m^3 per hour for Type-B wheels, necessitates a closed-loop system capable of maintaining a small gas pressure between 0 and 5 mbar with a stability of ± 0.5 mbar inside the detector.

2.3.3 TRT electronics

The TRT electronics is separated into three distinct parts: on-detector or Front End, intermediate Patch Panel and counting room Back End [89]. The Front End electronics use full TRT custom radiation hard integrated circuits (the ASDBLR and DTMROC). The Patch Panel boards located in the midst of the ATLAS muon system use radiation tolerant commercial parts plus several CERN designed custom chips, and the Back End electronics in the counting room are designed entirely with commercial components except for a few specialized LHC custom timing circuits. Power for the Front End and Patch Panel areas relies on LHC custom analog regulators supplied from commercial bulk voltage supplies especially designed for LHC conditions. HV power for the straw detectors is provided by semi-custom crates of precision low current HV supplies with monitors and adjustable trips. The basic TRT electronics blocks are shown in Figure 2.15.

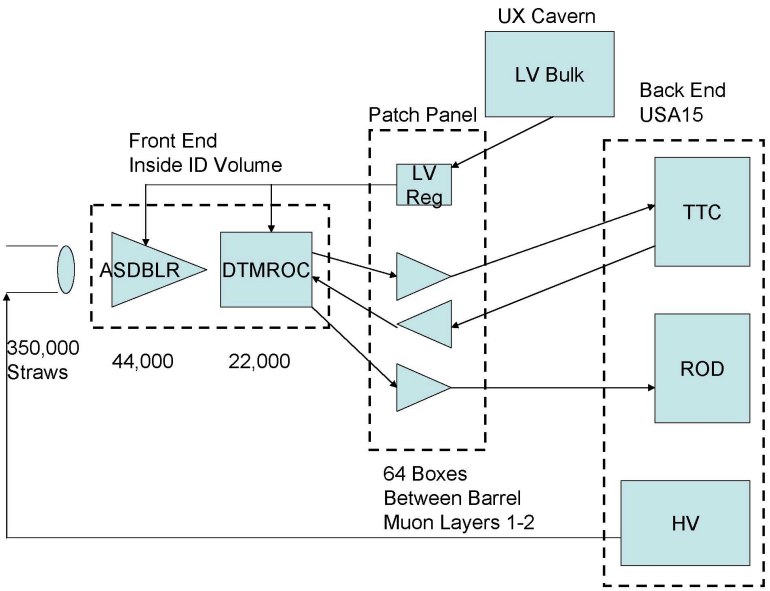

Figure 2.15: Overview of the TRT electronics from straws to Back End hardware. Figure taken from [86].

The basic operational mode of the TRT is the detection of avalanche currents on the anode wire initiated by clusters of primary ionization electrons from a through-going track. The arrival time of the cluster depends upon the distance from the wire of the primary ionization. This cluster arrival time relative to the time of a track from a collision coupled with knowledge of the drift velocity in the gas is what allows the TRT to make a precise measurement of track position. The analog read-out is performed on 8 wire groups by a custom-designed ASIC which performs Amplification, Shaping, Discrimination, and Base-Line Restoration (ASDBLR). The ASDBLR is fabricated in bi-CMOS radiation tolerant DMILL technology. The analog outputs of the ASDBLR are sampled by a second ASIC, the Drift Time Measuring Read Out Chip (DTMROC), which makes the time measurement of the signals and provides a digitized result to off-detector electronics for up to 16 straw channels. For avalanche currents above threshold, the ASDBLR sends a pulse to the DTMROC: the leading edge of the pulse corresponds to the distance of closest approach and the trailing edge is roughly fixed to the 2 mm maximum drift time. This fixed maximum drift time is useful to discriminate if a hit is associated with the beam crossing of interest. The ASDBLR employs a traditional fixed time shaping technique by building a mirror image impulse response into the signal processing electronics so that the ion tail and mirror signal cancel after the initial avalanche signal. After this cancellation process only a small fraction of the total avalanche signal is available. In this case about 5% or 0.15 fC per primary electron at a gas gain of 2.5×10^4. Since the objective is to detect the earliest clusters of electrons arriving at the wire, the electronics must add as little noise as possible to the incoming signal. An electronics peaking time of 7.5 ns with a semi-Gaussian shape after ion tail cancellation is used. This allows integration of the avalanche signal from the first few clusters of drift electrons arriving at the wire to give a trigger point based on a signal significantly higher than the intrinsic and systematic noise.

The secondary operational mode takes advantage of transition radiation photons created by energetic electrons transiting layers of polypropylene radiator placed between the straws. These TR photons are stopped primarily by xenon atoms in the gas mixture. This high-Z inert gas allows efficient absorption of TR photons whose energy is in the range of 5-15 keV, well above the typical 2 keV deposited by a minimum ionizing track. Extending the peaking time of the TR photon detection circuit to 10 ns allows integration of the direct and reflected signal from the far end of the unterminated 0.5–0.7 m straw. The extended peaking time reduces the variation in amplitude versus position of the avalanche along the straw.

The complementary digital read-out chip for the TRT is the Drift Time Measurement/Read Out Chip (DTMROC). It is implemented in a commercial 0.25 micron CMOS process and is designed to operate using the LHC 40 Mhz clock. The DTMROC accepts 16 ternary inputs from two ASDBLRs. The ternary signal encodes time over threshold for the two separate discriminators on the ASDBLR. The low-threshold signal is used for tracking and the DTMROC records it in 3.12 ns bins. The high-level discriminator is sensitive to the presence of a transition radiation signal and the output of that high-level discriminator is latched as a single bit during each 25 ns clock cycle that it is active. The DTMROC contains four 8 bit Digital to Analog Converters (DACs) to set the low- and high-thresholds on each of the two ASDBLRs to which the DTMROC is connected. There are also a pair of one bit digital outputs that are used to control the shaper of the ASDBLR. The DTMROC stores these data for up to 6 ms, until a L1 trigger signal is received. On the receipt of a Level-1 Accept from the central ATLAS trigger, the DTMROC data for 3 LHC crossing times is shipped to the Back End RODs and assembled into events for Level-2 trigger discrimination and later processing.

Signal transmission from the Front End to the Patch Panels is, unlike most other ATLAS subdetectors, implemented entirely with LVDS signals running on 36 shielded twisted pair. This solution was chosen because of the distributed nature of the data sources (each DTMROC chip produces a 40 Mbit/sec data stream at the full L1 Accept rate and the almost 22 000 DTMROCs are spread over many square meters of detector surface). In addition, the cost and power penalties associated with many low speed radiation tolerant optical links are avoided. The TRT output data is converted to optical fiber only at the Patch Panels where 30 DTMROC outputs can be merged to form a single 1.2 Gb/s fiber output using commercial optical devices located in a region that can be accessed relatively easily.

The Back End design includes TRT specific Read Out Driver (ROD) and Trigger Timing Control (TTC) units. The ATLAS timing, trigger and control signals, in fact, are distributed by a central system. Anyway a protocol change is needed before transmitting signals to the detector, in order to minimize the functionality required in the Front-End. The DTMROC chips need to receive only the following information from the TTC module: Clock, Level-1 Accept Trigger, Event Counter Reset, Bunch Counter Reset, Test Pulse (for calibration purposes), Hard Reset and read and write commands for the parameters to configure the chips registers. These signals and values are transmitted via a serial protocol which is carried on four lines. Forty separate Front-End boards (each having between 9 and 15 DTMROC chips) can communicate independently with one TTC module. The clock and hard-reset lines are com-

mon for ten Front-End boards and are fanned out at the TTC Patch Panel. However, each Front-End board has its own dedicated command and read-back lines. The TTC also controls the interfaces to the Patch Panel in order to remotely adjust the Clock phase for each Front-End board. The communication to the Front-End boards is carried on four 25 pair cables from 60 to 100 m long. The large difference in length of the installed cables requires a set of timing and transmission adjustments. In addition to a 0.5 ns step clock phase adjustment on the Patch Panel, the duty cycle of clock signal can be adjusted on the TTC module as can the clock polarity. Each command line can also be phase-shifted, in 0.5 ns steps, and the read-back lines can be latched at any of four different phases, each 6 ns apart.

2.4 A use case: *b*-tagging to select top pair events

One of the many applications of the Inner Detector measurements is the possibility to discriminate tracks associated to the decay of short-life particles. These particles in fact decay in a displaced position with respect to the primary interaction vertex. The discrimination capability applies in particular to jets stemming from the hadronization of b quarks: in this case, the ability to identify jets containing b-hadrons is known as *b-tagging* and is very important for the high-p_{T} physics program of a general-purpose experiment at the LHC such as ATLAS. b-tagging is in particular useful to select very pure top samples, to search and/or study Standard Model or supersymmetric Higgs bosons which couple preferably to heavy objects or are produced in association with heavy quarks, and to veto the large dominant top pair background for several discovery channels.

The b-tagging capabilities are often associated with the discrimination of events containing top quarks. In the Standard Model, in fact, the decay of top quarks take place almost exclusively through the $t \to Wb$ decay mode. The W boson, then, decays in about 1/3 of the cases into a charged lepton and a neutrino. All three lepton flavors are produced at approximately equal rate. In the remaining 2/3 of the cases, the W boson decays into a quark-antiquark pair, and the abundance of a given pair is instead determined by the magnitude of the relevant CKM matrix elements. Specifically, the CKM mechanism suppresses the production of b quarks, since both $|V_{cb}|^2 = (1.70 \pm 0.06) \times 10^{-3}$ and $|V_{ub}|^2 = (1.5 \pm 0.2) \times 10^{-5}$ [90] are much smaller than unity. Thus, while for each top decay one b-jet is expected, the W boson decay can be considered as a clean source of light quarks.

When studying top pairs events, one can characterize the $t\bar{t}$ decay by the number of W bosons that decay leptonically. A value of 10.8% and 67.6% can be estimated for each leptonic and the total hadronic branching ratio of the W boson, respectively [90]. The following signatures can thus be identified for top pairs decay:

- *Fully leptonic*: represents about 1/9 of the $t\bar{t}$ events. Both W bosons decay into a lepton-neutrino pair, resulting in an event with two charged leptons, two neutrinos and two b-jets. This mode is identified by requiring two high p_{T} leptons and the presence of missing transverse energy ($E_{\mathrm{T}}^{\mathrm{miss}}$), and allows a clean sample of top quark events to be obtained. However, this sample has limited

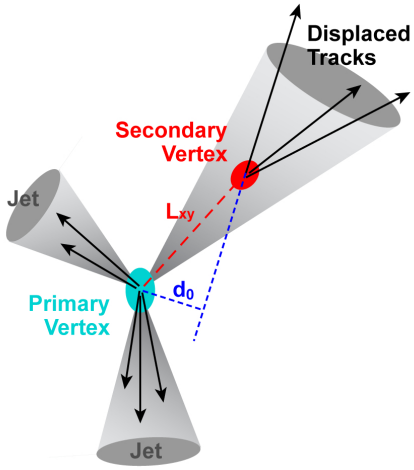

Figure 2.16: Schematic concept of the *b*-tagging using the vertex displacement.

use in probing the top quark reconstruction capability of the ATLAS experiment, due to the two neutrinos escaping detection.

– *Fully hadronic*: represents about 4/9 of the $t\bar{t}$ decays. Both W bosons decay hadronically, which gives at least six jets in the event: two *b*-jets from the top quark decay and four light jets from the W boson decay. In this case, there is no high-p_{T} lepton to trigger on, and the signal is not easily distinguishable from the abundant Standard Model QCD multi-jets production, which is expected to be orders of magnitude bigger than the signal. Another challenging point of this signature is the presence of a high combinatorial background when reconstructing the top quark mass.

– *Semi-leptonic*: represents about 4/9 of the $t\bar{t}$ decays. The presence of a single high-p_{T} lepton allows to suppress the Standard Model W boson+jets and QCD background. The p_{T} of the neutrino can be reconstructed as it is the only source of $E_{\mathrm{T}}^{\mathrm{miss}}$ for signal events.

In order to illustrate how *b*-tagging is implemented by using Inner Detector informations, Section 2.4.1 presents the algorithms available in ATLAS to perform *b*-tagging. Section 2.4.2 reports an estimation of *b*-tagging algorithms performance when the Inner Detector resolution is worse than nominal. In Section 2.4.3, instead, the relevance of *b*-tagging is presented, by describing how the default algorithm is used to improve the purity of the $t\bar{t}$ candidate events with respect to a basic selection, in the analysis for the measurement of top pair cross-section.

2.4.1 Algorithms to tag jets

The identification of *b*-jets takes advantage of several of their properties which allows to distinguish them from jets which contain only lighter quarks. First the fragmentation is hard and the *b*-hadron retains about 70% of the original *b* quark momentum. In addition, the mass of *b*-hadrons is relatively high (> 5 GeV). Thus, their decay products may have a large transverse momentum with respect to the

jet axis and the opening angle of the decay products is large enough to allow separation. The third and most important property is the relatively long lifetime of hadrons containing a b quark, of the order of 1.5 ps ($c\tau \approx 450$ μm). A b-hadron in a jet with $p_{\mathrm{T}} = 50$ GeV will therefore have a significant flight path length $\langle L \rangle = \beta\gamma c\tau$, traveling on average about $L_{xy} = 3$ mm in the transverse plane before decaying. Such displaced vertices (see Figure 2.16) can first be identified inclusively by measuring the impact parameters of the tracks from the b-hadron decay products. The transverse impact parameter, d_0, is the distance of closest approach of the track to the primary vertex point, in the R-Φ projection. The longitudinal impact parameter, z_0, is the z coordinate of the track at the point of closest approach in R-Φ. The tracks from b-hadron decay products tend to have rather large impact parameters which can be distinguished from tracks stemming from the primary vertex. The other more demanding option is to reconstruct explicitly the displaced vertices. These two approaches of using the impact parameters of tracks or reconstructing the secondary vertex will be referred to later on as *spatial b-tagging*. Finally, the semi-leptonic decays of b-hadrons can be used by tagging the lepton in the jet. In addition, thanks to the hard fragmentation and high mass of b-hadrons, the lepton will have a relatively large transverse momentum and also a large momentum relative to the jet axis. This is the so-called *soft lepton tagging* (the lepton being soft compared to high-p_{T} leptons from W or Z decays) [91].

Common requirements for spatial algorithms

The tracks reconstructed in the ATLAS Inner Detector are the main ingredient for spatial b-tagging. The properties of the Inner Detector allow the tracker to measure efficiently and with good accuracy the tracks within $|\eta| < 2.5$ and down to $p_{\mathrm{T}} \sim 500$ MeV. The b-tagging performance strongly depends upon the tracking efficiency and in particular on the tracking performance inside jets, where the track density may be high, originating tracks that shares some hits. The resolution of the track impact parameter is a crucial ingredient to be able to discriminate tracks coming from long-lived hadrons and prompt tracks.

Another key ingredient for b-tagging is the primary vertex of the event. The impact parameters of tracks are recomputed with respect to its position and tracks compatible with the primary vertex are excluded from the secondary vertex searches. At LHC the beam-spot size will be $\sigma_{xy} = 15$ μm and $\sigma_z = 5.6$ cm: therefore the primary vertex measurement is especially important for the z direction, while in the transverse plane only the beam-line could be used. The efficiency to find the primary vertex is very high in the high-p_{T} events of interest, and the resolution on its position is around 12 μm in each transverse direction and 50 μm along z. With pile-up, the presence of additional minimum bias vertices makes the choice of the primary vertex less trivial: at a luminosity of 2×10^{33} cm^{-2}s^{-1} (on average 4.6 minimum bias events per bunch-crossing) a wrong vertex can be picked up as the primary vertex in about 10% of the cases [92], thus causing a deterioration in the b-jet tagging efficiency.

A dedicated track selection is designed for b-tagging, in order to select well-measured tracks and reject fake tracks and tracks from long-lived particles (K_s, Λ or other hyperon decays) and material interactions (photon conversions or hadronic interactions). The *b-tagging quality* tracks feature at least seven hits in silicon detector, at least two in the Pixel Detector and one in the b-Layer. The transverse and longitudinal impact parameters must fulfil $|d_0| < 1$ mm and $|z_0 - z_{\mathrm{pv}}| \sin\theta < 1.5$ mm respectively,

where z_{pv} is the longitudinal location of the primary vertex and θ is the angle between the track and the z axis. Only tracks with $p_{\text{T}} > 1$ GeV are considered.

Algorithm based on impact parameter

The spatial b-tagging algorithms, built on tracks and subsequently vertices, are the most powerful ones. Most of them are based on a likelihood ratio approach, but simpler and more robust tagging algorithms are also available. All tracks in the jet fulfilling the *b-tagging quality* are considered for the spatial b-tagging algorithms.

For the tagging itself, the impact parameters of tracks are computed with respect to the primary vertex. On the basis that the decay point of the b-hadron must lie along its flight path, the impact parameter is signed to further discriminate the tracks from b-hadron decay from tracks originating from the primary vertex. The sign is defined using the jet direction $\vec{P}_j$ as measured by the calorimeters, the direction $\vec{P}_t$ and the position $\vec{X}_t$ of the track at the point of closest approach to the primary vertex and the position $\vec{X}_{\text{pv}}$ of the primary vertex:

$$\text{sign}(d_0) = \text{sign}\left\{\left(\vec{P}_j \times \vec{P}_t\right) \cdot \left[\vec{P}_t \times \left(\vec{X}_{\text{pv}} - \vec{X}_t\right)\right]\right\}. \tag{2.1}$$

The experimental resolution generates a random sign for the tracks originating from the primary vertex, while tracks from the b-/c-hadron decay tend to have a positive sign. The sign of the longitudinal impact parameter z_0 is given by the sign of $(\eta_j - \eta_t) \times z_{0t}$ where again the t subscript refers to quantities defined at the point of closest approach to the primary vertex. The distribution of the signed transverse impact parameter d_0 is shown on Figure 2.17(a) for tracks coming from b-jets, c-jets and light jets identified in simulated collision events. Figure 2.17(b) shows the significance distribution $S_i = d_0/\sigma_{d_0}$ which gives more weight to precisely measured tracks. Combining the impact parameter significances of all the tracks in the jet is the basis of the first method to tag b-jets.

Three tagging algorithms are defined in this way: `IP1D` relies on the longitudinal impact parameter, `IP2D` on the transverse impact parameter and finally `IP3D` which uses two-dimensional histograms of the longitudinal versus transverse impact parameters, taking advantage of their correlations. For all these algorithms, a likelihood ratio method is used: the measured value S_i of the discriminating variable is compared to pre-defined smoothed and normalized distributions for both the b- and light jet hypotheses, $b(S_i)$ and $u(S_i)$. Two- and three-dimensional probability density functions are used for the `IP2D` and `IP3D` tagging algorithms. The ratio of the probabilities $b(S_i)/u(S_i)$ defines the track weight, which can be combined into a jet weight W_{Jet} as the sum of the logarithms of the N_T individual track weights W_i:

$$W_{\text{Jet}} = \sum_{i=1}^{N_T} \log W_i = \sum_{i=1}^{N_T} \log \frac{b(S_i)}{u(S_i)} \tag{2.2}$$

To select b-jets, a cut value on W_{Jet} must be chosen, corresponding to a given *efficiency*. The relation between the cut value and the efficiency depends on the jet transverse momentum and rapidity.

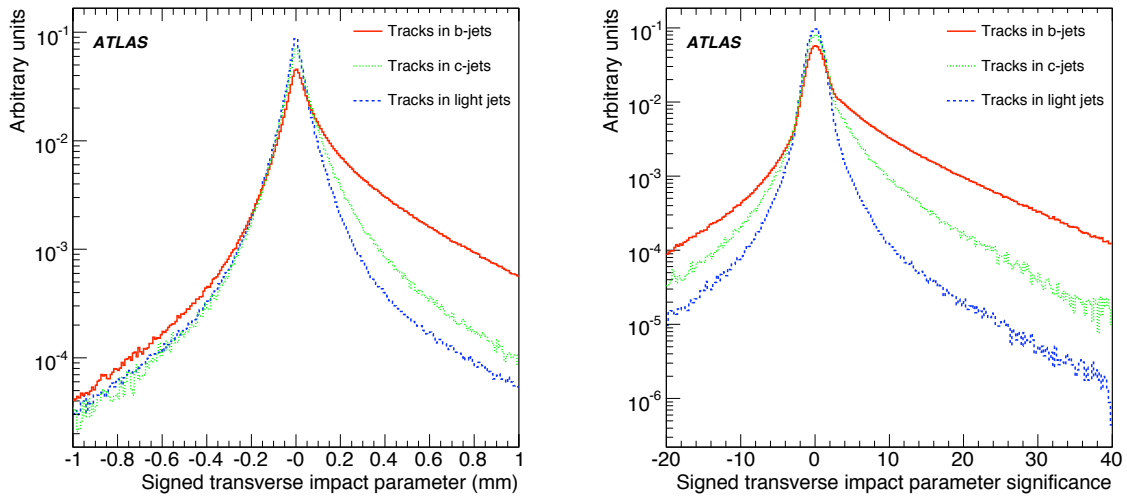

(a) (b)

Figure 2.17: 2.17(a): signed transverse impact parameter d_0 distribution. 2.17(b): transverse impact parameter significance $S_i = d_0/\sigma_{d_0}$ distribution. Both distributions are drawn for b-jets, c-jets and light jets. Figures taken from [91].

Secondary vertex tagging algorithms

To further increase the discrimination between b-jets and light jets, the inclusive vertex formed by the decay products of the bottom hadron, including the products of the eventual subsequent charm hadron decay, can be sought. The search starts by building all two-track pairs that form a good vertex, using only tracks far enough from the primary vertex [92]. Vertices compatible with a V_0 or material interaction are rejected. All tracks from the remaining two-track vertices are combined into a single inclusive vertex, using an iterative procedure to remove the worst track until the χ^2 of the vertex fit is good. Three of the vertex properties are exploited: the invariant mass of all tracks associated to the vertex, the ratio of the sum of the energies of the tracks participating to the vertex to the sum of the energies of all tracks in the jet and the number of two-track vertices.

The so-called `SV` tagging algorithms make different use of these properties: `SV1` relies on a 2D-distribution of the two first variables and a 1D-distribution of the number of two-track vertices, while `SV2` is based on a 3D-histogram of the three properties which requires quite some statistics. The secondary vertex finding efficiency depends in particular on the event topology, but the typical efficiency $\varepsilon_b^{\mathrm{SV}}$ is higher than 60% in b-jets. The `SV` taggers require an a priori knowledge of $\varepsilon_b^{\mathrm{SV}}$ and $\varepsilon_u^{\mathrm{SV}}$.

Combining tagging algorithms

Currently the likelihood-based tagging algorithms can be combined, in order to increase their discriminating power. The likelihood formalism is straightforward in this case: the weights of the individual tagging algorithms are simply summed up. The most commonly used tagging algorithm, `IP3D+SV1`, is

actually such a combination. It should be noted that the SV tagging algorithms have been optimized to work in conjunction with the IP ones.

2.4.2 Performance of *b*-tagging algorithms

The effect of a degradation in the Inner Detector performance in the *b*-tagging has been evaluated in [93]. A number of different alignment scenarios for the Inner Detector were considered and the Monte Carlo simulation was used to introduce misalignment between detector modules at the simulation stage. Four alignment sets were used in this study:

- *Perfect*: This data set is the ideal case where the same set of alignments used in the simulation are used in the reconstruction and so one does not see any misalignment.
- *Aligned*: This data set uses an alignment set produced using the actual track based alignment algorithms developed for the ATLAS detector (see Section 5.1.5). It is expected to include any systematic deformations that the alignment procedure itself causes. While some systematic effects were included in the misalignments introduced in the simulation, such as clocking effects where each subsequent layer was rotated by increasing amounts, it does not contain all the systematic deformations which are expected. In particular large scale structures such as layers and discs were treated as rigid objects without any internal deformations such as a twist. Also pixel stave bows which are known to occur were not introduced. So it is possible that this set is still optimistic. This set is a first attempt at the full scale alignment of the Inner Detector and so should not be considered the final word on what will be seen in the real detector. However, it is considered to be the most realistic case studied in this analysis.
- Random10: This data set takes the misalignment set used in simulation and randomly shifts the module positions by small amounts. These residual misalignments were introduced at different levels in the hierarchy. Random shifts and rotations were made to individual modules, and whole layers and disks. A small shift and rotation was also made to the whole pixel structure. Since the degradation of the *b*-tagging performance is expected to be dominated by the alignment of the pixel system, only pixel residual misalignments were introduced. The SCT and TRT were corrected perfectly as in the perfect alignment case. Due to movements of higher level structures in this set, some systematic effects may exist. The levels of misalignment are given in Table 2.9. The axis definitions for the module level uses a local frame where x and y are the R-Φ and η measurement directions respectively and z is out of the plane. For higher levels they correspond to the global frame with z-axis along the beam direction. *RotX*, *RotY*, *RotZ* are rotations around the corresponding axes. The module level shifts in the R-Φ measurement direction are around 10 μm. The set attempts to emulate the level of misalignments expected during the early running period. It is not well known what levels of misalignments are expected after certain running periods so this is just an indication rather than being a firm prediction of what is expected at

Level	x	y	z	*RotX*	*RotY*	*RotZ*
Module	10	30	30	0.3	0.5	0.2
Layer	10	10	15	0.05	0.05	0.1
Disk	10	10	30	0.2	0.2	0.1
Whole pixel	10	10	15	0.1	0.1	0.1

Table 2.9: Residual misalignment for *Random10*. Random misalignments were generated with a Gaussian distribution with σ as tabulated. Shifts are in micron and rotations are in mrad. Table taken from [93].

Level	x	y	z	*RotX*	*RotY*	*RotZ*
Module	5	15	15	0.15	0.3	0.1
Layer	7	7	10	0.02	0.02	0.05
Disk	7	7	20	0.1	0.1	0.05
Whole pixel	7	7	10	0.05	0.05	0.05

Table 2.10: Residual misalignment for *Random5*. Random misalignments were generated with a Gaussian distribution with σ as tabulated. Shifts are in micron and rotations are in mrad. Table taken from [93].

start up. Comparison with the real alignments (*Aligned* set) shows this to be a rather pessimistic scenario.

– *Random5*: As with *Random10*, but with levels of misalignment better by about a factor of 1.5 to 2. This is an estimate of what might be expected after several years of running. Like *Random10*, this set introduces misalignments at the three levels of hierarchy with levels of misalignment given in Table 2.10.

In order to evaluate b-tagging performances, two estimators are introduced. The tagging *efficiency* is naturally defined as the fraction of jets labelled in simulation as b-jets which are actually tagged as b-jets by the tagging algorithm under study. The *mistagging rate* is the fraction of jets not labelled as b in simulation which are actually tagged as b-jets. For historical reasons the jet *rejection* is used instead: this is simply the inverse of the mistagging rate.

Figure 2.18 shows the rejections for different taggers for light jets. The `SV1` tagger is the most affected by misalignment with the *Aligned* set showing 10% lower rejections than the *Perfect* case and up to a factor 4–5 degradation for the largest misalignment. The impact parameter based taggers does not suffer when considering *Aligned* geometry, but perform a factor 2 worse when considering misalignments of about ten microns. Finally, the combined performances of the combined tagger follow the performance of the worst case, having a factor 5 degradation when considering *Random10* misalignments.

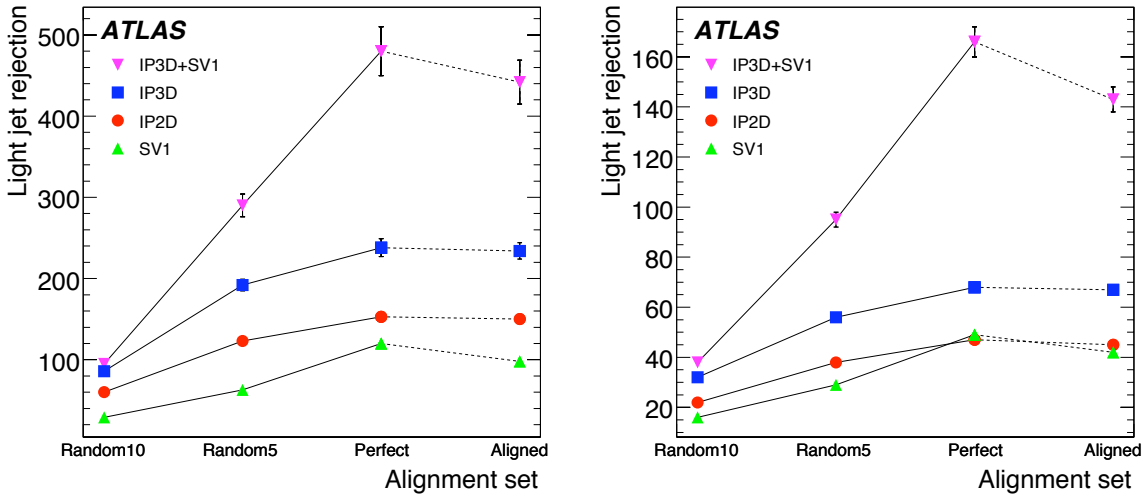

(a) (b)

Figure 2.18: Comparison of the light jet rejections for the different taggers, `IP2D`, `IP3D`, `SV1` and the combined tagger `IP3D+SV1` when using $t\bar{t}$ simulated events. 2.18(a): results for 50% b-tag efficiency. 2.18(b): results for 60% b-tag efficiency. Figures taken from [93].

2.4.3 Measurement of top pair cross-section

The determination of the top quark pair production cross-section is one of the measurements that will be carried out once the first data samples are available at the ATLAS experiment. It casts light on the intrinsic properties of the top quark and its electroweak interactions. Cross-section measurements are also an important test of possible new production mechanism, as non Standard Model top quark production can lead to a significant increase of the cross-section. New physics may also modify the cross-section times branching ratio differently in various decay channels, as for example predicted by Supersymmetric models with charged Higgs particles, $t \to H^- \bar{b}$, or with super-partners of the top quark, $t \to \tilde{t}\tilde{\chi}^0$ [94].

The desired cross-section can be obtained by performing a counting experiment:

$$\sigma = \frac{N_{\text{sig}}}{\mathscr{L} \times \varepsilon} = \frac{N_{\text{obs}} - N_{\text{bkg}}}{\mathscr{L} \times \varepsilon}. \tag{2.3}$$

The number of background events (N_{bkg}) is estimated from Monte Carlo simulations and/or data samples, and is subtracted from the number of observed events (N_{obs}) meeting the selection criteria of a defined top-event signature. This difference is divided by the integrated luminosity $\mathscr{L}$ and the total efficiency ε. The efficiency must include the geometrical acceptance, the trigger efficiency and the event selection efficiency.

	Trigger eff (%)	Lepton eff (%)	$E_{\mathrm{T}}^{\mathrm{miss}}$ eff (%)	Jet req. (I) eff (%)	Jet req. (II) eff (%)	Combined eff (%)
$t\bar{t}$ (electron)	52.9	52.0	91.0	70.7	61.9	18.2
$t\bar{t}$ (muon)	59.9	68.7	91.6	65.5	57.3	23.6

Table 2.11: Fraction of events passing the selection criteria and the combined selection efficiency for semi-leptonic (electron and muon) analyses described in [94]. The statistical uncertainties on these numbers are negligible.

Basic event selection

The counting method can be applied to the semi-leptonic decay mode of the top pair. This channel, which has a branching fraction of approximately 45%, has a clear signature, is experimentally easily accessible and is expected not to suffer from large backgrounds. The identification of semi-leptonic $t\bar{t}$ events starts by requiring a high-level lepton trigger to have fired. Further, a candidate top pair event should have one reconstructed high-p_{T} isolated lepton (electron or muon), a minimal amount of missing energy and at least four reconstructed jets. For a typical selection [94], the events are required to fulfil the following:

- One lepton (electron or muon) with $p_{\mathrm{T}} > 20$ GeV.
- $E_{\mathrm{T}}^{\mathrm{miss}} > 20$ GeV.
- At least four jets with $p_{\mathrm{T}} > 20$ GeV.
- Of which at least three jets with $p_{\mathrm{T}} > 40$ GeV.

The fraction of events passing the individual selection requirements and the overall selection efficiency for the analysis detailed in [94] are shown in Table 2.11 for semi-leptonic top pairs. This analysis uses 100 pb^{-1} of data, simulated to reproduce collisions with 14 TeV center of mass energy. The efficiencies are divided according to the W decay in the Monte Carlo generator: $t\bar{t}$ (electron) where it decayed to an electron and a neutrino and $t\bar{t}$ (muon) where it decayed to a muon and a neutrino.

In order to estimate the number of background events that fulfill the basic selection introduced, several processes are considered. The dominant expected background is W boson+jets, but also single top production, Z boson+jets and $Wb\bar{b}$ are sizeable. Tables 2.12 and 2.13 summarise the expected numbers of signal and background events for the electron and muon analysis respectively. The second column of the two tables shows the event numbers obtained by applying the basic selection just presented.

Selection criteria based on mass constraints

Apart from the default event selection as described above, a number of additional criteria should be defined to further increase the purity of the top sample and to reach a signal to noise ratio better than 2.2. These criteria can be introduced by considering mass constraint on the reconstructed jets. In the $t\bar{t}$

Electron analysis						
Sample	default	W const.	m_t win	W const. + $\|\eta\| < 1$	W const. + 1 b-tag	W const. + 2 b-tag
$t\bar{t}$	2555	1262	561	303	329	208
hadronic $t\bar{t}$	11	4	0.0	0.8	0.6	0.0
W+jets	761	241	60	38	7	1
single top	183	67	23	12	18	7
$Z\rightarrow ll$ +jets	115	35	8	5	2	0.4
$W\ b\bar{b}$	44	15	3	5	5	0.7
$W\ c\bar{c}$	19	6	1	1	0.4	0.0
WW	7	4	0.4	0.0	0.0	0.0
WZ	4	1	0.4	0.2	0.0	0.0
ZZ	0.5	0.2	0.1	0.0	0.0	0.0
Signal	2555	1262	561	303	329	208
Background	1144	374	96	63	33	10
S/B	2.2	3.4	5.8	4.8	10.0	20.8

Table 2.12: Number of events which pass the various electron selection criteria for the $t\bar{t}$ signal and for the most relevant backgrounds normalised to 100 pb^{-1}. Table taken from [94].

Muon analysis						
Sample	default	W const.	m_t win	W const. + $\|\eta\| < 1$	W const. + 1 b-tag	W const. + 2 b-tag
$t\bar{t}$	3274	1606	755	386	403	280
hadronic $t\bar{t}$	35	17	7	6	5	2
W+jets	1052	319	98	47	11	0.0
single top	227	99	25	19	19	10
$Z\rightarrow ll$ +jets	84	23	3	2	0.5	0.0
$W\ b\bar{b}$	64	19	4	4	5	2
$W\ c\bar{c}$	26	9	3	0.7	0.1	0.0
$W\ W$	7	3	0.7	0.7	0.0	0.0
$W\ Z$	7	3	0.8	0.5	0.0	0.0
$Z\ Z$	0.7	0.3	0.1	0.0	0.0	0.0
Signal	3274	1606	755	386	403	280
Background	1497	495	143	84	42	14
S/B	2.2	3.2	5.3	4.6	9.6	20.1

Table 2.13: Number of events which pass the various muon selection criteria for the $t\bar{t}$ signal and for the most relevant backgrounds normalised to 100 pb^{-1}. Table taken from [94].

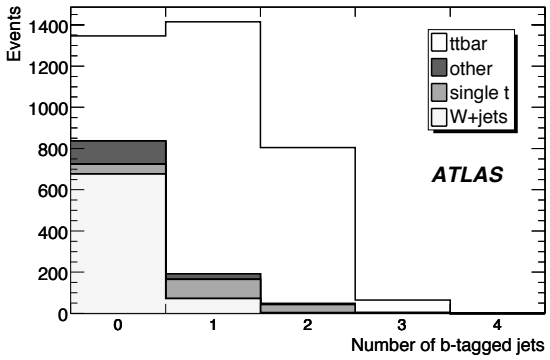

Figure 2.19: Number of jets tagged as coming from a b-quark in $t\bar{t}$, single top and W boson+jet events after the basic electron selection. Figure taken from [94].

candidates, three of the reconstructed jets are expected to form the hadronic top quark. In the absence of b-tagging there is an additional ambiguity in choosing the correct three-jet combination among the reconstructed jets: the top-quark decay candidate can be defined as the three-jet combination of all jets that has the highest transverse momentum sum. Furthermore, the three-jet combination that originates from a top decay also contains a two-jet combination that originates from a W boson decay. To illustrate the presence of the W boson, the three jets that constitute the top quark are considered. Among the three possible combinations of two-jets, at least one should be within 10 GeV of the reconstructed mass of the W boson, in order to satisfy the W *constraint*. The efficiency of this constraint is evaluated in the third column of Tables 2.12 and 2.13.

To give an indication of the signal purity in the top mass peak region, in the fourth column of Tables 2.12 and 2.13 the number of events in the hadronic top mass region $141 < m_t < 189$ GeV is reported. Although not all signal events are correctly reconstructed, in both the electron and muon analyses the purity of the signal in the top mass window is close to 80%.

Additional ways to kinematically select top events other than the W boson mass constraint, or to improve the signal purity after having applied the W boson mass cut itself, can be explored. In the commissioning phase, for example, it can be convenient to consider only the barrel calorimetry, that will be better calibrated than the forward one. Therefore, it can be useful to apply the additional request that the three highest p_{T} jets are all at $|\eta| < 1$. Tables 2.12 and 2.13 show, in the fifth column, the signal-over background and signal efficiencies for the electron and muon analyses if this centrality requirement is applied in addition to the W boson constraint.

Selection using b-tagging

Even if the analyses described already reach good signal to background ratios, the possibility to identify b-flavoured jets will definitively improve the signal to background ratio of the selection. The number of "tagged" b-jets in the $t\bar{t}$, single top and W boson+jet events which pass the default selection for the analysis described in [94] is shown in Figure 2.19. The algorithm that have been used to tag jets is the `IP3D+SV1` with a chosen efficiency of 60%.

Tables 2.12 and 2.13 list the number of top pair and background events in the electron and muon channel which survive the default selection plus the W boson mass constraint, and the request of having one and only one, or two and only two b-jets (column six and seven). For all these cases, the corresponding signal to background ratios are given.

In these cases, the W-boson mass constraint can then be applied to the jets which are not b-tagged, reducing combinatorial effects. Furthermore, the hadronic top candidate can be chosen as the three-jet combination with the highest possible p_{T}, obtained by requiring that one and only one of the three jets is a b-jet. If the three-jet combination chosen is such that the two non-b-jets do not combine to give a satisfactory W boson candidate, that event can be rejected.

Requiring one or two b-tagged jets improves the purity of the sample by more than a factor of four, while the signal efficiency is only reduced by a factor of two. In the case of 14 TeV collisions, that has been analyzed in this section, such an improvement is appreciable but not necessary to obtain a reasonable sample of $t\bar{t}$ events. In the first year of operation, anyway, the ATLAS detector will benefit only of collisions at 10 TeV maximum in the center of mass. A naïve estimate of the cross sections for both top pair events and background at 10 TeV can be made by inspecting Figure 1.1: while the background is expected to be nearly constant (as the total cross section σ_{tot}), the number of top pair events (σ_t) is expected to decrease by one half. In this situation, the improvement brought by b-tagging would be extremely valuable, if not fundamental, in order to obtain a good signal over background ratio.

Chapter 3

Cosmic muon data

In this chapter some general information about cosmic ray data-taking in ATLAS is presented, to introduce the commissioning activities described in Chapter 4 and 5. Section 3.1 describes the origin of cosmic ray muons, and their global characteristics. In Section 3.2 the commissioning activity on the ATLAS Inner Detector is presented: the data sample is reported and the conditions of different subsystems during data-taking is described. Section 3.3 is dedicated to the description of the triggers used to register cosmic ray data and their efficiency and acceptance together with modulation given by the geometry of the cavern where the ATLAS detector is placed. Section 3.4 details the treatment of cosmic ray data: in order to test and improve the tracking software, these data were reconstructed several times, using different calibration datasets of the detectors. The reprocessed datasets chosen for the analyses reported in the following chapters are described in this section. Finally, Section 3.5 illustrates how cosmic ray events were simulated in order to provide a comparison with measured data.

3.1 Cosmic rays

The cosmic radiation incident at the top of the terrestrial atmosphere includes all stable charged particles and nuclei with lifetimes of order 10^6 years or longer. Technically, primary cosmic rays are those particles accelerated at astrophysical sources, and secondaries are those particles produced in interaction of the primaries with interstellar gas. Thus, electrons, protons, and helium, as well as carbon, oxygen, iron, and other nuclei synthesized in stars, are primaries. Nuclei such as lithium, beryllium, and boron (which are not abundant end-products of stellar nucleosynthesis) are secondaries. Antiprotons and positrons are also in large part secondary [95].

Apart from particles associated with solar flares, the cosmic radiation comes from outside the solar system. The motion of incoming charged particles is largely determined by the solar magnetic field: a significant anticorrelation between solar activity and the intensity of the cosmic rays with energies below ~ 10 GeV is observed. In addition, the lower-energy cosmic rays are affected by the geomagnetic field, which they must penetrate to reach the top of the atmosphere. Thus the intensity of any component of the cosmic radiation in the GeV range depends on both location and time.

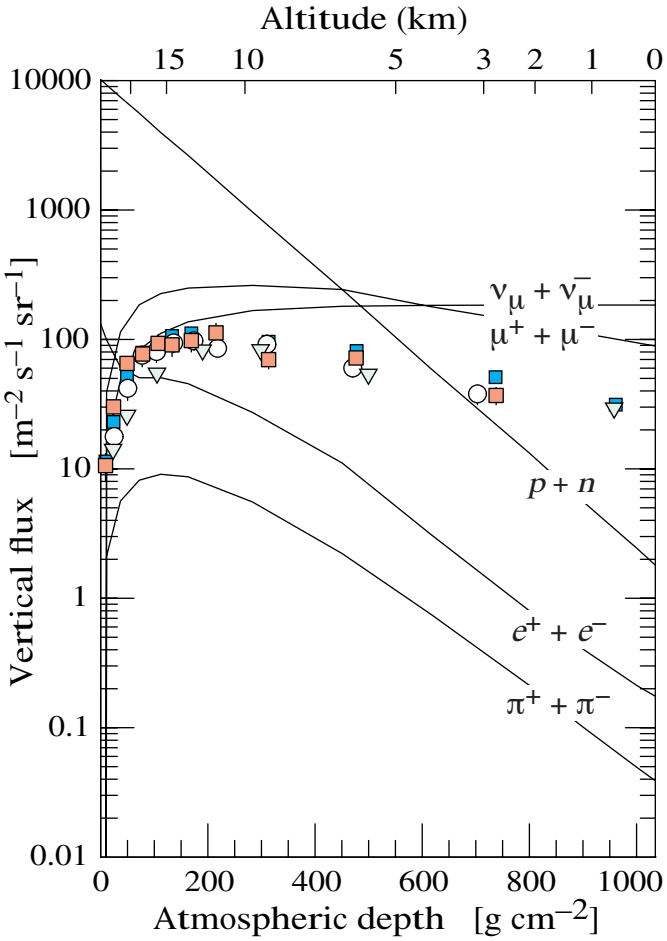

Figure 3.1: Estimation of the vertical fluxes of cosmic rays in the atmosphere with $E > 1$ GeV. The points show measurements of negative muons with $E > 1$ GeV. Figure taken from [95].

Figure 3.1 shows the vertical fluxes of the major cosmic ray components in the atmosphere in the energy region where the particles are most numerous (except for electrons, which are most numerous near their critical energy, which is about 81 MeV in air). Except for protons and electrons near the top of the atmosphere, all particles are produced in interactions of the primary cosmic rays in the air. Muons and neutrinos are products of the decay of charged mesons, while electrons and photons originate in decays of neutral mesons.

Muons are the most numerous charged particles at sea level. Moreover, only muons and neutrinos penetrate to significant depths underground, being able to reach the cavern where the ATLAS experiment is located. Since neutrinos cannot be detected by ATLAS, when mentioning cosmic rays in the following, only muons will be considered.

Most cosmic ray muons are produced high in the atmosphere (typically 15 km) and lose about 2 GeV to ionization before reaching the ground. Their energy and angular distribution reflect a convolution of production spectrum, energy loss in the atmosphere, and decay. The mean energy of muons

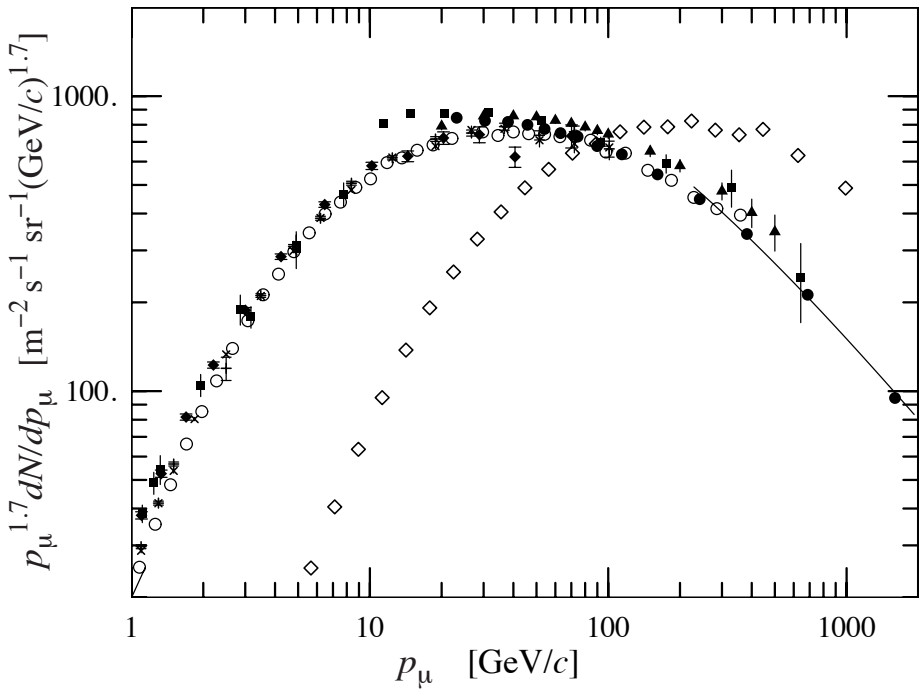

(a)

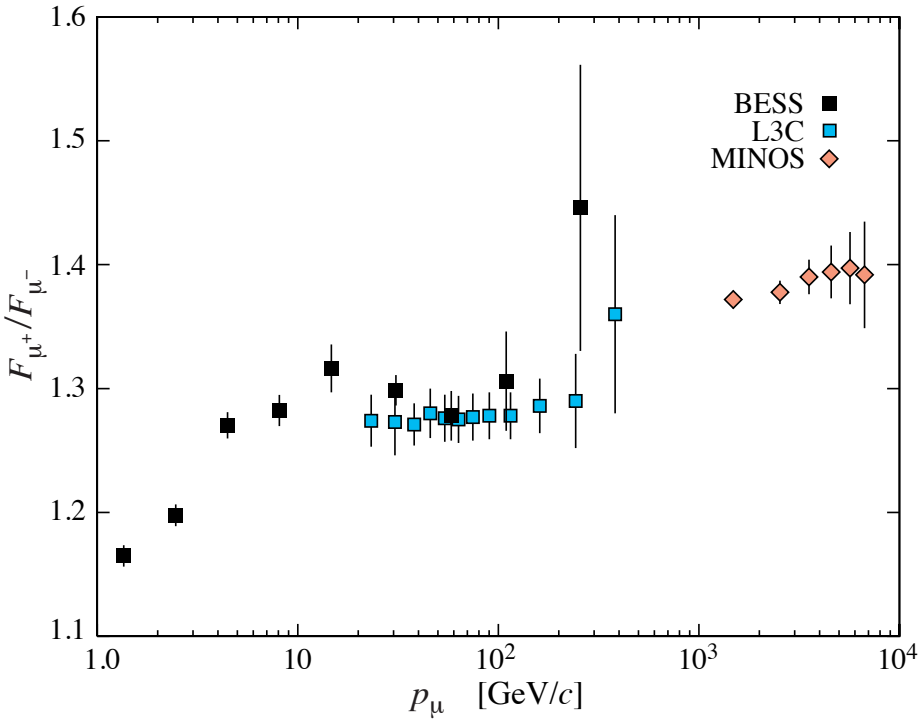

(b)

Figure 3.2: 3.2(a): spectrum of cosmic muons at $\theta = 0°$ and $\theta = 75°$ (open squares). The line plots a theoretical result for vertical showers. 3.2(b): cosmic muons charge ratio as a function of the muon momentum. Figures taken from [95].

E_μ	R	a	b_{brems}	b_{pair}	b_{nucl}	$\sum b_i$	$\sum b(\text{ice})$
GeV	km.w.e.	MeV g^{-1} cm^2	———	10^{-6} g^{-1} cm^2		———	
10	0.05	2.17	0.70	0.70	0.50	1.90	1.66
100	0.41	2.44	1.10	1.53	0.41	3.04	2.51
1000	2.45	2.68	1.44	2.07	0.41	3.92	3.17
10000	6.09	2.93	1.62	2.27	0.46	4.35	3.78

Table 3.1: Average muon range R and energy loss parameters calculated for standard rock. Range is given in km-water-equivalent (10^5 g cm^{-2}). Table taken from [95].

at ground is ~ 4 GeV. For muons of this energy there is also a solar activity and a latitude effect that results from the geomagnetic effects. The energy spectrum is almost flat below 1 GeV, steepens gradually in the 10–100 GeV range, and steepens further at higher energies because moderate energy pions tend to interact in the atmosphere before they decay. Figure 3.2(a) shows the muon energy spectrum at sea level for two incident angles of cosmic muons. At large angles low-energy muons decay before reaching the surface and high-energy pions decay before they interact, thus the average muon energy increases. The muon charge ratio (see Figure 3.2(b)) reflects the excess of π^+ over π^- and K^+ over K^- in the forward fragmentation region of proton initiated interactions, together with the fact that there are more protons than neutrons in the primary spectrum of cosmic rays.

When considering cosmic muons detected underground, the energy loss in rock must be accounted. Muons lose energy by ionization and by radiative processes [96]: bremsstrahlung, direct production of e^+e^- pairs, and photonuclear interactions. The total muon energy loss may be expressed as a function of the amount of matter traversed as

$$-\frac{\mathrm{d}E_\mu}{\mathrm{d}X} = a + bE_\mu, \tag{3.1}$$

where a is the ionization loss and b is the fractional energy loss by the three radiation processes. Both are slowly varying functions of energy. The quantity $\varepsilon \equiv a/b$ (≈ 500 GeV in standard rock) defines a critical energy below which continuous ionization loss is more important than radiative losses. Table 3.1 shows a and b values for standard rock as a function of muon energy. The second column of the table shows the muon range in standard rock ($A = 22$, $Z = 11$, $\rho = 2.65$ g cm^{-3}).

3.2 Inner Detector commissioning in 2008

The 2008 Inner Detector operation consisted of three main data-taking periods: single-beam LHC, combined cosmic ray and a devoted ID commissioning run.

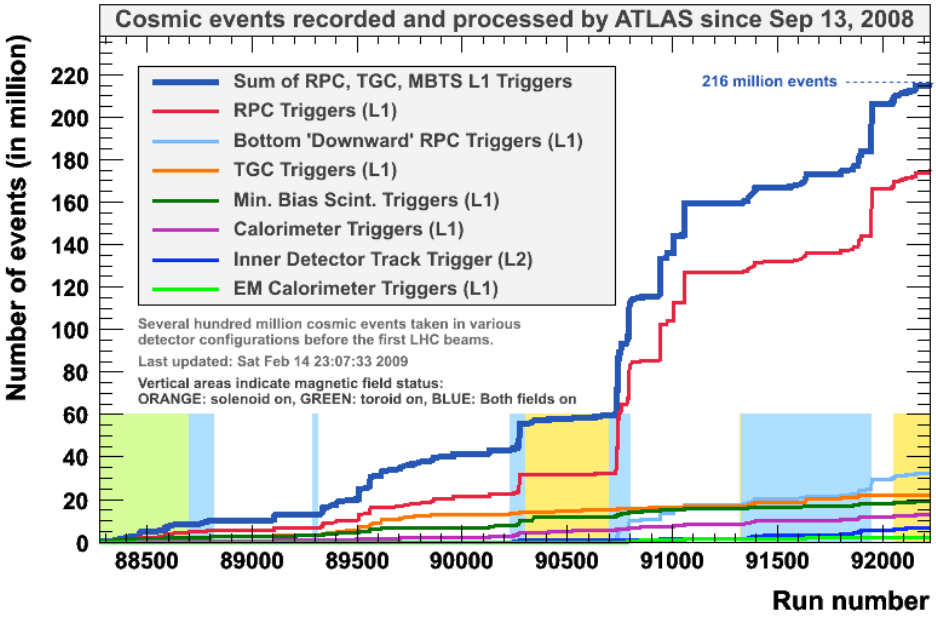

Figure 3.3: Number of cosmic ray events registered by ATLAS in the period September 2008–February 2009, for different trigger setups and as a total number. Data analyzed in this thesis have run number contained in the range 90260–92082.

The single beam LHC running period went from 10th till 13th of September. The LHC beams were directed to scrape into the tertiary collimators located at 150 m from the interaction point, in order to provide secondary particles crossing the whole section of the ATLAS detector. For reasons of detector safety, during this period only the TRT and the SCT end-caps were switched on. Since the incident particles have a direction almost parallel to the beam axis, they cross many detector layers and can be used for synchronization of the individual read-out unities.

A combined cosmic ray data-taking, involving the whole ATLAS experiment started immediately after the initial LHC single beam running and lasted till 23rd October. Operation was performed with different setting for the magnetic field, with the ATLAS toroid and solenoid switched on and off independently. For Inner Detector calibration the most relevant condition is the status of the solenoid (see Section 1.3.2): in the following, the term *field on* will indicate the condition in which the solenoid field is switched on to its design value of 2 T, and *field off* refers to the condition when the solenoid is switched off. A one week long ID standalone run was performed at the end of November 2008. It used a newly introduced Level-1 tracking trigger. All data taken during this period were with field-off. A summary of the collected statistics in both cosmic ray data-taking periods in 2008 is shown in Figure 3.3.

3.2.1 Inner Detector sub-systems availability

Most of the detector was operational during the cosmic ray data-taking periods. Loss of coverage were mainly due to issues with the optical links (see Sections 2.1.3 and 2.2.3) and the cooling system (see

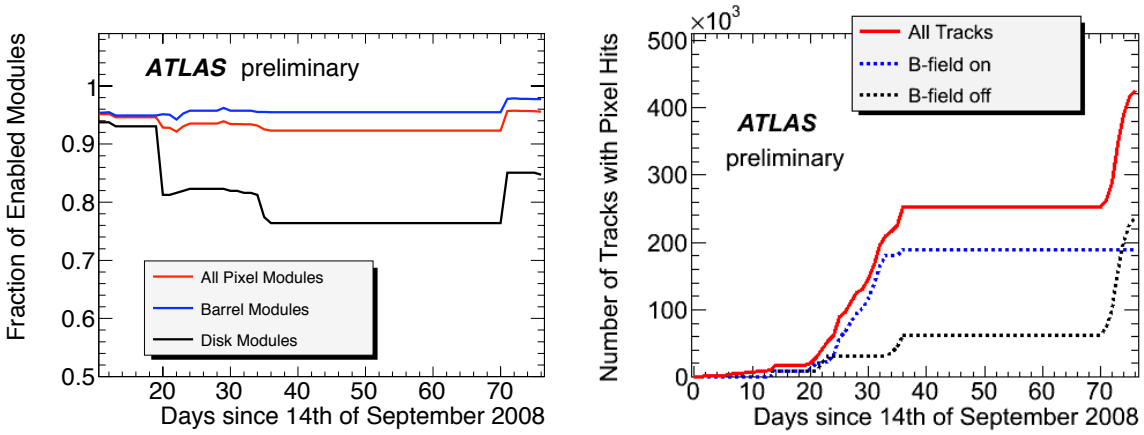

(a) (b)

Figure 3.4: 3.4(a): fraction of Pixel Detector modules enabled during cosmic ray data-taking. 3.4(b): integrated number of tracks with at least one pixel hit. Both distributions are shown as a function of day for the running between September 14th and December 1st 2008.

Section 2.1 and 2.2.2). The one major problem with the optical links for the SCT and Pixel detectors was the death of the laser transmitters in the off-detector interfaces (BOC in Figure 2.6). This did not lead to any loss of data for the SCT because of the redundancy system, but was strongly affecting the Pixel Detector active fraction. Moreover, the evaporative cooling system was showing significant leaks on few loops. For safety these loops were not operated in 2008, affecting 36 modules in both the Pixel Detector and the SCT. The resulting active fraction was therefore 96% for the Pixel Detector barrel and 98% for the SCT and TRT. The fraction of available modules in the Pixel Detector is reported in Figure 3.4(a): two main events determined its evolution. On 4th October (day 20) three cooling loops (corresponding to 36 modules) in the disks were turned off. In November (before day 70) a new tuning of the optical links was performed and some new components were installed resulting together in the recovery of about 3% of the modules.

Figure 3.4(b) shows the number of tracks that feature at least one hit in the pixels. Tracks used in this thesis for the commissioning of the Inner Detector always included at least one pixel hit. The total number of tracks with this characteristics is about 240,000 without magnetic field and 190,000 with magnetic field. The number of tracks with at least 4 pixel hits is about a factor 2 lower: only these tracks will be used in Chapter 5 to measure tracking system performance (see Section 5.4.1).

3.3 Triggering cosmic muons

The ATLAS trigger implementation is described in Section 1.3.7, where its functionality on collision events is presented. During the October 2008 cosmic ray data-taking, RPC, TGC and Liquid Argon Calorimeter were used to trigger on cosmic ray events. For the November 2008 data-taking, a L1 TRT trigger was added based on a fast digital OR of TRT straws in groups of approximately 200. The RPC L1

trigger was the most efficient for triggering cosmic tracks passing through the central ID region. Due to its high rate, ID tracking triggers were used at software-level (L2) to select RPC-triggered events with an ID track.

Three Inner Detector tracking algorithms were run as Level-2 triggers. One of these algorithms, `TrigTRTSegFinder`, was specifically designed for cosmic running and uses only barrel TRT information. It reconstructs tracks in a search window of up to about 45° to the vertical in azimuthal angle. The other two algorithms, `IDSCAN` and `SiTrack`, were designed for collisions but have been adapted for cosmic running in order to exercise the algorithms online in cosmic running and also to complement the coverage of the TRT trigger. These algorithms start with track reconstruction in the Silicon detectors and then extrapolate tracks to the TRT. As a consequence of being designed for collisions, the cosmic particle trajectory is reconstructed as two tracks; one going upwards and the other downwards. `IDSCAN` and `SiTrack` use a common input consisting of hits in the Pixel Detector or in the SCT. The two algorithms share common tools for track fitting and extrapolation to the TRT, but differ in the initial track-finding step:

- `SiTrack` is based on a combinatorial method. It first looks for pairs of space-points in the inner layers consistent with beam-line constraints, then combines these pairs with space-points in other layers to form triplets and finally merges triplets to form track candidates.
- `IDSCAN` uses a three-stage histogramming method to first determine the z-coordinate (position along the beam) of the interaction point (IP) in collision events, and then look for track candidates consistent with this IP.

In order to allow these algorithms, designed for collisions, to run with good efficiency in cosmic data-taking, some adaptations were made. For `SiTrack`, the beam constraint was relaxed and for `IDSCAN`, a first step was introduced which shifts the space-points in the direction transverse to the beam-pipe, so that the shifted points lie on a trajectory passing close to the nominal beam position.

The efficiency of these L2 triggers have been determined by using events triggered by the L1 muon trigger and containing an Inner Detector track that has been subsequently identified by standard reconstruction algorithms. In Figure 3.5(a) the efficiency is shown as a function of the distance of the track from the beam axis (d_0) for each of the three different algorithms as well as for the combined trigger. In Figure 3.5(b) the efficiency is a function of the transverse momentum of the particle, while in Figure 3.5(c) it is plotted with respect to the TRT event phase (see Section 3.3.1).

The efficiency was calculated for tracks that featured, after reconstruction, three silicon hits in the barrel for both the upper and the lower track segment. The track is also required to be within the TRT read-out time window. The efficiency for `IDSCAN` and `SiTrack` falls off for tracks with d_0 approaching the radius of the inner SCT layer (300 mm). The space-point shifting step that precedes `IDSCAN` fails for high-curvature tracks, and this is reflected in a lower efficiency for tracks at low momentum. The combined efficiency of the Inner Detector L2 triggers is close to one.

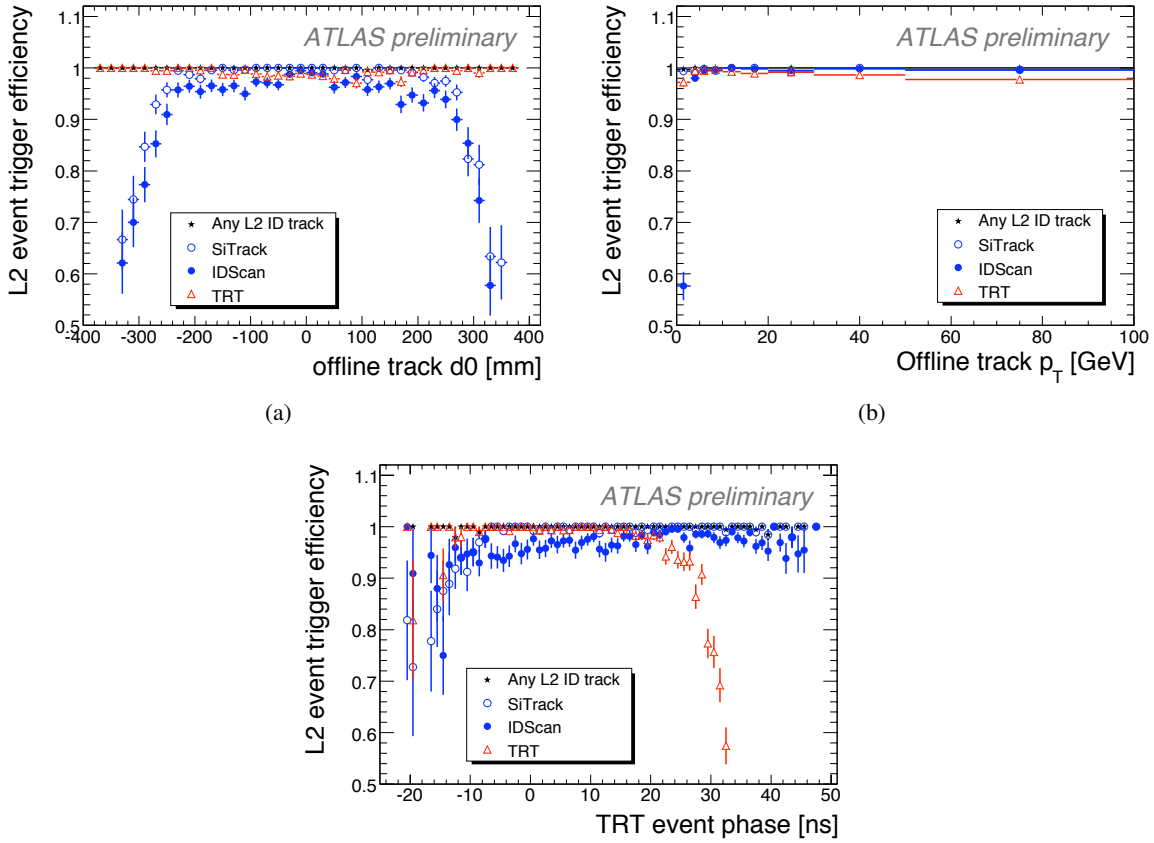

Figure 3.5: Efficiency of the Inner Detector L2 trigger algorithms in cosmic ray data-taking. The efficiency is reported as a function of the distance of the track from the beam axis $d0$ (3.5(a)), of the track momentum in the transverse plane (3.5(b)) and of the event phase with respect to the TRT (3.5(c)).

The High Level Trigger (HLT) was configured to add information to the events for streaming, but not to reject events. For example, any L1-triggered event with an Inner Detector track reconstructed at L2 was stored in the `IDCosmic` stream. This stream contains events from all L1 triggers as input and uses the logical `OR` of the three L2 track trigger algorithms to increase the rate of tracks passing through the Inner Detector. All the analyses presented in this thesis are based on events registered in the `IDCosmic` stream.

The spectrum of measured cosmic rays is strongly influenced by the existence of the construction and elevator shafts above the ATLAS detector (see Figure 3.6). L1 trigger acceptance effects also contribute to the observed spectra, due to the lower efficiency for low momentum muons. As a result, tracks were recorded by the Inner Detector that mostly pass through the barrel components of the Inner Detector, going from the upper hemisphere into the lower hemisphere.

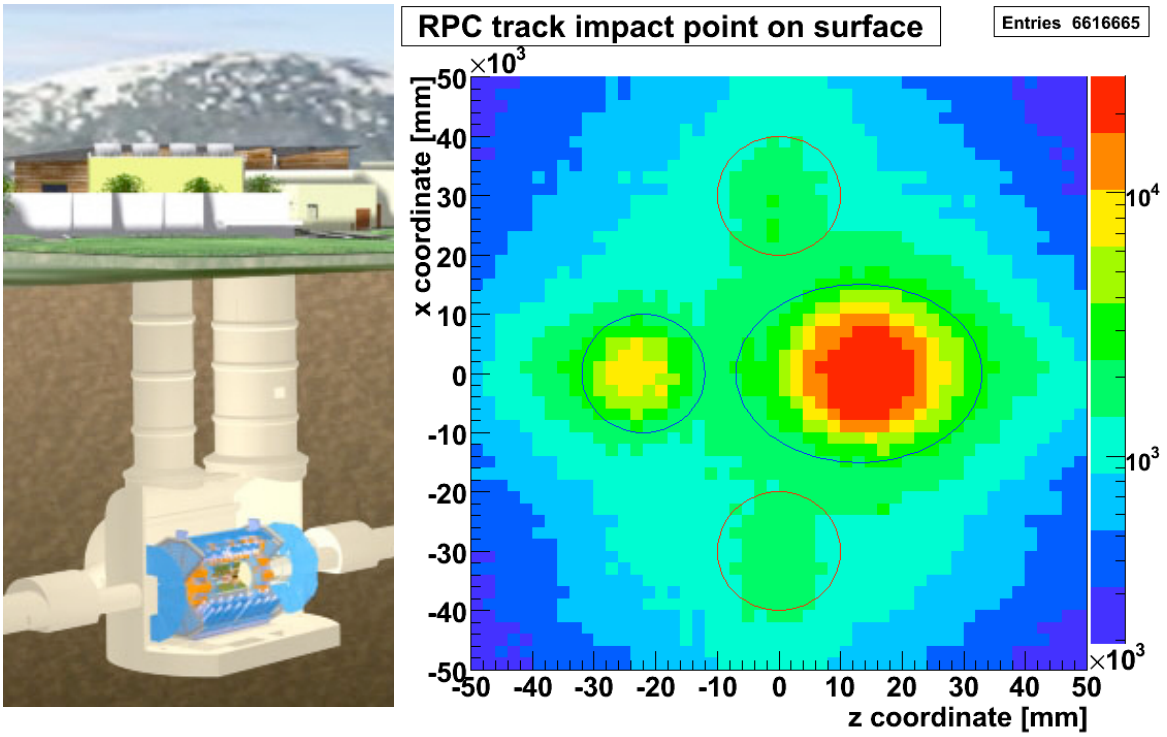

Figure 3.6: Left: a picture of the cavern that hosts the ATLAS experiment. The two access shafts are clearly visible, while elevators are not drawn. Right: the spatial distribution of cosmic rays that can reach the ATLAS detector, extrapolated at earth level. The big peaks due to the access shafts are evidenced, together with the smaller peaks due to the elevator shafts.

3.3.1 Detector timing

The ATLAS detector is built to measure particles coming from p-p interactions. For this reason, each sub-system clock is designed to be synchronized with the general LHC clock, based on *bunch-crossing*s (BC). Each BC is thus a 25 ns time interval, defining the temporal distance between two collisions at LHC design collision rate. When cosmic ray data are acquired, they are not synchronised with BC transitions. Due to short read-out time windows of SCT and TRT, the Inner Detector data-taking efficiency is very sensitive to variations in the L1 trigger timing. In addition to an unavoidable 25 ns spread in the time of arrival of cosmic rays with respect to the signal defining the bunch-crossing separation, there was a large RPC L1 trigger timing jitter present as different regions of the RPC detector were not yet fully synchronized with respect to one another. Moreover, cosmic rays rate is much lower than one for BC, thus allowing to use a read-out time composed of several bunch-crossing, in order to carefully studying the synchronization of each sub-system with respect to the others.

TRT

The TRT is the Inner Detector component that has the most stringent timing requirements. In order to fully contain and measure a valid signal, its leading-edge ($0 \rightarrow 1$) transition and trailing-edge ($1 \rightarrow 0$) transition must be within a three bunch-crossing read-out window (i.e. 75 ns). The maximum electron

drift time in the TRT tubes is estimated to be about 47 ns (see Section 2.3.1), while earliest to latest differences within a given front-end board are about 12 ns. Thus the time window in which tracks are properly phased in order to be optimally reconstructed is reduced to about 10–15 ns. For this reason, the TRT read-out timing must be synchronized with very high precision. This synchronization was first done by using hardware based calibrations, measuring the lengths of the different cables and adjusting time delays based on the results. As a result of this first step, all the TRT Trigger Timing Control (TTC, see Section 2.3.3) units were initially timed to ± 5 ns in the TRT barrel. In the barrel region, cosmic data were used to improve these time delay settings: the time offset T_0 for each TTC unit was measured from an offline analysis of cosmic ray tracks and the corresponding corrections were applied to the hardware settings. Finally, the hardware tuning was validated and improved by using beam splash events, which feature many particles passing through the ATLAS detector at the same time.

While the TRT is the detector needing the most precise time alignment, it is also the detector which measures time most precisely: the accuracy of the leading-edge measurement is about 3 ns. In the cosmic ray data-taking the TRT time measurement was used to determine the time of the cosmic ray passing through the ID. This measurement is known as *TRT event phase* (φ_{TRT}) and it was determined by taking a simple average of measured TRT leading-edge times for all hits on a track, corrected for electron drift time and offline T_0 calibration constants. However, to fit the track, a measurement of φ_{TRT} is first needed, as the cosmic-ray tracks are not synchronous with the LHC clock. To measure φ_{TRT}, the track parameters are needed. This circle was broken by first fitting the track using only the position of the centre of each hit wire using no drift time information. These track parameters were then used to estimate φ_{TRT} and this estimate of φ_{TRT} used to calibrate the TRT hits and repeat the track fit with newly calibrated hits. The accuracy of this φ_{TRT} measurement procedure is studied by the split track method (see Section 5.4.1) and it is shown to be about 1 ns. This TRT time measurement is extremely useful for other ATLAS detectors, since it provides an accurate external time reference which can be used to improve timing of any other system and synchronize the entire system.

Pixel Detector

The large number of channels and the low-occupancy requirement of the Pixel Detector, even at high luminosity, imposes a strict single bunch crossing restriction on the read-out window. The timing information provided by the Pixel Detector is the BC in which a hit has crossed the read-out threshold. This time depends on the signal amplitude (time-walk) and on the spread of the crossing time. The low data acquisition rates inherent in cosmic ray data-taking allow for an enlarged multi-BC read-out of the Pixel Detector. The observation of the distribution of collected hits among the relative BC cycles in the read-out windows (L1A) can be used to measure the detector timing. Furthermore, by utilising the precise measurement of the muon crossing time from the TRT (φ_{TRT}) it is possible to account for the spread of trigger timing.

The L1A distribution for hits from cosmic ray muons shows a spread due to the convolution of the time-walk, which results in low pulse height hits going over threshold in a late L1A, and to the uniform distribution of cosmic rays with respect to the clock edge which separates the BCs. From the

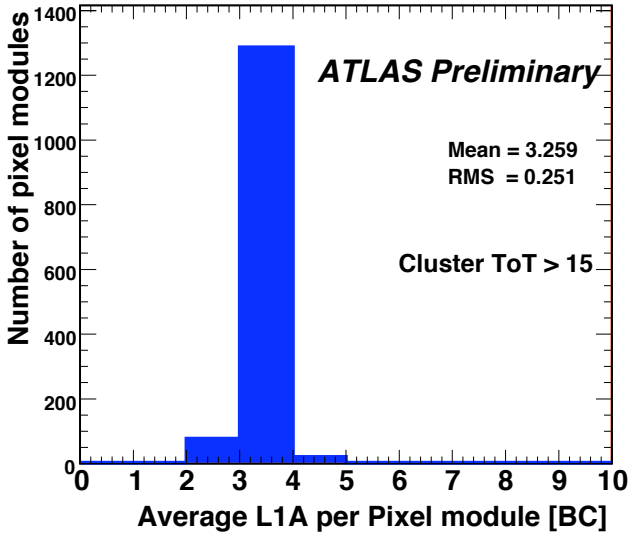

Figure 3.7: The average cluster arrival time for each module in units of bunch crossings. The timing distribution peaks at 3 BC and it is seen that all modules are timed in within ± 1 bunch crossing.

commissioning measurements, for a 3 BC read-out configuration, which is expected to be in place for the majority of the LHC commissioning phase, 99.87% of all clusters on track fall within the read-out window. Module-to-module synchronization can be assessed averaging the L1A of clusters with a pulse height > 15 ke, for which time-walk is significantly reduced. The measurement of the average L1A is shown in Figure 3.7 and indicates that 100% of the barrel modules fall within the read-out window and 96% fall within a single BC.

Measurements of the Pixel Detector timing and synchronization using cosmic ray data demonstrate good timing performance and full efficiency for a three BC read-out window to be used for initial collisions at luminosity below 10^{32} cm^{2}s^{-1}. The main limitation in a refinement of the timing is due to the uniform time distribution of cosmic rays. Early collision data, in phase with the BC, will allow to reach the nominal single bunch crossing read-out configuration.

SCT

Read-out of the SCT needs to be synchronized with the bunch crossings of the LHC to ensure that the signal is sampled at the peak of the charge-response curve. In cosmic ray data-taking, hit information was recorded in 3 BC (i.e. the triggered clock cycle, the preceding and subsequent ones). Figure 3.8 shows the distribution of SCT barrel hits as a function of read-out time, for different trigger streams. When the detector is correctly timed in, the majority of the hits should arrive in the middle bin, with some charge also collected in the last bin. Modules which are not timed in with the bunch-crossing cycle, can send signal outside the 75 ns window causing inefficiency.

The latency of the Level-1 Accept signal can be tuned by two methods. Firstly the transmission of the clock-and-control stream from the off-detector control electronics to the modules can be tuned

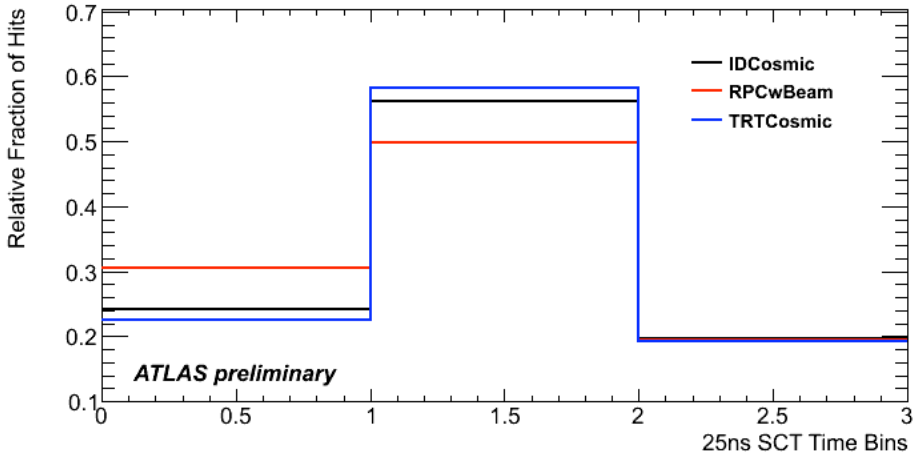

Figure 3.8: Distribution of SCT hits as a function of read-out time. The SCT reads out three bunch crossings, and the majority of the hits should arrive in the middle bin, with some charge also collected in the last bin.

00090260	00090262	00090264	00090270	00090272	00090275	00090731
00090732	00090733	00090749	00090755	00090757	00090758	00090784
00090786	00090792	00091361	00091387	00091389	00091391	00091400
00091464	00091627	00091636	00091639	00091800	00091801	00091808
00091860	00091861	**00091885**	**00091888**	**00091890**	**00091891**	00091897
00091898	**00091900**	00092082				

Table 3.2: Identification number of the data-taking runs used in the analyses. Bold font numbers refer to runs privately reconstructed in the dataset with extended charge sharing constants.

in steps of 25 ns LHC clock cycles and/or steps of $\sim$ 280 ps. Secondly, the Timing Interface Module (TIM, see Section 2.2.3) can be used to delay signals relevant to triggering in steps of 25 ns LHC clock cycles. The transmission delays were used to compensate for fibre-length variations between the off-detector controls and the modules prior to the cosmic ray runs, while during cosmic ray data-taking, the SCT was timed in by gradually changing the TIM delays until a peak in occupancy associated with tracks was observed.

3.4 Data selection and reconstruction

Data discussed in this thesis were taken during combined ATLAS cosmic ray data-taking in October 2008 (see Section 3.2). In particular, runs registered with the 2 T solenoidal magnetic field on were chosen. This allows to have better performances of the tracking system, since the momentum of the particles can be measured and many effects depending on particle momentum (e.g. multiple scattering,

Data set	Software Release	Alignment tag	Charge sharing tag (PixelOfflineReco-)	Notes
REAL DATA				
Initial data	14.5.0.5	InDet-Cosmic-2008-03	02 (Initial tag)	158 147 events
Reprocessed data	15.0.0.7	InDetAlign-REPC-01 TRT-Cosmic-2008-06	COS-02	162 598 events
Data with extended charge sharing constants	15.5.2	InDetAlign-REPC-01 TRT-Cosmic-2008-06	Extended-COS-01	Only five runs reprocessed: 58 099 events
SIMULATION				
Simulated cosmic rays	15.0.0.7	–	COS-02	998 634 events
Pixel clusters reconstruction	15.5.2	–	Extended-COS-01	Simulated cosmic rays with no track fitting

Table 3.3: Different sets of data used in the analysis. For each one the software released used, as well as the alignment tag and the charge sharing calibration tag are reported. Information about simulated events used are listed as well.

see Section 5.1.3) can be evaluated by the tracker. The identification number of the runs used for the analyses are listed in Table 3.2.

Several streams of data were registered for each data-taking run, according to different triggers (see Section 3.3). Since many events resulted to be duplicated among the streams, the `IDCosmic` stream alone is used in the analyses presented. This stream, in fact, uses the logical `OR` of three Level-2 track trigger algorithms, allowing the largest statistics of track traversing the Inner Detector.

Cosmic ray tracks were analyzed and reconstructed several times during commissioning phase, in order to take advantage of new sets of calibration and alignment constants and to incorporate improvements in the software, as soon as new findings were available. In order to develop the analysis presented in this thesis only a subset of all datasets available has been used. The list of these datasets is reported in Table 3.3, together with the details about the calibration constants that have the most important impact on the studies performed. Three different versions of the data are used:

– *Initial data*. This dataset has been reconstructed at the beginning of the commissioning activity. The TRT event phase calculation algorithm was still preliminary, causing minor problems in the description of detector timing. The alignment of the detector did not include the internal alignment of TRT and the charge sharing algorithm (see Section 4.4) for the Pixel Detector was not calibrated.

The Athena software version used for reconstruction was `AtlasProduction-14.5.0.5`. Two additional packages were added to the software, in order to provide the *track splitting* algorithm (see Section 5.4.1). These packages were subsequently integrated in the official software. The conditions database information was retrieved by using the tag `COMCOND-REPC-001-03`, while the geometry database was accessed with tag `ATLAS-GEO-03-00-00`.

– *Reprocessed data*. These data have been reconstructed when the commissioning activity was advanced. TRT internal alignment has been included and an improved version of alignment constants for the silicon detectors is used. A preliminary version of the calibration for the pixel charge sharing has been added.

  Software version `AtlasTier0-15.0.0.7` is used to reconstruct tracks, since it features the algorithm for track splitting, as well as small fixes in the track fitting algorithms. These include the final algorithm for TRT event phase computation, and the ability to provide informations about *holes*, i.e. missing hits on detector modules. The dataset uses new conditions tag `COMCOND-REPC-002-13`, while the geometry tag is unchanged.

– *Data with extended charge sharing constants* were privately produced on a subset of available data-taking runs (see Table 3.2), in order to complete the validation of charge sharing constants for the Pixel Detector (see Section 4.7). The same setup of *Reprocessed data* is used, except for the charge sharing constants tag and for the software release. In fact, the possibility to have user defined ranges for charge sharing constants is only available starting from Athena version `AtlasProduction-15.5.2`.

3.5 Simulated data

Cosmic ray events in ATLAS are simulated by a sequence which first generates single particles at the surface above ATLAS, then filters them for acceptance in the detector and finally runs the standard ATLAS detector simulation and digitization, as it is described in Section 1.4.3.

The generator follows the flux calculations in [97] and uses a standard cosmic ray momentum spectrum [95]. For efficient use of computing resources, only those muons pointing to a sphere of about 20 m, representing the inside of the ATLAS cavern, are selected. Then, the Geant4 simulation propagates the muons through the rock 100 m below, where the ATLAS detector lies. Once in the cavern, a second filter level is applied in order to reduce the simulation time: only events with at least one hit in a given volume inside of the ATLAS detector are selected. In this thesis, a cosmic ray Monte Carlo sample produced with the full magnet system on and in which events were filtered in the Pixel Detector package volume has been used. The sample contains one million of events.

The emulation of the electronics (digitization) has been adapted from the one used for collision events in order to take into account the difference in the timing. The simulated data can be compared with real data with some caveats. In the simulation, the whole detector is assumed to be read out, the

three trigger levels are not simulated and the ratio of positive and negative charged generated muons is larger than the measured value.

Details about the reconstruction of simulated events are reported in Table 3.3. The official simulation and digitization of the sample used Athena version `AtlasProduction-15.4.1.4`, while reconstruction was performed with the same setup that was used for the reconstruction of *Reprocessed data* (see Section 3.4). All relevant conditions were collected in the global tag `OFLCOND-SIMC-00-00-00` and the detector geometry was described by using the tag `ATLAS-GEO-07-00-00`. Other than the official reconstruction of simulated events, a private version of the same events have been digitized with Athena version `AtlasProduction-15.5.2`, in order to validate the Pixel Detector charge sharing calibration.

Chapter 4

Optimization of the Pixel Detector resolution

The ATLAS Pixel Detector is the innermost device composing the Inner Detector tracking system. It has been designed to provide high-resolution measurements of the position traversed by particles emerging from collisions at few centimeters from the interaction point. The hardware implementation of the detector has been described in Section 2.1, while this chapter will illustrate how the performance of this detector was measured and optimized during autumn 2008 data-taking and in the following data analysis.

One of the main tasks performed using cosmic muon data was the optimization of the spatial resolution of the Pixel Detector, that is discussed in this chapter. Section 4.1 describes the interaction of particles with material, and in particular with silicon detectors. In order to compare measurements and theoretical expectation, the ATLAS official simulation of the Pixel Detector is introduced in Section 4.2. In Section 4.3 the collection of the charge released by particle passage is detailed. This section will describe the typical measurements registered by the ATLAS Pixel Detector. Section 4.4 describes the intrinsic resolution of the detector. In particular the charge sharing interpolation is considered in order to improve the resolution with respect to the simple digital read-out of the pixels. Section 4.5 describes the tuning procedure for the charge sharing algorithm: results obtained from cosmic muon data are discussed. The final effect of the calibrated algorithm on cosmic ray tracks measurement is presented in Section 4.6, where resolution studies based on real data are reported.

4.1 Particle interaction in silicon detectors

A charged particle that traverses a layer of matter undergoes interactions that can cause ionization or atomic excitation in the material. The theory that describes the mean energy loss given by interactions is summarized in the Bethe-Block equation (see [96] and references therein):

$$-\frac{\mathrm{d}E}{\mathrm{d}x} = Kz^2\frac{Z}{A}\frac{1}{\beta^2}\left[\frac{1}{2}\log\frac{2m_ec^2\beta^2\gamma^2T_{\max}}{I^2} - \beta^2 - \frac{\delta(\beta\gamma)}{2}\right]. \tag{4.1}$$

In this equation, several parameters are introduced:

- K is defined as $4\pi N_A r_e^2 m_e c^2$,

- m_e and r_e refer to the mass and the classical radius of the electron,
- z is the charge of the incident particle in e units,
- Z and A are the atomic mass and the atomic number of the material traversed,
- $T_{\max}$ represents the maximum kinetic energy that can be imparted to a free electron by a particle of mass M in a single collision. It is given by the expression:

$$T_{\max} = \frac{2m_e c^2 \beta^2 \gamma^2}{1 + 2\gamma m_e/M + (m_e/M)^2}, \tag{4.2}$$

- I is the mean excitation energy of the material,
- $\delta(\beta\gamma)$ term takes into account the density effect correction to energy loss, that become important at high energy.

Eq. 4.1 describes with sufficient accuracy all high-energy particles in very broad momentum and mass spectra. A minor dependence on the particle mass is introduced through the $T_{\max}$ parameter but, other than this term, the energy deposition is only function of β. For low energies ($\beta\gamma \lesssim 0.1$), corrections related to the atomic structure of the material should be applied to the Bethe-Block equation. Similarly, for energies higher than $\beta\gamma \gg 1000$, radiative effects gain importance. As a conclusion, for the all the cases regarding the ATLAS Pixel Detector, Eq. 4.1 is a sufficiently good approximation.

While Eq. 4.1 provides the mean energy loss, the behaviour of single particles cannot be described by using this variable. This is because collisions releasing high energy greatly influence the calculation of mean energy loss, even if they correspond to very rare events. A realistic description of single particle energy loss, however, is useful to understand the Pixel Detector operation. Since the energy loss Δ is a stochastic quantity, a probability density function $f(\Delta)$ is used to describe its distribution. This function is usually known as *straggling function*. For detector of moderate thickness, the straggling function is described by a Landau distribution. This approximation is not satisfactory for thin absorbers as the Pixel Detector. In these cases the straggling functions should be calculated with numerical methods. The most recent computation is based on the convolution method [98]. Figure 4.1(a) shows the straggling function calculated for 500 GeV pions traversing layers of silicon of different thicknesses. The main parameters used to describe the energy loss are evidenced: the most probable value (MPV) Δ_p/x is much smaller than the mean energy loss. The value used to describe the spread of this function is the full width at half maximum w (FWHM). Figure 4.1(b) shows the dependence of the most probable value of energy loss in silicon on the particle momentum. The momentum at which the energy loss is minimum ($\beta\gamma \approx 3.4$) identifies the *Minimum Ionizing Particle* (MIP). For a muon, as it is the case when cosmic rays are analyzed, a MIP corresponds to a momentum of 363 MeV. The MIP mean energy loss per unit length is calculated to be 388 eV/μm in silicon detectors and it is independent on the material thickness. On the contrary, the most probable value of the energy loss per unit length exhibits a dependence like $a\log x + b$ on the path length in material x [96, 98].

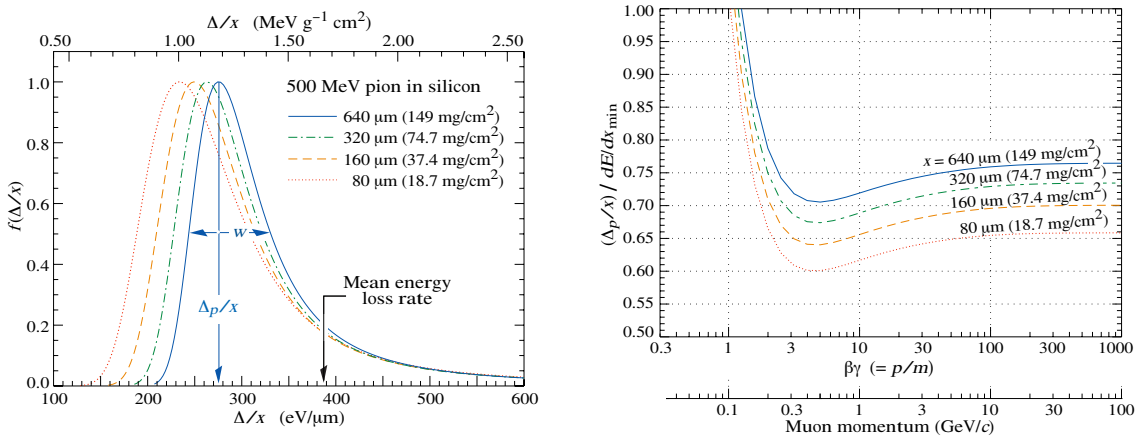

(a) (b)

Figure 4.1: 4.1(a): straggling functions in silicon for 500 MeV pions, normalized to unity at the most probable value Δ_p/x. The width w is the full width at half maximum. 4.1(b): most probable value of energy loss in silicon, scaled to the mean loss of a minimum ionizing particle, 388 eV/μm. Figures taken from [96].

4.1.1 Ionization

The sensitive part of the ATLAS Pixel Detector is a reverse biased silicon *pn* junction (see Section 2.1.1). The energy released in the silicon by particle passage produces electron-hole pairs. The electron and the hole drift in opposite directions under the effect of the electric field inside the depleted region of the junction, until they reach the electrodes that apply the bias voltage. Under these conditions, the Ramo theorem [99] ensures that the integral of the induced current in each electrode by charge motion is equal to the number of charges collected by that electrode. In the case of ATLAS Pixel Detector, the read-out system is applied to the n^+ pixels that collect electrons. The number of charge pairs released in the silicon is known as ionization J and it is related to the total released energy Δ by the following formula:

$$\Delta = WJ, \tag{4.3}$$

where W is the average energy needed to produce an electron-ion pair. It depends on the particle type and energy, as well as on the temperature of the material. For the silicon, W ranges in the interval 3.63–3.68 eV, where differences arise according to the calculation method [100–103]. A straggling function $f(J)$ can be calculated for ionization, as for the energy loss.

For example, Figure 4.2 shows the charge distribution for measurements in the Pixel Detector (clusters) that are associated to cosmic ray tracks, after some quality cuts have been applied. In Figure 4.2(a) the distribution has been fitted using a Landau distribution, convoluted with a Gaussian, to take into account various experimental effects. The free parameters of the fit were the most probable value of the Landau and the width of the two distributions, whose values are reported in the plot. When considering

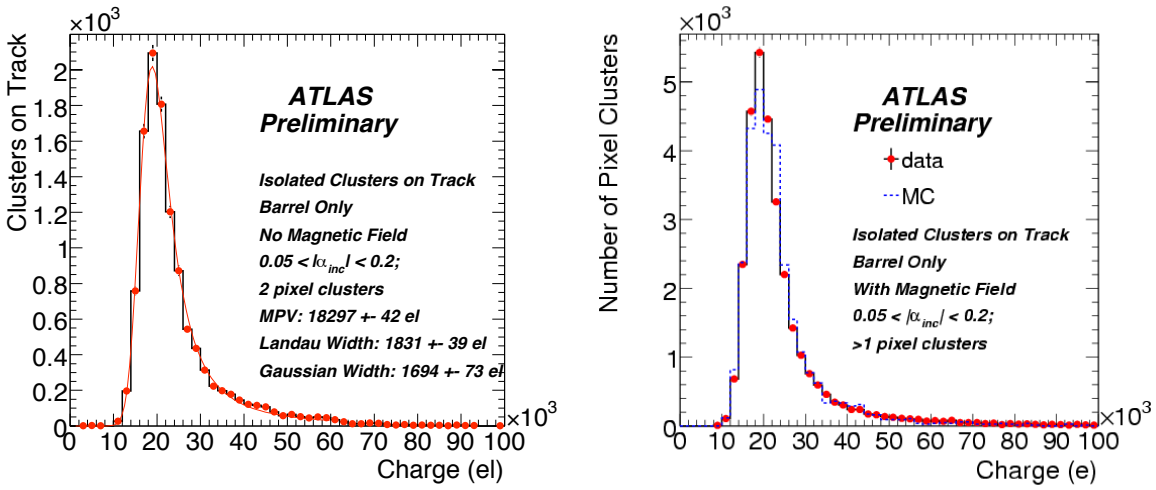

(a) (b)

Figure 4.2: The charge distributions for clusters associated to cosmic ray tracks. The tracks have been selected to have an incidence angle close to normal on the module. 4.2(a): the fit performed in order to compute the most probable value of the distribution. The fitted function is a Landau distribution, convoluted with a Gaussian. 4.2(b): a comparison between measurements and simulated cosmic ray events.

$W = 3.68$ eV, the expected charge release for a MIP would be 19 ke. The fitted value is therefore very close to the theoretical calculation. Several effect can be taken into account to explain the 4% mismatch, such as the shape of the fitting function, or a less-than-perfect calibration of the ToT scale of the detector (see Section 4.3.1).

When considering charge measurements in the ATLAS Pixel Detector, as in the previous example, all particles are treated as minimum ionizing particles. According to Figure 4.1(b), this introduces a 10% error at maximum on the particle energy, at least up to momenta of the order of 100 GeV. This error has no impact on detector performance, since the Pixel Detector is a tracking device and the charge is only measured in order to improve the spatial resolution (see Section 4.4). Even if the Pixel Detector is not optimized for absolute charge measurements, the dependence of energy loss on the momentum of the incident particle is visible in cosmic ray data. Figure 4.3 shows the MPV (left) and the FWHM (right) of the charge distribution as for clusters associated to cosmic ray tracks. Charge distribution has been corrected by taking into account the particle incident angle. The MPV and the FWHM values have been reported as a function of the momentum of the associated particle. The expected rise is clearly visible in the MPV, when momentum increases, and it is compatible with the theoretical prediction. Real data and simulated events are compared showing a small discrepancy as in the previous Figure 4.2(b).

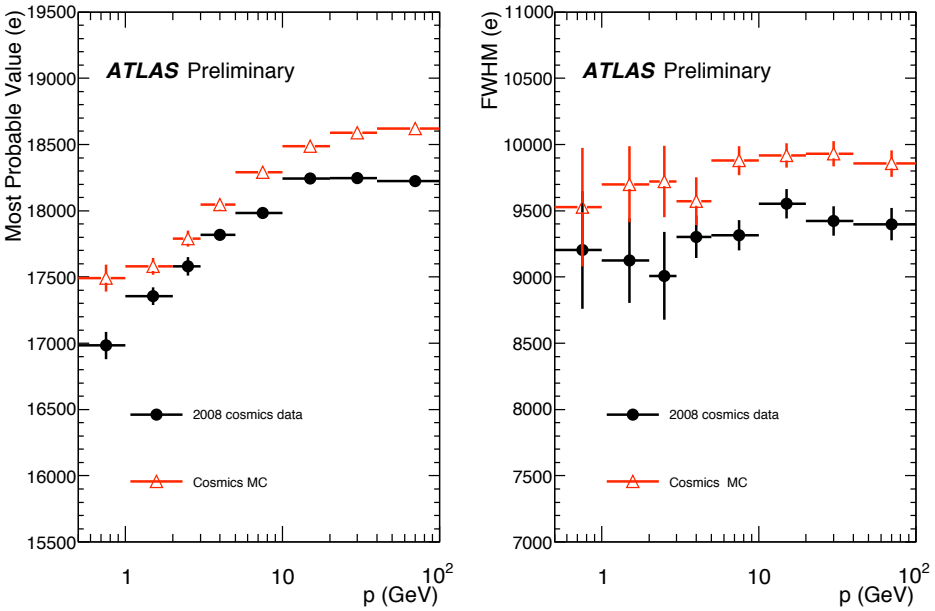

Figure 4.3: Most Probable Value (left) and FWHM (right) of the charge distribution for pixel clusters associated to cosmic ray tracks as a function of the track momentum. Distribution are obtained for data as well as for simulated events.

4.1.2 Charge mobility

As already introduced, the Pixel Detector is based on a p^+n junction. This is implemented by using an high doping concentration of acceptors N_A on the p-side and a much smaller concentration of donors N_D on the n-side (see Section 2.1.1). When operated at high reverse bias voltage (V_{bias}), a *depleted zone* exists around the junction. This region is characterized by the absence of free charge carriers.

Figure 4.4 schematically shows the net charge density of the depleted zone, the electric potential and the electric field profiles as a function of the coordinate perpendicular to the p^+n interface. The depletion zone is actually the real sensitive zone of the detector (i.e. the zone from where charge is collected, when ionization happens). The thickness of this zone is described by the following equation [104]:

$$d = \sqrt{\frac{2\varepsilon_0\varepsilon_{SI}V_{bias}}{N_D e}} \quad \text{for } V_{bias} < V_{dep} \tag{4.4}$$

Here e is the electron charge, ε_0 is the vacuum dielectric constant, and $\varepsilon_{SI} = 11.9$ is the silicon relative dielectric constant. When the entire silicon layer is depleted, the corresponding bias voltage is called V_{dep}: for larger values of V_{bias}, the depletion zone thickness is unchanged, while the electric field increases. As the amount of collected charge depends on the depth of the depleted zone, it is desirable to set the bias voltage such that the detector is fully depleted, in order to maximize the sensitive area.

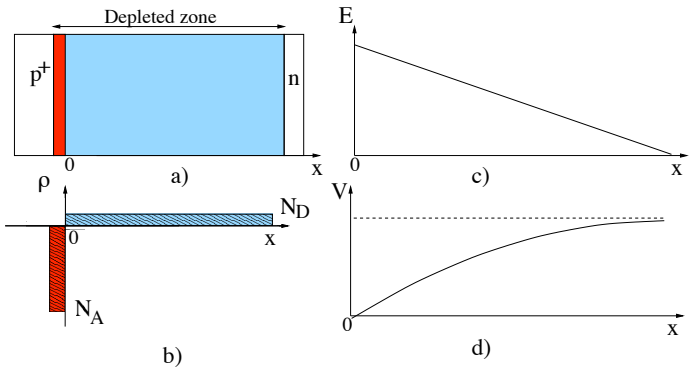

Figure 4.4: Scheme of a p^+n junction, representing: (b) charge density, (c) electric field, (d) the potential near the junction. N_A and N_D are the doping concentration of the p-side and the n-side respectively. Figure taken from [105].

The depletion voltage V_{dep} depends on the silicon thickness, and on the material lattice quality. For the ATLAS Pixel Detector sensors, a thickness of 256 ± 3 μm has been measured [70]. Low doping concentration (in the order of 10^{-32} cm^{-3}) was used for the silicon substrate, resulting in a depletion voltage of the order of 100 V. This value will be modified by radiation damage (see Section 2.1.1), but as far as the commissioning activity is involved, it can be considered stable. During cosmic ray data-taking the detector was operated by using $V_{bias} = 150$ V and it was fully depleted.

Charge drift

As described by Figure 4.4, the depletion zone is characterized by an electric field. The field causes both electrons and holes to drift in opposite directions with an average speed proportional to the field strength:

$$v_d = \mu_d E, \tag{4.5}$$

where μ_d is the drift mobility. It is related to the mean free time τ between collisions of the charge with the lattice [106, 107]:

$$\mu_d = \frac{q\tau}{m^*}. \tag{4.6}$$

This relationship is derived by assuming that charges move in the lattice with an effective mass m^*, that is bigger for holes with respect to electrons. Another assumption is that the average velocity is zero after each interaction. These conditions yield to an overall drift velocity described by:

$$v_d = \frac{qE}{m^*}\tau. \tag{4.7}$$

From a comparison of Eq. 4.5 and 4.7 the expression for the mobility can be derived.

In this model, collisions can happen due to crystal modifications with respect to a perfect geometrical lattice. These modifications are due either to the presence of impurities (e.g. the doping atoms), or because of the thermal vibrations. The crystal vibration quanta are called phonons. The interaction probability with impurities increases with doping concentration and decreases with temperature. On the contrary interaction with phonons increases with temperature. Given the doping concentration of the ATLAS Pixel Detector sensors, the mobility is determined by phonon scattering alone.

If the electric field becomes sufficiently large, the linear relationship with the drift velocity is lost. This results in a field-dependent mobility, eventually reaching saturation. The field expected in the Pixel Detector sensors is ~ 600 kV/m. As a result, this parameterization can be used to describe charge mobility [108]:

$$\mu_d = \frac{v_s/E_c}{\left[1+(E/E_c)^\beta\right]^{1/\beta}}. \tag{4.8}$$

Here v_s represent the saturation velocity, that slightly depends on temperature (i.e. it decreases with temperature), while E_c is the electric field scale at which the transition from linear dependence to saturation regime occurs. Finally, the β parameter is related to the rapidity of this transition. In the case of the Pixel Detector sensors at $T = 300^\circ$ K, the drift velocity is calculated to be 5.29×10^6 cm/s.

Charge diffusion

Along with a drift motion towards the electrodes, charges also experience a lateral spread. This spread is proportional to the square root of the drift time and of the *diffusivity* coefficient D, having a Gaussian distribution with standard deviation:

$$\sigma = \sqrt{2Dt}. \tag{4.9}$$

The spreading effect is known as *charge diffusion*. When charge carriers are in thermal equilibrium, the Einstein relation holds:

$$D = \frac{kT}{q}\mu_d. \tag{4.10}$$

The equilibrium exists for low electric fields. When the velocity saturation is reached, the mobility dependence on the fields should be taken into account, as well as substituting the kT term with the mean charge carrier energy. The effects of these changes partly compensate, such that the final dependence of the diffusivity on the electric field is moderate. The diffusivity for electrons in silicon has been measured as a function of the electric field and the value foreseen for the Pixel Detector modules ($E = 600$ kV/m, room temperature) is D = 25 cm^2s^{-1}, with an uncertainty of 9% [109].

4.1.3 δ-rays

The energy lost in collisions (see Eq. 4.1) may results in ionization processes with energetic electrons. These knock-out electrons are known as δ-rays. The distribution of secondary electrons with kinetic energies $T \gg I$ is:

$$\frac{\mathrm{d}^2N}{\mathrm{d}T\mathrm{d}x} = \frac{1}{2}Kz^2\frac{Z}{A}\frac{1}{\beta^2}\frac{F(T)}{T^2} \tag{4.11}$$

for $T \leq T_{\max}$, where $T_{\max}$ is given by Eq. 4.2. In this expression, β is the velocity of the primary particle and the factor F is spin-dependent, but is about unity for $T_{\max} \gg T$. Even if δ-rays of even modest energy are rare, their occurrence should be taken into account when dealing with the Pixel Detector. A δ-ray with kinetic energy T_e and corresponding momentum p_e is produced at an angle θ_e given by

$$\cos\theta_e = (T_e/p_e)(T_{\max}/p_{\max}), \tag{4.12}$$

where $p_{\max}$ is the momentum of an electron with the maximum possible energy transfer $T_{\max}$.

4.2 Simulation of the Pixel Detector

In order to study the intrinsic properties of the ATLAS Pixel Detector and to disentangle different experimental effects contributing to the final measurements, a Monte Carlo based simulation of the detector is put in place. The simulation of the Pixel Detector is actually integrated into a more general framework that provides the description of the full ATLAS detector (see Section 1.4.3). In this paragraph specific issues regarding the Pixel Detector simulation are presented.

4.2.1 Energy loss

The propagation of particles inside the silicon is computed by the GEANT4 package [46, 47]. In order to have sustainable computer requirements, the simulation is based on two main approximations:

- the energy release inside the simulated material volume is computed in discrete steps;
- only secondary particles that have a range larger than a defined value are tracked independently.

Step limitation

The energy loss of a particle traversing the detector volume is computed in discrete steps. For further processing, the information of a step is stored in an object named `SiHit` which contains the start and the end-point of the step, the energy loss and the time at which the particle crossed the detector. The end of each `SiHit` occurs either because of a change in the volume crossed by the particle or when an interaction is simulated. Interactions can be multiple scattering, hard bremmstrahlung, δ-ray emission or nuclear interaction.

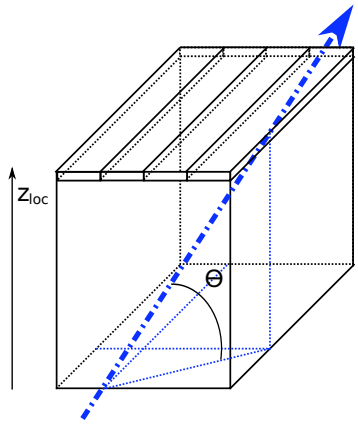

Figure 4.5: Sketch of a part of a Pixel Detector sensor, traversed by a particle.

The *step limitation* parameter allows to tune the accuracy in the energy loss fluctuations along the trajectory, by setting a maximum length for each step. In this case, energy loss is computed even if no interaction or no material change happens. In the simulation of cosmic ray events, the step limitation was not set, in accordance with studies described in [110].

Secondaries range

The range for secondary particles was set to 50 μm for the simulation of cosmic ray events. This means that only particles that move farer than 50 μm from the primary particle are simulated independently. In the other cases, their energy loss is just summed to the one of the incident particle.

4.2.2 Detector measurements

The *digitization* is the software algorithm that converts the `SiHits` into the expected output, similar to what could be measured by detector electronics channels. Since real measurements depend on the detector conditions, many informations are read from the conditions database (see Section 1.4.1) by the digitization, in order to accurately reproduce detector operation.

Charge drift

For each `SiHit`, the energy loss is uniformly spread over 50 points along its length. The energy loss is converted into ionization, by using a pair-creation energy of $W = 3.62$ eV. The charge associated to each segment is divided into 10 bunches, resulting in 500 individual charge carriers clouds. These charge carriers are then drifted to the electrodes, according to the description reported in Section 4.1.2. If z_{loc} is the coordinate perpendicular to the sensor surface, the drift time is approximated to be $t = z_{\text{loc}}/(v_d \tan\theta)$ (see Figure 4.5), where v_d is taken independent from z_{loc} — even if it actually depends on the (variable) electric field — and θ is the total incident angle of the measured particle. The Lorentz angle (see Section 4.3.3) effect is added, according to the temperature and the bias voltage taken from conditions database. The diffusion of the charge is added as a Gaussian smearing of the carriers position, according to Eq. 4.9.

Charge collection

After charge propagation, each carrier is assigned to the pixel where it arrives. A cross-talk charge is then assigned to neighbour pixels. The cross talk C_x depends on the length of the shared side between pixels L_c and on the original charge of the carrier C_0:

$$C_x = C_0 L_c f_c. \tag{4.13}$$

The cross-talk coefficient is set to be $f_c = 0.03$ mm^{-1}, in order to reproduce the typical value observed on production sensors [70], while the length of the shared side depends on the pixel type, i.e. *normal*, *long*, *ganged* or *inter-ganged* (see Section 2.1.1). Charge collected in both ganged pixels is added in the same read-out channel. Dead or disconnected pixels, instead, are excluded from read-out.

The thermal noise is simulated by adding a Gaussian smearing ($\sigma = 220\ e$) to the charge collected by each pixel. At the same time random noisy pixels are simulated, according to a map retrieved from the conditions database. The charge of these pixels is simulated following noise curves measured during detector operation.

After all computations, the charge in each pixel is finally compared to a threshold, as in real detector operation (see Section 4.3.1). The main difference is that threshold is calculated as the mean for all pixel threshold on the given chip and it is then smeared according to the threshold distribution width, corrected for a noise term. The time-over-threshold associated to the charge is computed. The mean ToT and the corresponding variance are determined from the calibration parameters stored in the conditions database. The time-walk effect is simulated according to a parameterization of experimental data [111] and added to the time of the `SiHit`. The bunch crossing corresponding to this time is then computed and assigned to the pixel channel.

After these steps, the collection of hit pixels can be treated by the same algorithms that reconstruct events from data-taking.

4.3 Cluster properties in the Pixel Detector

The geometry of the Pixel Detector sensors is described in Section 2.1.1, as well as the local reference system that allows to identify the position of each pixel. Normally, charge released by particle interaction with the sensor is deposited in few neighbouring pixels. These compose a *cluster*. Similarly, in the reconstruction software, raw informations such as the charge registered by a group of pixels, the module they belong to and their row and column numbers, are associated to form `SiCluster` objects. `SiClusters` are processed, in order to compute their position with associated uncertainty (see Section 4.4). Once the position is computed, the cluster can be described using a three-dimensional `SpacePoint`. Two coordinates, in fact, are given by the cluster position on the module, while the third one is the distance of the module mid plane from the beam axis. `SpacePoints` are then used as input for tracking algorithms (see Section 5.2.1).

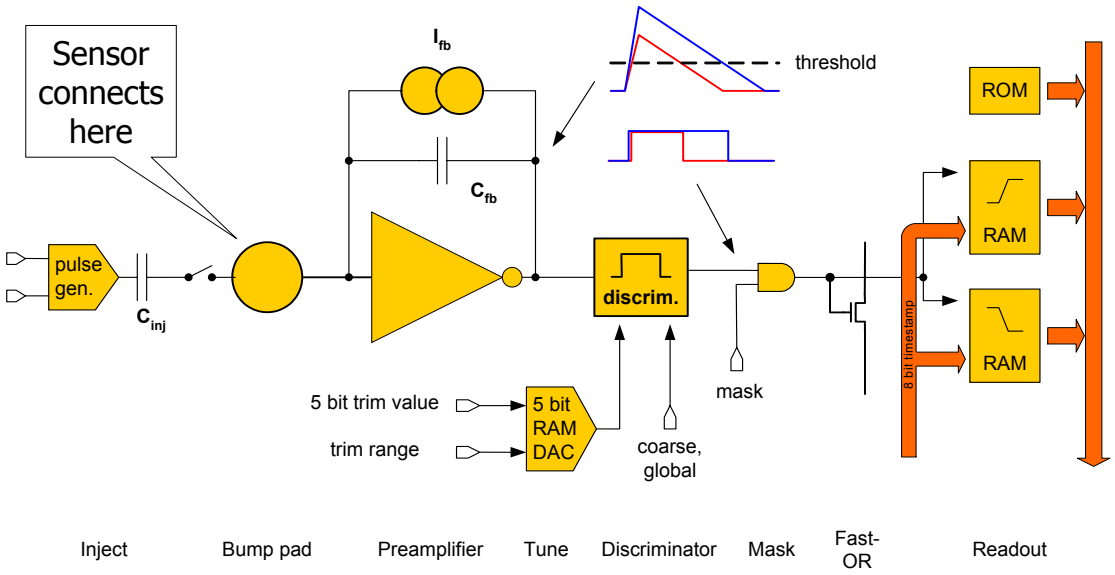

Figure 4.6: Schematic representation of the ATLAS Pixel Detector read-out system.

Using cosmic ray data collected in 2008, several properties of the clusters measured by the Pixel Detector were analyzed. Here the most important cluster characteristics are reported. Since the position of the cluster is computed from these measurements, an accurate comprehension of all these aspects is fundamental in order to be able to optimize detector resolution.

4.3.1 Charge measurements

The read-out system of the Pixel Detector (see Section 2.1.3) is ToT based: by design, the period of time during which the signal is read is nearly proportional to the charge collected. Figure 4.6 shows the main components of the read-out system: it comprises an analogical part (preamplifier) and a digital output (discriminator and readout). The charge released at particle crossing is collected by the preamplifier through the bump pad. The feedback of the preamplifier is a direct current: the peak time can be regulated by varying this feedback current. The shape of the signal formed by the preamplifier is triangular and its height is determined by the charge collected. This signal is analyzed by the discriminator, that computes the time spent over a tunable threshold by the signal itself. The digital output of the discriminator is expressed in BC units. The ToT is thus read out as the difference between the leading edge and the trailing edge of the discriminator output signal. The time taken by the signal to exceed the threshold — starting from the BC in which the particle is triggered — is called *time-walk* and it is dependent on the signal height.

Threshold tuning

A limit to the precision of the charge measurement comes from the electronic noise level. The major noise sources are related to detector capacitance and to leakage current. As already introduced, the ATLAS Pixel Detector design uses a charge threshold to decide whether a signal is read out or not.

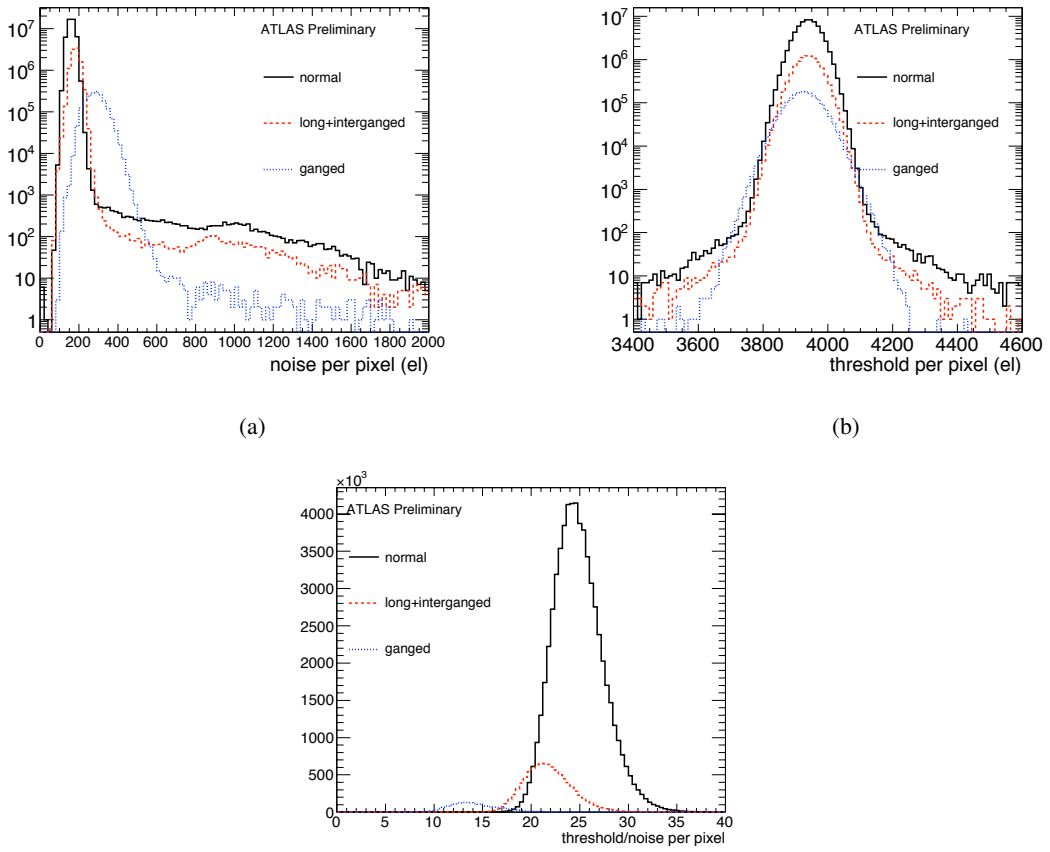

Figure 4.7: Noise (4.7(a)), threshold (4.7(b)) and the threshold over noise ratio (4.7(c)) for normal, ganged and long and inter-ganged pixels. The noise is typically about 200 electrons while the threshold is 4000 electrons.

Figure 4.7(a) shows the distribution of the noise as it is measured in the detector during dedicated scans. Pixel with modified geometries (see Section 2.1.1) have higher capacitance and worse noise distributions, showing higher most probable values with respect to normal pixels. The threshold can be adjusted pixel by pixel: Figure 4.7(b) shows the threshold distribution after the tuning that sets the nominal value of the threshold to 4000 e. The resulting threshold over noise ratio is reported in Figure 4.7(c): the peak for normal pixels is at 25, while for modified pixel geometries it is at smaller values: 21 and 13 for long and ganged pixel, respectively. In all cases, however, the threshold is at least 10 times bigger than the expected noise.

ToT calibration

In order to know the charge associated to a given time-over-threshold for the pixel signal, a calibration is needed. In general the ToT of a fixed signal depends on the threshold and on the feedback current. The threshold is fixed to be 4000 electrons, as already described, in order to have a favorable threshold

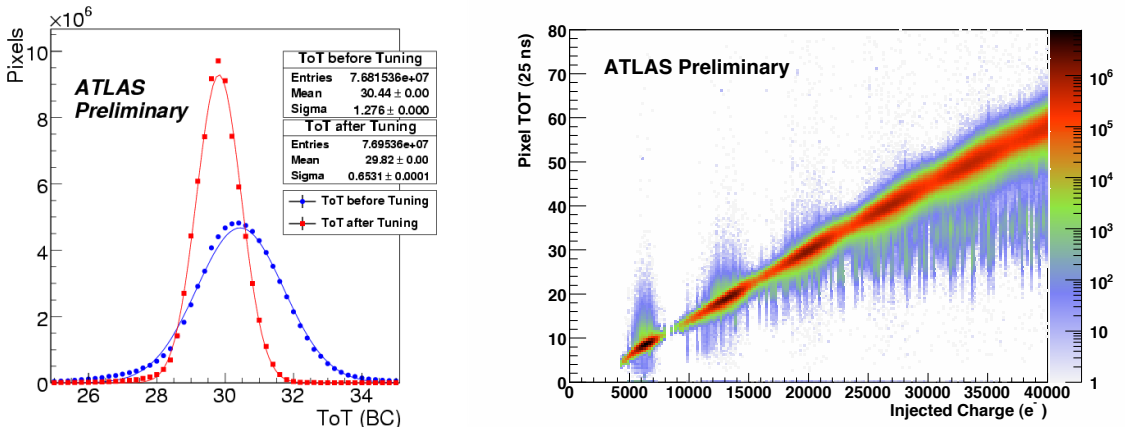

(a) (b)

Figure 4.8: 4.8(a): Time-over-threshold (ToT) distribution for pixel with an injected charge of 20 ke, before and after the tuning of the detector. 4.8(b): ToT versus injected charge for all pixels.

over noise ratio. The feedback current, instead, is tuned for each pixel in order to have a fixed value for the most probable signal generated by a minimum ionizing particle.

Figure 4.8(a) shows the ToT distribution for the pixels before and after the tuning of the detector. Distributions are obtained by injecting 20 k electrons through a dedicated circuitry in the front-end electronics (see Figure 4.6). A narrower distribution, well centered on the nominal value (i.e. 30 bunch crossing), is the result of the calibration.

Even if only one value of charge is used for the tuning, the relationship between charge and ToT is measured over a very large range of charges. Figure 4.8(b) shows a plot containing the ToT response of each pixel as a function of the injected charge. The overwhelming majority of the pixels shows a nearly linear relationship. There is only a small fraction of pixels that contributes to the tails. When Pixel Detector measurements are analyzed by reconstruction software, a parameterization extracted from data as in Figure 4.8, with the granularity of the FE chip, is used to assign the correct charge to each pixel.

Charge sharing

When `SiClusters` are considered, the total charge is computed by adding the charges collected by the individual pixels. In the case of multiple-pixel clusters, some more information about the charge distribution is desirable, since the *charge sharing* among pixels determines the shape of the clusters.

According to a geometrical model developed during test-beam studies [105, 112], the charge threshold of the front-end electronics can be associated to a minimal path-length x_{min} in the sensor. When the path-length of a particle under a given pixel is less than x_{min}, the charge collected by that pixel is under threshold and it is thus lost. On the contrary, if the path-length is larger than x_{min}, the pixel signal is over threshold and can contribute to the cluster. Following this model, the charge released in each read-out channel can be explicitly calculated by considering the path-length of the particle under each

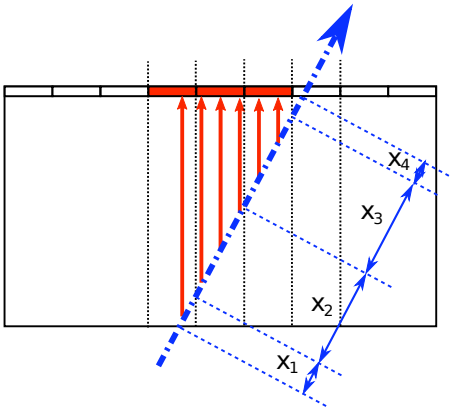

Figure 4.9: A simple geometrical model allows to compute the charge released in each read-out channel, by considering the path-length of the particle under each pixel.

pixel. Figure 4.9 shows a two dimensional sketch of a pixel sensor, traversed by a particle that intersect the area associated with four pixels. The path-length under each pixel has been labelled as x_i. Since x_4 is supposed to smaller than x_{min}, no charge is read-out from the fourth pixel. Moreover the charge released in the central pixels is identical, since $x_2 = x_3$, while the charge in the first pixel is less than the others ($x_1 < x_2$). Such a simple model can be sufficiently accurate to figure out the general properties of the clusters, even if it does not take into account Landau fluctuations in energy release, as well as δ-rays, diffusion, cross-talk and electronics inefficiencies.

In Section 4.4, the charge sharing is taken into account to improve the spatial resolution of the ATLAS Pixel Detector. For this reason, the variable Ω is computed for both the directions in which the cluster extends:

$$\Omega_{x\,(y)} = \frac{q_{\text{last row (col)}}}{q_{\text{first row (col)}} + q_{\text{last row (col)}}}. \tag{4.14}$$

Basically, the ratio between the charge measured in the last (rightmost) row of the cluster and the sum of the charges registered in the two outermost rows is considered for local x direction, while columns are used for the computation along the local y. The charge released in the central pixels of the cluster is neglected, since it is does not provide spatial information, according to the geometrical model presented.

Figure 4.10 shows the distribution of the Ω_x and Ω_y variable for clusters associated to cosmic ray tracks. The distributions are almost flat, with a clear decrease of statistics for $\Omega > 0.9$ and $\Omega < 0.1$. According to the geometrical model presented, the edges of this distribution depend on the incident angle of the particle that gives origin to the cluster considered. This effect, however, is barely visible in data, and will not be taken into account when using the charge sharing to improve spatial resolution.

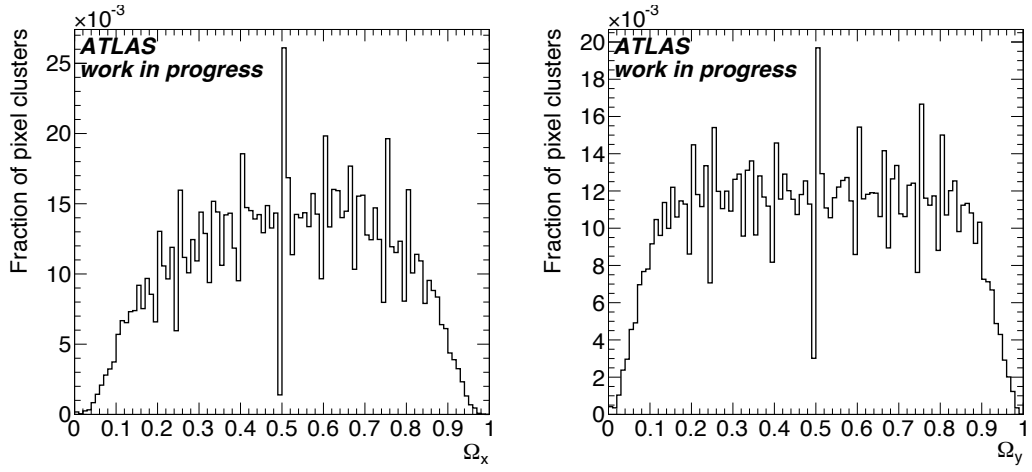

(a) (b)

Figure 4.10: Distributions of Ω_x (4.10(a)) and Ω_y (4.10(b)) variables for cosmic ray data.

Total charge of the cluster

The total charge collected in clusters has been extensively studied by using cosmic ray data. This analysis provided feedback to the tuning activity that was performed during dedicated calibration sessions, in order to optimize threshold and ToT calibration. Figure 4.2(b) shows for example the comparison between the MPV of the charge collected at a minimum ionizing particle passage, when using the simulation of the detector and when considering the cosmic ray data. When this comparison is performed, an accurate selection of clusters should be used, in order to discard clusters that exhibit charge losses due to threshold effects (see Section 4.3.2). The total track incidence angle α in the local reference frame is defined by using the polar incident angle θ_i and the incident angle in the transverse plane ϕ_i:

$$\tan\alpha = \sqrt{\tan^2\theta_i + \tan^2\phi_i}, \tag{4.15}$$

and only clusters associated to tracks that feature $0.05 < |\alpha| < 0.2$ are considered. A good agreement between data and simulation is visible, even if the charge measured in data is systematically lower than the value predicted by simulation. A scale factor of 98.6% has been measured. The most probable reasons of this discrepancy are the relatively big experimental error on the 20 k electrons charge injected during ToT calibration, as well as the uncertainty on the experimental value of W and on the energy loss models.

4.3.2 Cluster size

The size of a cluster can be defined along local x or local y direction. Since most of the tracking algorithms consider independently the cluster projection in the two directions (see Section 5.2), the size of the cluster in each direction will be described separately.

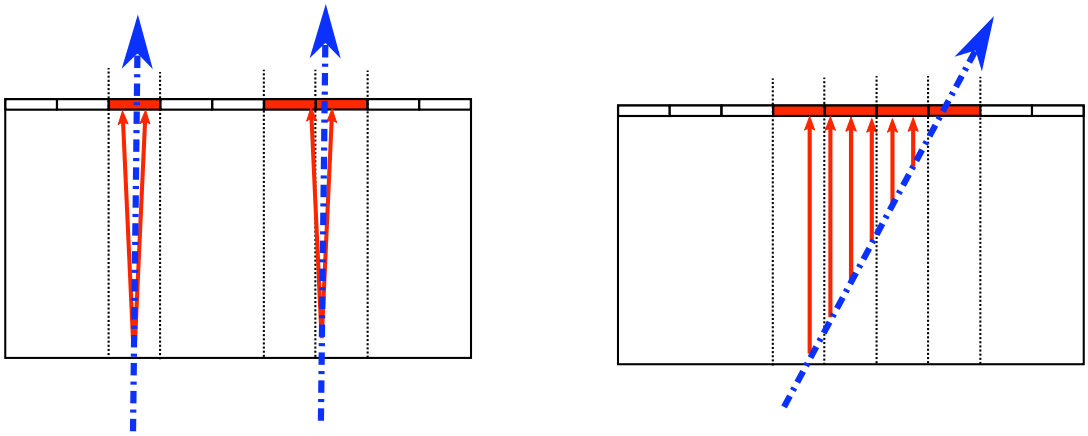

(a) (b)

Figure 4.11: Cluster size strongly depends on the particle incident angle. In the sketches, pixels that give signal are coloured. 4.11(a): the cluster size is minimum for tracks perpendicular to the module surface. Due to charge diffusion two-pixel clusters are possible, if the particle crosses the detector close to pixel border. 4.11(b): cluster size increases when increasing the incident angle with respect to the normal to the sensor surface.

Cluster size is determined by the position where charge is released and by charge mobility in silicon, as well as by the read-out system. If no magnetic field is present, charges drift perpendicular to the module surface: in this conditions, the size of the cluster is minimum when the particle is perpendicular to the module surface (incident angle is null), while it increases when the incident angle with respect to the direction perpendicular to the module surface becomes larger (see Figure 4.11). Even if a particle hits the detector perpendicularly, it can fire two pixels if the particle crosses the detector very close to pixel border, due to charge diffusion. In this case the spatial probability distribution for two-pixel clusters is just wide as the small zone in which the charge can diffuse to the nearby pixel (see Section 4.1.2). On the other hand, the spatial probability distribution of one pixel clusters is a uniform distribution wide nearly as the pixel itself.

When the incident angle increases, the probability of two-pixel clusters increases, while the one of single pixel clusters decreases. At a certain angle, the numbers of one-pixel and two-pixel clusters are equal: at this point their probability distributions have the same width. If the angle is increased further, the probability distribution associated to two-pixel clusters almost reaches the width of the entire pixel and three-pixel clusters appear due to diffusion. From this angle on, the probability of three-pixel clusters extends: the mechanism is replicated up to the largest cluster sizes.

Figure 4.12 shows the distribution of the pixel clusters as a function of the incident angle for cosmic muons, both in simulated and in real events. Clusters belonging to real events have been selected according to Section 4.5.1, without introducing any significant bias. Data were registered with magnetic field on: the measured incident angle has been corrected for the Lorentz effect (see Section 4.3.3), by

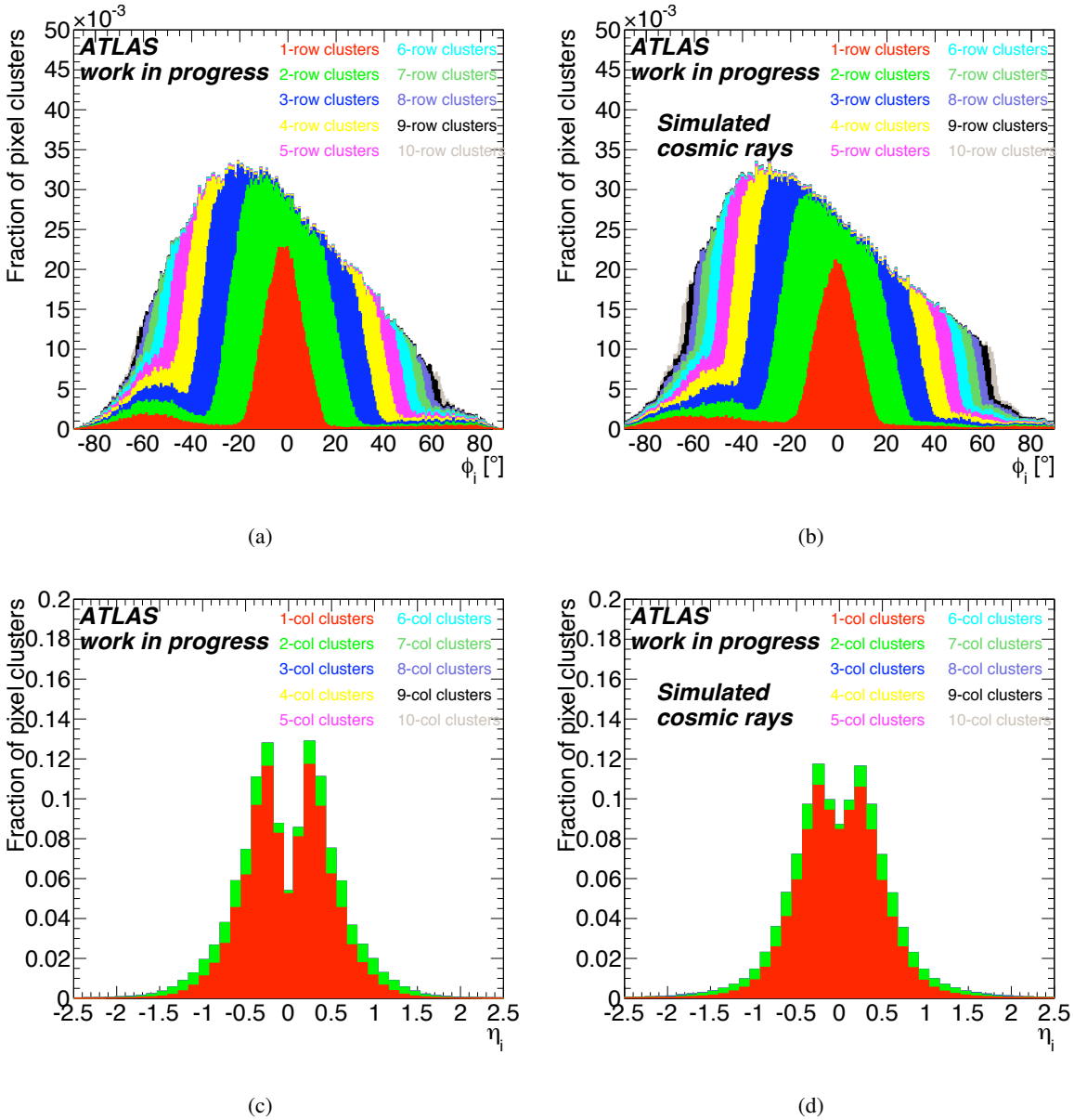

Figure 4.12: Number of clusters as a function of the track incident angles for cosmic ray tracks. Clusters with different dimensions are plotted using different colors and cumulative distributions. 4.12(a): local x direction, real data. 4.12(b): local x direction, simulation. 4.12(c): local y direction, real data. 4.12(d): local y direction, simulation.

subtracting the Lorentz angle from the measured angle. The contributions of clusters with different sizes are evidenced by using different colors.

In Figures 4.12(a) and 4.12(b) the local x direction is considered. For small incident angles, as explained, cluster made by only one row are the most probable. The angle at which single row and double row clusters have the same probability is 8°. Increasing further the angle, the number of two-row clusters reaches a maximum at 16°. The distribution shows an asymmetric shape due both to

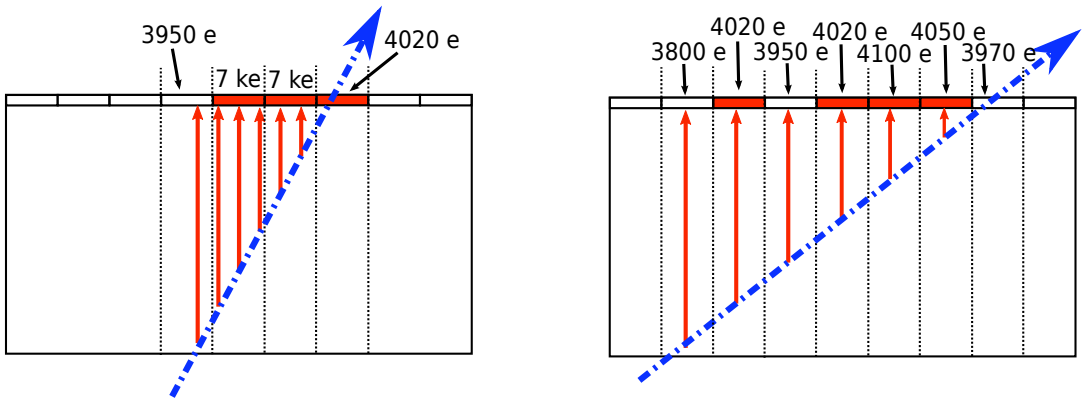

(a) (b)

Figure 4.13: Cluster size and charge collected are influenced by threshold effects. In the sketches, the amount of charge collected by different pixels is written, while pixels that give signal are coloured. 4.13(a): one of the outermost pixels that collect charge is lost due to charge release fluctuations. 4.13(b): a particle that gives origin to a split cluster.

the geometrical structure of the detector with respect to the direction of cosmic ray tracks and to the correction applied to compensate the Lorentz angle effect. Clusters up to 10 rows have been considered in the plots: larger clusters are present in cosmic ray events, but they would not be visible in the figure, due to limited statistics. A noticeable feature of cluster size distribution is that, at every incident angle, two sizes of clusters describe the great majority of the measurements.

The simulation features a good description of the cluster size along the x direction, even if some discrepancies are visible for large incident angle. In these regions, the effect of threshold on cluster size must be considered. Figure 4.13 shows two possible effects. In Figure 4.13(a) the case where four pixels collect charge, but only three of them are over threshold is shown. In Figure 4.13(b), the case of a *split cluster* is shown: since the particle has a very long path in the silicon, charge is divided on many pixels, and the final amount collected by each of them is close to the threshold. If some of the pixels that correspond to the center of the path do not reach the threshold, two small clusters are measured instead of a single bigger one. The presence of split clusters is clearly visible in Figure 4.12(a) from $-40°$ to $-80°$, where single and double row clusters are an important fraction of the total number of clusters, despite the large incident angle.

In the local y direction (Figure 4.12(c) and 4.12(d)), the larger dimension of the pixels only allows for small clusters. Along this direction, the number of two-column clusters became comparable to that of one-column clusters for $\eta > 1$. Moreover, only very little statistics is available for $\eta > 1.5$, where also a tiny number of three columns clusters is present. In this case, the agreement with simulation is good for the cluster size description, except at small $|\eta_i|$.

A final note must take into account the expected cluster size distributions for tracks coming from collisions. In this case only particles with azimuthal incident angle in the range $\phi_i \in [-20°; 20°]$ are

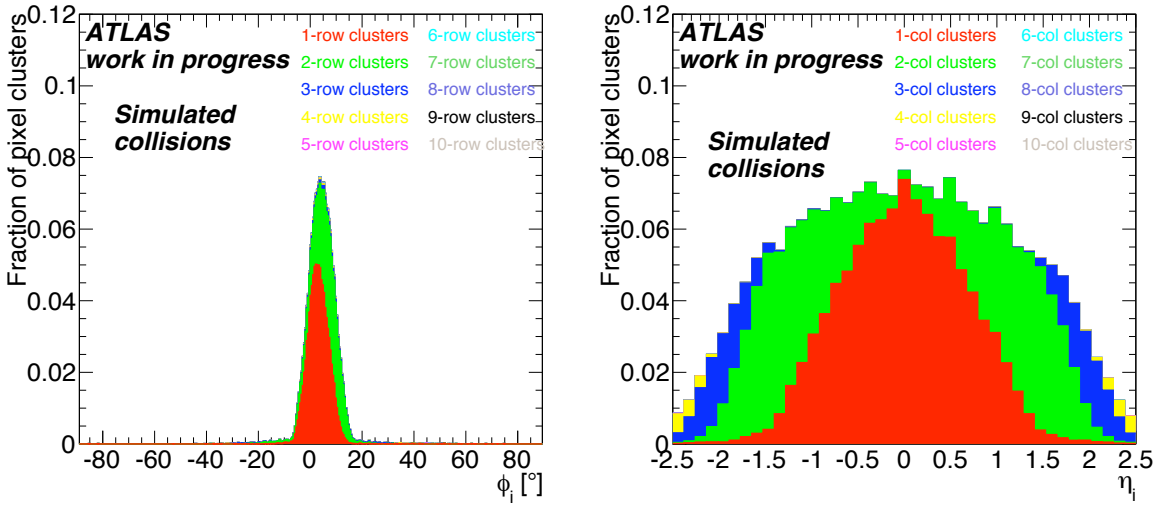

(a) (b)

Figure 4.14: Number of clusters as a function of the track incident angles for simulated collision events. Clusters with different dimensions are plotted using different colors and cumulative distributions. 4.14(a): local x direction. 4.14(b): local y direction.

foreseen (see Figure 4.14(a)). For this reason, the following analysis will be optimized only for small angles and only for clusters up to three rows. In the local y direction, on the contrary, a wider range of incident η is expected, leading to clusters made of up to 4 columns of pixels (see Figure 4.14(b)).

4.3.3 Lorentz Angle

The Pixel Detector, as the rest of tracking system, is immersed in a magnetic field, in order to measure the momentum of the particles (see Section 5.1.1). The effect of magnetic field should be summed to the drift motion of charges to correctly describe the detector. In the barrel modules, the electric and the magnetic field are perpendicular, while in the disks they result to be parallel. In the latter case, the Lorentz force is null. In the barrel, instead, the force gives origin to the *Lorentz angle* [105, 113–117]: the charges drift along a direction that forms an angle α_L with respect to the electric field. Given the geometry of the detector, this angle is always projected in the transverse (R-ϕ) plane.

The value of the Lorentz angle depends on the magnetic field and on charge carriers mobility:

$$\tan \alpha_L = \mu_H B = \mu_d r B. \tag{4.16}$$

The μ_H factor is called *Hall mobility*, while μ_d is the *drift mobility* introduced in Eq. 4.5. Since the ATLAS Pixel Detector collects electrons, in the following the electron mobility is considered. The *Hall factor* connects the two definitions of mobility and it is related to the mean free time between collisions: $r = \langle \tau^2 \rangle / \langle \tau \rangle^2$. The Hall factor for silicon has a weak dependence on temperature, but does not depend

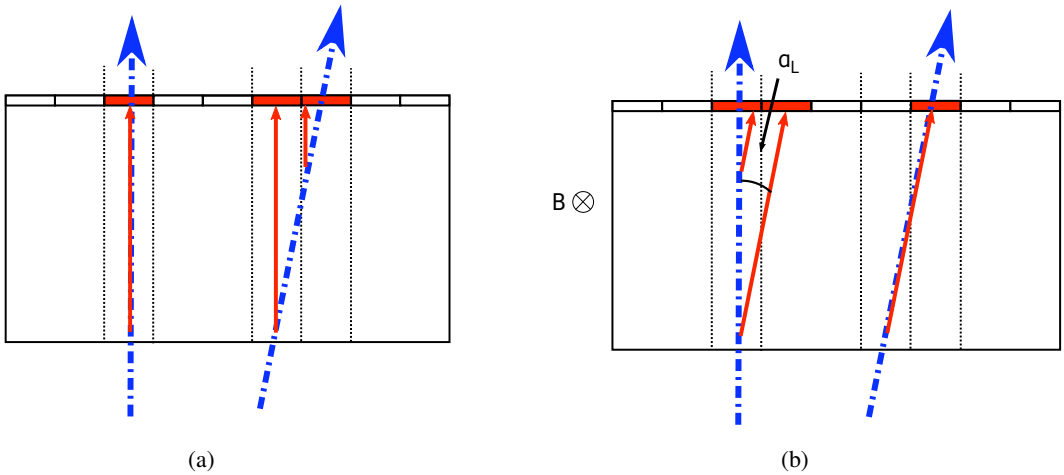

Figure 4.15: Lorentz effect with magnetic field off (4.15(a)) and on (4.15(b)). When magnetic field is present, charges released by a particle perpendicular to the module surface drift forming an angle α_L with the particle direction: they are spread over a large area. On the contrary, charges release by a particle with incident angle equal to the Lorentz angle drift along the particle direction. As a result, they are focused on a single pixel (if diffusion is neglected).

on the doping level, in the relevant range for the Pixel Detector. For electrons, in particular, $r = 1.15$ at 300° K and $r = 1.12$ at 264° K. As a result, the Lorentz angle value depends on magnetic field, on temperature and on the electric field only.

The effect of the Lorentz angle is a shift of the local x position where the charge is collected, with respect to the case in which no magnetic field is present. This shift is visible both on the position of clusters and on the cluster size distribution as a function of the azimuthal incident angle: Figure 4.15 sketches these effects. When considering distributions that are function of the azimuthal incident angle, the Lorentz effect can be taken into account as a correction term to be subtracted from the measured incident angle. The expected average value of the Lorentz angle is 225 ± 27 mrad for the cosmic ray data-taking detector conditions. The main contribution to the uncertainty comes from the uncertainty on the electron mobility.

Cosmic rays were used to measure the Lorentz angle. For this measurement, isolated clusters were used. Furthermore, clusters that contained ganged pixels and clusters placed at the border of modules were discarded. Finally a requirement on the polar incident angle ($\theta_i < 45°$) and on the extrapolated position of the cluster ($x_{\text{first row}} \leq x_{\text{extr}} \leq x_{\text{last row}}$) were imposed, in order to have the extrapolation contained in the module. The mean cluster size was then computed as a function of the azimuthal incident angle: the Lorentz angle is expected to be the angle where the cluster size is minimum.

Figure 4.16(a) shows such distributions for data registered with or without magnetic field. The measured Lorentz angle is compatible with zero in the case of field off data, while it results to be $\alpha_L = 213.9 \pm 0.5$ mrad in the case of field on data. In order to extract the minimum, the distributions

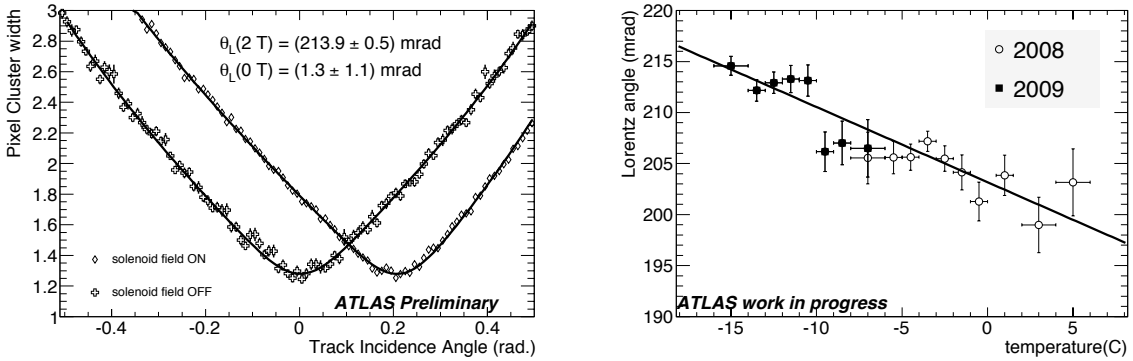

(a) (b)

Figure 4.16: 4.16(a): cluster width versus the azimuthal incidence angle of the track for clusters on tracks. The minimum of this distribution determines the Lorentz angle and the fit result is shown. 4.16(b): measured Lorentz angle versus the temperature of the Pixel Detector module where it is measured.

are fitted with a function:

$$F(\alpha) = \left[a\,(\tan\alpha - \tan\alpha_{\mathrm{L}}) + b/\sqrt{\cos\alpha}\right] \otimes G(\alpha), \tag{4.17}$$

where the diffusion has been taken into account by the term $b/\sqrt{\cos\alpha}$. Free parameters of the fit are the width of the Gaussian $G(\alpha)$, the coefficients b and a, and finally α_{L}.

Since the error on the fit is small, the dependence of the Lorentz angle on temperature was studied. Clusters were grouped according to the temperature of the module they belonged to and the fit was repeated for each group. Figure 4.16(b) shows the result of this analysis. A dependence of -0.74 ± 0.06 mrad/K is observed. This is in optimal accordance with the expectation of -0.74 mrad/K, computed by using Eqs. 4.16 and 4.8.

4.4 Position resolution of the ATLAS Pixel Detector

The main task of the Pixel Detector is to provide high-resolution measurements of the positions where it is crossed by particles, at few centimeters from the interaction point. Optimal resolution is a primary request in order to have a precise measurement of the impact parameter, when tracks are reconstructed (see Section 5.1.2). The resolution is mainly determined by the pixel size and by the incident angle of the particles and it can be improved by using pulse height information measured by the detector, such as the charge released in each pixel. In this case, further dependencies of the resolution on detector conditions are introduced and an accurate calibration becomes necessary.

The position of a charged particle crossing point can be estimated using different algorithms. A first estimation is performed by using only the cluster properties. A *recalibration* of the position is then

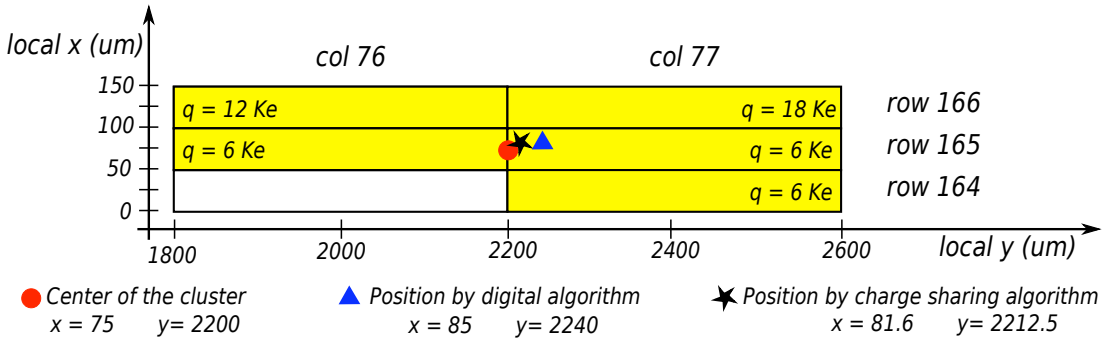

Figure 4.17: Comparison of different position definitions for a realistic cluster (see Section 4.4). The hit pixels are sketched as colored rectangles and the amount of charge collected in each of them is reported. This cluster is defined by $x_{\text{first row}} = 25$ and $x_{\text{last row}} = 125$; $y_{\text{first col}} = 2000$ and $y_{\text{last col}} = 2400$; $\Omega_x = 5/6$ and $\Omega_y = 5/8$; $q = 48$ ke.

performed after track reconstruction, if a track candidate is found. To illustrate the different algorithms used by the ATLAS Pixel Detector reconstruction, an example of a realistic cluster is sketched in Figure 4.17, where the charge collected by each pixel is reported, as well as the reference system of the module and the identifiers of the rows and of the columns that compose the cluster itself.

Center of the cluster

The simplest algorithm for the position of multiple-pixel clusters involves computing the geometrical center of the cluster in the local reference frame:

$$x_{\text{center}} = \frac{x_{\text{first row}} + x_{\text{last row}}}{2} \tag{4.18}$$

$$y_{\text{center}} = \frac{y_{\text{first col}} + y_{\text{last col}}}{2} \tag{4.19}$$

where x_{row} and y_{col} are the coordinates of the center of the row (column). The computation of the center of the cluster does not require information from the tracking system.

Digital algorithm for the position of the cluster

The position algorithm described above does not take into account any asymmetry in the cluster. The digital position algorithm, instead, assigns an individual coefficient w_i to the rows and to the columns according to the number of pixels n_i that they contain:

$$w_i^{\text{row (col)}} = \frac{n_i^{\text{row (col)}}}{\sum_i n_i^{\text{row (col)}}}. \tag{4.20}$$

For example the cluster represented in Figure 4.17 is described by $w_{76}^{\text{col}} = 2/5$, $w_{77}^{\text{col}} = 3/5$, $w_{166}^{\text{row}} = 2/5$, $w_{165}^{\text{row}} = 2/5$ and $w_{164}^{\text{row}} = 1/5$.

These coefficients are then used to compute a weighted mean using the coordinates for the center of each row (column):

$$x_{\text{dig}} = \sum_i w_i^{\text{row}} \cdot x_i \tag{4.21}$$

$$y_{\text{dig}} = \sum_i w_i^{\text{col}} \cdot y_i. \tag{4.22}$$

This position algorithm is currently used as default in the reconstruction software if no track has been associated with the cluster, since it takes into account the two-dimensional cluster shape when computing each coordinate.

Charge sharing algorithm for the position of the cluster

Another possibility to compute the cluster position uses the information about the charge collected in the hit pixels. Here, only the pixels at the edge of the cluster become significant, since they are the most sensitive to the exact position of the crossing point. In this case the position is calculated by adding the coordinates for the center of the clusters (Eqs. 4.18 and 4.19) with a correction based on charge sharing:

$$x_{\text{cs}} = x_{\text{center}} + \Delta_x \cdot \left(\Omega_x - \frac{1}{2} \right), \tag{4.23}$$

$$y_{\text{cs}} = y_{\text{center}} + \Delta_y \cdot \left(\Omega_y - \frac{1}{2} \right); \tag{4.24}$$

where Ω is defined in Eq. 4.14, and Δ represents the weight of the correction.

Eqs. 4.23 and 4.24 take into account the fact that for $\Omega = 1/2$ the charge is equally distributed among the outermost pixels, suggesting that the particle crossed the detector at the center defined by the pixel edges, whereas for larger (smaller) values, the particle crosses the detector nearer to (farther from) the last (rightmost) pixel in the cluster. The cluster sketched in Figure 4.17, for example, has $\Omega_x = 5/6$ and $\Omega_y = 5/8$. If the constants used are $\Delta_x = 20\ \mu$m and $\Delta_y = 100\ \mu$m[1], the position of the cluster according to this algorithm would be $x_{\text{cs}} = 81.6\ \mu$m and $y_{\text{cs}} = 2212.5\ \mu$m in the local reference frame. This means that the x coordinate is corrected by 6.6 μm — having a pixel pitch of 50 μm — while the y coordinate by 12.5 μm — having a pitch of 400 μm.

The Δ parameter depends both on cluster size and on particle incident angle. A dependence on the detector conditions is also expected, since e.g. threshold, bias voltage, cross talk and other parameters modify the pixel efficiency for charge collection. Figure 4.18 uses simulated data to show the difference between the particle crossing point on a module and the position of the center of the reconstructed cluster (only the local x direction is considered). This difference is plotted as a function of charge sharing, and the slope of the distribution corresponds to the Δ parameter according to Eq. 4.23. In Figure 4.18(a), the two data populations refer to two-row clusters created by particles with different

[1] These are typical values for three-row and two-column clusters (see Figure 4.27)

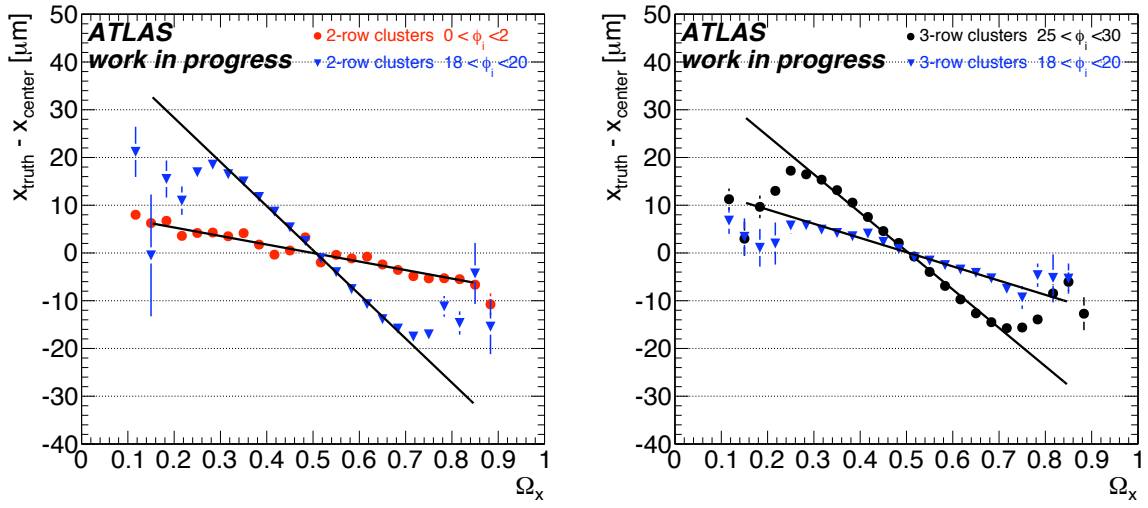

(a) (b)

Figure 4.18: Estimation of the Δ parameter from simulated data (see Eq. 4.23). The value of the parameter depends on the incident angle of the particle from which the cluster originates (4.18(a)) and on the cluster size (compare 4.18(a) and 4.18(b)).

incident angles and this plot shows that the Δ parameter depends on the incident angle. Figure 4.18(b) shows the same behaviour for clusters consisting of three rows of pixels. Also in this case the Δ parameter is dependent upon the incident angle and, for the same angular selection, it is different with respect to two-row pixels. The dependence of the Δ parameter on the incident angle implies that the track parameters are needed to achieve the maximum resolution when using the charge sharing algorithm.

This algorithm can also be applied before building track candidates. In this case some simplification must be done. A value of $\Delta_x = 30\ \mu$m can be used for the local x computation of two-row clusters, since this value is a reasonable average for the ATLAS geometry (see Section 4.5.2). On the other direction, for particles that are coming from the interaction point, the Δ_y parameter can be approximated using geometrical considerations:

$$\Delta_y = d \cdot \tan(\theta_{\text{module}}), \tag{4.25}$$

where d is the thickness of the sensor and θ_{module} is the angle formed by the module position with respect to the beam axis.

Given the multiple factors that determine the Δ parameter, its value should be optimize for different classes of clusters to maximize resolution. A detailed description of how a set of Δ parameters is extracted from data is reported in Section 4.5.

4.4.1 Average position resolution

Several studies [105, 115–119] were performed on test-beam data to show the improvement in resolution that can be achieved using Eqs. 4.23 and 4.24. Here the simulation of cosmic rays crossing the ATLAS detector (see Section 3.5 and 4.2) is used to give an estimate of the intrinsic resolution of the Pixel Detector. A dedicated reconstruction of pixel clusters has been made on simulated cosmic rays, in order to produce a detailed study of the resolution. The resolution is evaluated by considering the difference $x_{\text{truth}} - x_{\text{reco}}$, where x_{truth} is the true position where a particle crossed the detector (it is known from simulation) and x_{reco} is the reconstructed position of the cluster originated from the particle. In order to extract the resolution, the RMS of the 99.7% of data is used, according to the procedure that will be better described in Section 5.4.3. The reconstruction is done with all three algorithms mentioned above. The set of Δ constants used for the charge sharing algorithm are the ones described in Section 4.5.2.

Figure 4.19 shows the resolution of the Pixel Detector in local x, when using the three different position algorithms. Only clusters corresponding to particles with incident angle in the range $\phi_i \in [-20°, 20°]$ are used, since this is the most probable angular range in collisions. The global distribution (Figure 4.19(a)) shows that the charge sharing algorithm is the most precise method to compute cluster position, giving a resolution of 8.6 μm. Only a tiny difference, instead, is visible between the center of the cluster and the position computed by the digital algorithm: they feature a resolution of 11.7 μm and 11.5 μm, respectively. In order to detail the contribution of clusters with different number of row, the distributions relative to one-, two- and three-row clusters have been reported. One-row clusters local x position can only be calculated as the center of the row itself, yielding a 10.1 μm resolution (see Figure 4.19(b)). For two-row clusters (Figure 4.19(c)) a similar resolution (11.3 μm and 11.1 μm) is registered when using the center of the cluster and the digital algorithm. The charge sharing, instead, introduces a huge improvement, lowering the resolution to 4.5 μm. Finally, three-row clusters (Figure 4.19(d)) have a constant resolution of ~ 20 μm, for all the considered algorithms.

The resolution along the local y direction is reported in Figure 4.20. The global distribution RMS in Figure 4.20(a) is not greatly affected by the algorithm chosen to compute the position. At the same time, the shape of the distribution exhibits shoulders that can be explained only by detailing the contribution of different cluster sizes to the global plot. Clusters composed by only one column, reported in Figure 4.20(b), feature a square distribution with an RMS of 104.8 μm. They correspond to the majority of clusters and they give origin to the bulk of the global distribution. Clusters formed by two columns, instead, show a sharp distribution (see Figure 4.20(c)). In this case the resolution for the center of the cluster is 54.5 μm. The charge sharing algorithm introduces a substantial improvement, reaching 29.9 μm of resolution. The digital algorithm is characterized by two shoulders in the distribution, that limit the resolution to 53.3 μm. The shoulders are due to the presence of L-shaped clusters at very low incident angle (see Figure 4.21). If a particle is traversing a pixel next to a corner, at a very small incident angle, there is a certain probability to fire the adjacent pixel by diffusion, while the pixel that shares only the corner with the hit pixel does not collect enough charge to fire. In this case, the

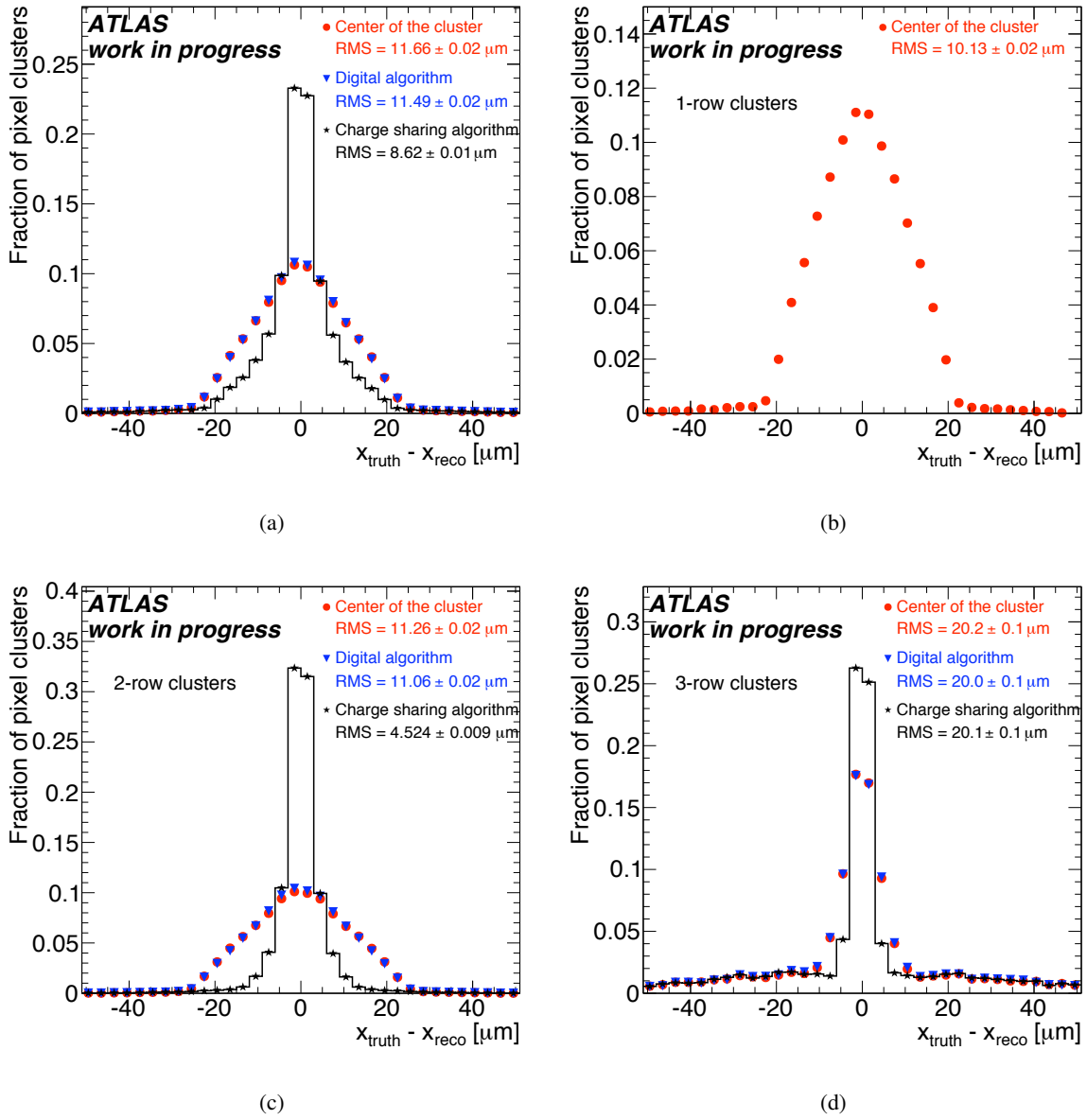

Figure 4.19: Comparison of the resolution in local x obtained when using different position algorithms in the Pixel Detector. The contributions of different cluster sizes are detailed. For one-row clusters (4.19(b)) only the center of the cluster is meaningful.

digital algorithm extracts a position that is definitively worse than the simple center of the cluster (see Figure 4.21(a)). In Figure 4.21(b), the two-column clusters distribution is reported for small incident angles ($|\eta_i| < 0.5$) and "L-shaped" clusters: the shoulders are more pronounced. In Figure 4.21(c), instead, clusters are selected only for large incident angle ($|\eta_i| > 1$): in this case the shoulders disappear and the digital algorithm performance is similar to the charge sharing algorithm one. Finally, clusters formed by three columns of pixels are considered in Figure 4.20(d). In this case, no charge sharing constants are available and the position has been computed only by using the center of the cluster and

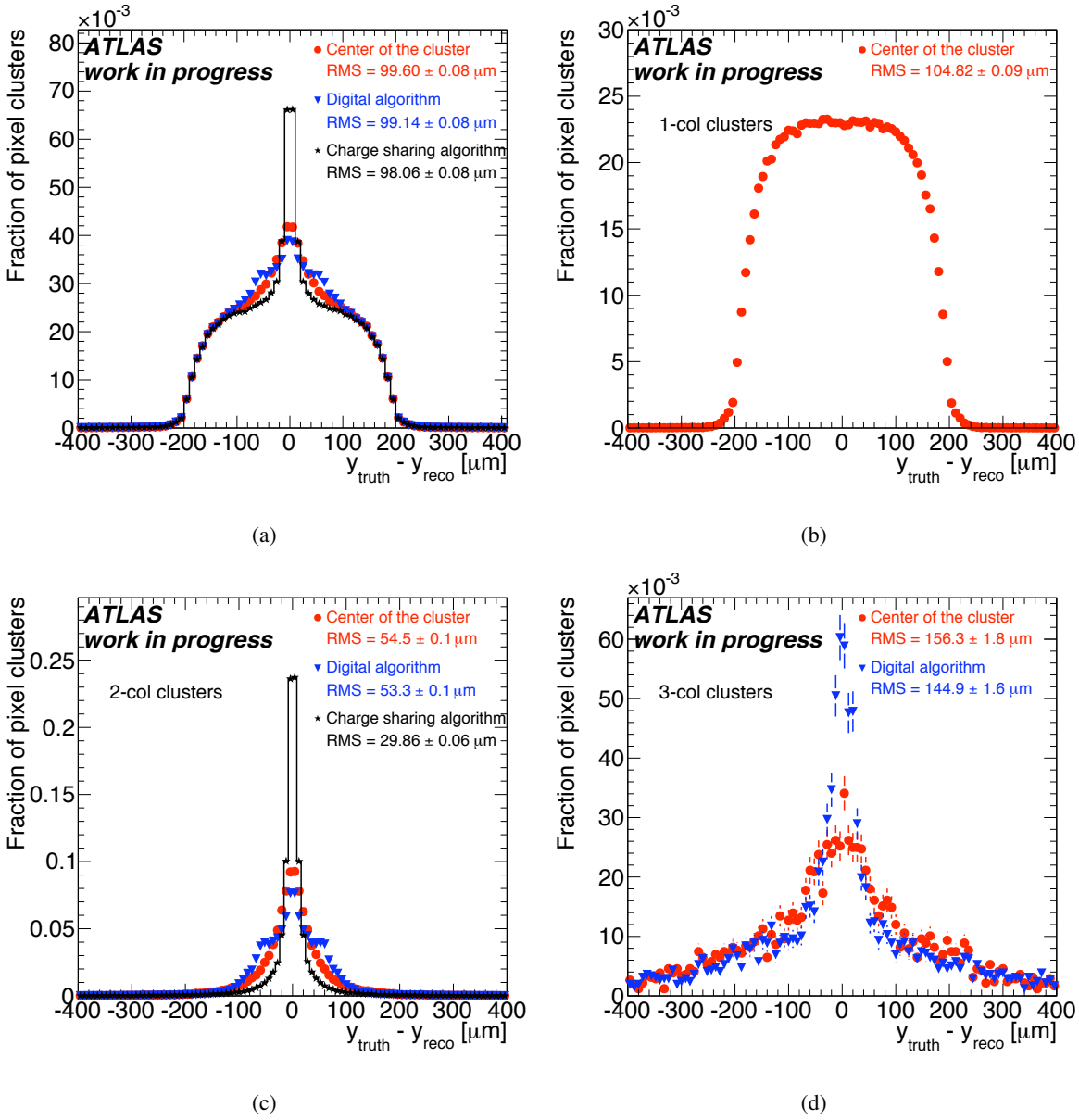

Figure 4.20: Comparison of the resolution in local y obtained when using different position algorithms in the Pixel Detector. The contributions of different cluster sizes are detailed. For one-column clusters (4.20(b)) only the center of the cluster is meaningful. For 3-column clusters (4.20(d)) charge sharing was not applied, because no calibration constants were available.

the digital algorithm. The latter shows a 12 μm improvement over the center of the cluster, even if the RMS of the distribution appears to be dominated by the tails.

4.4.2 Position resolution as a function of the incident angle

The resolution as a function of the incident angle is determined by the relative probability of cluster dimensions at that angle and by the algorithm used in position reconstruction. In Section 4.3.2 the

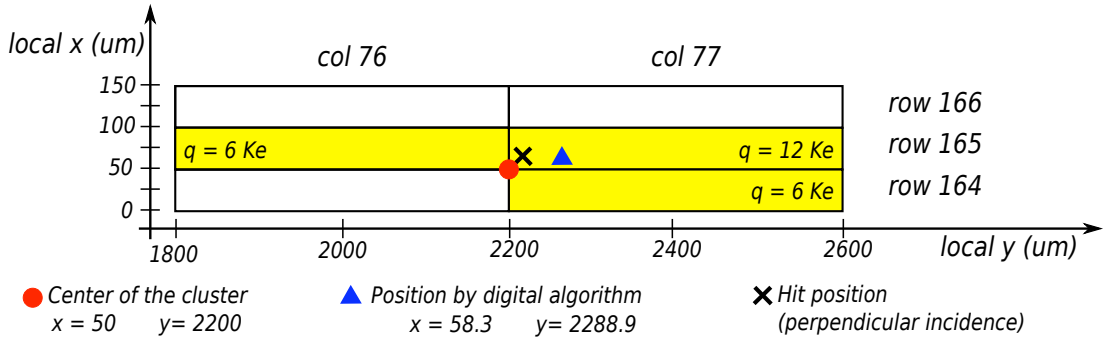

(a)

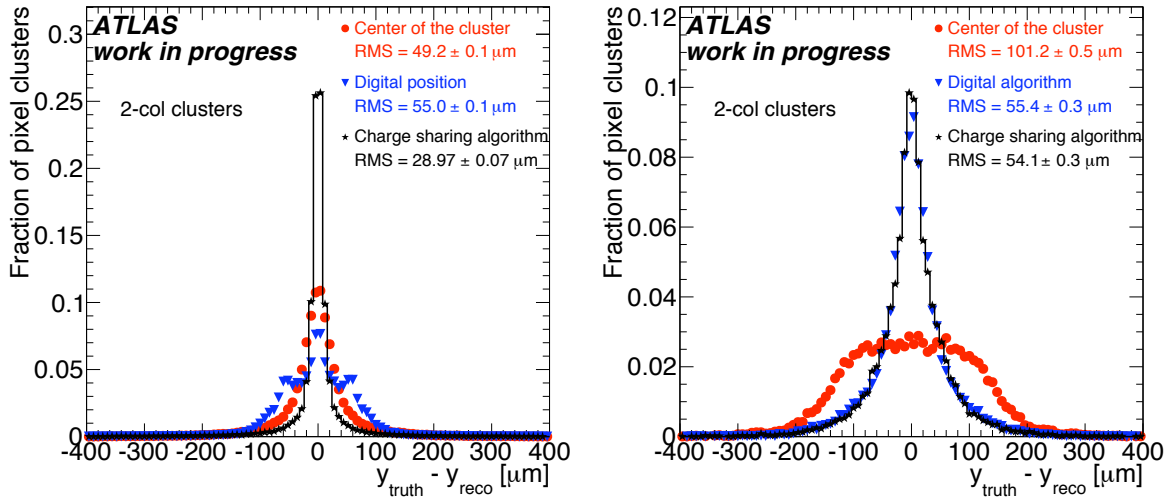

(b) (c)

Figure 4.21: 4.21(a): for small incident η, the digital algorithm can give worse results with respect to the center of the cluster. This applies in particular for "L-shaped" clusters. 4.21(b): resolution for two-column clusters associated with tracks featuring $|\eta_i| < 0.5$ and an odd number of pixels. 4.21(c): resolution for two-column clusters associated with tracks having $|\eta_i| > 1$.

dependence of cluster size on the incident angle has been described. In particular, it has been shown how the probability distribution for clusters formed by a different number of pixel varies as a function of the incident angle. Figure 4.22 shows the resolution dependence on the incident angle of the particle. Resolution is computed by using the RMS of the $x_{\text{truth}} - x_{\text{reco}}$ (or $y_{\text{truth}} - y_{\text{reco}}$) distribution for each of the angular bins. To understand the shape of this distribution, it should be compared with Figure 4.12: it must be remembered that for each incident angle, when excluding split clusters, the size distribution is completely dominated by only two classes of cluster size.

The resolution obtained by the center-of-the-cluster algorithm shows several minima and maxima. Each maximum corresponds to the angle at which clusters are almost entirely composed by one single size, while minima happen when the probability to have either of the appropriate cluster sizes is equal.

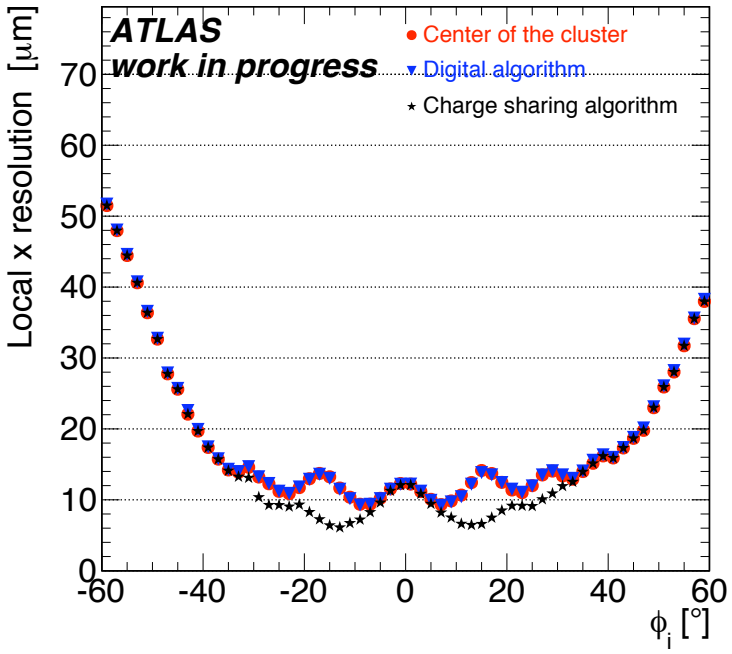

(a)

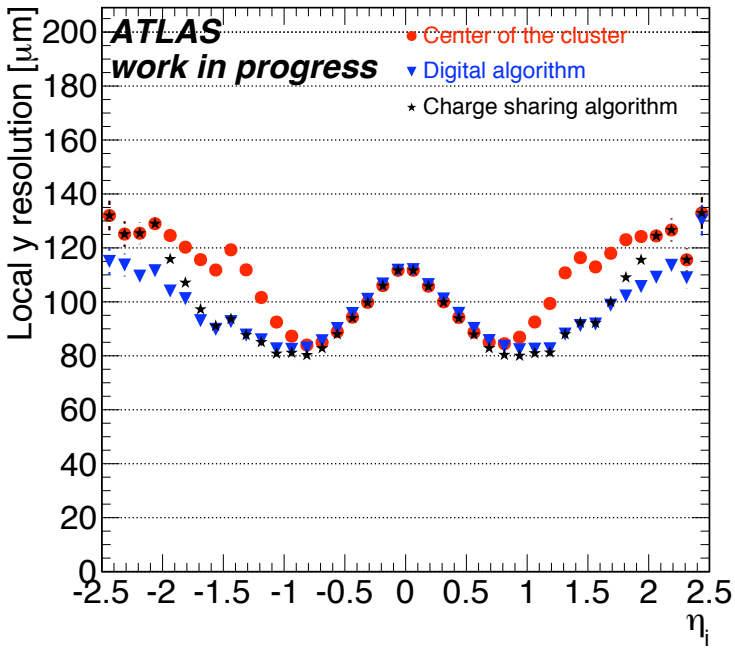

(b)

Figure 4.22: Intrinsic detector resolution as a function of angle using simulated events and three different position algorithms. 4.22(a): in the local x direction the improvement brought by the charge sharing algorithm is clearly visible for angles at which two-row clusters are dominant (see Figure 4.12). 4.22(b): local y direction.

Along the x direction, for example, single clusters are the most probable ones at 0° and a maximum is expected. On the contrary, at $\pm 8^\circ$, the probabilities of one-row and two-row clusters are equal, resulting in a minimum. Increasing further the angle, at $\pm 16^\circ$, the probability to have two-row clusters is maximum, leading to a maximum in resolution when position is computed as the center of the cluster. The same shape can be seen in the local y. Here the bigger size of pixels only allows for a single global minimum near $|\eta_i| = 1$. A less pronounced local minimum is visible for $|\eta_i| = 1.5$, where three-column clusters appears. The digital algorithm resolution is almost identical to the one of the center-of-the-cluster algorithm, along the local x direction. In the local y instead, a big improvement is visible for $|\eta_i| > 1$, when double clusters begin to be produced by the particle incident angle, instead of diffusion (see Figure 4.21). Finally, the charge interpolation algorithm is the best choice for local x measurement at every angle and for the local y direction, up to $|\eta| < 1.75$; for larger incident angle, the best algorithm is the digital one.

In order to understand the contribution of clusters of different size, the resolution of one-, two- and tree-row (column) clusters is shown in Figure 4.23(a) and 4.23(b) (Figure 4.23(c) and 4.23(d)). In Figure 4.23(a) and 4.23(c), the center of the cluster is used to reconstruct the position, while in Figure 4.23(b) and 4.23(d), the charge sharing algorithm is used. The global resolution can be computed as the weighted sum of the different distributions, where the weight for every angular bin is the probability of having a clusters of a certain size at that angle.

The value of the resolution for a given size of clusters at a fixed incident angle corresponds to the RMS of the spatial distribution associated to that size of clusters, when the center of the cluster algorithm is used. This is why, for the angle at which only one cluster size is dominant, the resolution is maximum and it is approximately equal to the the pixel pitch over $\sqrt{12}$, i.e. $(50\,\mu\text{m})/\sqrt{12} \approx 14\ \mu\text{m}$ for the x direction and $(400\,\mu\text{m})/\sqrt{12} \approx 115\ \mu\text{m}$ for the y direction. The true value is slightly smaller, because there is always a fraction of clusters with size bigger than the dominant one, due to diffusion and cross talk, that can cause additional pixels to fire if the particle is close to the border of the traversed pixel. The minimum of the resolution, instead, happens when the chosen cluster size is at minimum of its spatial probability.

When charge sharing is used to calculate position, the resolution of double row (column) is improved: the minimum of the resolution is constant over a wide range of angle. A similar effect is also observed for three-row clusters. In this case, the minimum of the global resolution is at the angle where is maximum the presence of two-row (column) pixels.

4.5 Calibration of the charge sharing algorithm

The Δ constant that appears in Eqs. 4.23 and 4.24 can be calculated from the simulation. However, since it depends on running conditions, it is preferable to develop a method that allows for a computation from data. The analysis described in this section was developed to create sets of constants that *calibrate* the charge sharing algorithm in order to optimize the resolution in the detector.

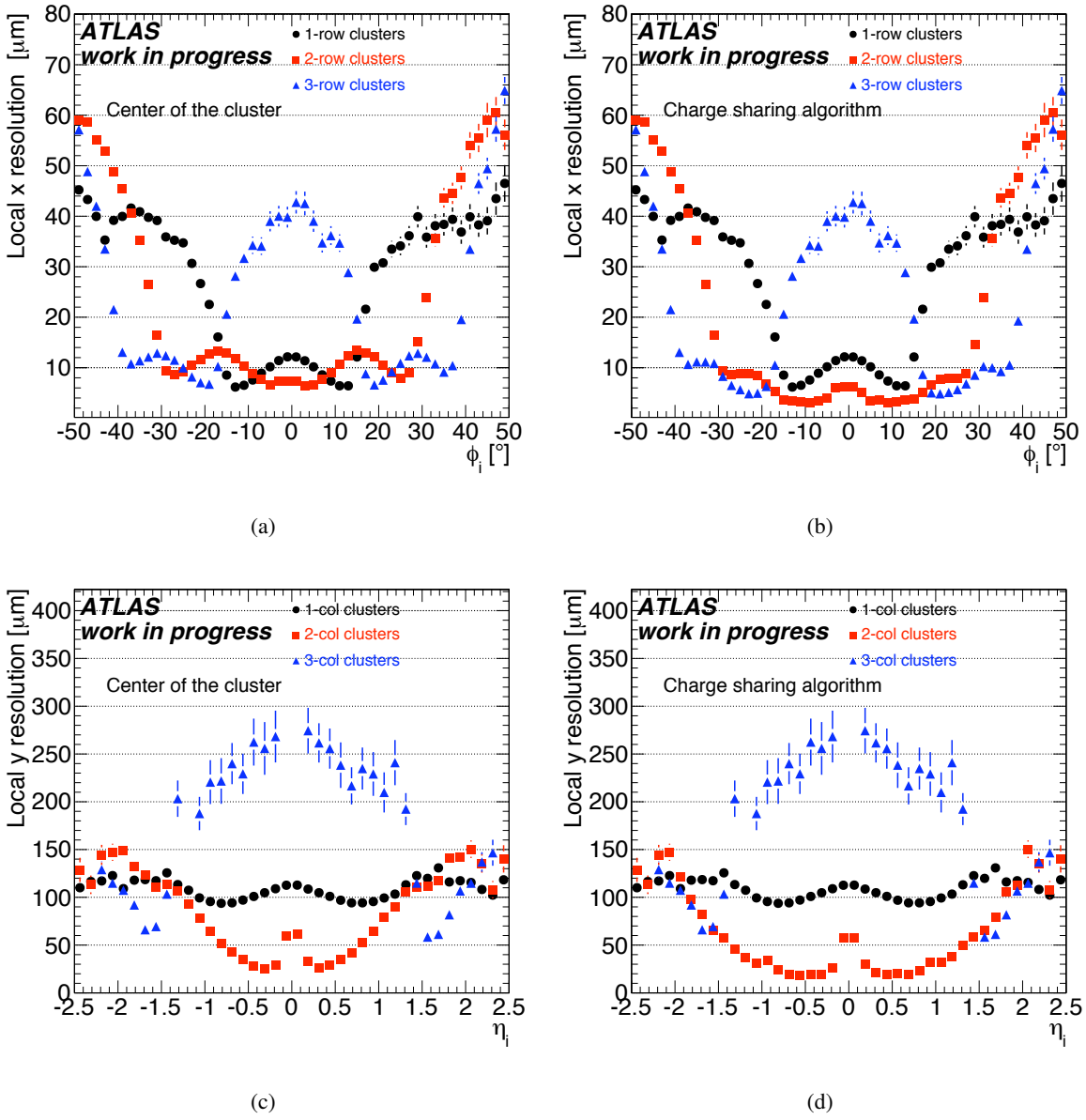

Figure 4.23: Intrinsic detector resolution as a function of angle using simulated events and two different position algorithms. The resolution relative to different cluster sizes are reported. 4.23(a): local x direction, center of the cluster. 4.23(b): local x direction, charge sharing algorithm. 4.23(c): local y direction, center of the cluster. 4.23(d): local y direction, charge sharing algorithm.

Using the equation for the position according to the charge sharing algorithm (Eqs. 4.23 and 4.24), Δ can be represented as the slope of a residual distribution:

$$x_{\text{center}} - x_{\text{extr}} = -\Delta \cdot \left(\Omega_x - \frac{1}{2} \right). \tag{4.26}$$

This distribution is studied for different incident angles and for clusters made of two and three rows (columns) of pixels. The Δ parameter is fitted in each case and the values that are obtained are used to calibrate the charge sharing algorithm. Some examples of the distributions that are used is reported in Figure 4.24.

In this section the procedure developed to perform the calibration and the results obtained are described. Since the precision of the residuals in Eq. 4.26 depends on the alignment quality, the analysis was performed on the set of *Reprocessed data* (see Section 3.4). The charge sharing calibration of the Pixel Detector is foreseen to be part of the shifter task during data-taking. Therefore the procedure has been implemented in a set of scripts that will be run periodically and whose results will be uploaded to ATLAS conditions database. Further details, as well as a comparison among the different calibration constant sets are given in Section 4.7.

4.5.1 Data and selection cuts

Reconstructed tracks were selected in order to consider only clusters and tracks clearly associated with real particles. For each track, it was required:

- at least 1 hit in the pixel barrel,
- a suitable number of hits in the SCT and in the TRT barrel:

$$N_{\text{TRT hits}} + 5 \times N_{\text{SCT hits}} > 30. \tag{4.27}$$

Only hits in the barrel were taken into account, because of the lack of alignment for the disks in the samples that have been used.

Furthermore, for the fit of the residual distribution, it is important to consider only clusters that are associated with tracks within a small uncertainty. Clusters that show big residuals can be characterized by δ-rays (see Section 4.1.3), that spread the charge among many pixels, or by threshold effects, that causes inefficiencies and split clusters. Furthermore, it is known that the resolution in the low momentum region is dominated by multiple scattering interactions. All these cases can affect the Δ parameter fit, broadening the errors associated to the bins of the residual distribution. Therefore, the following selection cuts were applied:

- for tracks:

$$p_T > 5 \text{ GeV} \tag{4.28}$$

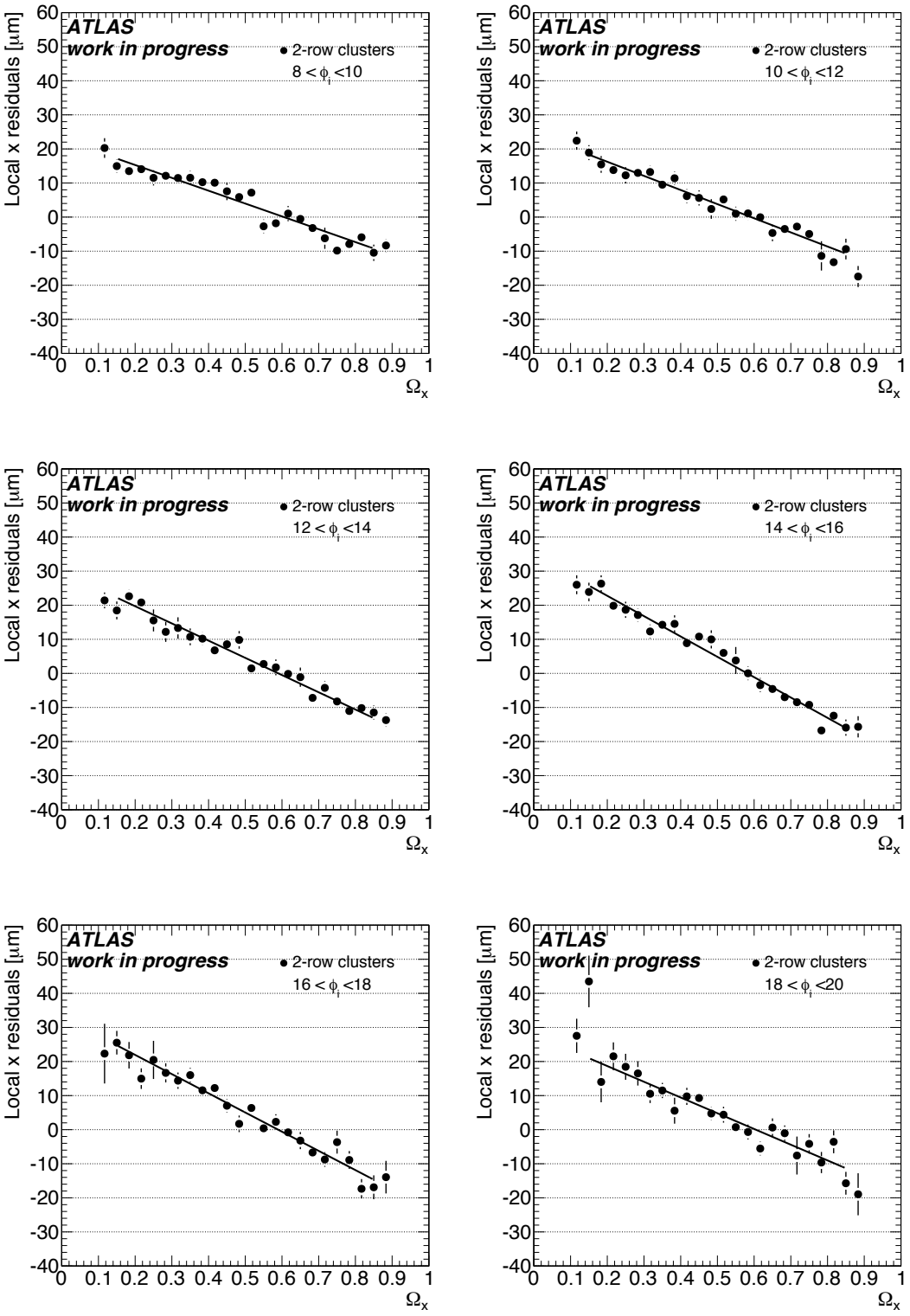

Figure 4.24: The residual between the center of the cluster and its extrapolated position using the associated track is shown as a function of charge sharing for different track incident angles. A clear correlation, corresponding to the value of the Δ parameter, is observed.

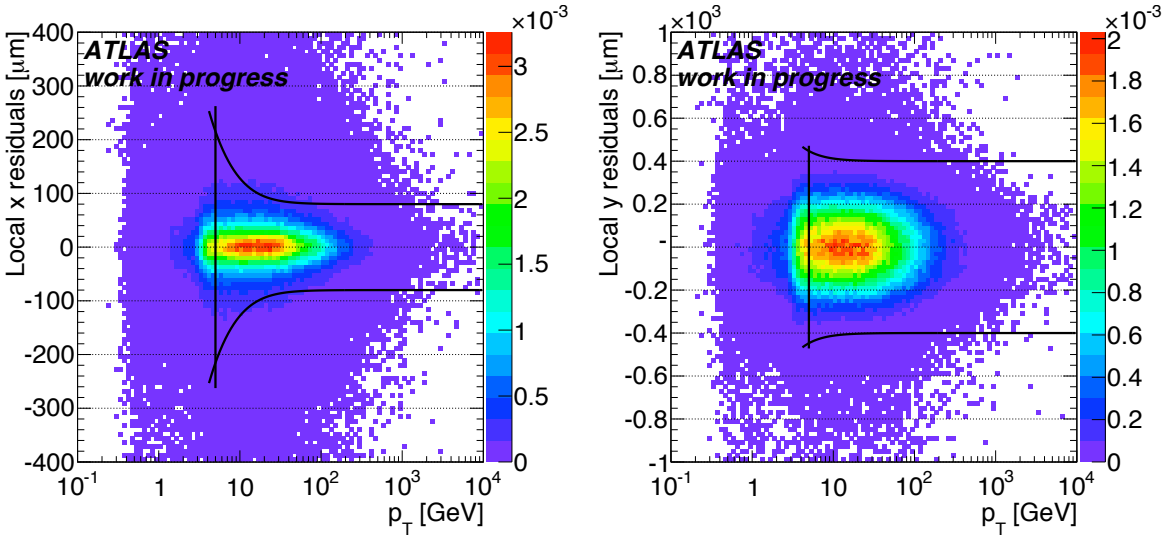

(a) (b)

Figure 4.25: Figures show the cut (solid lines) described in Eqs. 4.29 and 4.30 superimposed on the plots of the fraction of pixel cluster as a function of residuals and transverse momentum of the associated particle. 4.25(a): local x direction. 4.25(b): local y direction.

– for clusters:

$$\left|x_{\text{extr}} - x_{\text{center}}\right| < \frac{1000\,\mu\text{m}}{p_T\,[\text{ GeV}]} \oplus 80\,\mu\text{m} \tag{4.29}$$

$$\left|y_{\text{extr}} - y_{\text{center}}\right| < \frac{1000\,\mu\text{m}}{p_T\,[\text{ GeV}]} \oplus 400\,\mu\text{m} \tag{4.30}$$

The cut on the residuals (Eqs. 4.29 and 4.30) was chosen to be very tight, in order to eliminate all the outliers and to obtain a constant value of the residual resolution as a function of the momentum. A graphical visualization of the cuts is provided by Figure 4.25, that shows the fraction of pixel clusters as a function of the residual (using the center of the cluster) and of the momentum. The cuts described in Eqs. 4.29 and 4.30 are reported as solid lines. It is clearly visible that only the tails, in which a minority of the events is contained, are removed by the cuts. At the end of the cluster selection, 388 171 cluster over an initial number of 605 311 are used. Among these, 119 094 (66 650) are composed of two rows (columns) and 81 656 (1 332) of three rows (columns). Figure 4.26 shows the RMS of residual distribution as a function of the track transverse momentum before and after applying the selection cuts.

The multiplicity distribution of accepted clusters has been already reported in Figure 4.12, as a function of the incident angle of the track associated with the cluster. Only limited statistics are available for $|\eta| > 2$ and for clusters made of three columns. As a result, the correct calculation of constants for higher values of η and for three-column cluster is not possible.

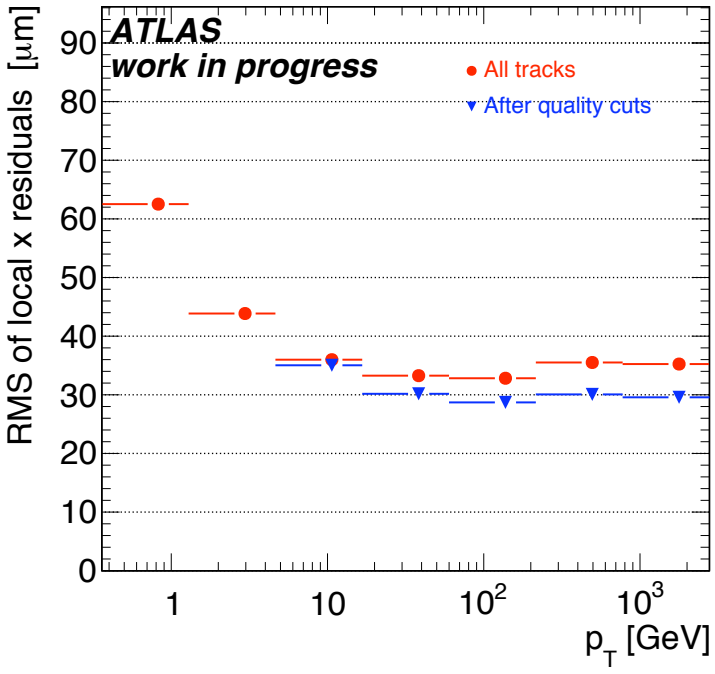

(a)

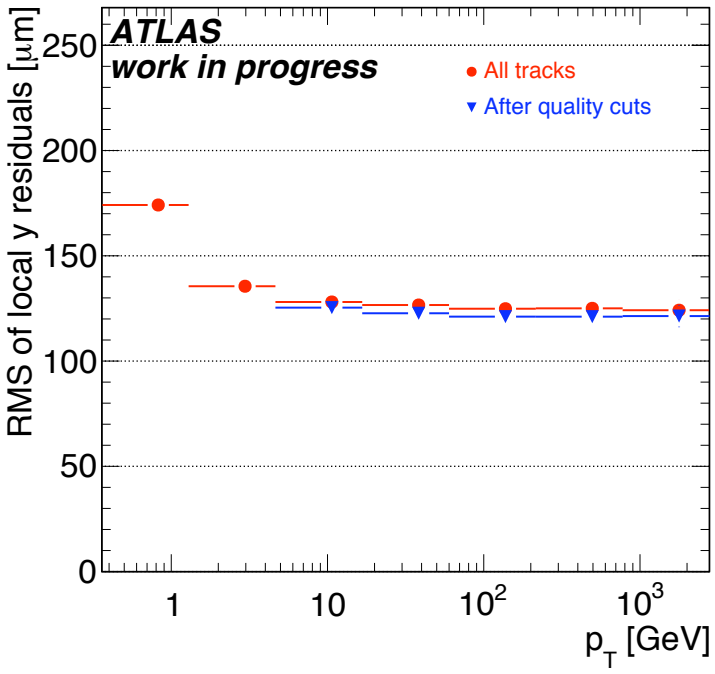

(b)

Figure 4.26: RMS of the distributions of residuals for local x and local y versus the transverse momentum of the associated track, before and after applying the cuts described in Section 4.5.1. In the distribution without cuts the effect of multiple scattering on the resolution is clearly visible for low momentum. 4.26(a): local x direction. 4.26(b): local y direction.

4.5.2 Calibration constants

In order to consider the dependence of Δ on the track incident angle, the clusters were divided into bins of 2° for the calculation of Δ_x in the range $\phi_i \in [-20^\circ, 20^\circ]$. Bins were enlarged to 5° in the interval $|\phi_i| \in [20^\circ, 40^\circ]$ and to 10° in the interval $|\phi_i| \in [40^\circ, 60^\circ]$. The higher granularity in the central range is used in order to enhance the precision in the incident angle range that is typical for particles produced in collisions. A similar operation was performed to calculate Δ_y: in this case the angular bins were 0.5 wide in η units. Furthermore two-row and three-row clusters were studied separately. For each of these bins a histogram similar to the ones reported in Figure 4.24 was filled and fit.

The fit function was a straight line defined for $\Omega \in [0.15, 0.85]$ because the statistics decreased dramatically near the limits of the Ω distribution (Figure 4.10). Only histograms that contained more than 100 entries were used. This requirement allows calculation for constants with two-row and three-row clusters, but only with two-column clusters since the statistics for larger clusters was minimal in the considered range (see Figure 4.12(c)). The result of the fit was only accepted if it was not compatible with zero within twice the associated error, otherwise the corresponding constant was set to zero.

Figure 4.27 shows the resulting constants as a function of the incident angle. Constants extracted from data are drawn in black. They are compared with values obtained from a simulation of cosmic ray events (see Section 3.5). The values are quite similar, even if the simulation features a general overestimation of the constants, with respect to data. The only exception is the interval $\phi_i \in [-6^\circ; 6^\circ]$ in Figure 4.27(a), where simulation also fail when fitting the constant relative to $-2^\circ < \phi_i < 0^\circ$. The most problematic fit are the ones relative to three-row clusters (see Figure 4.27(b)) and to high incident angle. Here the statistics (for the local y direction) or the larger angular bins (for the local x) result in lower accuracy of the fits.

In order to provide calibration constants that can be used for the reconstruction of data, the set displayed using blue markers in Figure 4.27 is calculated. In this case, a symmetric distribution is desired, in order to smooth statistical effects. The value of the constant in each angular bin is thus computed as the mean of the constants relative to the same angle in the positive and in the negative direction. This set of constants is used for resolution studies reported in Section 4.4, while its effect when using real data is described in the following section.

4.6 Validation of the charge sharing calibration

In order to validate the charge sharing algorithm and the calibration constants that were extracted from cosmic ray data (see Section 4.5), a subset of the *Reprocessed Data* (see Section 3.4) has been privately reconstructed. The residuals distributions of these data are studied and compared with the official simulation of cosmic rays in ATLAS (see Section 3.5). Data from simulation will be marked as "MC" in all the plots. The charge sharing constants that were available for simulated data reconstruction are restricted to the range $\phi_i \in [-6^\circ; 14^\circ]$ (see Section 4.7), as a consequence, a meticulous comparison

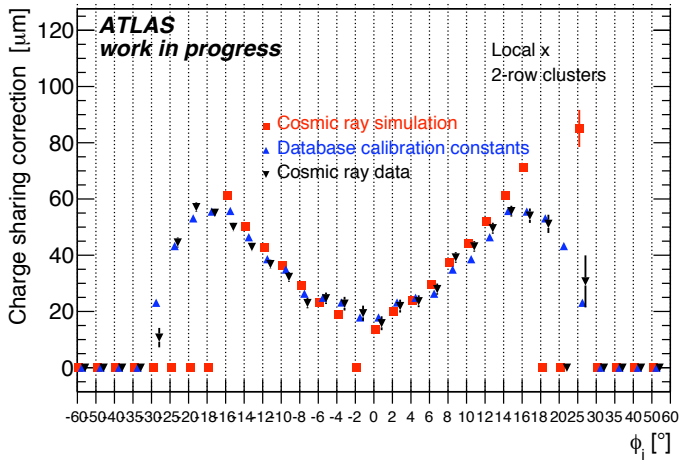

(a)

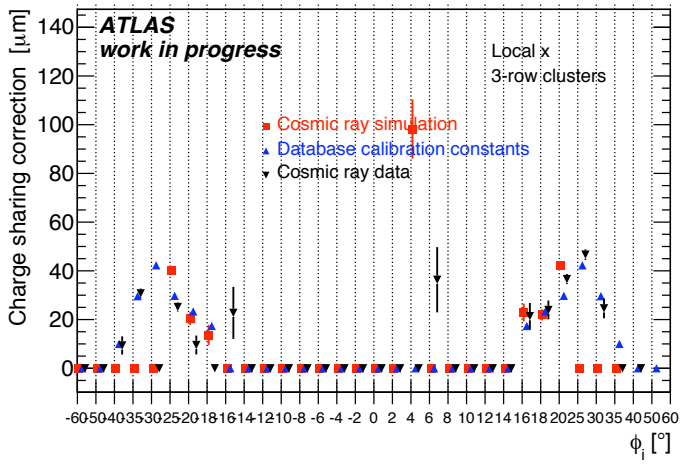

(b)

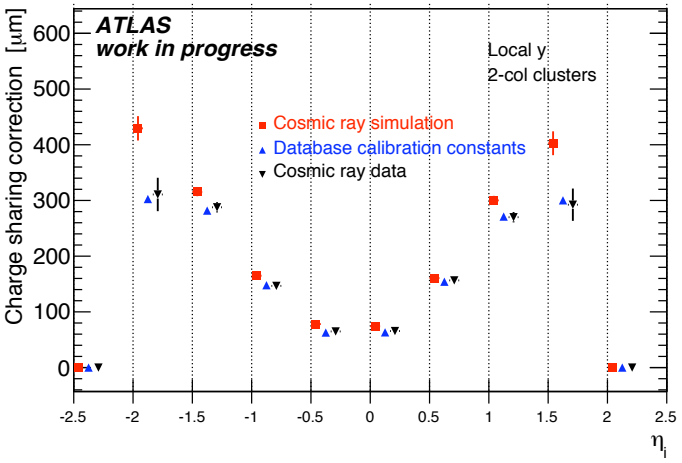

(c)

Figure 4.27: The Δ constants fit from data compared to those fit using simulated events as well as the set that was saved to the database, in order to be used in future data reconstruction. 4.27(a): local x direction, two-row clusters. 4.27(b): local x direction, three-row clusters. 4.27(c): local y direction, two-column clusters.

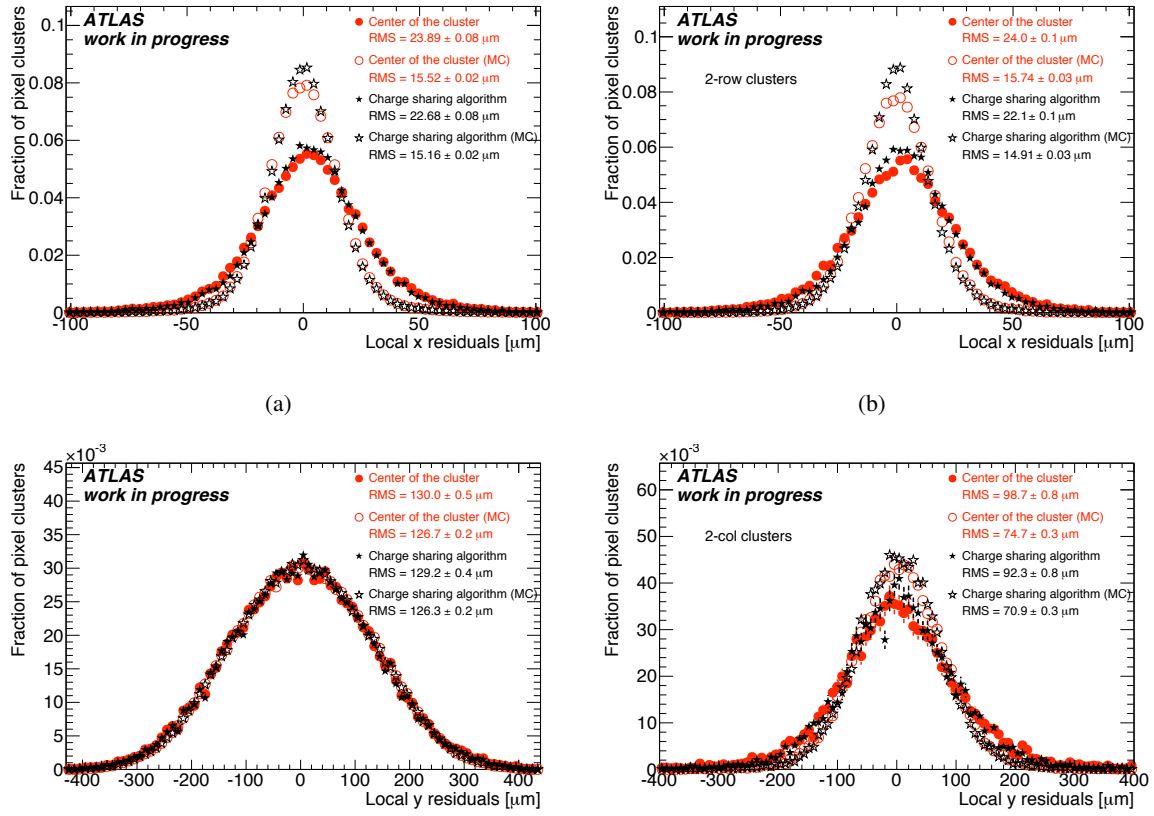

Figure 4.28: Comparison of the residuals in the local x direction and the local y direction using different position algorithms. For both direction the residual width for data is broader than expected for a perfectly aligned detector ("MC"). 4.28(a): local x direction, all clusters. 4.28(b): local x direction, two-row clusters. 4.28(c): local y direction, all clusters. 4.28(d): local y direction, two-column clusters.

between real and simulated events is possible only in this angular range. The main discrepancy between the two sets, anyway, is due to misalignments in the real detector and it is expected to be larger with respect to the charge sharing effect. This consideration leads to study both datasets in a wide incident angle range, regardless the difference in the charge sharing application.

Figure 4.28 shows the global residual distribution obtained when using the charge sharing algorithm and the center of the cluster in order to estimate cluster position. In Figure 4.28(a), the distribution of the residuals along local x is reported for all clusters that are associated with tracks having incident angle $\phi_i \in [-20°; 20°]$. The overall resolution of real data clusters improves from 23.9 μm to 22.7 μm (5%) when using the charge sharing algorithm. In Figure 4.28(b), the distribution of two-row clusters is studied, to evidence clusters to which the charge sharing algorithm is directly applied: in this case the improvement on real data is 8%. The residual distribution was studied for three-row clusters as well, but no visible improvement has been found due to the lower intrinsic resolution of these clusters.

In Figure 4.28(c), the residual distributions for local y direction is shown: in this case the effect of charge sharing is small, since the great majority of clusters is composed of only one column (see Figure 4.12(c)). The effect is evaluated directly on two-column clusters, in Figure 4.28(d): in this case the charge sharing improvement reaches 6% in real data. The minor impact with respect to the two-row case is due to the larger dimensions of the pixels in the local y direction.

Similar to the analysis reported in Section 4.4.2, the resolution dependence on the incident angle is studied on reconstructed data by considering the RMS of the residual distribution. Figure 4.29 shows the distribution for the real data and simulated events. The effect of track extrapolation can be seen by comparing the Monte Carlo distributions with the ones reported in Figure 4.22, while a comparison between simulation and data points out the effect of detector performance and misalignments.

In Figure 4.29(a), the residuals in local x direction are shown as a function of ϕ_i. The improvement due to charge sharing usage is clearly visible in the range $\phi_i \in [-6^\circ; 14^\circ]$ for simulated data. As expected, the larger improvement is seen after 8°, where two-row clusters become the most probable with respect to single row ones. In real data a similar effect is present and, in the negative ϕ_i direction, a noticeable improvement is even more visible. Outside the range $\phi_i \in [-30^\circ; 30^\circ]$ no difference between charge sharing algorithm and center of the cluster is seen.

In Figure 4.29(b), local y direction is studied. In this case, residual distribution is dominated by the available statistics for $|\eta_i| > 1.5$. The effect of charge sharing correction, instead, is important in the range $|\eta_i| \in [0.5; 1.5]$. A clear minimum is visible in simulated data at $|\eta_i| \approx 1.25$, while in real data the best resolution is obtained at $|\eta_i| \approx 1$.

As final plots for this section, the residual distributions of cosmic ray data are reported separately for each cluster size in Figure 4.30. In this figure, local x residuals are shown on top as a function of ϕ_i when using the center of the cluster (Figure 4.30(a)) and the charge sharing algorithm (Figure 4.30(b)). Local y distributions, instead, are shown on the bottom (Figure 4.30(c) contains the center of the cluster distributions and Figure 4.30(d) the charge sharing distributions) as a function of η_i. Also for this picture, a comparison can be made with the resolution distribution (see Figure 4.23). While in the case of Figure 4.23, the resolution of each type of cluster was clearly different for each incident angle, residuals in the x direction appear to be almost identical for each cluster size and only tiny improvements are possible when using the charge sharing algorithm. This is the expected behaviour when resolution is limited by detector alignment, which is independent of cluster size.

4.7 History of charge sharing calibration tags

The charge sharing calibration of the Pixel Detector is a task that is foreseen to be accomplished every week, during data-taking. This should ensure to have calibration constants always up to date, whenever running conditions of the detector can change. Moreover, a continuous comparison of the calibration constants as well as of the residual distributions is an important check of the data quality.

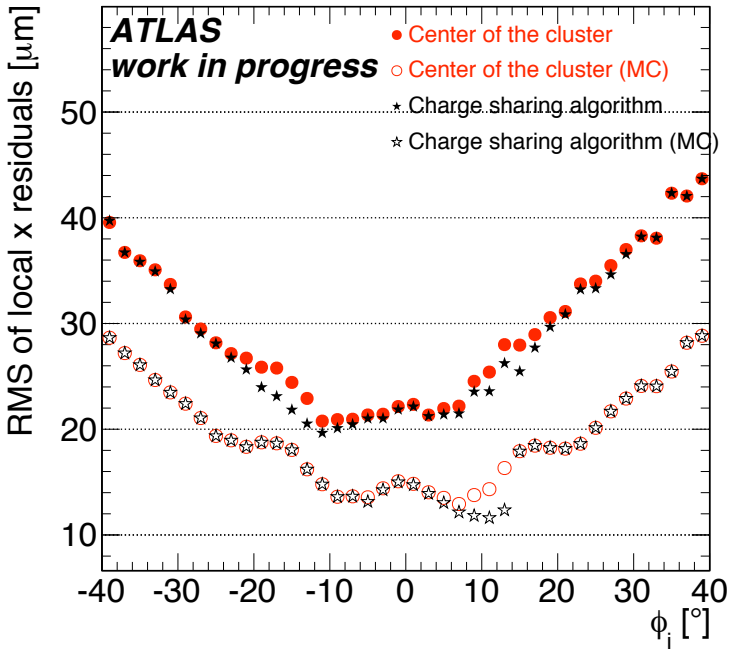

(a)

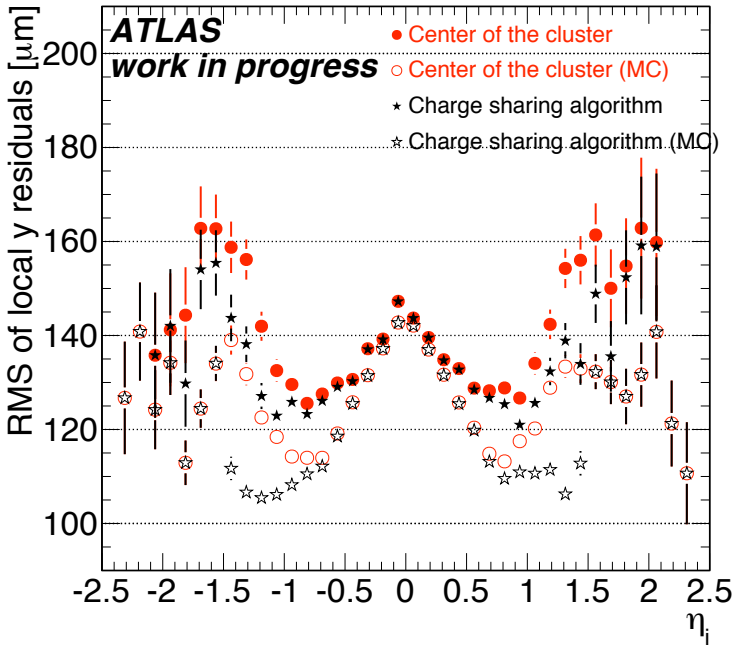

(b)

Figure 4.29: Comparison of the RMS of residuals in the local x direction (4.29(a)) and the local y direction (4.29(b)) for different position algorithms.

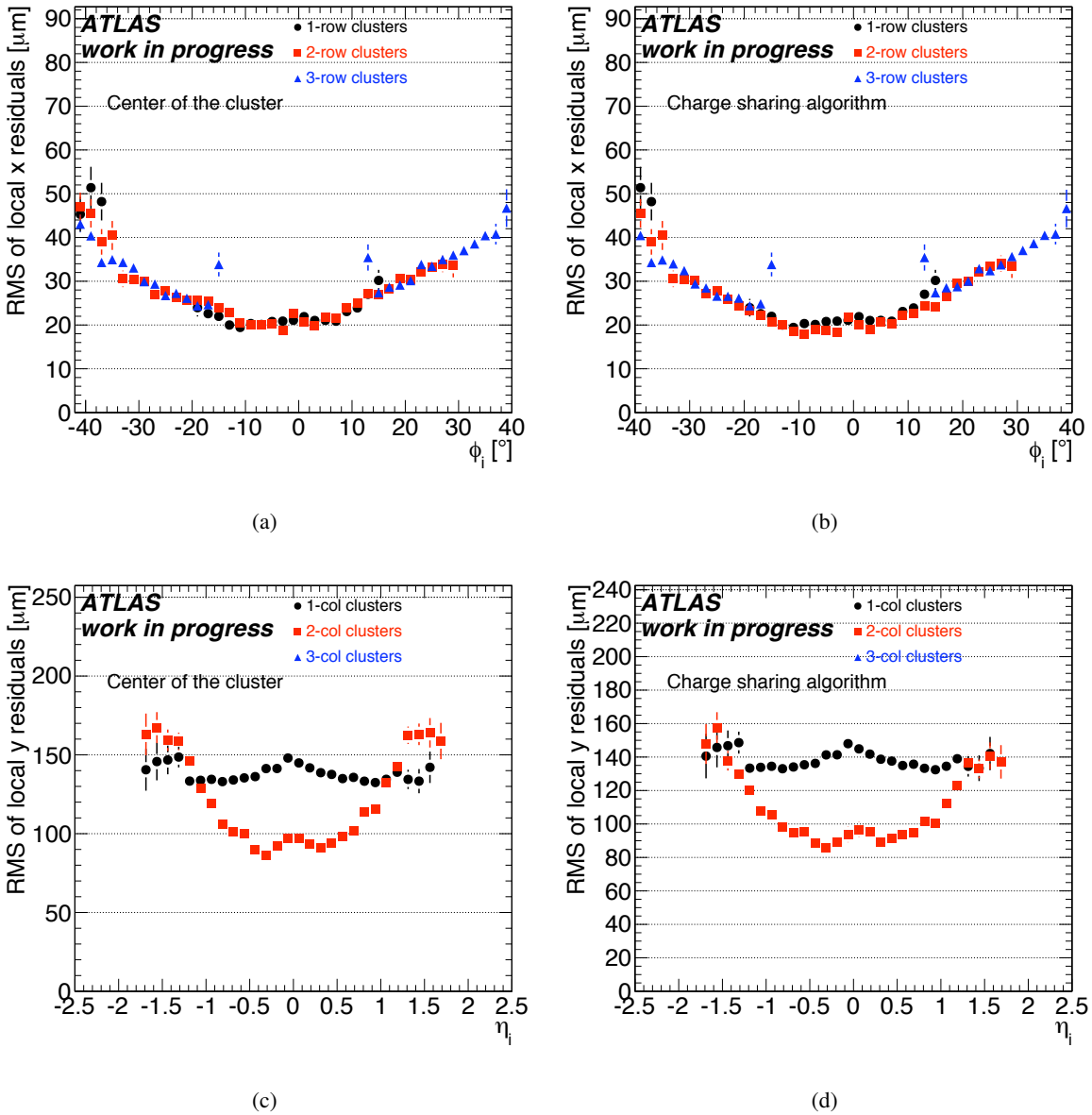

Figure 4.30: Comparison of the RMS of residuals in the local x direction and the local y direction for different cluster sizes and using different position algorithms. 4.30(a): local x direction, center of the cluster. 4.30(b): local x direction, charge sharing algorithm. 4.30(c): local y direction, center of the cluster. 4.30(d): local y direction, charge sharing algorithm.

For these reason, the analysis described in this chapter has been integrated into the ATLAS official software and it is meant to be run automatically by a shifter on a weekly base. During detector commissioning, the procedure was tested after each data reprocessing as well as on simulated data. All results were compared by using the same plots that will be available to the shifter, in order to check their completeness. The plots showed in Section 4.5 and 4.6 have been produced using this tool.

Calibration tag	Dataset used for the fits	Notes
PixelOfflineReco-02	—	Default *before* commissioning. Displayed in Figure 4.31
PixelOfflineReco-COS-01	Initial data, before official reconstruction	Missing local x constants.
PixelOfflineReco-COS-02	Initial data	Used for MC data reconstruction. Displayed in Figure 4.31.
PixelOfflineReco-Extended-COS-01	Reprocessed data	Described in Section 4.5. Displayed in Figure 4.27 and 4.31.

Table 4.1: Calibration tags used during commissioning for the charge sharing algorithm. The names of the datasets used for the fit of the calibration constants are defined in Table 3.3.

Due to the limited track rate during cosmic ray data tacking (about 0.5 Hz for the Pixel Detector), the procedure has been executed several times on the full track sample. In order to illustrate the evolution of the calibration procedure, a timeline of the production is presented here. Table 4.1 reports the list of the calibration sets that were used during Pixel Detector commissioning with cosmic ray data and stored in the ATLAS conditions database (Section 1.4.1), in order to be retrieved during data analysis. Figure 4.31, instead shows the comparison among some of these sets.

The `PixelOfflineReco-02` constants were available at the beginning of commissioning activity, as the result of a previous study based on test-beam data and simulated collision events. These constants were used for the first reconstruction of cosmic ray data, in October 2008.

As soon as data were available, anyway, the effort to obtain new charge calibration constants was begun. The first result was the `PixelOfflineReco-COS-01` tag. It was obtained even before than the first official reconstruction of data. Since alignment of the detector was still very preliminary, as well as the charge sharing analysis itself, it was not possible to fit constants for the local x direction.

When initial alignment was available, the `PixelOfflineReco-COS-02` tag was built. It is limited to the range $\phi_i \in [-6°; 14°]$ and features no constants for three-row clusters. It shows asymmetric distribution with respect to $\phi_i = 0°$ in local x direction (see Figure 4.31(a)). The distribution of local y constants (Figure 4.31(c)), instead, is symmetric around η_i. In this case, `PixelOfflineReco-02` shows large discrepancies with respect to `PixelOfflineReco-COS-02`. The impact of these two sets of constants was checked by using validation plots and `PixelOfflineReco-02` was found to systematically worse resolution in local y direction, with respect to the center of the cluster position. For these reasons, `PixelOfflineReco-COS-02` was considered better than the default `PixelOfflineReco-02`, and it was used for the reconstruction of reprocessed data and simulated cosmic ray events.

After the reprocessing of data, studies continued in order to extract charge sharing constants that could be applied over the full range of track incident angle, as well as to three-row clusters. The resulting tag, named `PixelOfflineReco-Extended-COS-01`, has been used for the resolution studies

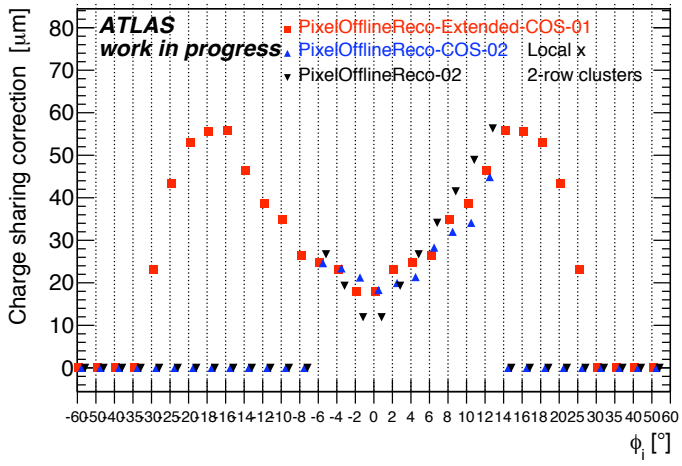

(a)

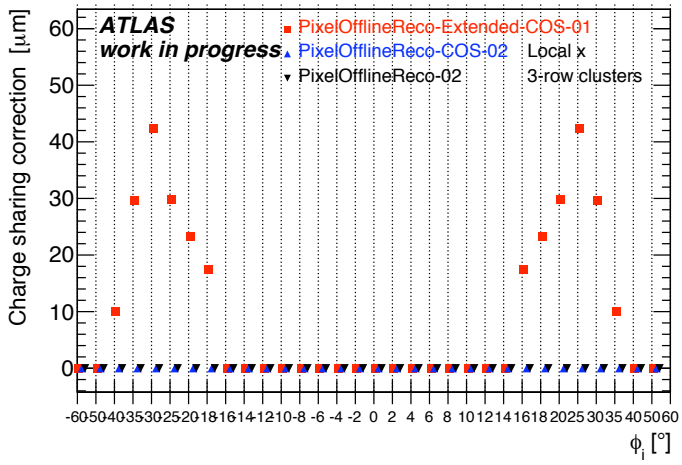

(b)

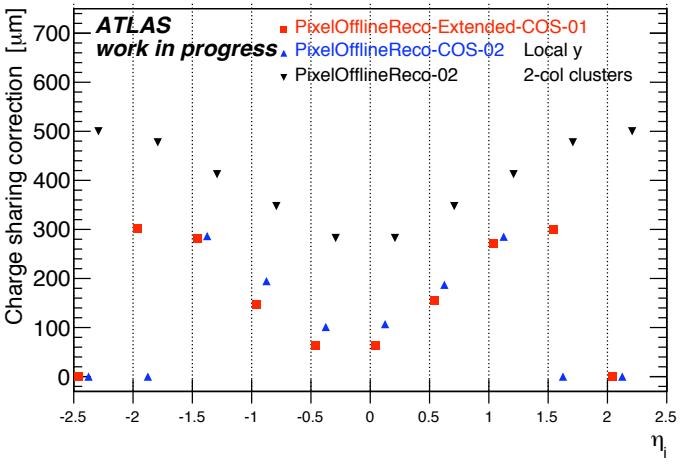

(c)

Figure 4.31: The Δ constants at different stages of the commissioning activity, identified by their tag in the conditions database. 4.31(a): local *x* direction, two-row clusters. 4.31(b): local *x* direction, three-row clusters. 4.31(c): local *y* direction, two-column clusters.

in this chapter. These constants are similar to the `PixelOfflineReco-COS-02` in the range where both are defined. At the same time, they recover the local x symmetry around $\phi_i = 0°$. This tag will be the initial default to be used with collision data, starting from the beginning of 2010.

4.8 Conclusion

In this chapter the resolution of the ATLAS Pixel Detector has been studied using autumn 2008 cosmic ray datasets.

In particular, the charge sharing algorithm for cluster position calculation has been analyzed. This algorithm implements a correction of the cluster position that improves resolution with respect to the position evaluated as the center of the cluster. The correction for the local x (y) position is based on the ratio between the charge collected in one of the external rows (columns) of the cluster and the total charge collected in both external rows (columns). The weight of the correction is dependent upon cluster size and track incident angle. In order to have optimal results, the weight should be calibrated by using detector measurements.

During commissioning activity, a procedure to tune the charge sharing algorithm by computing sets calibration constants has been developed and implemented in the official ATLAS reconstruction software. In the future, charge sharing calibration will be applied on a weekly base during the ATLAS data-taking, in order to ensure the optimal precision for the Pixel Detector measurements, even if running conditions change.

From the analysis of cosmic ray data, different sets of calibration constants have been extracted. Their effect on data have been studied, and their effectiveness have been improved, until a satisfactory calibration set has been computed. The calibration constants that will be used as default for first collision data cover a large incident angle range ($\phi_i \in [-60°; 60°]$, $\eta_i \in [-2; 2]$) and can be applied to two-row, three-row and two-column clusters. The improvement seen in the resolution when using the charge sharing algorithm with these constants can be more than 50% in local x direction and up to 25% in local y, depending on the incident angle.

The effect of charge sharing algorithm has been evaluated on cosmic ray data, by studying the RMS of residual distributions. In this case the improvement is less pronounced with respect to the one on intrinsic resolution, due to the higher contribution of the extrapolation error and of the alignment. When considering two-row (two-column) clusters the improvement is 8% in local x and 6% in local y.

Chapter 5

Commissioning the tracking system

The ATLAS Inner Detector tracking system is devoted to the identification of the tracks associated to particles emerging from the interaction point during collisions. The hardware devices that constitute the Inner Detector (i.e. Pixel Detector, SCT and TRT) have been described in Chapter 2. This chapter, instead, discusses the performances of the tracking system. These are compared when using different track fitting strategies and different stages of the alignment of the detector. The best performance that can be achieved at the present time is reported, as well as the description of some systematic errors that still affect the measurements. Finally, strategies to improve some of the results are presented. The main data source for the analysis are the cosmic ray data that were recorded during October 2008 (see Chapter 3).

Section 5.1 introduces the ATLAS approach to the reconstruction and the description of tracks. The reference system and the parameters used to represent tracks are introduced, as well as common concept like residuals, extrapolation and track fitting. In Section 5.2 the two algorithms used by ATLAS for track fitting are described in their general structure. Section 5.3 discusses the performance of the Inner Detector in the identification of the measurements that refer to each track. The method used in this study to estimate the resolution on track parameters is presented in Section 5.4, together with a discussion on the selection applied to identify good quality tracks. The performance of the two approaches to track fitting are reported in Section 5.5. In the same section, the measurements of the resolution in the impact parameter and in the momentum are shown. The description of the motion of a particle inside detector material is analyzed in Section 5.6, where the impact of multiple scattering on resolution is studied. Section 5.7 discusses the resolution as a function of the pseudorapidity. The final part of the chapter (Section 5.8) illustrates problems that can degrade the performance of the tracking system, the main issues being a good knowledge of the alignment of the detector elements. As a conclusion the resolution obtained in the impact parameter at the end of the commissioning phase of the Inner Detector is presented and compared with the required precision.

5.1 Tracking procedures

When a particle traverses a tracking device, the detector identifies the position where it is crossed. In the ATLAS environment, at the luminosity of 10^{34} cm^{-2}s^{-1}, approximately 1000 particles will emerge from the collision point during each event [120]. Each of them will generate a path of measurements trough the sub-detectors. The tracking system must be able to resolve the tracks associated to each particle and to describe it with a well defined set of parameters. Since the input of the software devoted to this task is a simple collection containing all the measurements, two conceptually separated steps are accomplished in sequence:

- the *pattern recognition* identifies the groups of measurements relative to the same particle, giving an initial estimate of its trajectory;
- the *track fitting* describes the trajectories with the best possible precision, taking into account details as e.g the different resolution of the sub-detectors, the interaction with different material layers, the variations of the magnetic field.

Many different approaches exists to each of the two problems and the ATLAS collaboration explored many of them. At present time two main routines are used to analyze cosmic ray data: the `CTBTracking` and the `NewTracking`. Both the approaches use common definitions to represent the input and the output data. These definitions are described in the ATLAS Event Data Model [121, 122]. In this section, common issues worked out by tracking procedures are presented. A more detailed description of the tracking software implementation used by ATLAS is instead reported in Section 5.2.

5.1.1 Track parameters

During tracking procedures, many local coordinate systems are considered, as well as the global one presented in Section 1.3.1. A typical issue is to identify a set of parameters that can describe a track in all these different systems. Furthermore, tracking devices are immersed in magnetic fields, in order to be able to measure the momentum of particles. A track can be parametrized with respect to a surface in many different ways, but it is convenient to choose some general set of parameters which have a physical interpretation when considering motion in a magnetic field and which can be consistently used when extrapolating particles to measurement surfaces and to the interaction region.

Motion of charged particles in a magnetic field

A charged particle that moves in a magnetic field is always subjected to a *Lorentz force*:

$$\frac{\mathrm{d}\vec{p}}{\mathrm{d}t} = q\vec{v} \times \vec{B} \tag{5.1}$$

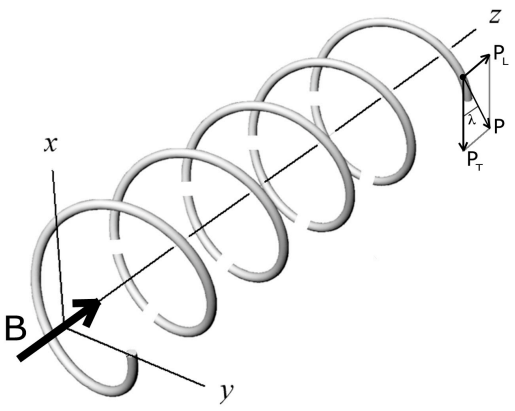

Figure 5.1: Trajectory of a particle in a uniform magnetic field.

that is perpendicular to the velocity $\vec{v}$ of the particle and to the magnetic field $\vec{B}$ itself. The force acts as a bending on the trajectory $\vec{r}$ of the particle:

$$\frac{\mathrm{d}^2\vec{r}}{\mathrm{d}s^2} = \frac{q}{p}\frac{\mathrm{d}\vec{r}}{\mathrm{d}s} \times \vec{B}, \tag{5.2}$$

where the trajectory length s has been used in place of time to describe the evolution of the system. The bending is clearly perpendicular to the magnetic field.

The ATLAS Inner Detector is immersed in a solenoidal magnetic field (see Section 1.3.2). In a first approximation, this field can be described as a uniform field directed along the z-axis. In this case, the Lorentz force acts only in the transverse plane. Since it does not produce any work, the transverse component of the momentum (p_{T}) is a constant of motion. If the curvature radius is called ρ, it can be concluded that:

$$p_{\mathrm{T}} = cB\rho \rightarrow p_{\mathrm{T}}[\,\mathrm{GeV}] = 0.3B[\mathrm{T}]\rho[\mathrm{m}] \tag{5.3}$$

introducing an error of less than 1‰ on the light speed.

The motion of the particle can thus be described by an helix. Figure 5.1 shows the trajectory, with the variables used to describe it, while the following equation describe an helix analytically:

$$\begin{cases} x(s) = x_0 + \rho\left[\cos\left(\Psi_0 + \frac{qs\cos\lambda}{\rho}\right) - \cos\Psi_0\right] \\ y(s) = y_0 + \rho\left[\sin\left(\Psi_0 + \frac{qs\cos\lambda}{\rho}\right) - \sin\Psi_0\right] \\ z(s) = z_0 + s\sin\lambda \end{cases} \tag{5.4}$$

Here the rotation direction is expressed by the charge of the particle q, while the λ angle is defined such that $p_{\mathrm{T}} = p\cos\lambda$. The x_0, y_0 and z_0 variables describe the starting position for the trajectory,

while Ψ_0 is the azimuthal position of the starting point (x_0, y_0) with respect to the center of rotation $(x_c, y_c) = (x_0 - \frac{p_T}{0.3B}\cos\Psi_0, y_0 - \frac{p_T}{0.3B}\sin\Psi_0)$.

When projecting the motion in the x-y plane, it is described by a circumference:

$$\left(x - x_0 + \frac{p_T}{0.3B}\cos\Psi_0\right)^2 + \left(y - y_0 + \frac{p_T}{0.3B}\sin\Psi_0\right)^2 = \left(\frac{p_T}{0.3B}\right)^2, \tag{5.5}$$

while on the z-y (as well as z-x) plane it has a sinusoidal behaviour:

$$y(z) = y_0 + \frac{p_T}{0.3B}\left[\sin\left(\Psi_0 + \frac{0.3B\,q\,(z - z_0)}{p_T}\frac{}{\tan\lambda}\right) - \sin\Psi_0\right]. \tag{5.6}$$

This expression can be approximated with a straight line when $p_T \tan\lambda \gg 0.3\,qB\,(z - z_0)$, which is equivalent to have $\rho \gg \frac{z - z_0}{\tan\lambda}$:

$$\begin{cases} x(z) \approx x_0 - \frac{q}{\tan\lambda}(z - z_0)\sin\Psi_0, \\ y(z) \approx y_0 + \frac{q}{\tan\lambda}(z - z_0)\cos\Psi_0. \end{cases} \tag{5.7}$$

In the case of uniform magnetic field, directed along the z-axis, the motion of a particle can thus be described using five variables. If the starting point (x_0, y_0) is chosen to be the closest point of the trajectory to the z-axis, the standard variables are:

$$\mathbf{T}_{\text{helix}} = (d_0, z_0, \phi_0, \cot\theta, q/p_T)^T, \tag{5.8}$$

where $d_0 = \sqrt{x_0^2 + y_0^2}$, $\phi_0 = \arctan(y_0/x_0) \equiv \Psi_0$ and $\cot\theta \equiv \tan\lambda$ have been defined.

ATLAS convention

When a reference system is chosen for ATLAS, a key point is that ATLAS features two different tracking devices: the Inner Detector and the Muon Spectrometer. Since their magnetic field setups are somewhat perpendicular (see Section 1.3.2), a helical parameterization bound to the Inner Detector solenoidal field would leave the Muon Spectrometer with an almost meaningless choice of parameters. For this reason, the parameterization chosen is closely bound to the constants of motion of both devices, using θ in place of $\cot\theta$ and q/p in place of q/p_T. The ATLAS parameter choice is thus:

$$\mathbf{T} = (l_1, l_2, \phi, \theta, q/p)^T \tag{5.9}$$

where l_1 and l_2 denote the local coordinate on a given surface, ϕ and θ are the azimuthal and polar angle of the track direction, respectively, and q/p is the inverse momentum multiplied by the charge of the particle q.

The local coordinates l_1 and l_2 in Eq. 5.9 can be adapted to describe the status of a track in proximity of different detector surfaces. An example can be the *local x* and *local y* coordinates defined in Section 2.1.1, when describing tracks and clusters on a Pixel Detector module.

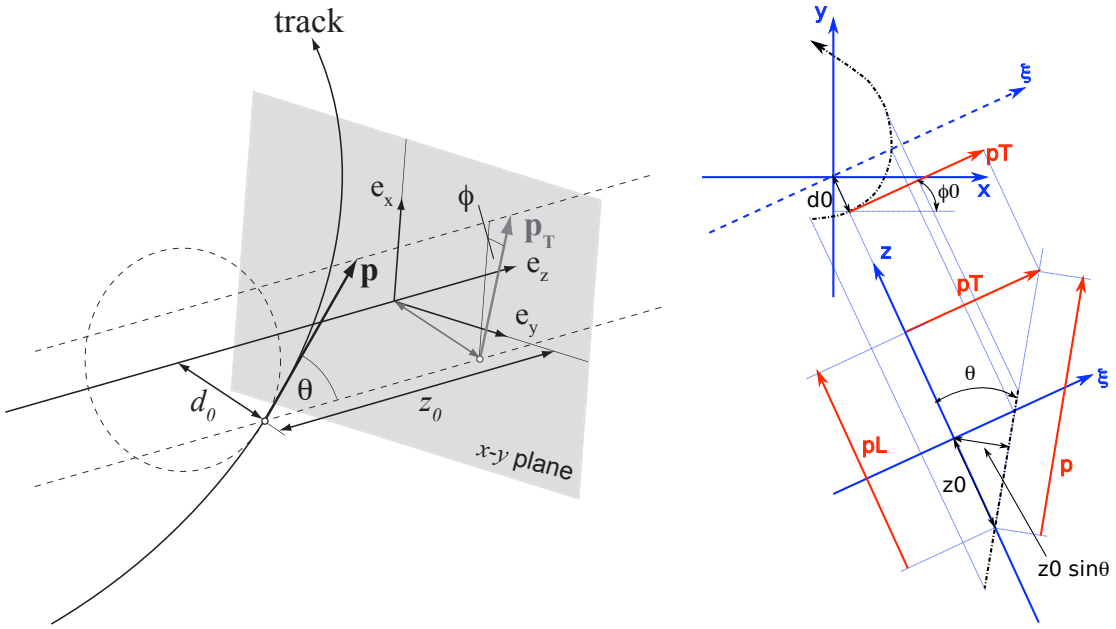

Figure 5.2: Representation of the track parameters at the perigee, according to ATLAS conventions.

The most significant case is defined by the state of the track in the interaction region, where the d_0, z_0 and ϕ_0 coordinates were defined for the helix approximation. In this case the closest approach to the beam axis (the *perigee*) is taken as a reference. In the perigee representation, the parameterization in Eq. 5.9 becomes:

$$\mathbf{T} = (d_0, z_0, \phi_0, \theta, q/p)^{\mathrm{T}}. \tag{5.10}$$

The d_0 and z_0 parameters are calculated as the local coordinate of the perigee in the R-z plane defined by the perigee itself and by the beam axis. The d_0 parameter results to be a signed quantity, defined to be positive when the direction of the track is clockwise in the x-y plane. Figure 5.2 shows a sketch illustrating the perigee representation using ATLAS conventions. The perigee parameterization will be used trough this chapter to describe the performance of the system.

Other common parameters that will be used are the pseudorapidity $\eta = -\log[\tan(\theta/2)]$ and $z_0 \sin\theta$. Using the latter, the pair d_0 and $z_0 \sin\theta$ corresponds to the distances of the track from the origin, projected respectively in the x-y plane and in the plane defined by the z-axis and by the momentum of the particle (ξ-z plane in Figure 5.2). They will be referred to as transverse and longitudinal impact parameter in the following.

5.1.2 Resolution in impact parameter and momentum

The variables that have the most important role in physics analysis are the momentum of particles, and their impact parameter. The momentum of particle is necessary in order to reconstruct invariant masses

of resonances and may allow to improve the calorimeter estimation of jet energy. The measurement of the impact parameter allows to discriminate particles that have an appreciable lifetime from particles that are instantly decaying in the primary interaction point. This section analyzes the different contributions to the uncertainty on these variables.

While track fitting is performed with sophisticated procedures (see Section 5.1.6) in order to take into account the inhomogeneity of the magnetic field and the contribution of detector material, most features can be qualitatively understood with simplified models. In this section, it will be assumed that the magnetic field is constant and uniformly parallel to the beam axis (z-axis). This allows to study the trajectory of particles in the transverse plane (x-y plane) and in the longitudinal one (z-R plane) independently [123].

Straight line fit in the z-R plane

The tracking system can be described by a set $i = 1 \dots N$ of detector surfaces (see Figure 5.3). In the barrel geometry, each surface measures a coordinate z_i on the particle path at a distance R_i from the beam axis, with resolution σ_i. The best straight line approximation can be found minimizing the χ^2:

$$\chi^2 = \sum_{i=1}^{N} \frac{(z_i - z_0 - R_i \cot\theta)^2}{\sigma_i^2}. \tag{5.11}$$

This problem can be solved using a matrix formalism. In the case of uncorrelated measurements and uncertainty equal to σ for each detector surface, the errors associated to the parameters z_0 and $\tan\theta$ can be computed as:

$$\sigma^2_{\tan\theta} = \frac{12N}{(N+2)(N+1)} \frac{\sigma^2}{R_N^2} \tag{5.12}$$

$$\sigma^2_{z_0} = \frac{1}{N+1}\sigma^2 + R_c^2 \sigma^2_{\tan\theta} \tag{5.13}$$

if R_c has been defined as $(R_N - R_0)/2$. It can be noticed that the uncertainties are highly correlated, due to the term $R_c \sigma_{\tan\theta}$ in Eq. 5.13.

Given the geometry of the system, z_0 is the longitudinal impact parameter, while $\cot\theta$ is the cotangent of the polar angle of the momentum direction. Similar arguments can be applied in the transverse plane, in order to find relations that apply to d_0. Some consideration can be made by looking at Eqs. 5.13 and 5.12.

- The uncertainty on the impact parameter is determined both by the distance of the "center of the detector" R_c and by the distance of the last layer from the perigee (lever arm). To take advantage of both aspects, modern tracking systems use a *vertex detector*, coupled with less precise detectors placed at a longer distance from the interaction point. An example of vertex detector can be the ATLAS Pixel Detector: it features a precision of 10 μm and it is placed close to the interaction point. The external part of the tracking system in ATLAS is constituted by the TRT, that have less precision (130 μm), but ensures a long lever arm. The center of the detector R_c can be thought

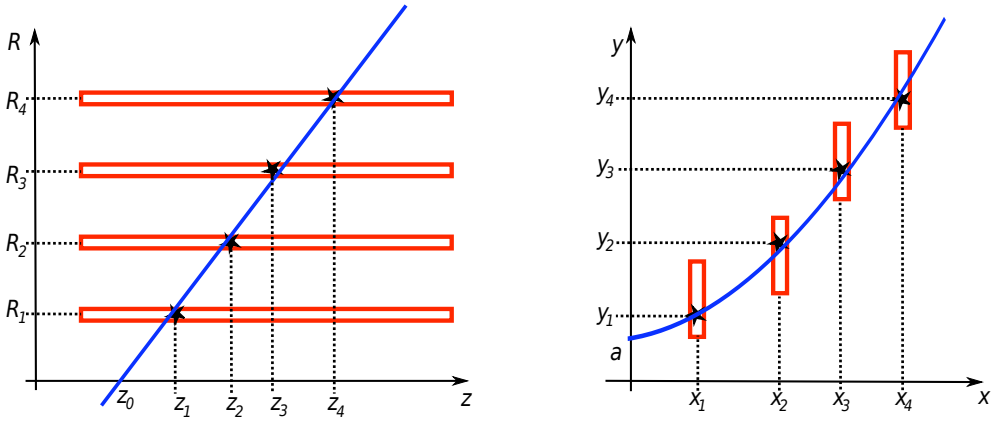

Figure 5.3: The linear and the parabolic fit.

as the weighted sum of the distances relative to the vertex detector and to the external device, resulting in a point closer to the vertex detector.

– The error on the impact parameter depends on the resolution of the vertex detector σ. The Pixel Detector device has been included in the ATLAS tracking system to ensure very high resolution. Furthermore, a realistic description of the uncertainty associated to measurements, during tracking procedures, is essential to benefit of the high resolution given by the vertex tracker. In this thesis a method to optimize Pixel Detector resolution is presented in Chapter 4.

– The number of detector surfaces N has a lower contribution in the impact parameter resolution. In addition, adding detector layers can be very expensive and increases the material traversed by particles. Since the presence of material can degrade resolution (see Section 5.1.3), increasing the number of detector layers is not the optimal solution to improve tracking performance.

Quadratic fit in the x-y plane

When considering the trajectory of the particle in the x-y plane, a similar procedure can be followed. For momentum larger that few GeV, the curvature radius ρ is much bigger that the dimension of the detector, allowing to approximate the trajectory with a parabola (see Figure 5.3):

$$y = y_c + \sqrt{\rho^2 - (x - x_c)^2} \approx y_c + \rho - \frac{x_c}{2\rho^2} + \frac{x_c}{\rho}x - \frac{1}{2\rho}x^2 \tag{5.14}$$

The procedure is then very similar to the linear problem. In this case, the χ^2 to be minimized is

$$\chi^2 = \sum_{i=1}^{N} \frac{(y_i - a - bx_i - cx_i)^2}{\sigma_i^2}, \tag{5.15}$$

when a, b and c are defined as:

$$\begin{aligned} a = &\quad y(0) &&= y_c + \rho - \tfrac{x_c}{2\rho^2} \\ b = &\quad \tfrac{\mathrm{d}y}{\mathrm{d}x}\big|_{x=0} &&= \tfrac{x_0}{\rho} \\ c = &\quad \tfrac{\mathrm{d}^2y}{\mathrm{d}x^2}\big|_{x=0} &&= -\tfrac{1}{2\rho}. \end{aligned} \tag{5.16}$$

After solving the fit by minimizing the χ^2 equation, the resulting uncertainties on the fit parameters are:

$$\begin{aligned} \sigma_a^2 = &\quad \sigma^2 \tfrac{3(3N^2+6N-4)}{(N-1)(N+1)(N+3)} \\ \sigma_b^2 = &\quad \tfrac{\sigma^2}{x_N^2} \tfrac{12N}{(N+1)(N+2)} \\ \sigma_c^2 = &\quad \tfrac{\sigma^2}{x_N^4} \tfrac{180N^3}{(N-1)(N+1)(N+2)(N+3)}. \end{aligned} \tag{5.17}$$

The a parameter can be identified as the impact parameter: in this approximation, its precision depends only on the resolution of the vertex detector. According to Eq. 5.16, the c parameter is instead related to the curvature radius of the trajectory and its uncertainty is equal to the one associated to the transverse momentum of the particle (see Eq. 5.3). The relative uncertainty on the transverse momentum can thus be expressed as:

$$\frac{\delta p_{\mathrm{T}}}{p_{\mathrm{T}}} = \frac{\sqrt{4C_N}}{0.3B} \frac{\sigma}{L^2} p_{\mathrm{T}}, \tag{5.18}$$

if $C_N = \frac{180N^3}{(N-1)(N+1)(N+2)(N+3)}$. Eq. 5.18 points out the strong dependence of the momentum resolution from the square of the lever arm $L \equiv (x_N - x_1)$. In addition, it shows that the relative resolution is worsening when the transverse momentum increases. One last aspect that arise from the computation of the uncertainty of the parabolic fit parameters is the correlation between the a parameter and the c parameter (i.e. the correlation between momentum and impact parameter resolution). In fact their covariance can be expressed as:

$$\sigma_{ac} = -\frac{15N^2}{(N-1)(N+1)(N+3)} \frac{\sigma}{L^2}. \tag{5.19}$$

5.1.3 Multiple scattering effect on resolution

The resolution that can be obtained on track parameters is greatly influenced by the quantity of material crossed by the particles. The main effects of material on particle motion are energy loss and directional scattering. The energy loss has been described in Section 4.1 for particles traversing silicon detectors. Its effect on the particle momentum can be neglected if considering thin detector layers, which is a good approximation for the Inner Detector material distribution.

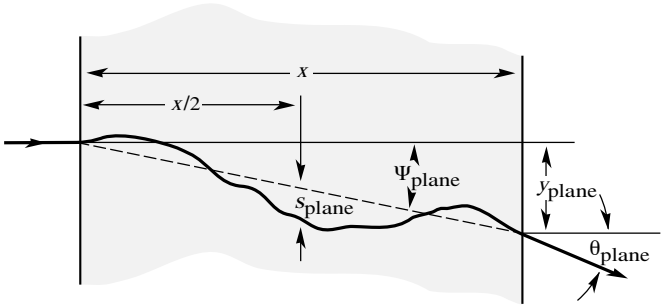

Figure 5.4: Quantities used to describe the multiple scattering effect. Figure taken from [96].

The multiple scattering effect arises because a particle that traverses detector material undergoes successive small angle deflections, caused by (mainly Coulomb) scattering on nuclei. An introduction to the multiple scattering effect can be found in [96] and in articles referenced there, while Figure 5.4 shows the main variables that should be considered to describe multiple scattering in a plane. The integration of all the interactions inside the material results in a final deflection θ_{plane} and in a displacement y_{plane} with $\langle y^2_{\text{plane}} \rangle \approx 1/3\, x^2 \langle \theta^2_{\text{plane}} \rangle$. The displacement can thus be neglected if the material layer is thin, as in the Inner Detector devices. The deflection θ_{plane}, instead, is Gaussian distributed and symmetrically centered around zero. However, large angle single scattering processes disturb the purely Gaussian probability density function and add some non-Gaussian tails (i.e. $\propto \sin^{-4}(\theta_{\text{plane}}/2)$).

The variance of the deflection θ_{plane} can be computed using the Highland formula [124], which derived from Molière's solution of the transport equation [125]:

$$\langle \theta^2_{\text{plane}} \rangle = \left(\frac{0.0136 \text{ GeV}}{\beta c} \frac{q}{p} \right)^2 \frac{x}{X_0} \left[1 + 0.038 \log \left(\frac{x}{X_0} \right) \right]^2 . \tag{5.20}$$

In this expression, the path x of the particle in the material enters in terms of radiation lengths X_0, while q/p represent the charge over momentum tracking variable. The logarithmic correction term is adopted for the slightly underestimated screening of the nucleus Coulomb potential in materials with lower Z.

The expression reported in Eq. 5.20 is used during reconstruction to evaluate multiple scattering contribution to the particle trajectory. In the ATLAS track parameterisation, the path length inside material can be expressed by using the thickness of each detector layer d_i:

$$x = \frac{d_i}{\sin \theta^{\text{loc}}} \approx \frac{d_i}{\sin \theta}, \tag{5.21}$$

where the azimuthal angle at the given detector surface θ^{loc} has been approximated by the global azimuthal angle θ.

The final effect of multiple scattering on the polar angle θ can thus be described by adding to its uncertainty a term computed from Eq. 5.20:

$$\delta\theta = \sqrt{\left\langle \theta^2_{\text{plane}} \right\rangle} = \frac{q}{p\sqrt{\sin\theta}} \frac{0.0136\ \text{GeV}}{\beta c} \sum_{i=1}^{n_{\text{layers}}} \sqrt{\frac{d_i}{X_{0i}}} = \frac{\sigma_{\theta\text{MS}}}{p\sqrt{\sin\theta}} \tag{5.22}$$

where the logarithmic term has been neglected. Similarly, the contribution to ϕ uncertainty can be computed. Since the azimuthal angle is projected in the transverse plane, one more correction term of $1/\sin\theta$ has to be applied in order to account for the out of plane projection:

$$\delta\phi = \frac{1}{\sin\theta}\sqrt{\left\langle \theta^2_{\text{plane}} \right\rangle} = \frac{\sigma_{\theta\text{MS}}}{p_{\text{T}}\sqrt{\sin\theta}}. \tag{5.23}$$

These multiple scattering contribution are managed by the fitting algorithms as described in Section 5.1.6. Their impact on remaining track parameters can be explicitly calculated. The contribution to momentum resolution, for example, is [126]:

$$\frac{\delta p}{p} = \frac{1}{0.3B} \frac{0.0136}{\beta} \sqrt{\frac{xC_N}{X_0 L}}. \tag{5.24}$$

If this equation is compared with Eq. 5.18, it can be noticed that, when multiple scattering dominates propagation, the relative resolution is independent on momentum and on detector resolution. Also the lever arm effect is reduced to a $1/\sqrt{L}$ dependence. As in the previous cases, the $\sin\theta$ dependence can be shown explicitly:

$$\frac{\delta p}{p} = \frac{\sigma_{p\text{MS}}}{\sqrt{\sin\theta}} \tag{5.25}$$

The impact parameter is affected by a contribution that can be written as [127]:

$$(\delta d_0)^2 = \sum_{i=1}^{n_{\text{layers}}} R_i^2 \left\langle (\theta_i^{\text{scat}})^2 \right\rangle, \tag{5.26}$$

where R_i is the distance of each layer from the perigee in the transverse plane and $\theta_i^{\text{scat}} = \theta_{\text{plane}}/\sin\theta$. Using Eq. 5.20, the uncertainty on the impact parameter becomes:

$$\delta d_0 = \frac{\sigma_{ip\text{MS}}}{p_{\text{T}}\sqrt{\sin\theta}} \tag{5.27}$$

Finally, when considering z_0, Eq. 5.26 can be used as a starting point. One obtains $\theta_i^{\text{scat}} = \theta_{\text{plane}}$, while the distance to be considered is $R_i/\sin\theta$. In addition, another $1/\sin^2\theta$ term must be added to Eq. 5.26, due to the fact that the longitudinal impact parameter is actually the *projection* of z_0,

perpendicular to the momentum. The complete expression becomes:

$$\delta_{z_0} = \frac{\sigma_{ip\mathrm{MS}}}{p_{\mathrm{T}}\sqrt{\sin^3\theta}} \tag{5.28}$$

As a general conclusion, the multiple scattering phenomena introduce a dependence of the resolution of each track parameter on the momentum and on the polar angle of the track.

5.1.4 Residuals and extrapolation of tracks

A fundamental quantity for all tracking algorithms is the *residual*, that is defined as the distance between a measured hit and a track prediction. Residual distributions are useful to estimate the resolution of the detector and are used in several procedures, such as the track fitting or the alignment of the detector. Residuals are defined using different algorithm, according to the detector measurement type.

Each Pixel Detector hit, for example, is a two-dimensional measurement on a plane surface (see Section 4.3). The surface describes the position of sensor mid-plane. The residual is then calculated as the distance between the intersection of the track with the plane and the position of the hit. The two-dimensional position is considered as two different measurements, each one projected along a local coordinate. This gives origin to two different residuals associated to each pixel cluster.

In the SCT, each sensor can only measure one coordinate, perpendicular to the strips direction. In order to identify both local coordinates of the hits, each SCT module is composed of two sensors rotated with their hybrids by ± 20 mrad around the geometrical centre of the sensors (see Section 2.2.2). In this case, a slightly different procedure is applied. If $\vec{m}_i$ is the position of the center of the hit strip, $\vec{t}$ is the intersection of the track with the sensor mid plane and $\vec{\varphi}$ is a unit vector on the measurement surface and perpendicular to the strip, the residual is defined as:

$$r = (\vec{t} - \vec{m}_i) \cdot \vec{\varphi}. \tag{5.29}$$

When considering the TRT, finally, each measurement has only information in the plane perpendicular to straw tubes (see Section 2.3.1). In this case, hits have a straight line associated (i.e. the wire), instead of a surface, and each measurement describes a circumference centered on the wire that collects the charge. The residual can thus be defined as:

$$r = R_{\mathrm{track}} - R_{\mathrm{drift}}; \tag{5.30}$$

where R_{track} is the distance of the track from the wire and R_{drift} is the drift radius of the hit. Both R_{track} and R_{drift} are signed quantities, the signs decides the side (left or right) with respect to the wire. Another definition can be used, if the *left-right* ambiguity is still unresolved:

$$r = |R_{\mathrm{track}}| - |R_{\mathrm{drift}}|. \tag{5.31}$$

A key point in the residual calculation is the prediction of the track parameters at the intersection with a given detector element. This is a very general tasks known as *track extrapolation*. Several software tools are implemented in ATLAS for the track extrapolation [128]. The simplest ones use analytical methods to describe the track as a straight line or as a helix. These algorithms are useful when there is no magnetic field or when considering very short distances (e.g. overlapping modules). The highly inhomogeneous magnetic field and the complex material distribution, anyway, requires a more flexible approach. In ATLAS, the Runge-Kutta formalism is used to numerically integrate the particle trajectory even if a complex magnetic field is present, taking into account also the effects of energy loss and the interaction with material.

Residuals can be *biased* or *unbiased*. Biased residuals use all the hits associated to the track when the extrapolation is performed. On the contrary, unbiased residuals are estimated by removing from the track extrapolation procedure the hit from which the distance is computed. In general, different aspects sum up in determining the width of the residual distribution: detector intrinsic resolution, track extrapolation precision and misalignments of the elements composing the detector.

5.1.5 Alignment procedures

To fully profit from a tracking device performance, the best possible knowledge of its component positions is essential. This problem is generally known as *alignment*. The alignment must deal with 6 degree of freedom for each detector module (3 translation axis and 3 rotation axis). In ATLAS, this results in considering ~ 35.000 degrees of freedom for the silicon detectors and ~ 700 for the TRT. The requirement imposed to the position knowledge is that alignment uncertainty should not degrade track parameter resolution more that 20% [129, 130].

Both hardware and software based technologies are applied to reach the desired precision. During the assembly of the detector, for example, a survey has been performed [131], reaching an accurate knowledge of the position of each sub-structure. The final precision was different for each part, down to $\mathcal{O}(10)$ μm for the positioning of pixel staves and $\mathcal{O}(1)$ mrad for their rotation. Moreover a Frequency Scanner Interferometer optical system has been integrated in the SCT package, to monitor the position of its structures with a micron-scale precision [69].

Besides survey constraints, software based alignment procedures are applied during track reconstruction. All these techniques are *track based*, i.e. track fitted to particle trajectories are used to determine the position and the orientation of the modules. The base assumption is that residual distributions for a perfectly aligned detector are centered around zero and their width is determined only by intrinsic detector resolution and by multiple scattering. When modules are shifted, instead, the mean of residual distributions shifts as well. Figure 5.5 shows how a misaligned module influences residual distributions. At the moment three implementations exist for silicon detectors alignment, while the TRT is treated separately by a dedicated procedure. All these algorithms output collections of *alignment constants* that are saved in the conditions database (see Section 1.4.1). During track reconstructions,

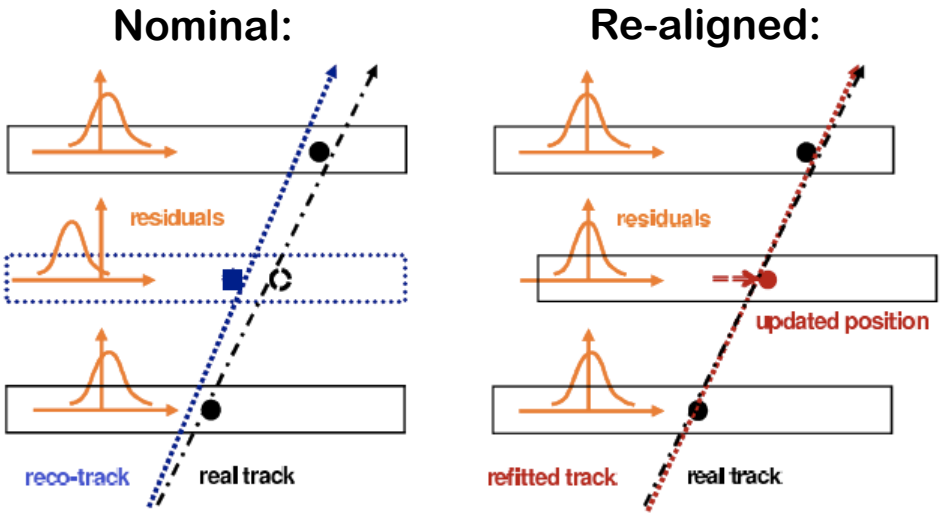

Figure 5.5: Connection between alignment of modules and residual distributions.

alignment constants are retrieved and used to correct the position of each module with respect to its nominal location.

Robust Alignment

The Robust Alignment algorithm [132] is based on centering the residual distribution for each silicon detector module individually. If a single module is misaligned by a quantity δ, a single application of the procedure should identify a δ shift in the corresponding distribution and apply a $-\delta$ correction to the module position. However, for a situation in which many modules are misaligned, an iterative procedure is used to take into account the correlations between module positions that are propagated in track fitting.

In the Robust Alignment algorithm *overlap residuals* are used as long as *unbiased residuals*. Overlap residuals are calculated when hits are found in the common area of two overlapping modules: in this case the *overlap residual* is computed as the difference between the residuals relative to each measurement. Overlap residuals have a main advantages over unbiased residuals, i.e. they suffer for smaller extrapolation and multiple scattering uncertainties, since overlapping modules are very close and there is no additional material layers between them.

For each silicon module, thus, three different residual distributions can be considered for both local x and y directions: unbiased residuals r_j ($j = x, y$), overlap residuals for modules that overlap in the local x directions o_{jx} and overlap residuals for modules that overlap in the local y directions o_{jy}. The final expression for the correction to be applied to each module sums up all the informations, assigning an increased weight ($w_o > 1$) to overlap residuals:

$$\delta_j = -\sum_{\text{tracks}} \left(r_j + w_o \sum_k o_{jk} \right). \tag{5.32}$$

Other than improving the shift computation in local x and local y directions, overlap residuals also allow to estimate deformations along the radial direction. If the overlapping modules are supposed to reside on a circumference, in fact, the sum of their residual means should vanish, as long as the radius is constant. If the radius is increased (decreased), instead, the sum of the means becomes positive (negative). Using this effect, detectors are divided into *rings* of modules and deformations of each ring can be evaluated.

The Robust Alignment algorithm cannot consider module rotation or deformation. Furthermore, shifts of the two wafers that constitute SCT modules are not treated.

Global χ^2 method

The Global χ^2 method [133] defines a figure of merit:

$$\chi^2 = \sum_{\text{tracks}} r^T V^{-1} r, \tag{5.33}$$

where a single vector r containing all the residuals relative to a single track is used. The matrix V, instead, is the covariance matrix of the track. The parameters that determine the χ^2 are the alignment constants a and the track parameters π. The problem is solved by linearizing the χ^2 expression, in order to find the variations δa that should be summed to the current alignment constants to minimize the χ^2:

$$\delta a = -\left(\sum_{\text{tracks}} \frac{\mathrm{d}r^T}{\mathrm{d}a} V^{-1} \frac{\mathrm{d}r}{\mathrm{d}a} \right)^{-1} \sum_{\text{tracks}} \frac{\mathrm{d}r^T}{\mathrm{d}a} V^{-1} r. \tag{5.34}$$

Since the track parameters actually depends on the alignment constants, the problem must consider derivatives like:

$$\frac{\mathrm{d}r}{\mathrm{d}a} = \frac{\partial r}{\partial a} + \frac{\partial r}{\partial \pi} \frac{\mathrm{d}\pi}{\mathrm{d}a}, \tag{5.35}$$

where $\partial\pi/\partial a$ should be computed from differentiation of a single track residuals:

$$\delta \pi = -\left(\frac{\partial r^T}{\partial \pi} V^{-1} \frac{\partial r}{\partial \pi} \right)^{-1} \frac{\partial r^T}{\partial \pi} V^{-1} r. \tag{5.36}$$

The main advantage of the Global χ^2 method is that it can take into account all possible degree of freedom and all possible correlations between track parameters, multiple scattering effect and shift of modules. The obvious drawback is that Eq. 5.34 involves the inversion of a matrix that grows like the square of the number of parameters considered. Furthermore, such a big matrix is inherently singular and thus inversion requires careful treatment. Some global deformations of the detectors, in fact, have very little effect on the χ^2 calculated from residuals. This deformations are usually known as *weak modes*. Collision data are usually not sufficient to spot out and solve weak modes. They can be detected by using cosmic ray tracks that traverse the entire detector or by studying the deformation

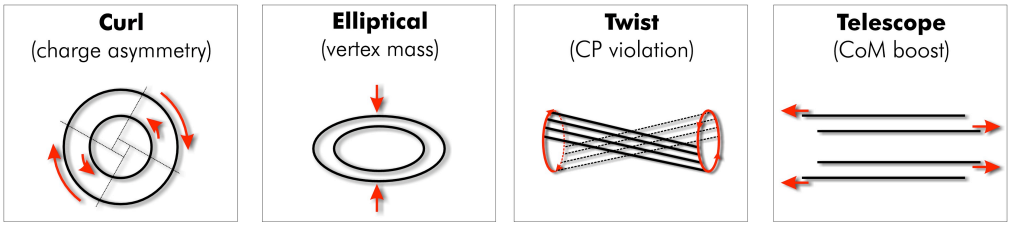

Figure 5.6: Selection of possible weak mode of deformation.

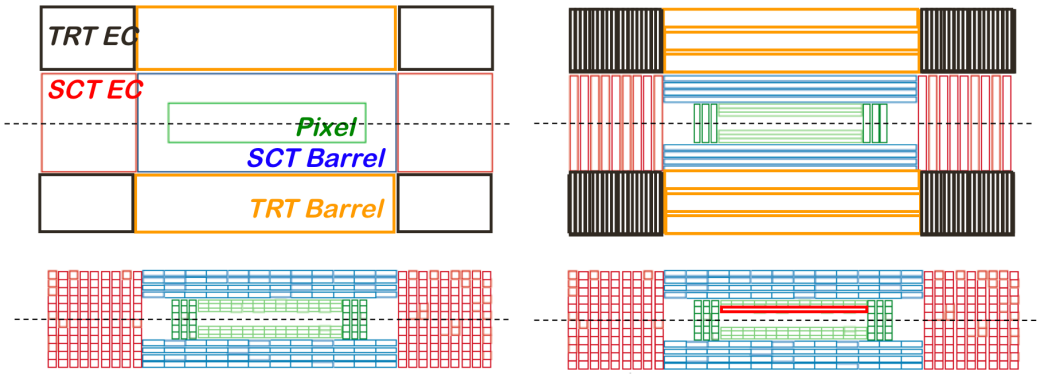

Figure 5.7: Different levels for the Global χ^2 algorithm, each one increasing the number of degree of freedom. From top left: *End-cap Barrel level*, *Layer level*, *Module level*. Mechanical constraints can be added to identify intermediate levels, like Pixel Detector *stave level* (see Section 2.1) on bottom right.

of invariant mass distributions in resonance decays. Figure 5.6 shows some weak mode deformations typical of the ATLAS Inner Detector.

In order to solve conveniently the minimization problem, the alignment procedure can be split into different *levels*. At first level, each detector is divided into rigid bodies defined by the barrel and the end-caps. At further stage, layers are considered, until the module level is reached. More intermediate levels can be defined by using mechanical constraints on modules (see Figure 5.7). When analyzing cosmic ray data, for example, due to the low statistic, the procedure cannot be run until module level: entire layers should be considered as rigid structures.

Local χ^2 method

The Local χ^2 method [130] is based on the same assumptions of the Global χ^2, until Eq. 5.34 is written. At this point all the correlations are discarded: the covariance matrix is substituted by the parameter errors, and the derivatives are computed as partial derivative only:

$$\delta a = -\left(\sum_{\text{tracks}} \frac{\partial r_i^T}{\partial a} \frac{1}{\sigma_i^2} \frac{\partial r_i}{\partial a} \right)^{-1} \sum_{\text{tracks}} \frac{\partial r_i^T}{\partial a} \frac{1}{\sigma_i^2} r. \tag{5.37}$$

The result is that the full system is divided into 6×6 matrices that can be treated more easily.

The assumptions that simplify the problem, by discarding all the correlations, is valid only as long as the tracking uncertainty is smaller than the uncertainty on the measurements. For this reason, an iterative procedure is used to take the correlations into account.

TRT alignment

The alignment of the TRT is based on a Local χ^2 algorithm, using reference tracks extrapolated from the silicon detectors. The TRT situation, anyway, is more complex than the silicon detector one. In fact, the TRT is a drift device, that needs an accurate calibration for each straw, in order to use the drift time measurement to improve resolution. The drift time calibration and the alignment interact each other, requiring an iterative procedure to obtain consistent results.

5.1.6 Track fitting strategies

A task that is performed several time during track finding is the optimization of the parameters that describe the track extracted from a set of measurements. Many procedures exists, and the most commonly used in ATLAS are presented in this section.

Global χ^2

The χ^2 procedure is the most used procedure to perform fits in many different applications. Its main feature is that all the measurements are considered at the same time, when optimizing track parameters (hence the name *global*). Given a function $f(z,T)$ described by a set of parameters T, and a set of measured space points $p_i \equiv (x_i, z_i)$, the χ^2 is defined as:

$$\chi^2(T) = \sum_i \frac{|f(z_i,T) - x_i|^2}{\sigma_i^2}; \tag{5.38}$$

where σ_i is the uncertainty on the measurement of x_i. The Gauss-Markov theorem states that minimizing Eq. 5.38 is the optimal algorithm to find the set of parameters T that best describe data, if the quantity $|f(z_i,T) - x_i|$ (i.e. the residual) is distributed according to a Gaussian. Tracks can be described by functions $f(z,T)$ based on the parameters introduced in Section 5.1.1. This implies that, given a set of measurement, the associated track can be found by minimizing the associated χ^2.

The actual implementation of the χ^2 algorithm uses the biased residuals, as they were described in the previous paragraph. Residuals are computed using the Runge-Kutta extrapolation method. The extrapolation procedure is relatively easy, because only the track parameter values are needed at each intersection, and not their associated errors. The uncertainty σ_i is, in fact, calculated as the error on the measurements. The minimization of the χ^2 is performed after a linearization of Eq. 5.38. That means that residuals are assumed to depend only linearly on track parameters. This assumption is true only for little variations of the track parameters. The final problem results in a set of linear equations that can be solved trough a matrix inversion.

The χ^2 procedure has been improved in order to consider the energy loss and the scattering of particles, when material is crossed. If only the Inner Detector is considered, the low material budget

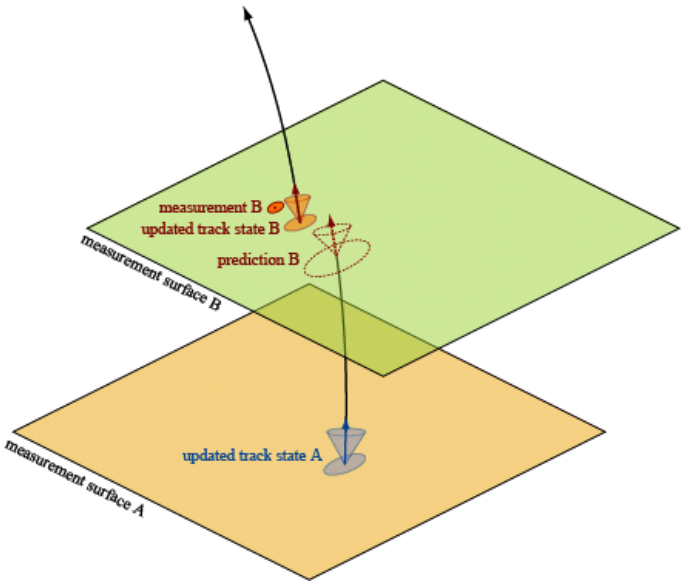

Figure 5.8: Sketch representing a *step* in the Kalman filter procedure.

leads to ignore energy loss. The multiple scattering effect, instead, is taken into account by considering two more parameters for each detector layer crossed by the particle. These are the scattering angles θ^{scat} and ϕ^{scat}, whose distributions are described by a Gaussian with width σ^{scat} (see Section 5.1.3). The generalized expression for the χ^2 becomes:

$$\chi^2(T) = \sum_i \frac{|f(z_i,T)-x_i|^2}{\sigma_i^2} + \sum_j \left(\frac{\theta_j^{\text{scat}\,2}}{\sigma^{\text{scat}\,2}} + \frac{(\sin\theta_j^{\text{loc}})^2 \phi_j^{\text{scat}\,2}}{\sigma^{\text{scat}\,2}} \right). \tag{5.39}$$

Here the first sum must consider all the measurements, while the second one all the scattering planes intersected by the particle. The angle between the track and the z-axis at the scattering plane has been called θ^{loc}. When considering scattering angles, the number of parameters implied in the χ^2 minimization can be very large. In this case, the inversion of the matrix associated to the problem can became a long time consuming task.

Kalman filter

As opposed to global χ^2 fits, the Kalman Filtering technique uses a progressive algorithm to obtain the optimal track parameters at the end of the process. The detailed mathematical background is presented in many papers, for example [134].

The algorithm acts as a series of *steps*, one for each detector layer intersected by the particle. Figure 5.8 illustrates how a single step works:

- From a previous step, or from a first measurement, an initial set of the local parameters (position and momentum direction) of the track are estimated on a measurement surface A.
- Track parameters are extrapolated to the next measurement surface B, resulting in a *prediction B* that estimates all the track parameters, as well as their uncertainties. The predicted position

of the hit is called $\mathbf{B}_p(\mathbf{T})$ and its uncertainty $\sigma_p(\mathbf{T})$ is computed from both the previous position measurement(s) and from the extrapolation uncertainty.

– The position $\mathbf{B}_p(\mathbf{T})$ associated to the *prediction B* is compared with the position $\mathbf{B}_m(\mathbf{T})$ of the *measurement B*. If the uncertainty on the position $\mathbf{B}_m(\mathbf{T})$ is called $\sigma_m(\mathbf{T})$, then the position of the *updated track state B* is computed using a weighted mean:

$$\mathbf{B}_u = \frac{\mathbf{B}_m/\sigma_m^2 + \mathbf{B}_p/\sigma_p^2}{1/\sigma_m^2 + 1/\sigma_p^2}, \tag{5.40}$$

$$\sigma_u = \frac{1}{\sqrt{1/\sigma_m^2 + 1/\sigma_p^2}}. \tag{5.41}$$

At this point, new informations arising from the updated position are used to perform a new estimation of all tracks parameters and of their uncertainties. The *updated track state B* is finally used as the starting point for the next step.

From Eq. 5.40, some interesting properties of the Kalman filter can be deduced. For example, the updated position can also be written as $\mathbf{B}_u = \mathbf{B}_p + K_K(\mathbf{B}_m - \mathbf{B}_p)$. In this case the *Kalman gain factor* is defined:

$$K_K = \frac{\sigma_p^2}{(\sigma_m^2 + \sigma_p^2)}. \tag{5.42}$$

The Kalman gain factor value is between 0 and 1. The first case happens when a measurement has infinite uncertainty (i.e. it does not provide additional informations on the track parameters). The value $K_K = 1$, instead, happens when the extrapolation has infinite uncertainty (i.e the predicted position provides constraints much weaker than the actual measurement resolution). The uncertainty on the updated position can be expressed as a function of K_K as well:

$$\sigma_u^2 = (1 - K_K)\sigma_p^2. \tag{5.43}$$

This expression shows that the precision is increased at each Kalman filter step.

During Kalman filter application, material effects are added as part of the prediction process. For this purpose the algorithm can control how the uncertainties from multiple scattering and energy loss are added to the extrapolated state. If a particle type hypothesis is provided, the description of these effects can be very detailed. The most common strategy to include material effects is based on a Gaussian distribution of the uncertainties, but other schemes exist. The Dynamic Noise Adjustment (DNA [135]) algorithm can adapt the variance of the Gaussian with respect to the amount of material traversed. The Gaussian Sum Filter (GSF [136]), instead, is dedicated to electron tracks and uses multi-Gaussian modelling of the bremsstrahlung.

From this brief description, some of the advantages of the Kalman filter are evident, since it does not need to invert huge matrices, like the global χ^2 algorithm. Unbiased residuals are easily calculated

from the predicted position, without needing a dedicated fit. Moreover, a pattern recognition capability is well integrated in the procedure, by comparing the prediction with the measured hits. Finally the characteristics of every detector module can be described with virtually unlimited accuracy. This allows, for example, to easily describe the surface orientation and position for each module independently, during alignment studies. The same problem requires a huge matrix to be inverted, if using a χ^2 algorithm.

Some drawbacks exists in any case: while through the extrapolation mechanism the filter becomes sensitive to track direction and momentum already after a few steps, the predictions are rather poor at the beginning of the process. In fact, the track parameters are known with optimal precision only after the last step of the fit. Since the aim of the track fit is to know the track parameters at the perigee, the ATLAS implementation of the algorithm can execute each filtering step both in the forward and in the opposite direction of the trajectory. This allows to refit the parameters at the interaction point, once the most external measurements have been added to the track.

Deterministic Annealing Filter (DAF)

The Deterministic Annealing Filter (DAF [137]) extends the Kalman filter with the concept of competition between measurements. Given a track prediction on a surface that contains several measurements, this algorithm uses an iterative procedure to decide which measurement can contribute to the definition of the updated track state.

At each iteration, the entire Kalman filter process is performed and a weighted mean of all the measurements relative to each surface is used to update the track predictions. The weight of each measurement is computed from its intrinsic uncertainty and its *association probability*, that is defined by considering the residual with respect to the track prediction. At the end of the Kalman filter process, a track candidate is found: association probabilities are recalculated using this result and a new iteration is started. If association probability for a given hit becomes bigger than a defined value, the iteration is stopped and the current track is retained.

In order to avoid local minima in the association probability space, an annealing parameter T [138] is introduced in the weighted position definition. At each step of the algorithm, in fact, the computed weighted position is replaced by a random value that differs less than T with respect to the computed value. Since T is gradually decreased during the process, the random displacement does not affect the final result if the algorithm is focusing towards a global minimum. At the same time, if the algorithm is choosing a position in proximity of a local minimum, the modification of the weighted position can avoid the convergence towards it.

The DAF algorithm is particularly convenient if more than one measurement is present on a single detector element or when all the measurements are projected on the same plane. The TRT case, for example, features both these aspects: moderate detector noise and left-right ambiguity for each drift circle, as well as measurements possible only in the plane perpendicular to the straw tubes. In addition to the TRT specific case, the DAF can help to reduce limitations of the track reconstruction performance, e.g. at high noise levels and in dense jets.

5.2 Tracking in the ATLAS Inner Detector

Track reconstruction in the Inner Detector is provided by a modular and flexible software framework. The event data model and detector description for this framework are made such that they allow track reconstruction across the entire ATLAS detector, using the same reconstruction tools for parameter extrapolation and track fitting including material corrections [121, 122]. The modular structure makes it possible to reconstruct cosmic ray events with only small changes to the software developed for collision events (the `NewTracking` package) and to the one developed during test-beam activities (the `CTBTracking` package). Only small amendments are needed, for instance to correct for differences in detector timing, to remove any assumption of a collision vertex (in the `NewTracking`) and to fit the traversing particle as a full track across both hemispheres in ATLAS.

5.2.1 Input to the tracking algorithms

The input to tracking algorithms consists in a list of measurements, taken by different sub-detectors, each providing different kind of information and accuracy. For example, measurements from the silicon detectors can be considered as three dimensional space points, while only measurements projected in a plane are provided by the TRT. An important aspect is that the raw information provided by detectors is enough to identify spatial measurements. Anyway a *recalibration* of the measurements can substantially improve resolution in the case of Pixel Detector clusters and TRT drift circles, as detailed in the following. Both `CTBTracking` and `NewTracking`, in fact, foresee a recalibration stage after a track candidate has been found, in order to update the information used for final track fitting.

Figure 5.9 shows the number of detector layers crossed by a particle coming from the interaction point. It can be noticed that in the range $|\eta| < 2.5$, regardless the polar angle, the particle typically intersect 3 Pixel Detector layers and 4 SCT layers. For the TRT, the minimum number of straws crossed by the particle is 22 in the barrel end-cap transition region and 36 in the other cases. In order to consider full cosmic ray tracks, that traverse both the upper and the lover part of detectors, these numbers should be roughly doubled.

Table 2.1 shows the intrinsic resolution of each sub-detector. For the Pixel Detector each measurements is determined by two coordinates. In the barrel, the local x corresponds to the global azimuthal direction while the local y is aligned to the beam axis. The short side of the pixels (i.e. 50 μm) is parallel to the local x, allowing a resolution of $50/\sqrt{12} \sim 14$ μm with a simple digital read-out. If a candidate track is associated to the clusters, anyway, a recalibration of the position is possible, by using a charge interpolation algorithms that takes advantage of corrections depending on the track incident angle (see Section 4.4). The charge interpolation algorithm can improve the mean intrinsic resolution up to 10 μm for particle coming from the interaction point. Along the local y, the 400 μm side of pixels allows an intrinsic precision of 115 μm. Since the interpolation algorithm needs information about the incident angle of the track, it can only be applied after the pattern recognition stage.

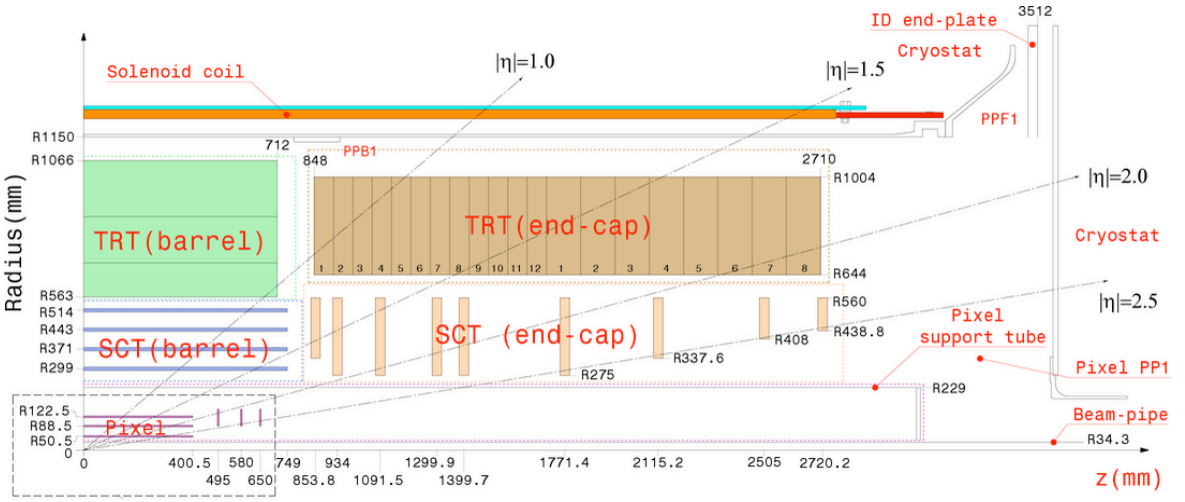

Figure 5.9: Section of the Inner Detector, showing the number of detector surfaces crossed by a particle coming from the interaction point with different polar angles.

In the SCT, each sensor can only measure one coordinate, perpendicular to the strips direction. Since the strips have an average pitch of 80 μm, a spatial resolution of about 23 μm is expected in the direction perpendicular to them. In order to identify both local coordinates of the hits, each SCT layer is composed of two sensors rotated with their hybrids by $\pm$20 mrad around the geometrical centre of the sensors (see Section 2.2.2). This fact allows to have in the barrel a precise measurement in the azimuthal direction (17 μm intrinsic resolution), while a comparison between the two sensor layers gives a sensitivity of 580 μm along the global z axis.

When pattern recognition algorithms are applied, measurements from the Pixel Detector and the SCT are treated as three-dimensional space points (`SpacePoints`) defined by the two measured coordinates and by the position of the module mid plane. For the TRT, instead, each measurement has only information in the plane perpendicular to the straw tubes (i.e. x-y plane for the barrel and R-z plane for the end-cap). The radius of each straw tube is 4 mm thus allowing an accuracy of $\sim$ 1100 μm for uncalibrated measurements. A more refined information is possible when the *drift time* is measured. This is the time intervening between the particle passage in the tube and the collection of the released charge by the electrode (see Section 2.3.1). An estimate of the drift time allows to describe a circumference centered on the wire that collects the charge: this so-called `DriftCircle` must contain the point where the charge originate. A `DriftCircle` have an intrinsic precision of 130 μm but a *left-right* ambiguity exists (see Figure 5.10).

When dealing with cosmic ray tracks, the TRT drift radii are formed in a two-step procedure, which takes into account the event phase φ_{TRT} , i.e. the difference between the L1 trigger time and the arrival of the cosmic particle (see Section 3.3.1). In the first step the TRT drift time is not used and tracks in the Inner Detector are formed using the 4 mm wide straws as coarse detecting elements. Such a first-pass track reconstruction allows a determination of the event phase φ_{TRT}. In the second step the

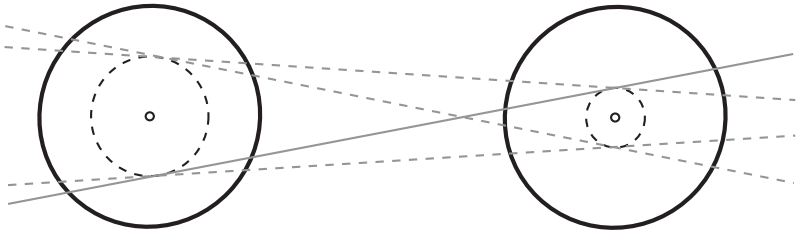

Figure 5.10: Sketch of two measurements taken by the TRT (drift circles). Each drift circle has an ambiguity associated, when describing if a particle traversed the straw tube on the left or on the right of the central wire. Given two hits, there are four possible paths that traverse both of them. Figure taken from [139].

drift circles are calibrated using this event-specific time offset and drift time information and the tracks are re-fitted using the calibrated hits.

5.2.2 The Cosmic+Test Beam Tracking

The `CTBTracking` is a software package that was developed in 2004 to analyze ATLAS test-beam data, and it is particularly suited for tracking in low multiplicity environment. It was also adapted to reconstruct cosmic ray data that were collected before the final integration of the ATLAS sub-detectors in the cavern [139]. This software has already been tested in the past on real data and it is considered as the reference in the commissioning of new algorithms.

Pattern recognition

Track search is started from the Pixel Detector and the SCT space points. All the modules that have at least one hit are counted. The number of these nodules is the highest number of points that can be associated to a single track. The search begins for tracks with exactly this number of points. Sets of measurements are formed such that each point lies in a different module. Three points are initially considered for each set and a fit is performed in the bending plane using a circle. A cut on the χ^2 selects only good track candidates. When a good track is found, other points of the set are added until either all the points are included or the fit fails. When all the sets have been analyzed, good track candidates are compared: some of them can share one or more hits. All these cases are analyzed and ambiguities are solved, by selecting the lower χ^2. After that, all the hits that have been associated are excluded and new sets containing a lower number of points are formed. The procedure is repeated to find new track candidates, until a minimal number of measurements per set is reached.

Pattern recognition in TRT can be done either by starting from a silicon track *seed* or by performing a full scan of the detector. If a seed is used, it is extrapolated to the TRT. This can introduce large uncertainties, because of the distance between the SCT and the TRT. Then drift circles that are found near the track are chosen. The first and the last drift circles are considered and four track candidates are defined though them using straight lines (see Figure 5.10). All the drift circles that lie in a determined

range from the track candidates are associated to them. A quality factor, based on the number of measurements associated and on their χ^2 is computed. The best candidate is selected according to its quality factor, provided that it has quality higher than a cutoff. If no track candidate is adequate, a new couple of drift circles is chosen and the procedure is iterated. If a candidate is accepted, its measurements are flagged as used and the procedure is continued with the remaining hits.

When the pattern recognition in the TRT is started without seeds, a fit is tried using all the hits in the TRT. If a track candidate is found, it is refined using only the hits closer than a fixed distance. The associated measurements are flagged and the fit is tried again on the remaining hits, until no more track is found. An extrapolation can be tried, pointing to the SCT, even if the missing spatial information out of the transverse plane can easily cause the extrapolation to fail.

Track fitting

The track fitting in `CTBTraking` is based on the global χ^2 approach (see Section 5.1.6). This approach was chosen because it had many advantages over the algorithms implemented before test-beam:

- it only needs as input an estimation of the track parameters, and not of their uncertainty;
- it does not need to have left-right ambiguity solved for TRT hits, as long as residual are defined as in Eq. 5.31;
- the algorithm can yields the scattering angles at each scattering surface.

5.2.3 The New Tracking

The `NewTracking` is a collection of software tools used to reconstruct tracks. Its main concept is to factorize the complex process of track reconstruction into well defined modules that represent a single task [140]. This approach allows to develop different versions of the tool that accomplishes a given task, providing that they all share the same interface and the same representation of the data. The common representation is defined in the Event Data Model specifications [121, 122]. Since the `CTBTracking` package has been built following these specifications, it can be considered actually integrated into the `NewTracking` software.

The `NewTracking` software will be the default choice to analyze collision data, and a specially tuned version has been provided to reconstruct cosmic data. This procedure is presented in the following, and it will be compared to `CTBTracking` in the rest of the chapter. This allows to validate `NewTracking` using the first data available for the entire Inner Detector.

The default `NewTracking` strategy has no clear border between the classical modules *pattern recognition* and *track fitting*. The pattern finding incorporates itself two stages: a global pattern search and a local pattern recognition which includes also track fitting. Moreover, the track fitting is done using a Kalman filter (see Section 5.1.6) which allows for a built-in pattern recognition and outlier rejection. The `NewTracking` procedure can currently be split into two sequences, the main *inside-out*

reconstruction and a consecutive *outside-in* tracking. When dealing with cosmic ray data, anyway, only the *inside-out* procedure is applied.

Inside-out track reconstruction

The track search is started from the silicon detectors, where *seeds* made of three space points are formed (global pattern search). Starting from these seeds, *roads* of detector modules are built. Each road contains all the silicon modules that can be intersected by the track relative to a seed. Once all the roads are defined, space points are not used anymore, but single strips (in the SCT) or single coordinates (in the Pixel Detector) are considered. For each road, the Kalman filter is applied, in order to associate all the compatible measurements to the initial track seed (local pattern search). This procedure progressively updates track parameters and their uncertainty using new measurements, while outlier hits are removed by looking at their residual.

At the end of track search, the track *segments* can share many hits, or be incomplete or be fake (i.e. the majority of associated hits are not due to the same particle). The ambiguities are solved by refitting all the tracks with the Kalman filter: since at this point they have well defined parameters, an improvement of the filter performance is expected. During this procedure a *track score* is assigned, depending on the total number of hits and on their features. Pixel hits and measurements on overlapping modules get an high score, while shared hits and holes (i.e. missing hits on a traversed sensor element) are considered as penalties. Only track segments that get the highest scores are accepted and shared hits are assigned to them.

The next step consists of extending silicon track segments using TRT measurements. During this procedure, existing track segments are not modified and the *track extensions* are built as independent segments. *Roads* of TRT detector elements compatible with the existing segments are built and hits within these roads are selected and assigned to track extensions by using either a fit or the DAF algorithm (see Section 5.1.6). At the end of the extension finding, each extension is matched with a silicon segment: one more Kalman filter application is used to decide whether the extended track is the most reliable trajectory or the silicon segment alone is.

Outside-in track reconstruction

The inside-out tracking procedure is based on finding track seeds in the silicon detectors. It can happen that seeds are not found, or that they do not exist. This is possible if particles are originating from secondary vertexes further inside the Inner Detector volume. A second track finding sequence is therefore implemented, starting from TRT track segments.

Since the TRT does not provide information in the direction parallel to drift tubes, the search of track segments is performed in projective planes. Furthermore, all particles with a transverse momentum greater than 500 MeV follow an almost straight line trajectory also in the R-ϕ plane when traversing the TRT. In this situation, the common method to find track candidates is the Hugh transform [141]. It is based on the transformation of the projection plane into the parameter space of a straight line. If a measured hit is described by coordinates (x_1, y_1) in the projection plane and the interaction point is

located at $(x_{\text{i.p.}}, y_{\text{i.p.}})$, a straight line $(y_1 - y_{\text{i.p.}}) = a + b\,(x_1 - x_{\text{i.p.}})$ can be associated to the hit. This allows to associate a pair of parameters (a,b) to each point. If the parameter space is then divided into cells, the points associated with the same track fall into the same cell. The global track segment finding can thus be reduced to a local maximum finding in a two-dimensional histogram representing the population of the straight line parameter space. Once track segments are available, the Kalman filter is used to refine them. Segments are also compared to the extensions found by the inside-out process and duplicates are removed.

The further step is the extrapolation of the TRT track *seeds* to the silicon detectors. Initially, pairs of silicon space points are created, excluding measurements already used in the inside-out procedure. The segments associated to each pair are analyzed, in order to be matched to TRT segments. If a match is found, a *road* of silicon detector elements is built. At this point the local pattern recognition stage can be performed as in the inside-out case. Final track refitting is done using the standard track fitter, as in the inside-out track reconstruction.

5.3 Sub-detectors performance

The first aspect of track reconstruction, the pattern recognition introduced in Section 5.1, depends on the performance of the sub-detectors, like noise occupancy and intrinsic efficiency, and on the quality of the extrapolation to the sub-detector active elements. In this section, these performances will be discussed, while the rest of the chapter will be devoted to the performance of the tracking system as a whole.

5.3.1 Occupancy in the Inner Detector

The pattern recognition procedure is greatly influenced by noise hits that detectors generate in addition to particle hits. In silicon detectors (Pixel and SCT) noise depends on detector capacitance and leakage currents as well as on front-end electronics settings and operational temperature. In the TRT, the main effects are the physical thresholds of ground offsets in the low voltage levels supplied to the front-end electronics and the cross talk between adjacent straws.

Figure 5.11 shows two typical events containing a cosmic ray track as they are recorded by the Inner Detector. The different rate of noise of the detectors is clearly visible, resulting in only one noise hit in the Pixel Detector over two events, while several tenth of them are present in the TRT. The very low noise rate in the Pixel Detector and in the SCT is the main reason why the pattern recognition always starts from the silicon hits. In order to quantify the noise rate, the *occupancy* is defined as the noise hits per channel and bunch crossing (25 ns). Figure 5.12 shows the occupancy measured in each of the Inner Detector constituents.

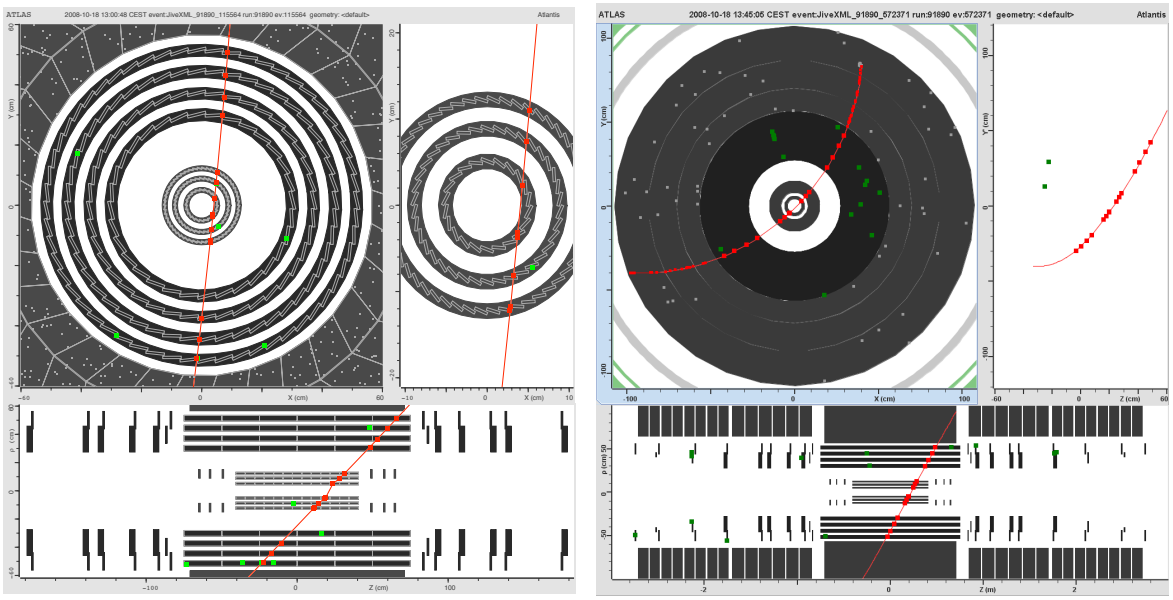

(a) (b)

Figure 5.11: Two cosmic ray events seen by the silicon detectors (5.11(a)) and by the entire Inner Detector (5.11(b)). Noise hits are visible as well as hits associated with real particle passage. The track associated to the cosmic muon is drawn as a red line.

Pixel Detector

For the Pixel Detector, the typical occupancy when no tracks are recorded is about 10^{-10}, i.e. the probability that a pixel fires in a 25 ns window is 10^{-10} (see Figure 5.12(a)). To achieve this result, the threshold for a pixel to fire is set to about 4000 electrons (see Section 4.3.1), while the typical Equivalent Noise Charge (ENC) is measured to be ~ 200 electrons.

Noisy pixel are extracted for each run, building a so-called *offline map* of pixels to be excluded from reconstruction. Single pixels are considered noisy if their occupancy during a data taking run exceeds 10^{-5} per bunch crossing. When a pixel is noisy over a long period of time, it is added to an *online map* that is used during data taking to exclude pixels from read-out. Figure 5.13 shows the number of noisy pixels in each of the two maps and the mean number of noisy hits per event resulting after masking noisy pixels. It can be noticed that the rate of noise is very stable over time: the only spike that is observed in the fraction of pixel included in the maps is due to a change in the running conditions.

SCT

In the SCT a mean occupancy smaller than 5×10^{-4} is measured in dedicated calibration runs (see Figure 5.12(b)). In this case, the threshold is similar to the Pixel Detector (i.e. 4000 electrons), but the noise from leakage is larger: ~ 1600 electrons, mainly due to the higher input capacitance of the strips. This is the primary cause for the observed difference in the occupancy of the two detectors.

The SCT is checked, during each run reconstruction, by a monitoring software that can locate noisy strips. Noisy strips are saved in maps similarly to the Pixel Detector procedure. During patter

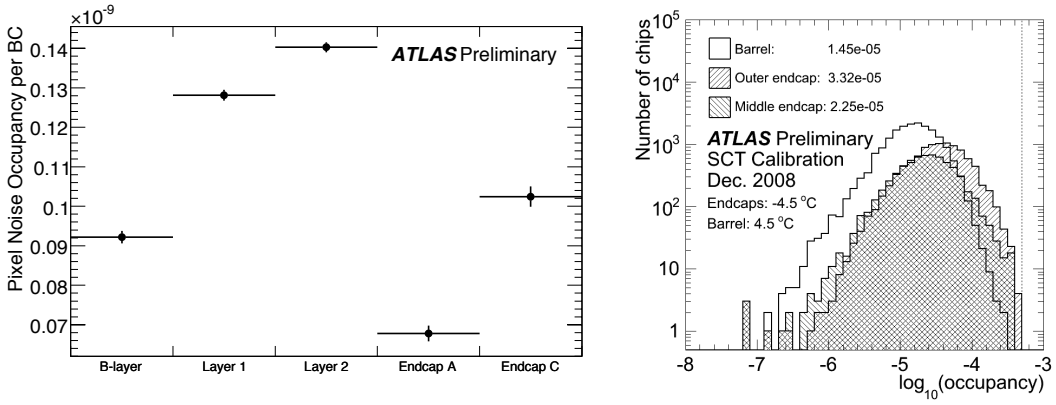

(a) (b)

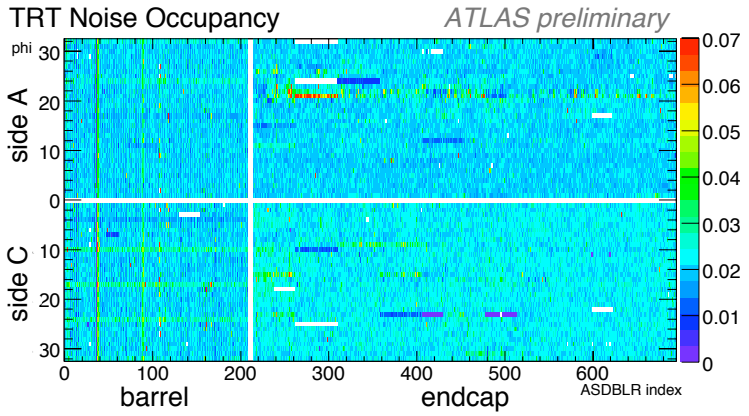

(c)

Figure 5.12: Occupancy plots for Pixel Detector (5.12(a)), SCT (5.12(b)) and TRT (5.12(c)). Detailed description in Section 5.3.1.

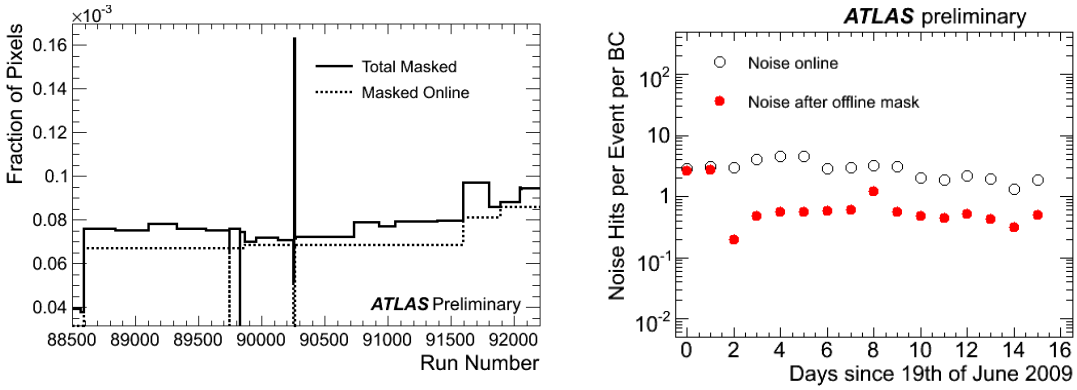

(a) (b)

Figure 5.13: Number of noisy pixels as a function of time (5.13(a)) and the resulting noise hits in the detector (5.13(b)). Detailed description in Section 5.3.1.

recognition and track fitting, strips that are known to be noisy can be removed to improve the efficiency of pattern recognition algorithms. The noise hits, however, always appear in the recorded data: this allows to examine noisy strips and to check if they can be recovered.

During pattern recognition the SCT space points formation features an intrinsic noise suppression at the very first stage, since it requires two different sensors with separate read-out for the creation of a single `SpacePoint`.

TRT

The TRT undergoes a noise calibration procedure, in order to achieve a uniform response to particles across the detector. During this process, the low discriminator thresholds of the front-end electronics (see Section 2.3.3) are adjusted to produce a straw noise occupancy close to 2%, similar for all channels.

Figure 5.12(c) shows the low threshold noise occupancy for the TRT in a single run, during cosmic ray data taking. Straw noise occupancy shown in this figure is averaged over all straws in a given read-out chip and permanently dead straws and straws with occupancy 100% are not used in the average. It can be observed that the noise occupancy is fairly uniform across the detector, at the prescribed level, confirming that the noise equalization procedure is performing well.

5.3.2 Residual distributions

In cosmic ray data, most of the events have only one track. Still the pattern recognition is not a trivial task because it must deal with misalignments and mis-calibrations of the detectors, that are under commissioning. The effect of alignment on the unbiased residuals for the barrel components of the Inner Detector is shown in Figure 5.14.

The *Nominal geometry* distributions are relative to cosmic ray data analyzed at the very beginning of commissioning studies. The only information that is used to determine the detector element position is taken from the survey performed during the installation of the detectors. The *Aligned geometry* plots contain the same events of the *Nominal geometry* ones. The difference between the two data samples is the set of alignment corrections that are used by tracking software to estimate the actual position of detector elements during track fitting (see Section 5.1.5). Finally, the *MC perfect geometry* distributions contains simulated data. In this case, no misalignment has been simulated among detector modules. For the TRT (Figure 5.14(d)) both the distributions *Before TRT Alignment* and *After TRT Alignment* are considering the final the alignment of the silicon detectors.

It is worthwhile to notice that, even if the misalignments of the detector are completely absent, as in the *MC perfect geometry* dataset, the width of residual distribution is still larger than the intrinsic resolutions. The difference between the two values is due to the track extrapolation error, coming from geometry and material of the tracking devices and from the momentum spectrum of incoming particles. When considering collision tracks, for example, narrower residual distributions can be obtained with respect to cosmic ray tracks, if geometrical constraints, i.e. a *vertex constraint*, are applied. The extrapolation contribution to the width of the residual distribution is computed as the term that should

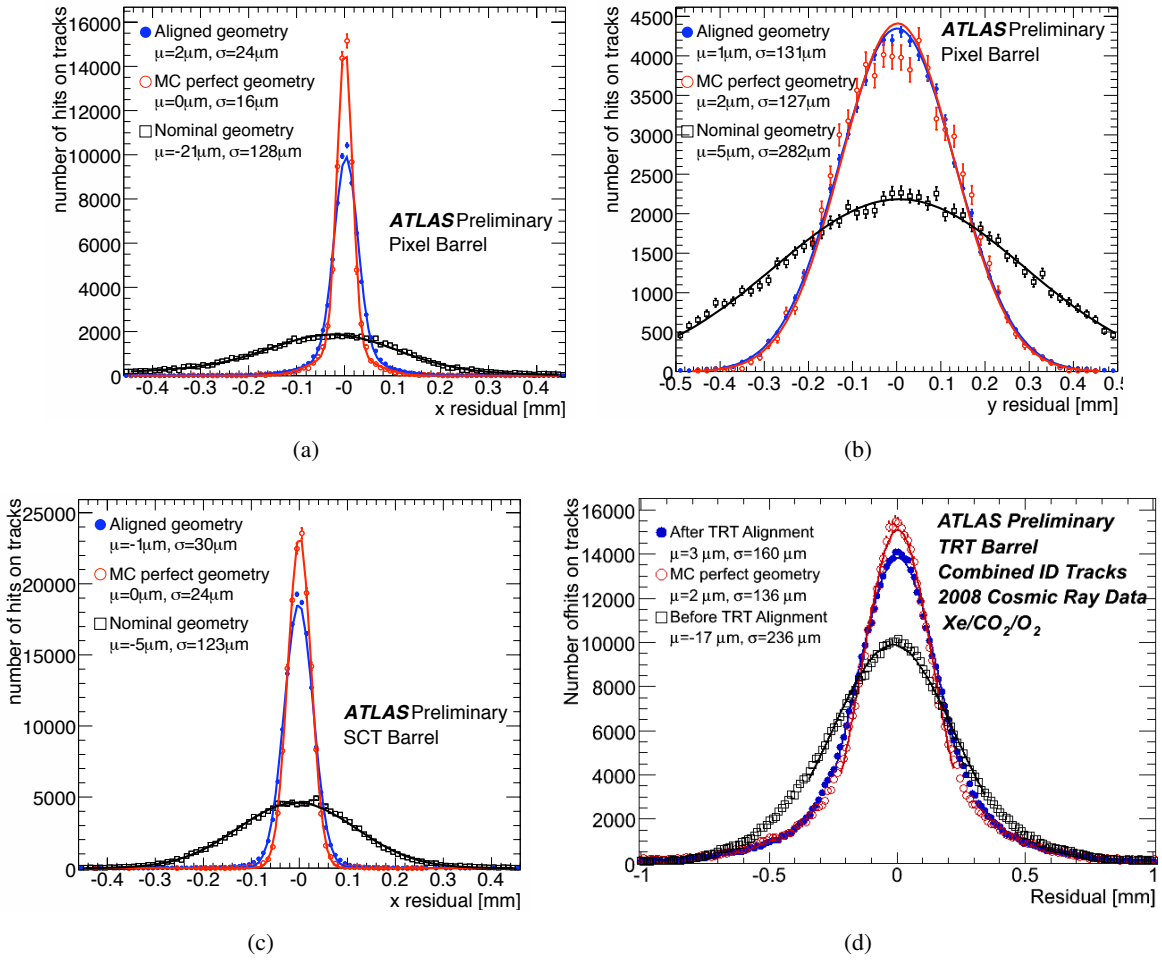

Figure 5.14: Residuals for the hits in the detector composing the inner tracking system. The σ is calculated from a single Gaussian fit in all cases except for the Pixel local x. The `NewTracking` procedure is used as fitting algorithms and *tight* (see Section 5.4.2) full tracks are considered with an additional cut $p_{\mathrm{T}} > 2$ GeV. 5.14(a): Pixel Detector, local x direction. A sum of two Gaussian is used for the fit, and the results shown refer to the narrower. 5.14(b): Pixel Detector, local y direction. 5.14(c): SCT, local x direction. 5.14(d): TRT, only tracks with no hits in the end-caps were used.

be summed in a quadrature to the intrinsic resolution of each detector, in order to get the *MC perfect geometry* residual distribution width. The resulting values are summarized in Table 5.1. It can be noticed that, for the most precise coordinates, the intrinsic resolution and the extrapolation uncertainty are roughly equal.

The comparison between *Aligned geometry* and *MC perfect geometry* in Figure 5.14 can be used to provide an estimation of the contribution to the resolution of the alignment uncertainty. As for the extrapolation error, the width of the *Aligned geometry* distribution can be described as the quadrature sum of two terms. The first contribution is due to the resolution of the tracking system and can be measured from the *MC perfect geometry* distribution width. The second one is due to remaining

	Residual distribution width			Alignment contribution		Extrapolation	Intrinsic
	Nominal	Aligned	MC perfect	Nominal	Aligned	contribution	resolution
Pixel local x	128 μm	24 μm	16 μm	127 μm	18 μm	12.5 μm	10 μm
Pixel local y	282 μm	131 μm	127 μm	252 μm	32 μm	63 μm	115 μm
SCT	123 μm	30 μm	24 μm	121 μm	18 μm	17 μm	17 μm
TRT	—	160 μm	136 μm	—	84 μm	40 μm	130 μm

Table 5.1: Different contributions to the width of residual distributions shown in Figure 5.14.

misalignments. Results from this estimate are reported in Table 5.1. A comparison with the required alignment tolerances on module position can be done using data in Table 2.1.

5.3.3 Error associated to measurements

The errors on the measured hits directly affect whether they can be associated to a track, resulting in variation of the track propagation and of track parameter errors. It is therefore necessary to have properly assigned hit errors. In particular, during the commissioning phase, the assigned hit errors should include an estimation of the uncertainty from the residual misalignments, giving values above the intrinsic resolution. An estimate of the errors can be made by a detailed study of residual distributions. In Section 5.3.2, the main contributions to residual width have been detailed: the intrinsic resolution of detectors, the extrapolation uncertainty and the alignment contribution. When cosmic ray tracks have been reconstructed, anyway, only an approximate estimation of the errors has been taken into account. Figure 5.15 shows the error associated to the different measurements.

For Pixel Detector and SCT hits, errors have been assigned by computing the RMS of a distribution wide as the cluster itself. This means that, for the local x directions, clusters composed of one pixel row feature $50/\sqrt{12} = 14.43$ μm errors. For clusters made of two rows, the error is $2 \cdot 50/\sqrt{12} = 28.86$ μm. The errors up to clusters made of 8 rows of pixels are visible in the plot reported in Figure 5.15(a). For the local y coordinate of pixel clusters, the errors associated to one- two- and three-column clusters are 115.47, 230.94 and 346.41 μm respectively. They are visible in Figure 5.15(b), together with the uncertainty associated to clusters that contain one long pixel column (173.71 μm) or one long and one normal column (288.68 μm). The error of two long column clusters is identical to the one of three normal columns. In Figure 5.15(c), the SCT distribution shows the errors computed for one-strip clusters, two-strip clusters and three-strip clusters.

The case of the TRT is reported in Figure 5.15(d) and it is slightly more complex. For the TRT, in fact, an attempt is made to parameterize separately the intrinsic resolution of the detector and the contribution due to misalignment and extrapolation, when computing the uncertainty of measurements. This is why a contribution of 151 μm has been summed in quadrature to the intrinsic resolution of drift circles in the barrel region. For the end-cap region, a similar contribution of 253 μm has been used.

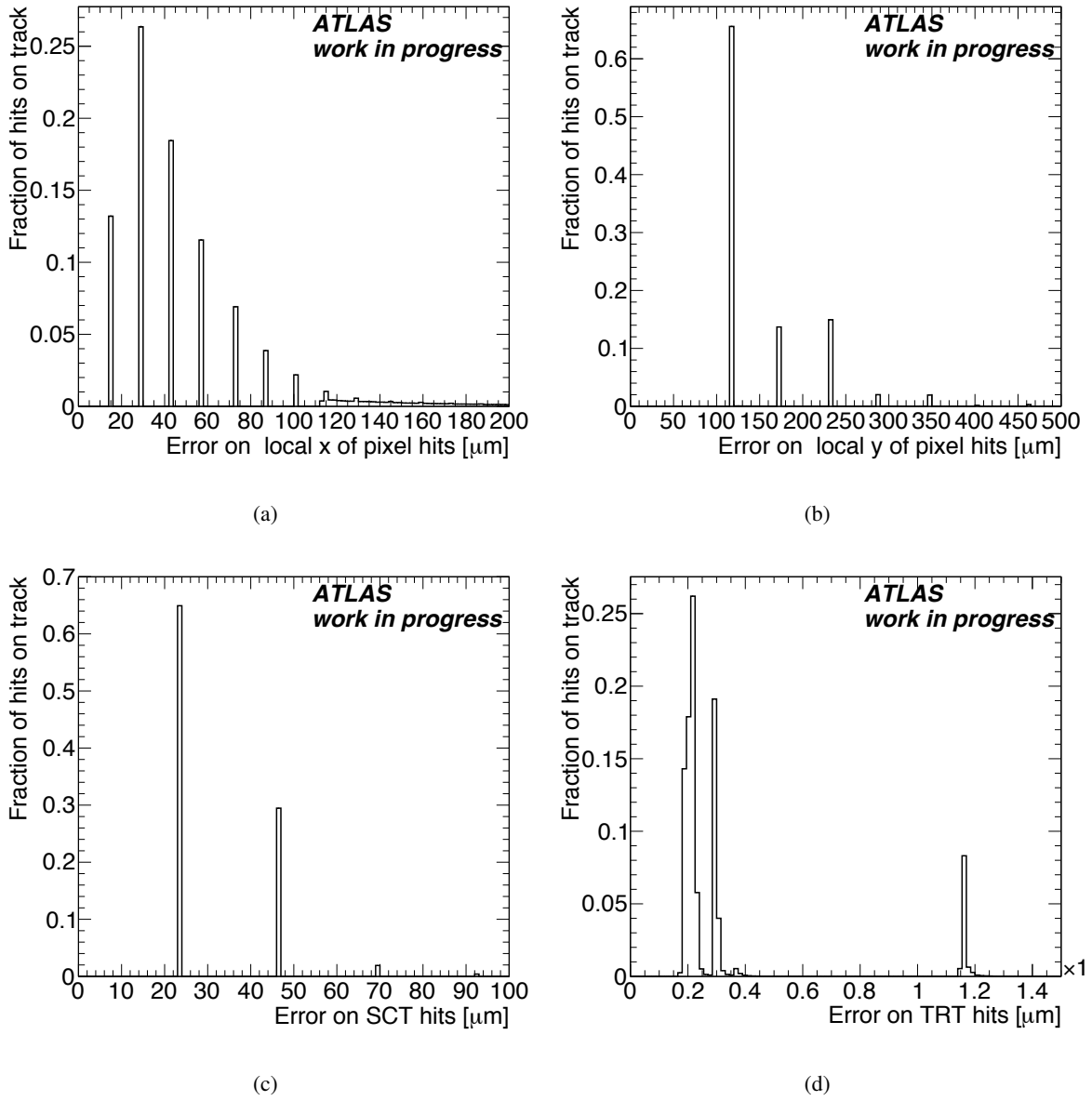

Figure 5.15: Errors associated to different measurements during track reconstructions. 5.15(a): Pixel Detector, local x direction. 5.15(b): Pixel Detector, local y direction. 5.15(c): SCT. 5.15(d): TRT.

The estimation of these contributions was made with a preliminary alignment of the detector, worse than the one presented in Section 5.3.2. This is why the contribution used in errors calculation is larger than the one estimated in Section 5.3.2. The method used for TRT hit errors gives origin to three main peaks in the error distribution. The first peak refers to calibrated drift circles in the barrel that feature intrinsic resolution of 130 μm and total error of $130 \oplus 151 = 199.25$ μm. The second peak contains calibrated drift circles in the end-caps, with associated errors $130 \oplus 253 = 284.44$ μm. The third peak, finally, is formed by uncalibrated hits that have intrinsic resolution equal to 1100 μm.

The method used to assign errors to measured hits leads to average uncertainties that are compatible with the global residual distributions observed in Figure 5.14. Anyway, a more detailed study of the residuals (see Section 4.6 for the Pixel Detector case) points out that a better description of the errors is preferable. This description should disentangle the effects due to intrinsic resolution, extrapolation error and alignment. The intrinsic resolution of a hit, in fact, depends on a number of factors such as the cluster width and track direction (see Section 4.23). These factors should be taken into account when calculating the *intrinsic error* of the hit σ_{intr}, that should be determined only by intrinsic resolution. If the sub-detector performance are worse than the expected ones, the intrinsic error may need to be rescaled by a factor a. Furthermore, the differences between the real positions of individual hits and those recorded by a misaligned detector lead to an additional error term that must be added in quadrature to the intrinsic error of the hits. As a conclusion, the proposed method to estimate the hit errors in future track reconstruction, uses two parameters a and c to adjust the intrinsic error [93]:

$$\sigma^2 = a^2\sigma^2_{\text{intr}} + c^2. \tag{5.44}$$

The parameters are adjusted by using the *pulls*, i.e. the residuals divided by their estimated uncertainty. If the uncertainties are correctly computed, the pull distribution should be Gaussian and have unity width. The calibration procedure necessary to compute the (a,c) parameters tries to make the pulls converge to 1, via successive iterations. Since each detector component can have significantly different behaviour, the granularity of each detector component has to be taken into account, and therefore different sets of (a,c) have to be computed separately for the barrel and end-cap regions for each detector technology, as well as for the different R-ϕ and η measurement directions in the case of the Pixel Detector. The a parameters can be obtained from simulated data, where there is no c contribution. On the contrary, the c parameter can be calculated on real data by an iterative procedure:

$$c_i^2 = (p^2_{\text{obs},i} - 1)a^2\sigma^2_{\text{intr}} + p^2_{\text{obs},i}c^2_{i-1} \tag{5.45}$$

where c_i and c_{i-1} are the values of the c factor obtained in the iteration i and $i-1$, respectively, $p_{\text{obs},i}$ is the hit residual pull width observed at step i, and σ_{intr} is the average intrinsic detector resolution.

5.3.4 Hit association efficiency

The efficiencies of the Pixel and SCT detectors are measured by extrapolating tracks through the detector and counting the numbers of hits on the track and holes where a hit would be expected but is not found. Any module (module side for the SCT) which does not have a cluster associated to the track is called a hole if the intersection point is more than three times the intrinsic resolution from the edge of the sensitive area. The effiency, ε is defined as the ratio of the number of clusters found to the number expected:

$$\varepsilon = \frac{N_{\text{clusters}}}{N_{\text{clusters}} + N_{\text{holes}}} \tag{5.46}$$

where N_{clusters} is the number of clusters found and N_{holes} is the number of holes. Only well-reconstructed tracks are used to measure the efficiency. This definition of efficiency includes both the active fraction of the sub-detectors and the effect of association due to pattern recognition cuts on track χ^2 or residuals with respect to extrapolation. For a detector performance study, it is more relevant to measure the *intrinsic* detector efficiency, by excluding non-functioning detector elements and widening association cuts to retrieve outliers due to particle interaction in the detector material.

Pixel efficiencies are determined using tracks with at least 30 TRT hits, at least 12 SCT hits and $\sin\alpha < 0.7$ where α is the angle between the track and the normal to the sensor. There must be only one track passing these cuts in the event. To reduce track reconstruction biases, any cluster not already associated to a track but within 10 mm of an intersection is included in the number of clusters, and removed from the number of holes. Furthermore, clusters or holes within 0.6 mm of ganged pixels in the local x direction, or within 1.0 mm of the sensor edge in both local direction are excluded from the calculation. The measured efficiency for the Pixel Detector is shown in Figure 5.16(a): the overall efficiency of the Pixel barrel is larger than 99.97%.

Tracks used to measure the SCT efficiency must have at least 30 TRT hits or 7 SCT hits, a hit both before and after the module side under investigation and $|\varphi| < 40°$, where φ is the angle between the track and the normal to the sensor in the plane defined by the normal to the sensor and the axis in the plane of the sensor perpendicular to the strip direction. This angular cut removes tracks with incident angle not expected in collision data, that cause the detector to perform less efficiently. A run-dependent cut on the TRT event phase is applied to ensure good timing. Unassociated clusters within 2 mm of an intersection point are included in the number of clusters, while the intersection of the track with the sensor is required to be at least 2 mm from the edge in global Φ and at least 3 mm in global z. The result of this analysis is shown in Figure 5.16(c). The efficiency is for each layer larger that 98.5%.

The efficiency of the TRT is determined in a similar manner to that of the silicon detectors, by extrapolating tracks through the TRT in a series of steps. To reduce tracking biases, at each point all straws in a region containing up to the third nearest neighbour are considered. The efficiency depends on the path length of a track inside a straw, and is therefore determined as a function of the distance of a track from the wire, by dividing the number of hit straws by the total number of straws within the region. Tracks are required to have at least 20 TRT hits, at least 6 SCT hits, an event phase between 5 ns and 25 ns and an angle to the vertical of less than 15°. The efficiency of the TRT barrel, for data with solenoid on, is shown in Figure 5.16(b). The overall efficiency over the plateau region is $97.7 \pm 0.5\%$.

5.3.5 Number of hits associated to tracks

The performance of the pattern recognition algorithms can be tested by looking at the number of measured hits associated to each track. In Section 5.2.1 the expected number of hits per track has been estimated by looking at the geometry of the Inner Detector sub-systems. Anyway, it should be remembered that the Inner Detector is optimized to work with particles coming from the nominal interaction

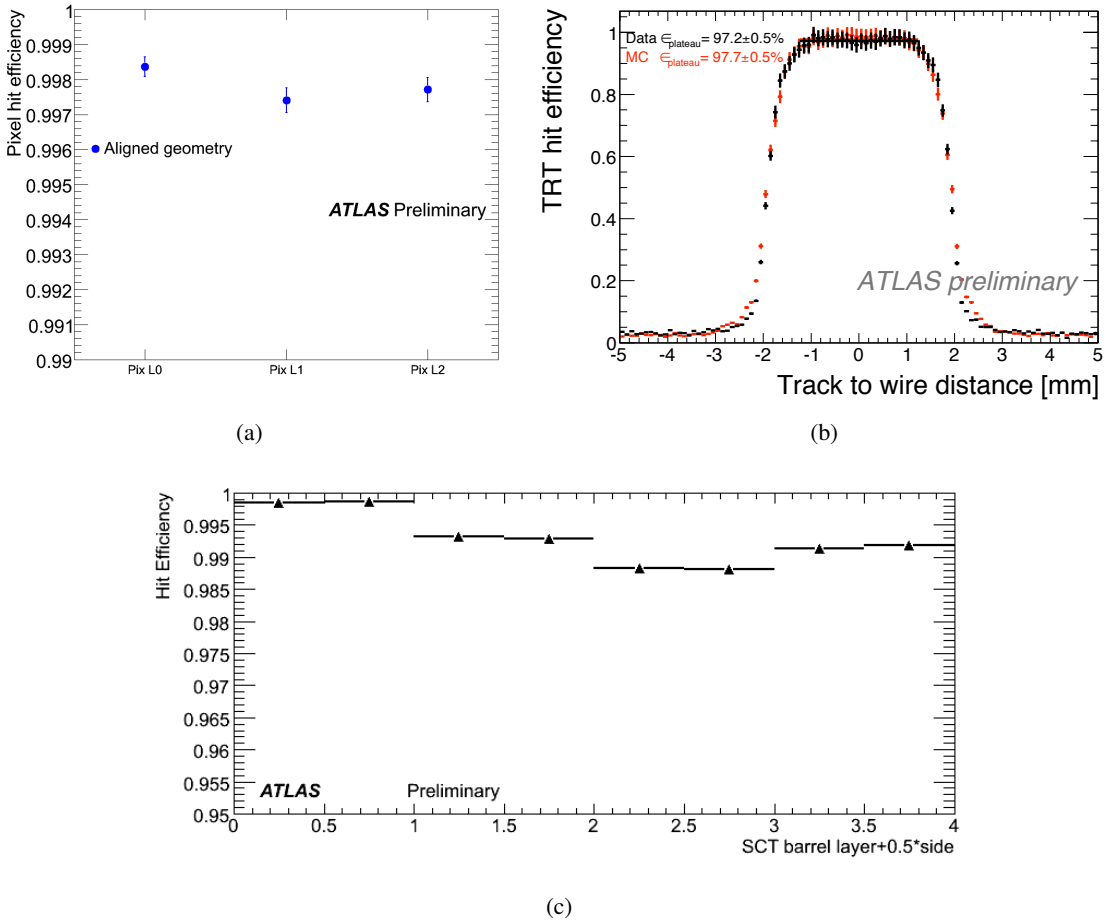

Figure 5.16: Efficiency plots for Pixel Detector (5.16(a)), SCT (5.16(c)) and TRT (5.16(b)). Detailed description in Section 5.3.4.

point, while cosmic ray tracks have non-pointing direction. For this reason cosmic ray tracks can miss some of the detectors or can cross them at unexpected incident angle, leading to inefficiencies in track fitting and non-trivial distribution of the number of measurements that gets associated to tracks.

Figure 5.17 shows the number of measured hits associated to each track. Tracks reconstructed by the reprocessing of data performed at the end of commissioning activity are used. The only request on the cosmic ray event, in order to be included in the analysis, is the presence of a hit in the Pixel Detector. This is done to tentatively select tracks that crossed the whole inner tracker. In each plot a comparison between the two ATLAS tracking algorithms (see Section 5.2) is shown. The efficiency of the two algorithms is similar, even if discrepancies are visible for low numbers of hits, were `CTBTracking` is less likely to associate low-hits track segments in the TRT to extensions from the silicon rackers.

For the Pixel Detector (Figure 5.17(a)), there is a peak at one or two hits, probably due to tracks that only partially cross the detector, while the most probable value corresponds to six hits. This is expected when tracks cross the entire barrel region of the detector. Higher number of hits is possible if hits are present in overlapping modules.

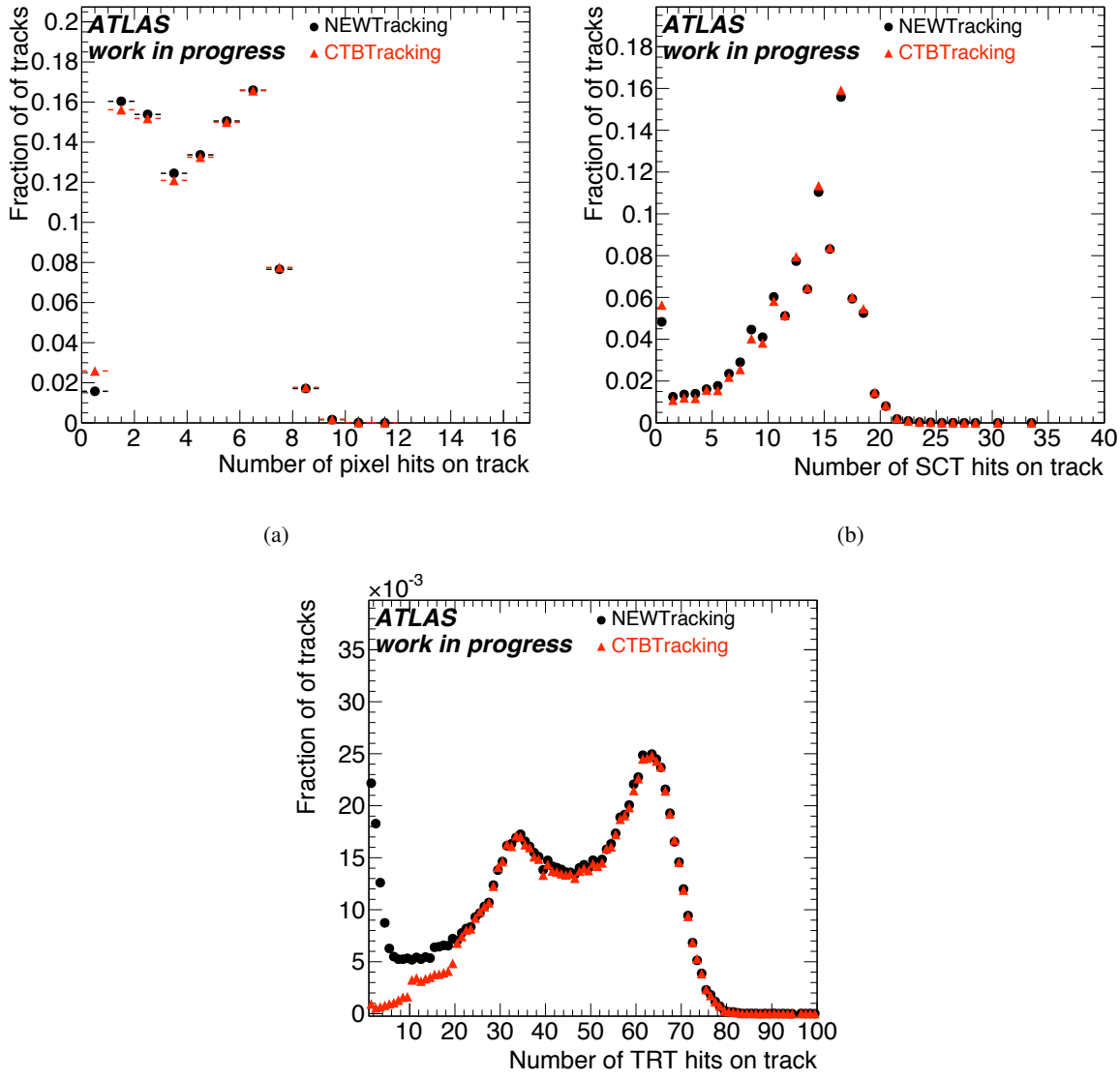

Figure 5.17: Number of hits associated to tracks for Pixel Detector (5.17(a)), SCT (5.17(b)) and TRT (5.17(c)). Detailed description in Section 5.3.5.

The SCT case is represented in Figure 5.17(b). Here the most probable value for the number of hits associated to a track is 16, i.e. two hits in each layer (one for each sensor) to be multiplied by four layers in the barrel. It can also be noticed that, starting from 8 associated hits, an odd number of hits is disfavoured with respect to the lower even number. This is because of the two sensors forming each SCT module: a track that traverse one of them is forced to traverse also the second one.

The distribution of TRT hits associated to tracks is reported in Figure 5.17(c), for tracks that have at least than one TRT hits. Approximatively 2% of tracks have zero TRT hits when using `NewTracking` and 13% when using `CTBTracking`: they are excluded from the plot, in order to maintain a reasonable

axis scale. In the plot two peaks are visible: they corresponds to tracks that are extended only in one half of the detector (peaking at about 30 hits in the TRT) or in both the upper and the lower half (peaking at 60 hits). Once more, the inefficiency of `CTBTracking` at low hit multiplicity is clearly visible.

5.4 Measuring performance from cosmic ray data

The analysis described in this chapter used the cosmic ray data collected during autumn 2008 to measure the performance of the Inner Detector. Since many of the studied reported were aimed to validate the improvements in the alignment, in the calibration and in the tracking software, the plots will contain comparisons among the same data, reprocessed with different calibrations and releases of the software. All changes that undergo between these processing are described in Section 3.4. Only the main features that determine the differences among the presented plots will be reported in this chapter.

Collected data are compared to the simulated sample described in Section 3.5 to compare a misaligned detector with unknown inefficiency (real detector) with a perfectly aligned one (the simulated detector), that have only well known inefficiency, simulated on purpose. Furthermore, the comparison is necessary to validate the simulation of the detector itself, since some quantities (e.g. geometrical acceptance and patter recognition efficiency) can only be computed on simulated events.

5.4.1 Split tracks

ATLAS tracking system has been built to efficiently measure the path of high-energy particles that originate from an interaction in the central point of the detector. Cosmic ray tracks, instead, are almost entirely coming from top to bottom, with an angular distribution defined by the geometry of the cavern that hosts the experiment (see Section 3.3). When measuring the performance of the detector with cosmic data, it is important to analyze only tracks that can be considered "similar" to the collision ones. For this reason, *split tracks* were considered and very selective requirements were imposed on the tracks used for the analysis.

The method that is used to analyze cosmic ray tracks relies on splitting each full-length Inner Detector track into an upper and a lower part. Cosmic rays, in fact, are coming mainly from the top: they traverse the entire ATLAS detector, they cross the horizontal plane containing the beam axis and they continue their path. In order to resemble tracks coming from collisions, these full-length tracks can be divided in two parts (see Figure 5.18). Once a *full track* is fitted, the split procedure is applied: each measurement of the original track is assigned either to a *upper track*, if its global coordinate y is positive, or to a *lower track*, if it is negative. At this point the upper and the lower tracks are fitted independently using the standard ATLAS track fitting algorithms (see Section 5.2).

The track splitting procedure is very convenient, because it offers a robust method to estimate the resolution that can be achieved on each track parameter. The two track parts, in fact, are fitted separately and are described by different parameter sets $\mathbf{T}_{\text{up}}$ and $\mathbf{T}_{\text{low}}$. At the same time, both tracks stem from

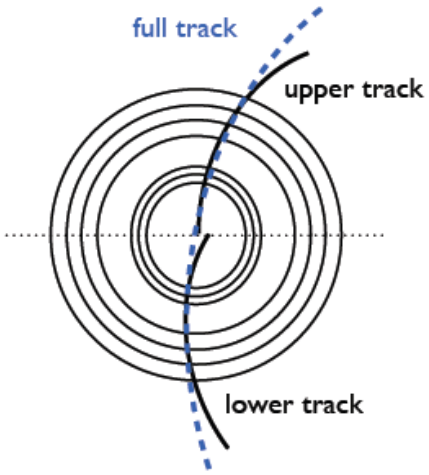

Figure 5.18: Example of split tracks.

the same particle and their parameters at the perigee are expected to be the same, within the resolution of the tracking system. More rigorously: the difference between the values of parameter τ, $\Delta\tau = \mathbf{T}_{\tau,\text{up}} - \mathbf{T}_{\tau,\text{low}}$, has expectation value equal to zero. The variance of the difference is instead defined by the uncertainty on the track parameters: $\text{var}(\Delta\tau) = \sigma^2(\mathbf{T}_{\tau,\text{up}}) + \sigma^2(\mathbf{T}_{\tau,\text{low}})$. Since, on average, the resolution on the upper and lower track are the same, the variance results to be equal to two times the square of the parameter resolution: $\text{var}(\Delta\tau) = 2\,[\sigma(\mathbf{T}_\tau)]^2$. The resolution of each track parameter can thus be calculated as the root mean square (RMS) of the $\Delta\tau$ distributions, divided by $\sqrt{2}$.

5.4.2 Quality of the tracks

At the beginning of the analysis, several sets of requests were put in place in order to select good quality tracks that could resemble the characteristics of collision tracks.

The first estimate of the quality of the track is based on the number of associated measurements for each sub-detector (see Section 5.3.5). Pixel clusters count as two different measurements, one for each coordinate. It was chosen to consider in this selection only hits in the barrel, for all detector. The majority of cosmic rays, in fact moves parallel to the detector disks that compose the end-caps, resulting in lower rate of hits. Moreover, most of them will have a bad resolution, due to high incident angle.

The second requirement that was imposed on tracks is based on the TRT event phase (see Section 3.3.1). This request ensures a good timing of the Inner Detector with respect to the trigger, and a good calibration of the TRT drift time (see Section 5.2.1). It must be noticed that TRT event phase calculation does not apply to simulated data, since timing is perfect there. It should also be noticed that the possibility to access this information was not available in early software releases. Part of the improvement that is observed in resolution when going from early software releases to the last ones will be due to this additional cut on detector timing.

	Tight	*Medium*	*Loose*
Number of barrel Pixel hits	$N_{\text{pix}} \geq 2$	$\left(2 \cdot N_{\text{pix}} + \right.$	$\left(\ 2 \cdot N_{\text{pix}} + \right.$
Number of barrel SCT hits	$N_{\text{SCT}} \geq 6$	$\left. N_{\text{SCT}} \right) \geq 8$	$\left. N_{\text{SCT}} \right) \geq 4$
Number of barrel TRT hits	$N_{\text{TRT}} \geq 25$	$N_{\text{TRT}} \geq 10$	**or** $N_{\text{TRT}} \geq 15$
TRT event phase	$\varphi_{\text{TRT}} \in [5,30]$ ns	$\varphi_{\text{TRT}} \in [5,30]$ ns	$\varphi_{\text{TRT}} \in [-10,40]$ ns **and** $\varphi_{\text{TRT}} \neq 0$ ns
Minimal transverse momentum	$p_{\text{T}} > 1$ GeV	$p_{\text{T}} > 1$ GeV	$p_{\text{T}} > 1$ GeV
Impact parameter	$\lvert d_0 \rvert < 40$ mm	$\lvert d_0 \rvert < 250$ mm	$\lvert d_0 \rvert < 500$ mm

Table 5.2: Description of the track classes used in the resolution studies. The number of hits applies to split tracks: it must be doubled for full tracks.

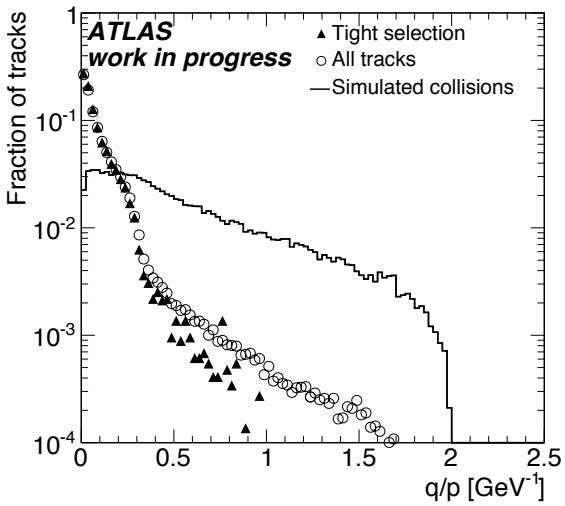

Figure 5.19: Distribution of the value of the inverse of the momentum for cosmic ray tracks and for simulated collisions. For cosmic ray data all tracks are shown, as well as the ones that satisfy tight selection cuts.

Tracks were thus classified as *tight*, *medium* or *loose*, from the best quality, to the worst. A detailed description of the selection criteria is reported in Table 5.2 for split tracks. When considering full tracks, the number of required hits should be doubled.

Cosmic ray tracks have different kinematic properties than tracks coming from p-p collisions. Figure 5.19 shows a comparison between the momentum of cosmic rays and the one associated to tracks from collision events. The q/p variable is used. The tracking algorithm sets a cut on momentum: tracks with $q/p > 2$ GeV^{-1} (i.e $p < 500$ MeV) are not reconstructed. However, the standard limit for considering tracks in physics analysis is 1 GeV. The same request has been applied for all the quality criteria presented and is clearly visible in tight tracks distribution. From the comparison between simulated collision tracks, it can be inferred that the momentum distribution is quite different: collision events feature more low-p_{T} tracks, having a flatter momentum distribution.

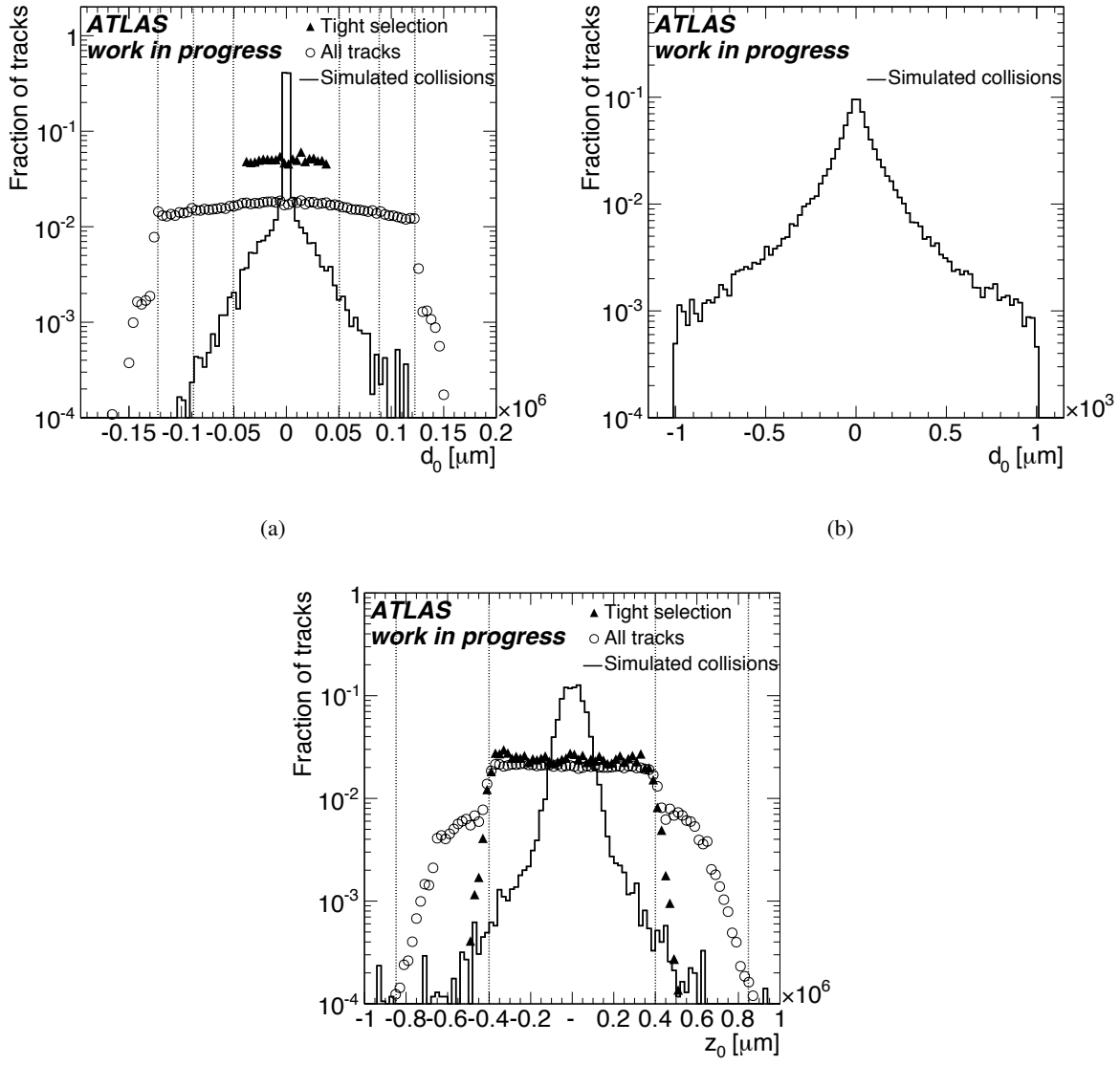

(a)

(b)

(c)

Figure 5.20: Distribution of the value of the transverse (5.20(a)) and longitudinal (5.20(c)) impact parameters for cosmic ray tracks and for simulated collisions. The distribution of transverse impact parameter for collisions tracks is shown in 5.20(b) with a larger scale. For cosmic ray data all tracks are shown, as well as the ones that satisfy tight selection cuts.

Figure 5.20 shows the distribution of the impact parameters d_0 and z_0. A clear peak can be seen in collision events, both for d_0 and z_0. On the contrary, cosmic ray events are characterized by an almost flat distribution. The radius of Pixel Detector layers is drawn as a dotted line on d_0 plots (Figure 5.20(a)), as well as the length of Pixel Detector and SCT barrel on the z_0 plot (Figure 5.20(c)). A threshold in the d_0 distribution in cosmic ray tracks is seen at about $\pm$130 mm. This is related to the radius of the Pixel Detector external layer, that is 122.5 mm (see Figure 2.1). Similarly for the z_0

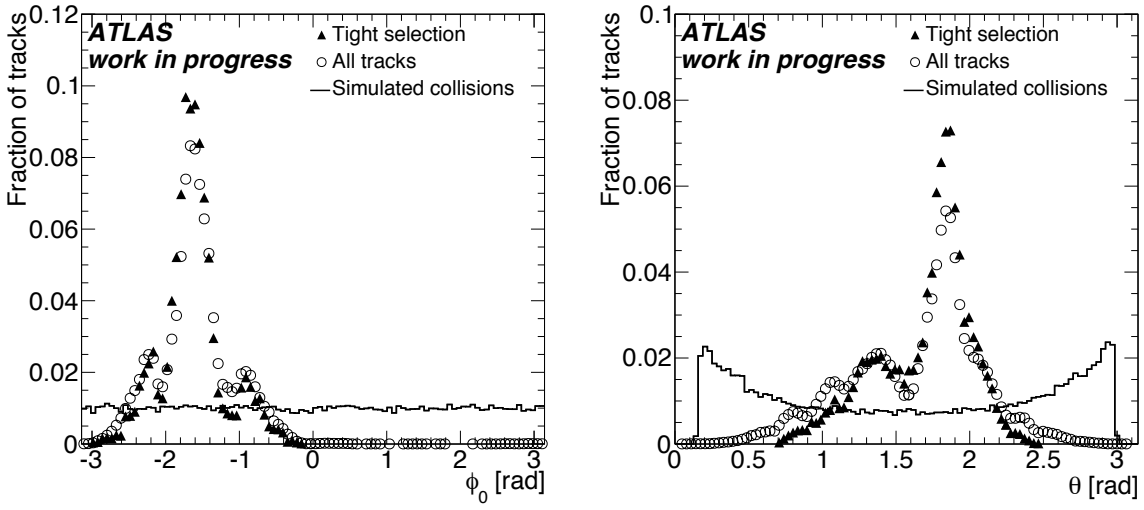

(a) (b)

Figure 5.21: Distribution of the angular parameters ϕ_0 (5.21(a)) and θ (5.21(b)) for cosmic ray tracks and for simulated collisions.

coordinate a threshold is seen after $\pm$800 mm, but a decrease is already present at $\pm$400 mm: in this case the Pixel Barrel is 400 mm long on each side of the reference system origin, while the SCT barrel ends at 848 mm.

When selecting quality requirements, it was tried to characterize cosmic ray tracks that could be similar to the ones coming from collisions. The cut on d_0, for example, chooses the limit for the distance of the track from an hypothetical interaction point located in the center of the ATLAS reference system. For tight tracks the request is $|d_0| < 4$ cm: it assures that the muon has passed through the beam-pipe. The effect of this cut is visible in Figure 5.20(a). A similar request for z_0 was not imposed, because the distribution is already limited by the request that a certain number of associated hits are in the pixel barrel. Also, due to the cylindrical geometry of the detector, a cut on z_0 is less critical for track quality than the one on d_0.

The remaining track parameters are shown in Figure 5.21. The angular distribution of cosmic ray tracks is clearly different respect to the one of collision data. The ϕ_0 distribution in Figure 5.21(a) is determined by the fact that cosmic muons that intersect the detector are coming from the top. This causes ϕ_0 to be mostly negative, approaching to zero when describing horizontal tracks (i.e. $\phi_0 = 0, -\pi$). Moreover, three peaks can be noticed in the distribution: they are caused by the pits that are used to bring material in the experimental hall (the big central peak) and by the elevator shafts (the two smaller peaks on the sides), as shown also in Section 3.3. The θ distribution in Figure 5.21(b) allows to distinguish the two big shafts that caused the central peak in the ϕ_0 distribution, showing also that one is larger than the other. When selection criteria were chosen, it was preferred to not impose requirements

	Total number of track couples	*Tight* track couples	*Medium* track couples	*Loose* track couples
DATA (initial software release)	158147	7569	67867	38028
DATA (final software release)	162598	4256	32816	53724
SIMULATION	998634	39208	392339	133126

Table 5.3: Efficiency of the different track selections on different datasets.

on the incident angles of tracks. This can be noticed in Figure 5.21(a) and 5.21(b), where tight tracks have the same distribution of the unselected events.

Yield of track selection

The yield of the selection cuts on different datasets are listed in Table 5.3. Since each event typically contains one full track, numbers are reported for *couples* of split tracks. A couple of tracks is defined as *tight* if both split tracks satisfy *tight* requirements. If one of the tracks is flagged as *tight* and the other as *medium*, the couple is considered *medium*. Other definitions are similar.

The yields for the two releases reported are slightly different, due to the fact that the TRT event phase information was not accessible in early releases. The different yield in selecting tracks from simulated events, instead, is mainly due to the geometrical cuts that were applied during event generation (see Section 3.5). The effect of these cuts can be noticed from the different distribution of the impact parameters in real data and in simulated events, as reported in Figure 5.22.

5.4.3 Average resolution of track parameters

As reported in Section 5.4.1, the resolution of each track parameter τ can be estimated from the RMS of the $\Delta\tau$ distribution. In this section, the split track method is validated, the global resolution of the parameters is studied and the RMS calculation is optimized in order to treat correctly outliers.

RMS computation

Several possibilities have been explored in order to choose a satisfactory way to compute the RMS. The right procedure should be robust against the outliers, but at the same time should be able to include the contribution of the most significant tails. Figure 5.23 shows the distribution of $\Delta(d_0)$, where the mean and the RMS are expressed according to different procedures.

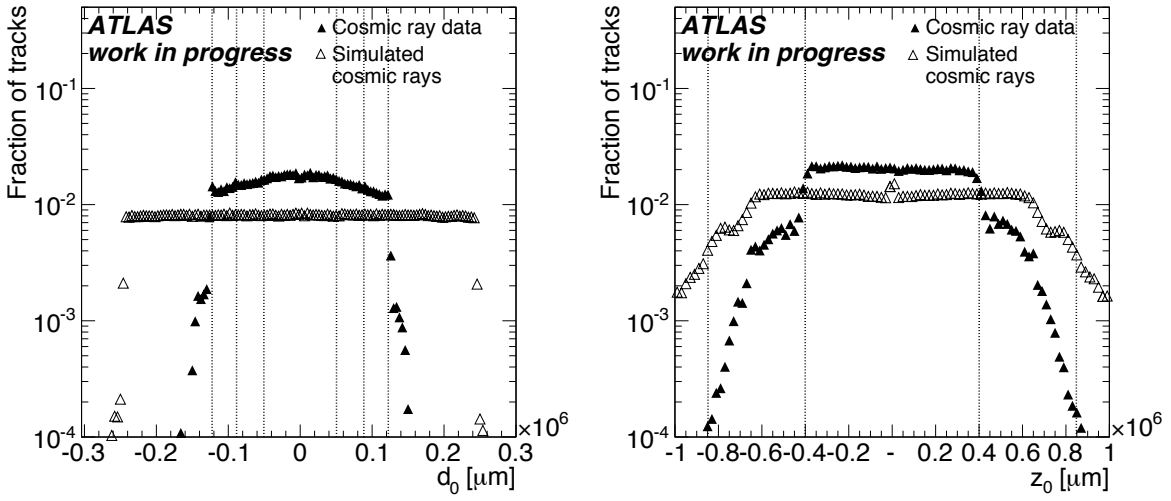

(a) (b)

Figure 5.22: Distribution of the value of the transverse (5.22(a)) and longitudinal (5.22(b)) impact parameters for cosmic ray tracks. A comparison between simulated and real events is reported, to point out the effect of the geometrical cuts applied by the Monte Carlo generator.

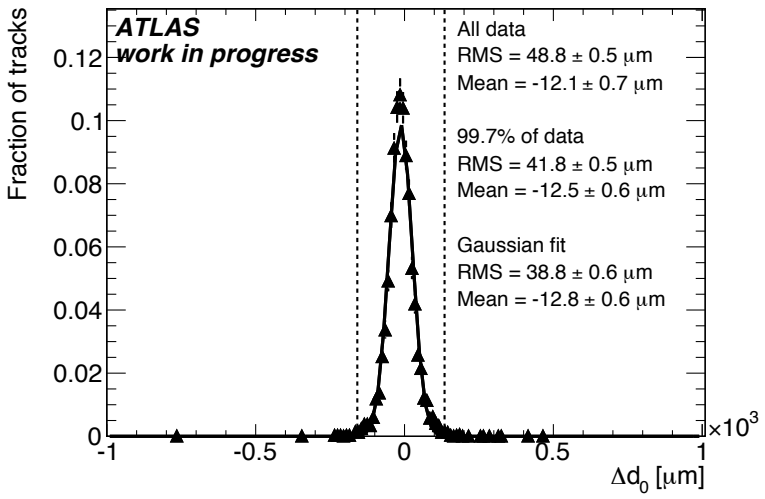

Figure 5.23: Distribution of the difference $\Delta(d_0) = d_{0\text{up}} - d_{0\text{down}}$ for tracks satisfying tight quality cuts (see Section 5.4.2). The mean and the RMS of the distribution are computed with different methods. The dashed lines show the limits including 99.7% of data. Tracks are reconstructed by the `NewTracking` algorithm.

The simplest procedure to extract mean and RMS, just computes these two values according to their definition, using all the N entries included in the distribution:

$$\text{Mean} = \frac{1}{N}\sum_{i=1}^{N} x_i, \tag{5.47}$$

$$\text{RMS} = \sqrt{\frac{1}{N}\sum_{i=1}^{N} x_i^2}. \tag{5.48}$$

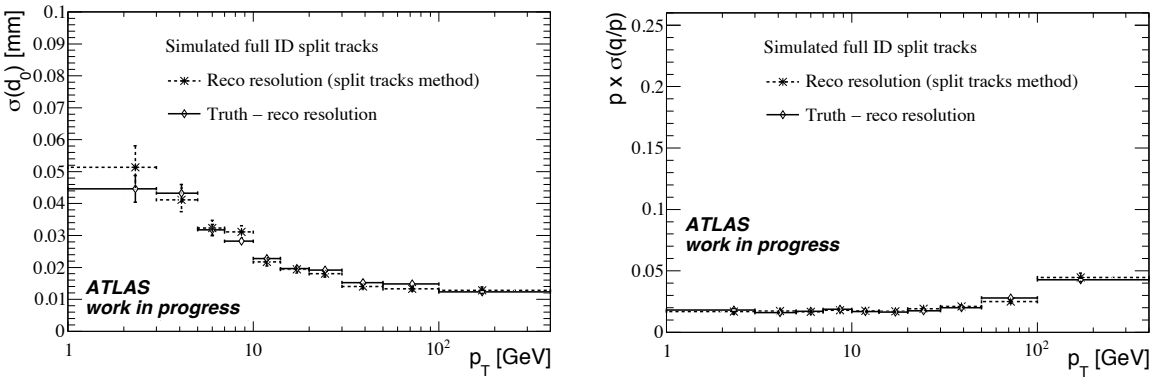

(a) (b)

Figure 5.24: Resolution in d_0 (5.24(a)) and in $p \times q/p$ (5.24(b)) as a function of transverse momentum for simulated tight tracks. The resolution computed by the split tracks method is compared with the difference between the true value of each parameter and its reconstructed value.

The problem concerning this method is that very few entries that are clearly due to imperfect track fitting (i.e. the outliers at $\Delta(d_0) \gtrsim 0.5$ mm in Figure 5.23) largely contribute to the value of the RMS.

Another common way to express the with of a distribution is to perform a Gaussian fit: in the case of a Normal distribution, the RMS of the distribution can be precisely approximated by the σ of the Gaussian. If the procedure is applied to the distribution shown, the tails and the peak are not described by the Gaussian shape. In particular the contribution of the tails tends to be systematically underestimated. These drawbacks are clear when comparing the fit Gaussian with the distribution in Figure 5.23.

The procedure that was chosen is the same chosen in the previous performance papers [120]. As a first step the mean_{all} and the RMS_{all} of all data are computed. Then boundaries are fixed, considering the $\text{mean}_{\text{all}} \pm 3$ times the RMS_{all}. Finally, the RMS and the mean values to be cited are computed using data included between the boundaries on a Gaussian distribution. This method is thus equivalent to reject 0.03% of the events. In Figure 5.23, the boundaries are drawn as dotted lines. It can be noticed that they include most of the significant tails while excluding extreme outliers, showing the robustness of the method. It should be remarked that other methods commonly used to compute the width of distributions (in particular Gaussian or double Gaussian fit of the distribution) would provide values substantially lower than the selected procedure. This fact can also be noticed comparing the results reported in Figure 5.23.

Validation of the track splitting method

In order to verify the validity of the split track method for resolution estimation, the simulation of cosmic ray data is used. Figure 5.24 shows the resolution in d_0 and in $p \times q/p$ as a function of transverse momentum for tight tracks. Simulated data have been used and resolution has been computed both by using the split tracks and by computing the difference between the true value of each parameter and its

	Tight tracks	*Medium* tracks	*Loose* tracks
d_0 [μm]	29.5 ± 0.4	69.2 ± 0.3	97.6 ± 0.4
z_0 [μm]	115 ± 1	479 ± 2	495 ± 2
ϕ_0 ($\times 10^{-4}$)	3.75 ± 0.04	6.09 ± 0.02	8.5 ± 0.3
θ ($\times 10^{-3}$)	0.97 ± 0.01	1.82 ± 0.01	2.0 ± 0.7
$p \times q/p$ ($\times 10^{-2}$)	3.29 ± 0.03	3.84 ± 0.01	6.17 ± 0.02

Table 5.4: Resolution of track parameters for the different track selections. Corresponding plots are shown in Figure 5.25.

value as reconstructed by track fitting. The equivalence of the two methods, and hence the reliability of the split track procedure, is verified by the plots.

Resolution of parameters

Figure 5.25 shows the Δ_τ distribution of the five track parameters, when using the selection described in this paragraph. Tracks were fitted by the `NewTracking` algorithm. The plots reported are normalized to allow for a comparison. A clear improvement of the RMS is visible for all the parameters when going from *Loose* quality tracks to *Tight* quality. Table 5.4 reports the resolutions obtained from the plots, for an easy comparison. Parameter resolutions are influenced by different aspects. For example, when considering the momentum ($p \times q/p$) in Figure 5.25(e), a big improvement is expected from loose to medium quality tracks, due to the fact that medium tracks should feature both silicon and TRT hits. The impact parameters resolution in Figure 5.25(a) and 5.25(b), instead, is mainly improved by requiring hits close to the perigee, in the Pixel Detector (i.e when going to medium to tight quality). The following of this chapter will analyze several of the aspects that characterize the resolution of the different parameters.

Other than the resolution, Δ_τ distributions can show informations about the global alignment of detectors. Since the mean of the distributions are expected to be zero, any statistically significant value for the mean should arise from systematic errors in the tracking procedure. Figure 5.26, for example, shows the $\Delta(d_0)$ distribution for both real and simulated data. Tracks reconstructed by the `NewTracking` algorithm are reported in Figure 5.26(a). In Figure 5.26(b) the same plot has been drawn with tracks from the `CTBTracking` algorithm. When looking to simulated data, in both plots, the mean is compatible with zero. Real data, instead, feature a 12 μm shift, regardless the tracking procedure. This suggests that the shift should be connected to some detector conditions not included in simulation, the most probable being the misalignment (see Section 5.1.5). Section 5.8 will analyze several systematic effects that were found in reconstructed tracks.

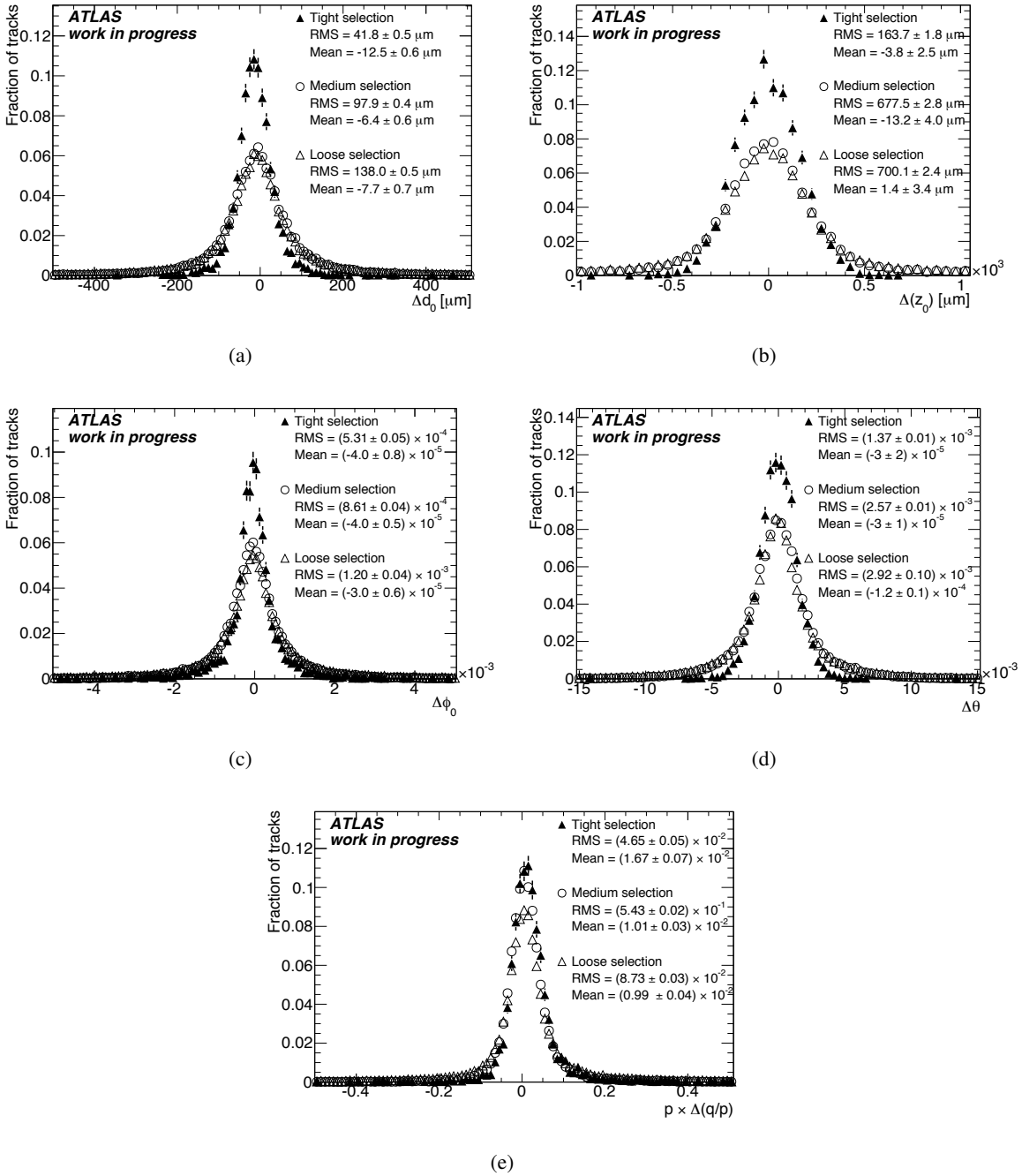

Figure 5.25: Δ_τ distributions of the five perigee track parameters for different track selections. Tracks are reconstructed by the `NewTracking` algorithm, using reprocessed data.

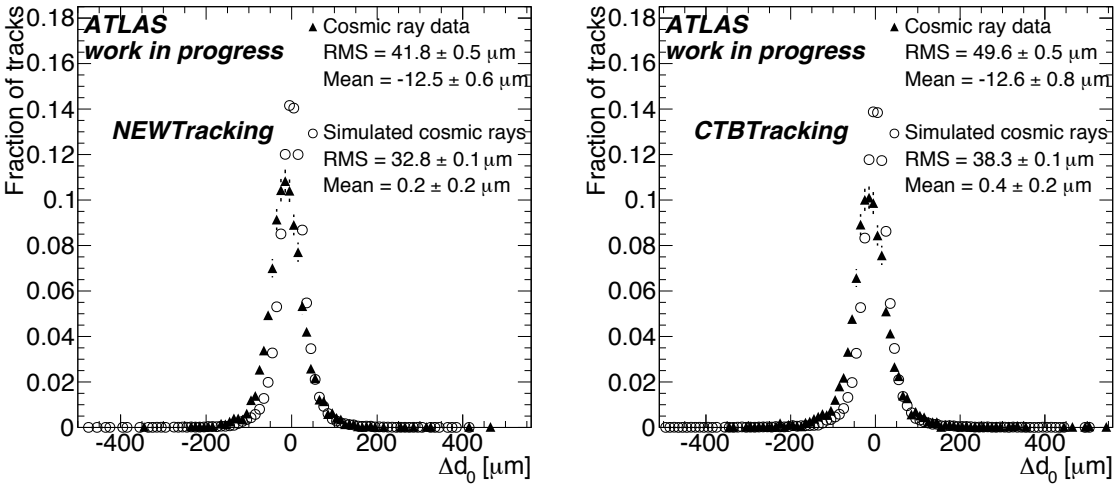

(a) (b)

Figure 5.26: Distribution of the difference $\Delta(d_0) = d_{0\text{up}} - d_{0\text{down}}$ for tracks satisfying tight quality cuts (see Section 5.4.2) when using the `NewTracking` algorithm (5.26(a)) and the `CTBTracking` one (5.26(b)). The plots include both simulated and real data. In the latter a clear shift of the mean of the distribution is observed, due to imperfect alignment.

5.5 Resolution as a function of impact parameters

Section 5.4.2 points out that cosmic ray tracks have a very specific impact parameter distribution. In particular, their impact parameter is uniformly distributed, while tracks from collisions come mostly from interaction point. In this section the resolution is studied as a function of the impact parameters, in order to understand how the resolution improves, when the perigee approaches the nominal interaction point.

In the following plots, real data are shown as well as simulated cosmic rays. The simulation provides a comparison to point out systematic errors due to poor alignment. At the same time, simulated tracks feature the better resolution that can be achieved with cosmic rays, by a fully commissioned detector. Real data have been analyzed using the software and the alignment constants released at the end of 2008 commissioning phase. All plots includes both `NewTracking` and `CTBTracking` track datasets, in order to compare the performance of the two algorithms.

In order to select data to be analyzed, tight tracks have been chosen. The requirement on the transverse impact parameter, anyway, has been relaxed to be:

$$|d_0| < 120 \text{ mm}. \tag{5.49}$$

This request allows to consider all tracks that feature an impact parameter smaller than the radius of the external pixel layer (see Figure 2.1). Furthermore, a tighter requirement on momentum has been

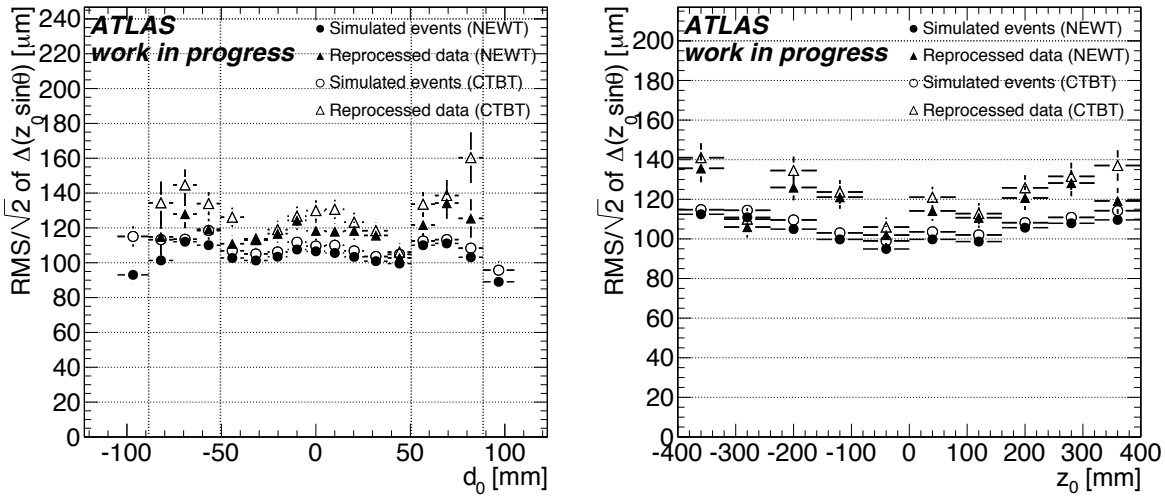

(a) (b)

Figure 5.27: Resolution of the longitudinal impact parameter $z_0 \sin\theta$ as a function of the transverse (5.27(a)) and of the longitudinal (5.27(b)) impact parameter of the track. Real data and simulation are shown, each dataset has been reconstructed with both `CTBTracking` and `NewTracking`, in order to compare the performance.

imposed, in order to mitigate the effect of multiple scattering, that is studied in Section 5.6:

$$p_{\mathrm{T}} > 5 \text{ GeV}. \tag{5.50}$$

Resolution in the longitudinal impact parameter

Figure 5.27 contains the plots showing the dependence of resolution in the longitudinal impact parameter $z_0 \sin\theta$ as a function of d_0 and z_0. Both simulation and real data exhibit the same pattern, pointing out that no systematic deformation derived from the misalignments of the detector.

When considering the transverse impact parameter dependence in Figure 5.27(a), the resolution is deteriorating when decreasing the impact parameter. This effect is due to the increase of the distance of the perigee from the last detector surface, that extend the length over which the extrapolation is performed. According to the convention introduced in Section 5.1.2, decreasing d_0 is equivalent to increase R_c. Furthermore, very clear dips are visible when the transverse impact parameter is near to the radius of the Pixel Detector layers. Dashed vertical lines have been used to mark the position of the Pixel Detector layers and to underline this discontinuities. This pattern is due to the fact that every time one less layer is crossed, the extrapolation length increases at once, resulting in a degradation of the resolution.

The plots in Figure 5.27(b) shows the $z_0 \sin\theta$ resolution as a function of z_0. The resolution improves when going toward the center of the detector and no major bias is seen in real data.

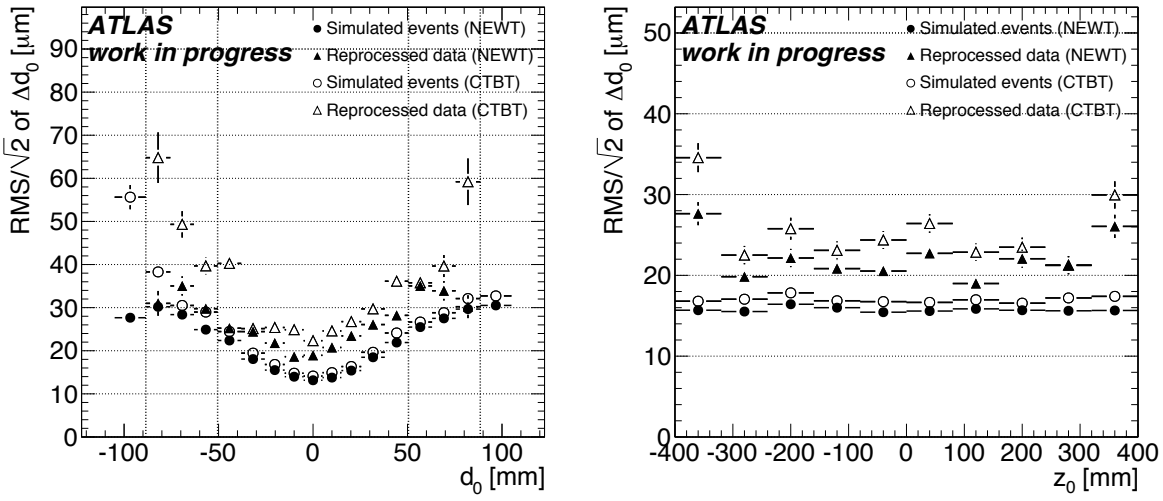

(a) (b)

Figure 5.28: Resolution of the transverse impact parameter d_0 as a function of the transverse (5.28(a)) and of the longitudinal (5.28(b)) impact parameter of the track. Real data and simulation are shown, each dataset has been reconstructed with both `CTBTracking` and `NewTracking`, in order to compare the performance.

As a conclusion, the expected resolution in the longitudinal impact parameter for tracks with small d_0 and z_0 can be quoted. When using `NewTracking` algorithm, a resolution between 110 and 120 μm is foreseen. From a comparison with the simulated cosmic rays, residual misalignments can be accounted for a ~ 30 μm contribution to the measured resolution.

Resolution in the transverse impact parameter

Figure 5.28 shows the resolution of the transverse impact parameter d_0. In Figure 5.28(a), resolution is drawn as a function of d_0 itself. The resolution is clearly improved when approaching the origin of the reference system. This improvement happens despite the longer distance between the perigee and the last measurement. In this case, tracks that feature a small d_0 are crossing the Pixel Detector modules within a small range of incident angle, where the resolution of the detector is optimal (see Section 4.6). The better performance of the Pixel Detector is enough to overcome the longer extrapolation uncertainty, resulting in an overall improvement of resolution in d_0. As in the previous case, some discontinuities can be noticed for d_0 similar to the layer radii. Anyway the effect is much smaller than in the z_0 resolution case.

In Figure 5.28(b), the dependence of the resolution of the transverse impact parameter is shown as a function of z_0. If looking at simulation, a flat distribution is seen. This behaviour is not found in data, where a oscillating pattern is found. This is more visible in `CTBTracking` reconstructed tracks. A possible explanation of this effect is a deformation of the detector as will be presented in Section 5.8.

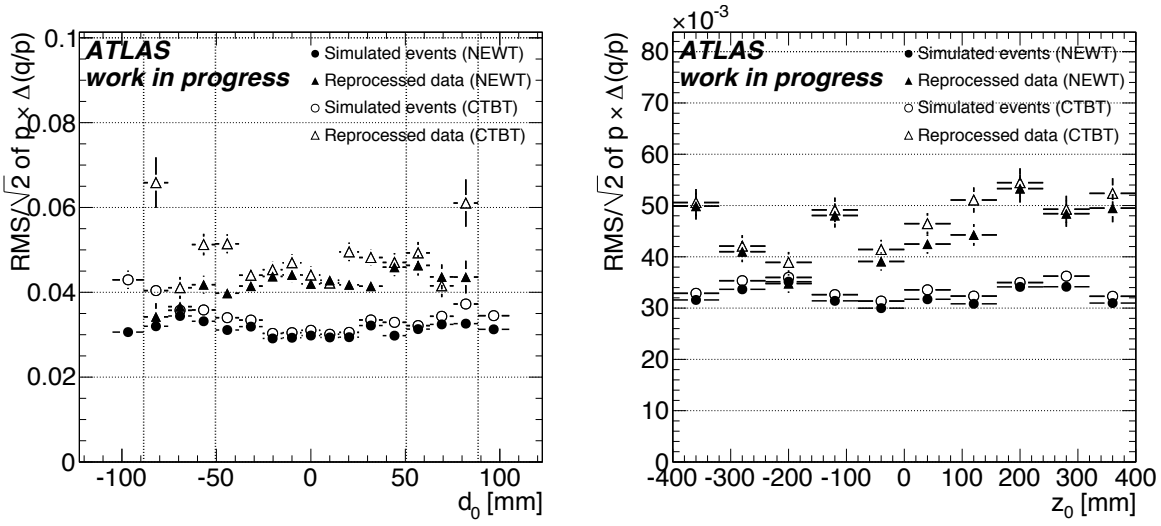

(a) (b)

Figure 5.29: Resolution of the q/p parameter as a function of the transverse (5.29(a)) and of the longitudinal (5.29(b)) impact parameter of the track. Real data and simulation are shown, each dataset has been reconstructed with both `CTBTracking` and `NewTracking`, in order to compare the performance.

The minimum obtained for the d_0 resolution is about 18 μm for the `NewTracking` algorithm, while a slightly worse value of 22 μm is reached by the `CTBTracking` procedure. This value can be compared with simulated data, that feature 12 and 14 μm, respectively. From the comparison, a contribution of ~ 15 μm is estimated from alignment. The effect of misalignment is thus smaller with respect to the $z_0 \sin\theta$ resolution.

Resolution in momentum

Figure 5.29 shows the resolution in momentum. In Figure 5.29(a) the resolution is plotted as a function of d_0. The simulated tracks feature a flat distribution in the central part of the plot, while a small worsening is seen when one less layer is crossed by particles. This is compatible with the dependence of the momentum resolution on the lever arm. The TRT maximum radius is in fact about 1 m (see Figure 2.1), while considering or not the inner Pixel Detector layer only varies the lever arm by about 4 cm, that means the 4% of the entire length. When considering real data, the flatness of the distribution is less evident, in particular for `CTBTracking` tracks, due to residual misalignments in the detector.

In Figure 5.29(b), the resolution in the momentum is plotted as a function of z_0. Also in this case, the resolution is almost flat for simulated cosmic rays. The distribution of data, instead, is dominated by misalignments and no clear pattern can be seen.

An overall estimate of the performance points out resolution in momentum of about 4% when using `NewTracking`. A comparison with simulated data allows to compute a contribution of 2.7% to the resolution due to the residual misalignments.

Comparison between NewTracking and CTBTracking

All the studies that are reported in his section have been performed both on tracks obtained by the NewTracking default algorithm and by the CTBTracking procedure. From a global comparison between the two algorithm, it can be concluded that NewTracking is more accurate in all the cases. Anyway, the difference between the two algorithms is greater when looking at real data with respect to simulation: CTBTracking seems to suffer more the poor alignment with respect to NewTracking. The largest difference is seen when studying the transverse impact parameter as a function of z_0: for small z_0 discrepancies reach 20% of the measured resolution.

All the analysis in the following sections have been replicated with both tracking algorithm. Since the performance has always resulted similar to what reported in this section, and since the discrepancies are homogeneous among different analysis, comparisons have been omitted from now on. Only results from NewTracking will be reported, unless stated explicitly.

5.6 Resolution as a function of transverse momentum

Resolution in momentum

In Section 5.1.2 an expression for the resolution in momentum has been derived, pointing out its dependence on the lever arm of the detector (i.e. the distance between the last detector layer and the first one) and on momentum itself (see Eq. 5.18). Figure 5.30 shows the RMS of the $p \times \Delta(q/p)$ parameter as a function of p_{T}, for different datasets. In the plot, a clear increasing in the resolution is seen going to higher momenta. Furthermore, tracks fitted by all the Inner Detector are compared to tracks fitted by the silicon detectors only. The full Inner Detector clearly outperform the silicon detectors alone, due to the longer lever arm. When going to low momentum, instead, the resolution approach a constant value, due to multiple scattering contribution (see Section 5.1.3) and the impact of lever arm difference is less effective. The agreement between the resolution on simulation and data at low momentum is a verification that the amount of material in the simulation properly describes the detector structures.

Multiple scattering effect

Other than the uncertainty of momentum, also the resolution of each generic track parameter τ can be expressed as a function of the transverse momentum p_{T}. This is due to the fact that multiple scattering is the dominant noise process in track fitting at low momentum (see Section 5.1.3). At high momentum, instead, multiple scattering vanishes and the parameter resolution is dominated by the intrinsic detector resolution. Thus, in a simplified model, the track parameter resolution can be expressed as the sum in quadrature of two terms [67]:

$$\sigma_\tau(p_{\mathrm{T}}) = A_\tau \oplus B_\tau / p_{\mathrm{T}}. \tag{5.51}$$

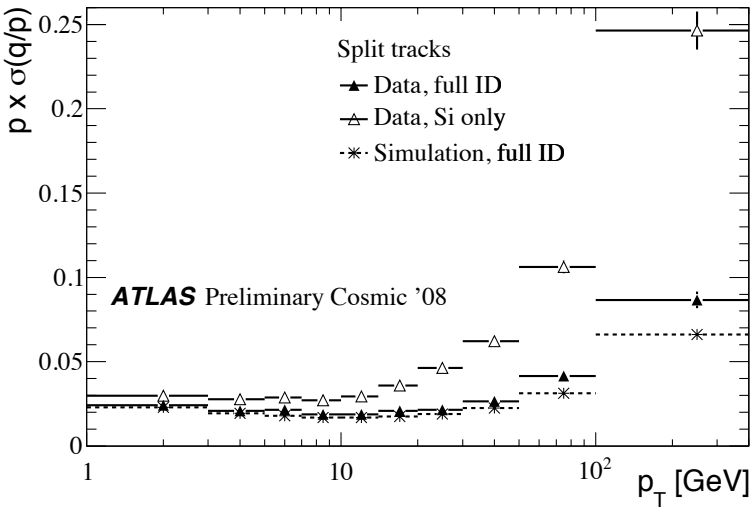

Figure 5.30: Resolution of the momentum for simulated cosmic rays and for data reconstructed by the full Inner Detector and by the silicon detectors only.

The A_τ contribution describe the detector intrinsic resolution, without considering particle interaction with the material. This term has been analyzed in Section 5.5 for momentum and impact parameters. Eq. 5.51 can also be expressed through the asymptotic resolution at infinite momentum $\sigma_\tau(\infty)$:

$$\sigma_\tau(p_\mathrm{T}) = \sigma_\tau(\infty)(1 \oplus P_\tau/p_\mathrm{T}), \tag{5.52}$$

where P_τ marks the critical momentum where the contribution of the intrinsic measurement error and the multiple scattering are equal. Eq. 5.51 and 5.52 are approximate, working well at high p_T and at low p_T, while they are not accurate in the median range. In this model, $\sigma_\tau(\infty)$ and P_τ are implicitly functions of θ. The dependence on θ of the multiple scattering term B_τ for each track parameter has been computed in Section 5.1.3. When analyzing cosmic ray data, the angular distribution of tracks is peaked on two single values, due to geometry of the detector hall. Therefore the dependence on θ cannot be observed and the dependence on p_T is sufficient to describe data.

In order to verify the proposed model, Figure 5.31 shows the resolution of the track parameters as a function of the transverse momentum of the associated cosmic muon. The set of parameters shown has been slightly adapted, in order to match the studies performed in [120, 142].

All the plots shown in Figure 5.31 have been built using `NewTracking` fitted tracks. Tracks have been selected according to *tight* selection cuts, and three different datasets are used. Simulated data are plotted as a reference, showing the resolution that would be expected with a detector perfectly commissioned. Real data are plotted using tracks from two different stages of the commissioning. Open markers represent tracks as they were reconstructed at the beginning of the commissioning phase. Closed markers represent the same data, as they are reconstructed at the end of the commissioning: new alignment and calibrations have been applied, as described in Section 3.4. While the expected shape is

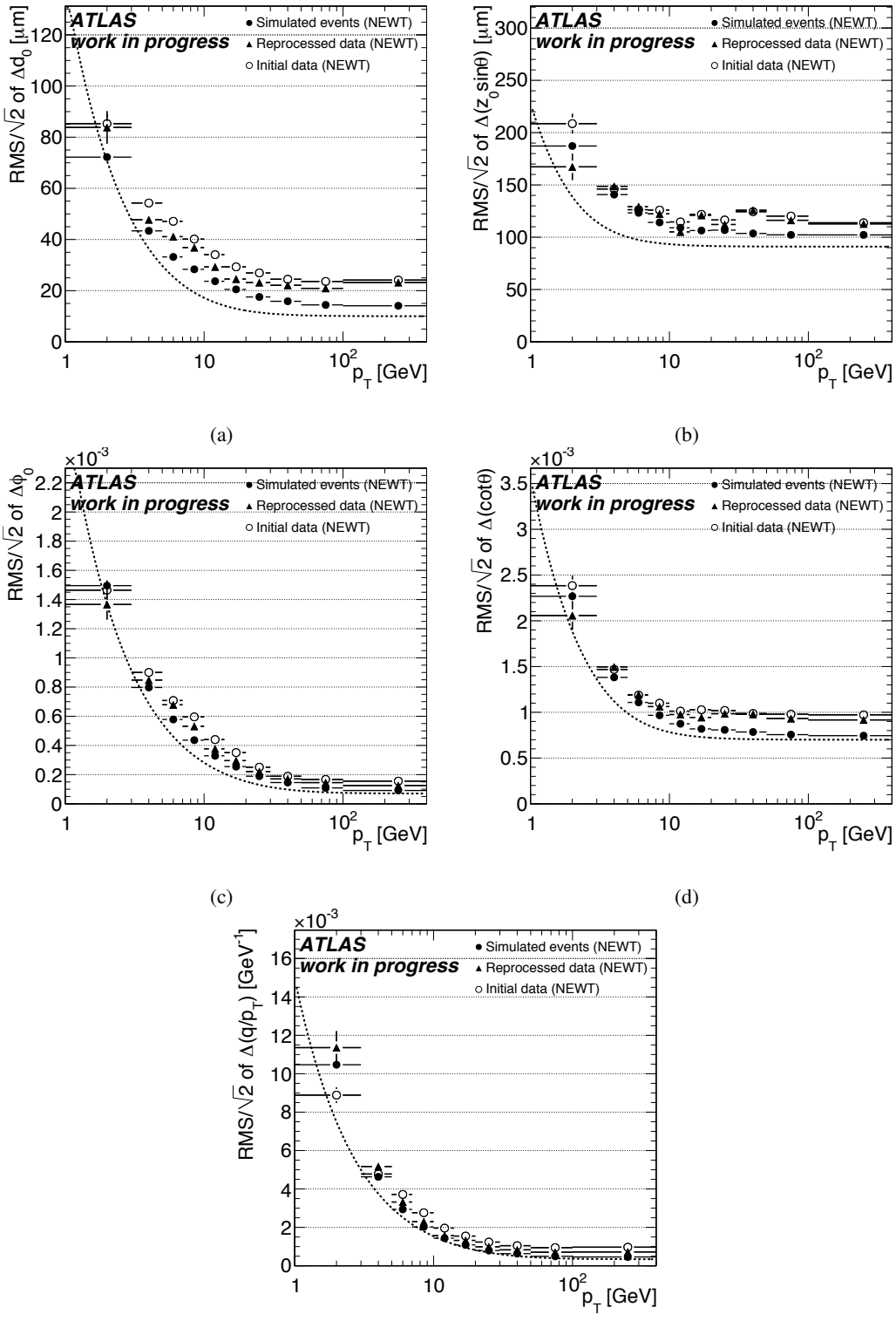

Figure 5.31: Resolution of the track parameters as a function of the momentum of the cosmic muon for different alignment calibration. The dotted lines represent an analysis developed on collision data. More details in Section 5.6.

	CSC analysis		Simulated cosmic rays		Reprocessed data	
	$\sigma_\tau(\infty)$	P_τ	$\sigma_\tau(\infty)$	P_τ	$\sigma_\tau(\infty)$	P_τ
q/p_{T}	0.34 TeV^{-1}	44 GeV	0.44 TeV^{-1}	38.6 GeV	0.67 TeV^{-1}	28.3 GeV
d_0	10 μm	14 GeV	15.4 μm	11.4 GeV	22.1 μm	8.5 GeV
$z_0 \sin\theta$	91 μm	2.3 GeV	105 μm	3.2 GeV	115 μm	2.6 GeV
ϕ_0	70 μrad	39 GeV	100 μrad	36 GeV	136 μrad	28.5 GeV
$\cot\theta$	0.7 $\times 10^{-3}$	5 GeV	0.8 $\times 10^{-3}$	6 GeV	0.9$\times 10^{-3}$	4.5 GeV

Table 5.5: Comparison of the parameters that describe resolution as a function of p_{T} for the analysis reported in this thesis with respect to the "CSC analysis".

clearly visible when using simulated tracks, some fluctuation are present in data, especially for $z_0 \sin\theta$ and $\cot\theta$ that describe the tracks in the longitudinal plane. Nevertheless, the enhancement in the resolution brought by the improved alignment is clearly visible over the full momentum range.

As a comparison with existing papers [120], a dotted line is drawn on the plots. It corresponds to an analysis performed with simulated single-particle (muons and pions) data, the so called "CSC analysis". In that analysis, the $\sigma_\tau(\infty)$ and P_τ values were calculated from a fit, after selecting optimal tracks and dividing the sample into several η bins: the results shown are computed for $0.25 < |\eta| < 0.50$. In particular the requirement on the impact parameters was much tighter than the one used for the cosmic data:

$$|d_0| < 2 \text{ mm}, \tag{5.53}$$

$$|z_0 \sin\theta| < 10 \text{ mm}. \tag{5.54}$$

Furthermore, single-particle data were simulated using perfect alignment and exact knowledge of the inert detector material. In this sense, the performance of the "CSC analysis" should be regarded as the nominal performance of the track reconstruction, while it is clearly recognised that these performance numbers will not be met with cosmic ray data.

For the cosmic ray data sample, the statistics is not enough to implement a selection of tracks similar to the "CSC analysis", so a simple fit of the distributions reported in Figure 5.31 is performed, using the function described by Eq. 5.52. Results are reported in Table 5.5, together with the parameters from the "CSC analysis". A comparison of the values shows that the current performance of the Inner Detector are a very good starting point, if considering that they show the performance that will be available already at the first collision data. When comparing with simulated cosmic rays, a difference of about 40-50% is found in the asymptotic resolution, for transverse parameters. The performance is better for longitudinal data, where the discrepancy is only 10%. The final improvement of the resolution will be possible only when high statistics of tracks coming from the interaction point will be available. This will allow to further investigate the systematic effects due to the misalignment of the detector that are outlined in Section 5.8.

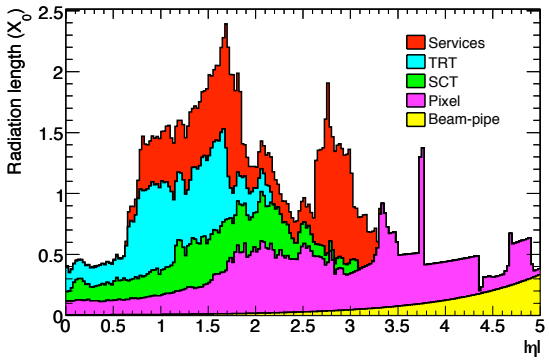

Figure 5.32: Material distribution (X_0) at the exit of the ID envelope, including the services and thermal enclosures. The distribution is shown as a function of $|\eta|$ and averaged over R. The breakdown indicates the contributions of external services and of individual sub-detectors, including services in their active volume. Figure taken from [120].

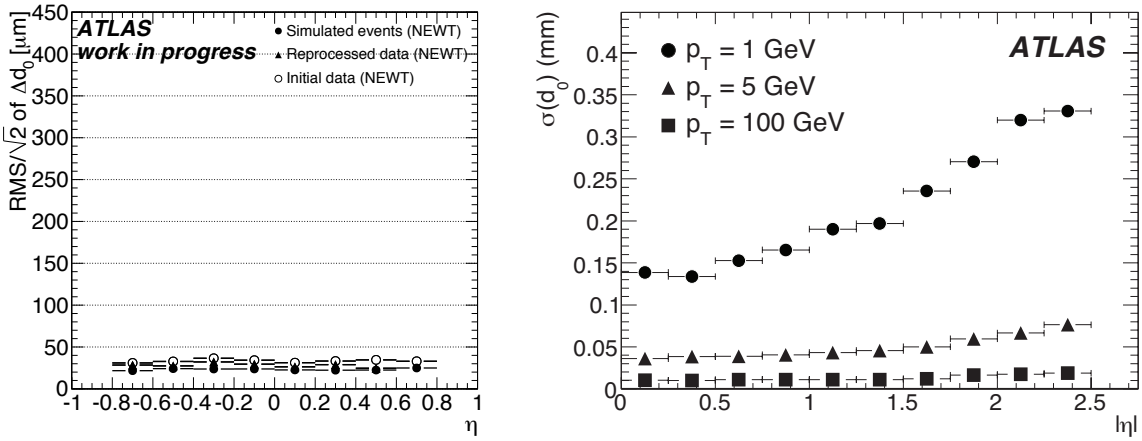

(a) (b)

Figure 5.33: Resolution of the transverse impact parameter d_0 as a function of the pseudorapidity of the track. 5.33(a): cosmic ray results for simulated data and for real particles. Data are analyzed with different alignment versions. 5.33(b): results for simulated collision pions.

5.7 Resolution as a function of pseudorapidity

It has been shown in Section 5.1.3 that the resolution of track parameters depends on the global θ of the track, due to multiple scattering effects. Figure 5.32, in fact, shows the material distribution of the Inner Detector as a function of $|\eta|$: its thickness is approximately described for by a $1/\sin\theta$ dependence for $|\eta| < 2$. A particle coming from the interaction point will traverse a very different amount of material, as per its pseudorapidity: this effect is the dominant cause of the resolution variations as a function of η. For the z measurement at high momentum, this effect is counterbalanced by the improved resolution of the Pixel Detector for high incidence angle, due to charge sharing interpolation (see Section 4.6).

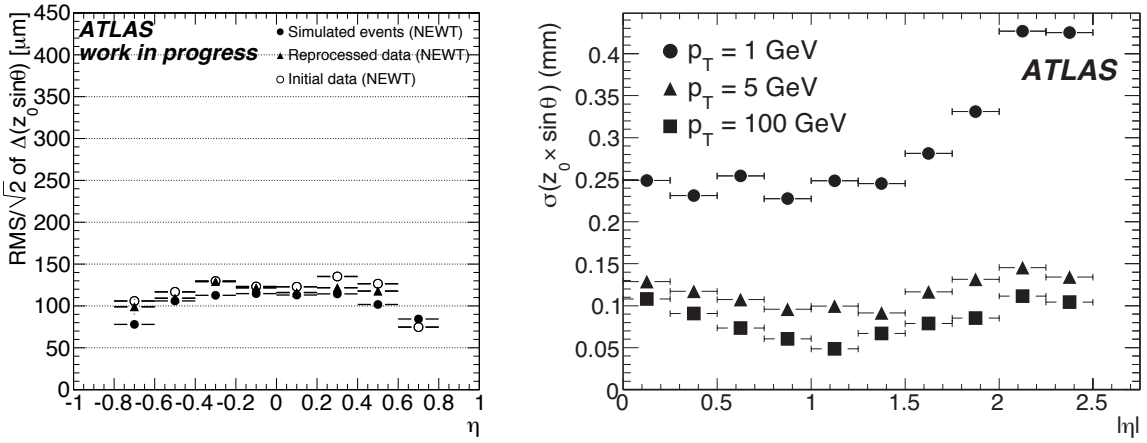

Figure 5.34: Resolution of the longitudinal impact parameter $z_0 \sin\theta$ as a function of the pseudorapidity of the track. 5.34(a): cosmic ray results for simulated data and for real particles, analyzed with different alignment versions. 5.34(b): results for simulated collision pions.

From Figure 5.33 to 5.36 the track parameter resolutions calculated from cosmic ray data are drawn as a function of η. The criteria used to analyze cosmic ray tracks are the tight ones. As a comparison, analogous plots taken from the "CSC analysis" [120] are reported for d_0, $z_0 \sin\theta$ and $p_T \times q/p_T$. Also in this case, the track selection is identical to the previous description. The CSC plots for the impact parameters resolution use simulated *pions*, while the one for momentum uses *muons*. This choice was made because strongly interacting particles suffer multiple scattering more that leptons. Impact parameter measurement is mostly used to tag b-jets, that are made of strong interacting particles. On the other side momentum resolution is crucial for muons used to reconstruct W and Z decays and resonances in $\mu^+\mu^-$ pairs. In the comparison reported, cosmic rays that traverse the detector are almost entirely composed by muons. Anyway the discrepancies due to the cosmic ray spatial distribution are expected to be more severe than the ones due to the mismatch in the particle type. Due to the restricted η distribution for cosmic rays, the comparison can only be performed for $\eta < 0.8$.

Figure 5.33 shows the transverse impact parameter resolution. No clear dependence is seen on η. The resolution that is obtained at the end of the commissioning lies between 20 μm and 35 μm slightly less than the performance obtained on 5 GeV pions in the CSC Analysis for the same η range.

Figure 5.34 displays the resolution for the longitudinal impact parameter $z_0 \sin\theta$. In this case a clear dependence on η is seen, also in simulated data, as the resolution improves when increasing the pseudorapidity. A similar slope is seen also in simulated collision data for $|\eta| < 1$. The main contribution to the resolution in the longitudinal impact parameter is the resolution of the Pixel Detector. From a comparison with Figure 4.29(b), this fact evident: when $|\eta| = 1$ the minimal resolution is reached for pixel local y coordinate and therefore also for the longitudinal impact parameter. The value

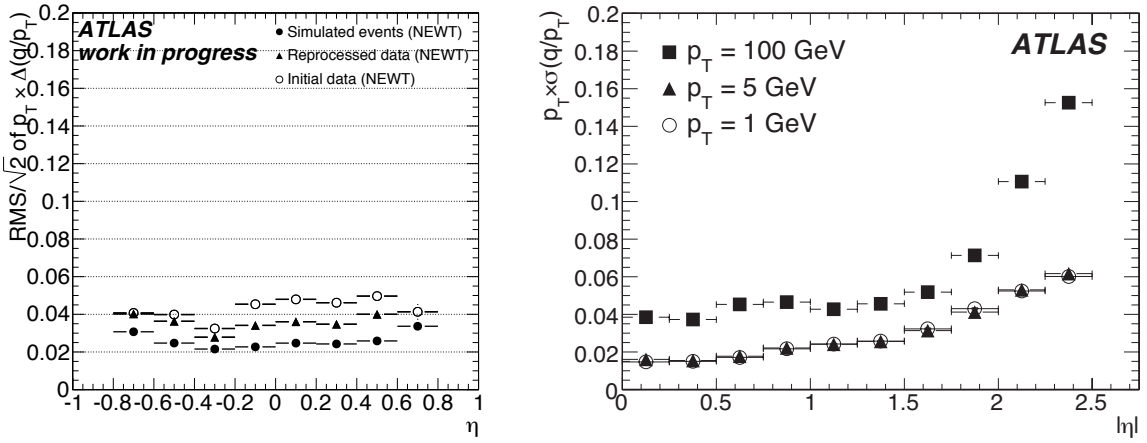

(a) (b)

Figure 5.35: Resolution of the relative inverse of the transverse momentum $p_{\mathrm{T}} \times q/p_{\mathrm{T}}$ as a function of the pseudorapidity of the track. 5.35(a): cosmic ray results for simulated data and for real particles, analyzed with different alignment versions. 5.35(b) results for simulated collision muons.

for the resolution in $z_0 \sin\theta$, when using cosmic ray tracks, is similar to the expected one for 100 GeV pions in collisions, ranging from 100 to 130 μm for data analyzed at the end of the commissioning.

Figure 5.35 shows the resolution obtained for the momentum. The $p_{\mathrm{T}} \times q/p_{\mathrm{T}}$ variable is used for compatibility with the CSC analysis. Some asymmetry is visible in cosmic ray data, because of the different momentum spectrum of cosmic ray tracks for different angular regions (due to the modulation by the access shaft). As a global effect, the resolution worses for $|\eta| > 0.5$. This result is understandable if considering that the main contribution to momentum resolution is the long lever arm provided by the TRT: when the incident angle get larger, the material (an thus the uncertainty on the measurements) traversed in the TRT increases. In all cases the observed resolution is bracketed by the CSC resolution for 1 GeV and 100 GeV particles. The impact parameters have values close to the expectation from 5 GeV particles, as expected on average given the cosmic ray momentum spectrum.

Finally, Figure 5.36 shows the resolution for the angular track parameters. Their distributions appear to be similar to the one of the corresponding impact parameter. For the ϕ_0 parameter in Figure 5.36(a) it can be noticed that the resolution has improved from the first reconstruction to the last reprocessing of data, almost reaching the values obtained using simulated cosmic rays. On the contrary, only little improvement is seen on the $\cot\theta$ variable in Figure 5.36(b). Finally, a clear improvement is seen also in the momentum resolution. Since the TRT has no impact on the measurement of longitudinal parameter, these observations can point out that the last version of the alignment constants has substantially improved the TRT position estimate, while the relative position of silicon elements is almost unchanged.

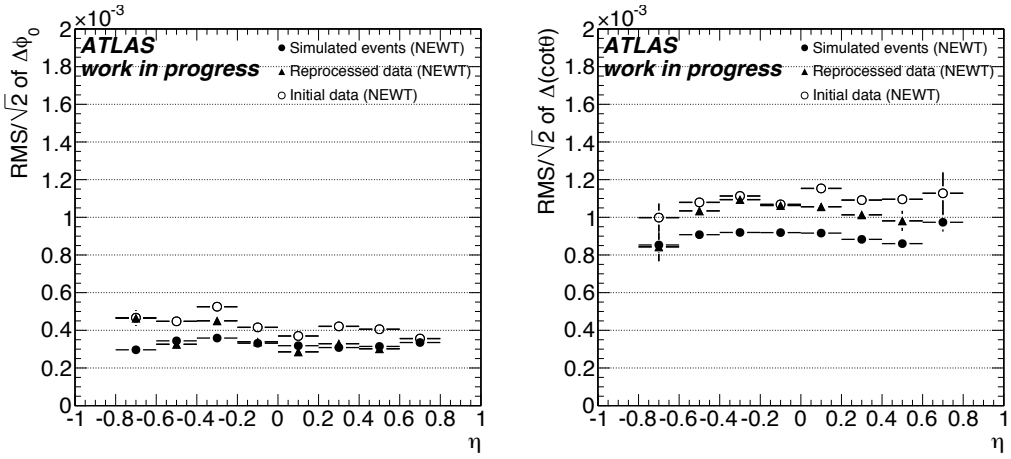

(a) (b)

Figure 5.36: Resolution of the track angular parameters ϕ_0 (5.36(a)) and θ (5.36(b)) as a function of the pseudorapidity of the track. Cosmic ray results are shown for simulated data and for real particles, analyzed with different alignment versions.

5.8 Systematic errors in tracking

Other than measuring resolution performance of the detector, the analyses done with cosmic ray data allowed to identify some systematic effects that appear during track fitting. The primary origin of these effects has been identified as the poor knowledge of the actual position of all the detector elements that compose the Inner Detector. Alignment procedures (see Section 5.1.5) are in fact applied to determine the shifts to which detector modules are subjected. The effect of the corrections calculated by alignment procedures is shown for example in Section 5.6, where resolution appears to have improved by about 5–10%. Nevertheless the reduced statistics of cosmic ray data in certain angular regions limits the overall alignment resolution. In addition, other detector specific contributions can play an important role in the determination of the tracking performances, sometimes mixing up with alignment issues. A clear example of these interplays between detector calibration and position estimate is reported in Section 4.3.3 where the *Lorentz angle* for charge drifting in the Pixel Detector is described. In this case, a wrong calibration of the Lorentz angle can be "absorbed" by alignment procedures as a shift of each pixel module. Anyway, when detector conditions change (e.g. magnetic field is switched off, temperature varies, ...) the Lorentz angle is modified and the alignment corrections result in fake shifts of the modules.

The analysis of cosmic ray data allowed to compute alignment constants using all the procedures described in Section 5.1.5. Furthermore, Section 5.3.2 introduced the improvement obtained on the residual distribution relative to each detector barrel. Figure 5.37(a) shows the effect of the constants calculated with different algorithms on the Δd_0 distributions. Tight split tracks from the first reconstruction have been used, with an additional requirement $p_T > 2$ GeV. Analyzing all the track parameters,

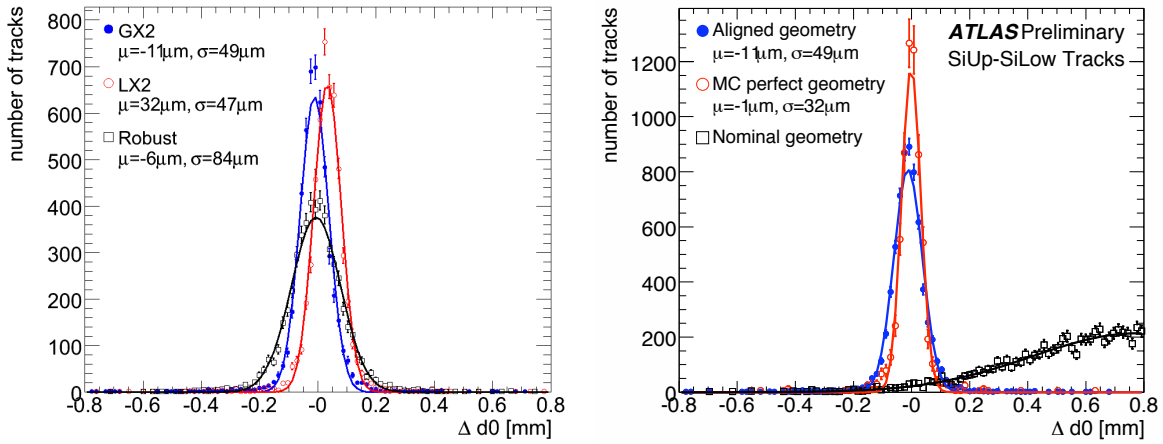

(a) (b)

Figure 5.37: 5.37(a): comparison of different alignment methods performance on cosmic ray data. 5.37(b): Δd_0 distribution before alignment, after alignment and for simulated tracks.

the algorithms that give the best results are the Local χ^2 and the Global χ^2, the latter being the default choice for the alignment. In this particular case, from a Gaussian fit, the resolution on d_0 is slightly better when using the Local χ^2, while the mean of the distribution is closer to zero for the Global χ^2. The Robust algorithm is clearly outperformed when dealing with the entire detector.

When comparing different algorithms it should be considered that differences in the implementation are optimized in order to solve misalignments of different structures. Since the alignment of the entire detector is divided into *levels* (see Figure 5.7), the procedures can be mixed in order to use different procedures at different levels. The Robust algorithm, for example, can give better results than the other methods, if considering small substructures that feature large overlapping areas. The alignment of the Pixel Detector substructures with overlap residuals often gives results better than the other procedures, as in the case of the successfully treatment of the stave bow in the Pixel Detector. Figure 5.38 shows the bow effect by plotting the position of the hits measured on two different Pixel Detector staves (see Section 2.1). The stave shown in Figure 5.38(b) has the expected straight distribution, while the one in Figure 5.38(a) shows a clear bending. The sketch reported below the plot clarifies the module shifts that cause the bending in the distribution of the hits.

Figure 5.37(b) compares the Δd_0 distribution for different alignment data sets. The nominal geometry distribution contains the tracks as they are reconstructed when no alignment constants are used. The MC perfect geometry data, instead, use simulated cosmic rays to describe a detector with all the module position perfectly known. Finally, the aligned geometry distribution shows the cosmic ray tracks reconstructed while applying the corrections calculated by the Global χ^2 algorithm. A very big improvement is seen when correcting the module position, resulting in only 10 μm shift for the mean and about 35% degradation for the resolution.

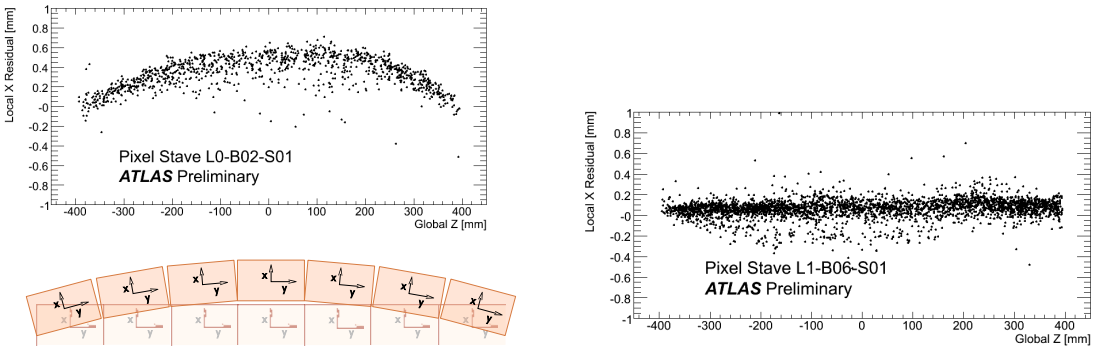

(a) (b)

Figure 5.38: Hits on two pixel staves. 5.38(a): a clear deformation is seen. 5.38(b): no deformation.

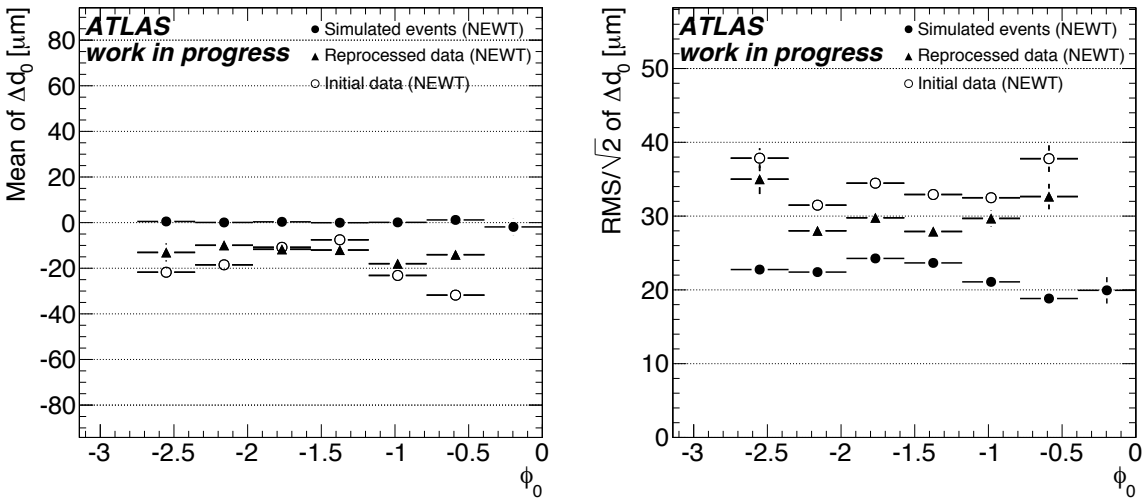

(a) (b)

Figure 5.39: Resolution in d_0 (5.39(a)) and mean of Δd_0 distribution (5.39(b)) as a function of ϕ_0.

The following of this section will identify some of the systematic effects observed after alignment. A special role in this study is assumed by *weak mode* deformations (see Figure 5.6). These are detector deformations that are not easily solved by alignment algorithm, since they do not influence the hit residual distributions. On the contrary, some of these deformation can be spot out by analyzing the mean of Δ_τ distributions.

Resolution as function of ϕ_0

Due to their peculiar angular distribution, cosmic ray tracks do not reach the detector uniformly over the azimuthal angle because the flux, especially for low momentum muons, is enhanced through the access pits (see Figure 5.21). This fact causes two main effects when reconstructing tracks:

– momentum of the muons as a function of ϕ_0 is not uniform,

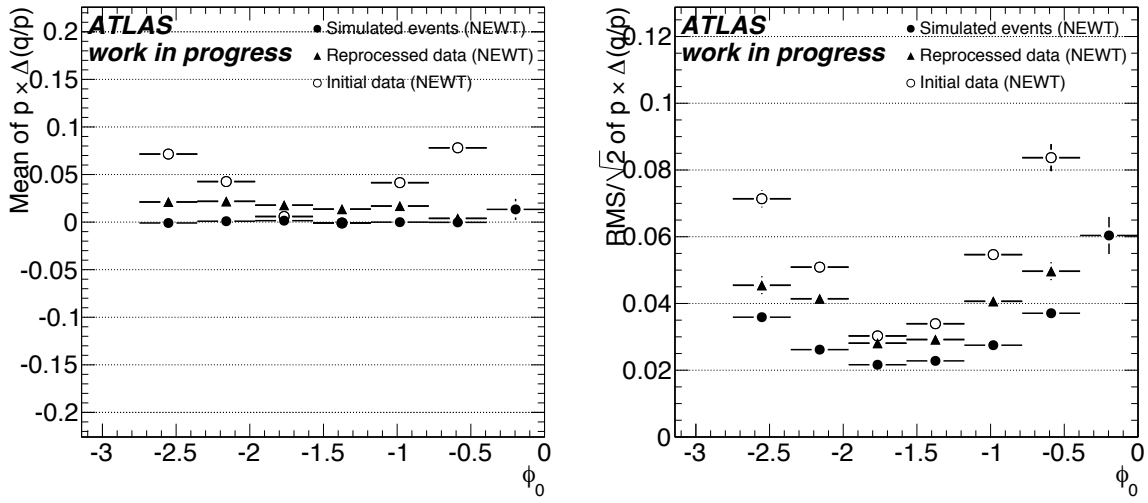

(a) (b)

Figure 5.40: Relative resolution in q/p (5.40(a)) and mean of $p \times \Delta(q/p)$ distribution (5.40(b)) as a function of ϕ_0.

– the alignment precision allowed by statistics as a function of ϕ_0 is not uniform as well.

While both effects act on the resolution, the alignment can be evaluated by looking at the mean of the Δ_τ distributions as a function of ϕ_0. Figure 5.39, for example, shows the mean of the Δd_0 distribution (Figure 5.39(a)) as well as the resolution in d_0 (Figure 5.39(b)). Both plots contain simulated events, that should exhibit no alignment bias, and real data. Real events have been analyzed by comparing the first reconstruction of the tracks, done with a preliminary set of alignment constants, with a reprocessing of the same events (see Section 3.4). The first reconstruction tracks show a resolution that worsen when approaching the horizontal direction ($\phi_0 \approx 0, \pi$), where the statistics is lower. When looking at the mean, simulated data show a flat distribution, perfectly compatible with zero. For real data a clear shift from zero is seen, which is larger for tracks near to the horizontal direction. The reprocessed dataset partially improves the resolution, getting closer to the simulated data, but a clear systematic effect is still present.

The same conventions are used in Figure 5.40, where the relative resolution in momentum and the mean of the $p \times \Delta(q/p)$ distribution are plotted. Also in this case, tracks from first reconstruction show bad resolution and large shift when approaching the horizontal direction. Reprocessed data recover the flatness of the mean distribution and obtain a resolution behaviour that is similar to the one measured from simulated cosmic rays. Anyway, a constant shift from zero is observed for the mean, as well as a constant worsening in resolution, with respect to the simulated data.

If comparing the mean of $\Delta(d_0)$ and $p \times \Delta(q/p)$, an anti-correlation is seen between the two distribution. Such correlation is expected, according to Eq. 5.19, and is clearly shown in Figure 5.41. In Figure 5.41(a), the fraction of full tracks is reported as a function of both the $\Delta(d_0)$ and the $\Delta(q/p)$

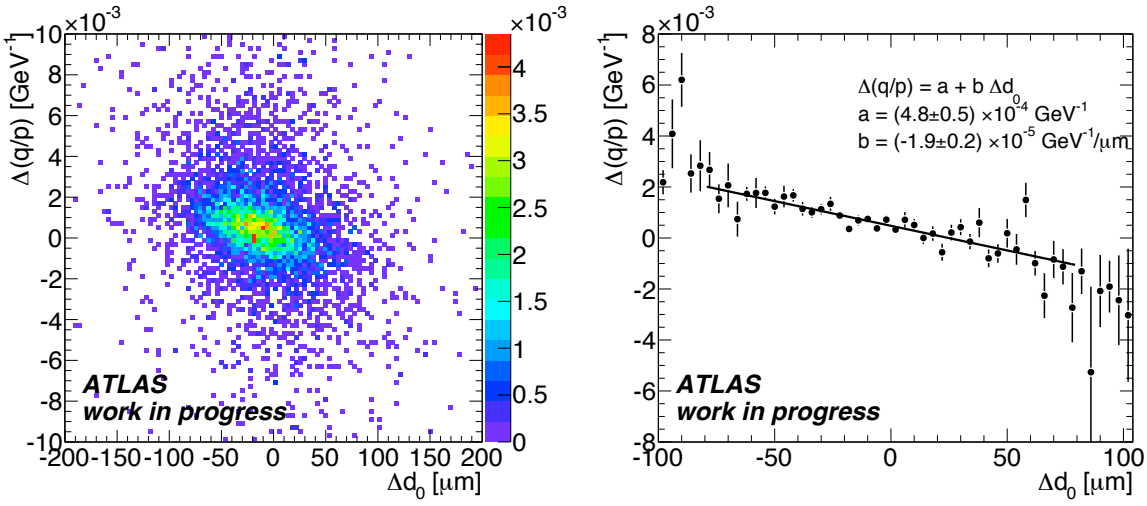

(a) (b)

Figure 5.41: Correlation between the resolution on the transverse impact parameter and the inverse of the momentum.

associated values. In Figure 5.41(b) instead, a fit is performed on the $\Delta(q/p)$ distribution as a function of $\Delta(d_0)$. A correlation of -1.9×10^{-5} GeV$^{-1}/\mu$m is measured.

As a final example, Figure 5.42 shows the resolution in $z_0 \sin\theta$ and the mean of the corresponding distribution. In this case, the resolution of data is closer to the one of simulated events, and the improvement due to the reprocessing is smaller with respect to other variables. If looking at the mean distribution, instead, a clear slope is seen with respect to ϕ_0 in data. The improved alignment corrections are not able to recover the slope that is clearly present in reprocessed data as well.

Resolution as function of z_0

The mean of the Δd_0 distribution has been studied as a function of z_0 to understand the z-dependent resolution in the first reconstruction of data. Even if the resolution has been improved in reprocessed data, some deformation still remains and have been reported in Figure 5.28. Figure 5.43(a) shows the mean distribution for simulated cosmic rays and for real events, as they appeared after the first reconstruction. A clear negative offset from zero is seen in data, increasing as z_0 itself. When tracks associated to particles with different charge are considered separately, as in Figure 5.43(b), they show the same negative offset. When looking at the mean of the $p \times \Delta(|q/p|)$ in Figure 5.43(b), a similar effect is seen as well. In this case the offset in data is positive for positive charged particles and negative for negative ones, increasing with z_0 as in the previous case. In simulated data, instead, the displacement from zero is smaller and always positive. The systematic shifts in the two plots are connected by the correlation that is foreseen between the impact parameter and the momentum (see Figure 5.41).

The variable $|q/p|$ has been used in order to show the variation in the absolute value of the curvature. In this case, since $\Delta(|q/p|) = |q/p|_{\text{up}} - |q/p|_{\text{down}}$, positive particles show a systematic overesti-

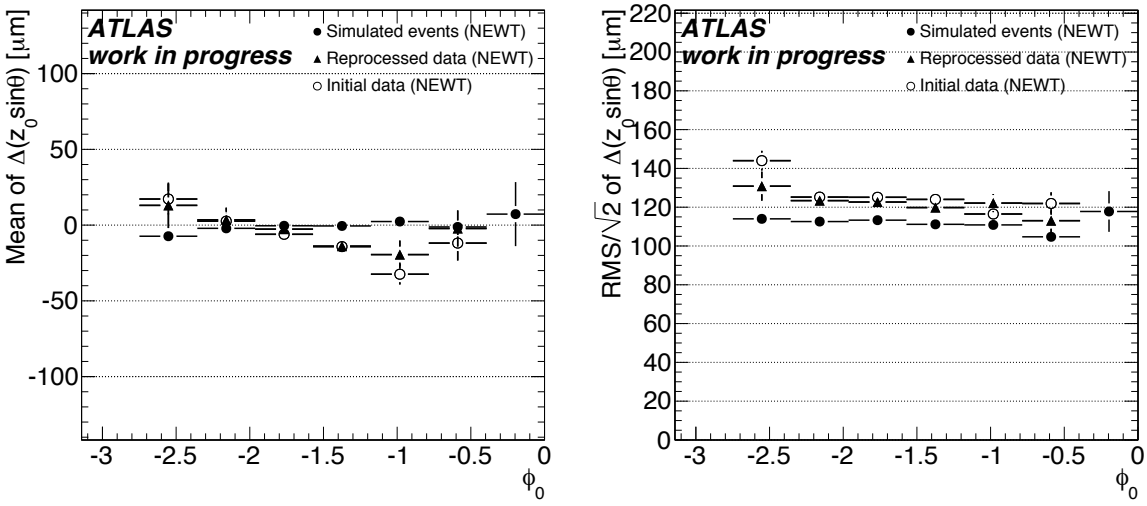

(a) (b)

Figure 5.42: Resolution in $z_0 \sin\theta$ (5.42(a)) and mean of $\Delta(z_0 \sin\theta)$ distribution (5.42(b)) as a function of ϕ_0.

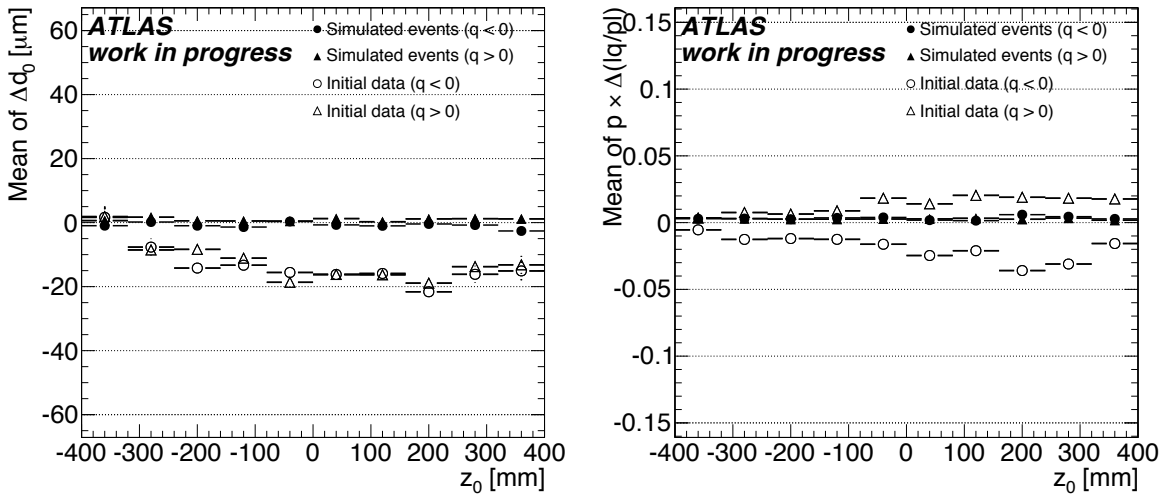

(a) (b)

Figure 5.43: Mean of the Δd_0 (5.43(a)) and $p\Delta(q/p)$ (5.43(b)) distributions as a function of z_0 for tracks associated to positive and negative charged particles, Tracks obtained after the first reconstruction of data are compared with simulated cosmic ray tracks. A evident slope is present in the distributions that contains real data.

mation of the curvature in the upper half of the detector with respect to the lower half, while negative ones are subjected to a systematic underestimation in the upper part. The z dependence is the one expected for a *twist* weak mode deformation (see Figure 5.6). The twist has been partially corrected by alignment procedures before executing the reprocessing of data. This is visible in Figure 5.44(a),

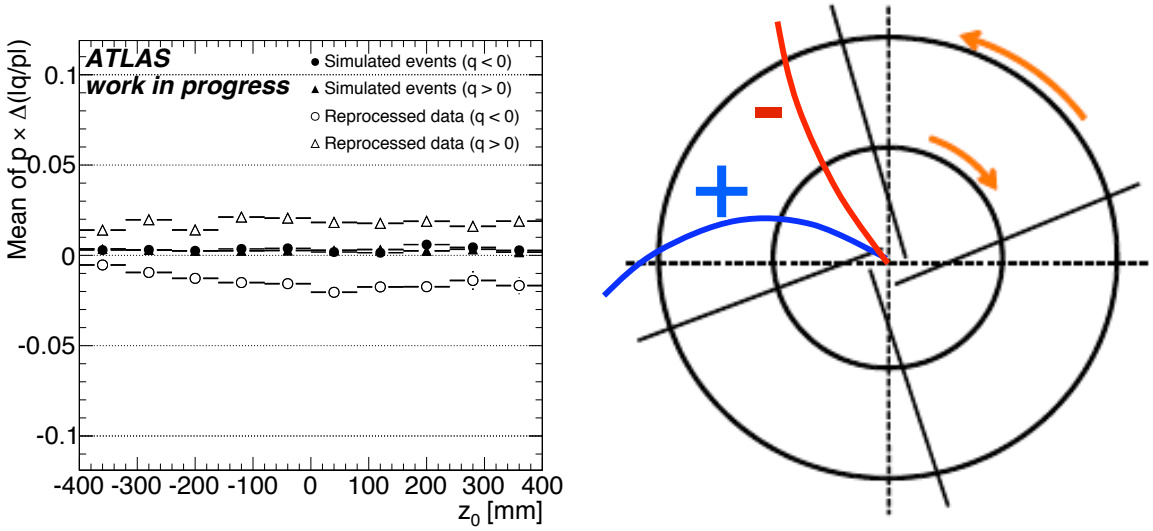

(a) (b)

Figure 5.44: 5.44(a): mean of the $p\Delta(1/p)$ distribution as a function of z_0 for tracks associated to positive and negative charged particles. 5.44(a): effect of the *curl* weak mode on track fitting for different charges. For the case shown, curvature is increased for negative charges and decreased for positive ones.

where the mean of the $p \times \Delta(|q/p|)$ distribution is closer to a constant as a function of z_0, when using reprocessed data. The wrong estimation of curvature instead is still present, as indicated by the displacement of the distributions from zero.

The sketch in Figure 5.44(b) shows the effect of the *curl* weak mode for a particular rotation. In this case a counter-clockwise rotation of the external layer with respect to the internal one, increase the curvature of positive tracks, while decrease the one relative to negative particles. The contrary happens in the lower layer, reproducing the effect seen in the plot on the left. This kind of deformation is thus a candidate to explain some of the degradation that is observed in resolution with respect to simulated data.

5.9 Conclusion

The ATLAS Inner Detector tracking system has been commissioned with cosmic ray tracks starting from October 2008. It showed low noise occupancy and excellent intrinsic efficiency. In order to asses the detector performance on LHC data, the properties of cosmic ray tracks have been analyzed and selection criteria have been implemented to select tracks that could resemble the trajectories of particles originating from collisions. Split tracks that traversed the barrel of the Inner detector gave the possibility to estimate the resolution in the different track parameters, as well as the biases caused by the misalignment of detector modules. This method allowed to monitor the improvements achieved in

the calibration of the detector and in the understanding of the alignment. All these efforts resulted in a reprocessing of all the data taken in autumn 2008. In this chapter, the performance at the end of this commissioning phase have been presented.

Two different reconstruction algorithm have been compared: the `CTBTracking`, that was used during test-beam operation, and the `NewTracking` that was applied on real events for the first time. The `NewTracking` performs better than `CTBTracking`, reaching a 30% better resolution in particular cases.

The effect of multiple scattering has been studied and compared with results obtained from simulated collisions as well as from simulated cosmic rays. The main difference between real and simulated detector has been identified in the alignment of detector structures, that is perfect in simulation. In particular, systematic effects due to weak mode deformations have been studied.

The top performance on the impact parameter measurement has been estimated using a selection of tracks that feature a transverse momentum larger that 5 GeV, and a number of measurements in all the detectors comparable with tracks coming from collisions. In this case, for tracks with transverse impact parameter smaller than 20 mm, a resolution of 18 μm has been measured in d_0. A similar selection of tracks features a resolution of about 110 μm in the longitudinal impact parameters, for tracks in the central region $|z_0| < 100$ mm.

These results can be compared with the nominal values of 7.5–14 μm for d_0 resolution, and 40–111 μm for z_0 resolution, depending on the incident angle of the track [142]. The nominal performance were computed from the simulation of single particles, originating from the interaction point and reconstructed with a perfectly aligned geometry. The tracks selected for the measurement featured $p_{\mathrm{T}} > 10$ GeV and $|d_0| < 2$ mm. These tight selections are not compatible with cosmic ray tracks geometrical distribution and much looser criteria have been used on data. It can be concluded that the resolutions of 18 μm in d_0 and of 110 μm in z_0 measured from cosmic rays, are a conservative estimate of the resolution foreseen for the first collisions.

Despite the above mentioned kinematic differences, cosmic ray tracks have been shown to be of particular importance for detector commissioning, giving the opportunity to measure tracking performance and to align the detector well before LHC collisions. Their different kinematics also allows to access regions not populated by collision tracks and therefore provide an additional handle for understanding alignment weak modes.

Conclusion

The studies presented in this thesis started in 2006, with the work on the usage of charge sharing for the improvement of position resolution in the Pixel Detector simulated data, and have been accomplished during 2009, by analyzing cosmic ray data collected during the commissioning of the ATLAS Inner Detector. The commissioning activity allowed to verify the perfect integration of all the sub-systems in the global ATLAS infrastructure, both from the hardware and from the software point of view. The analyses reported in this thesis have focused on two main objectives: the optimization of the Pixel Detector resolution and the evaluation of the performance of the tracking system, in particular the resolution in the impact parameter of the tracks from charged particles. The resolution in the impact parameter is correlated to the resolution in momentum and is determined by the quality of the Inner Detector measurements as well as by the precision of the track fit. The largest detector contribution is given by the resolution of the Pixel Detector, due to its close distance (5 cm for the innermost layer) with respect to the beam axis.

An optimal resolution in impact parameter is desired in order to apply b-tagging algorithms during event reconstruction. These algorithms allow to discriminate jets that contain b-hadrons from *light* jets — determined by the fragmentation of u, d, s or c quarks — and are based on the possibility to discern the fly path length ($c\tau \sim 450\ \mu$m) of b-hadrons. A reliable application of b-tagging is useful to select very pure top samples, to search Standard Model or supersymmetric Higgs bosons which couple preferably to heavy objects, to veto the large dominant top pair background for several searches of physics beyond the Standard Model. The case of top pair sample selection has been studied by using simulated data and the nominal performance of the ATLAS detector: the possibility to identify one or two b-jets can improve the purity of the sample by more than a factor of four, while reducing the signal efficiency only by a factor of two. At the same time, it has been demonstrated that the performance of the Inner Detector (and of the pixel sub-system in particular) are fundamental to reach the nominal b-tagging performance.

The Pixel Detector resolution was studied extensively in Chapter 4. The accuracy in the measurement of cluster position is determined in first approximation by pixel dimensions and by the number of pixels contained in the cluster. Pixel dimensions are fixed parameters, while cluster size depends on particle incident angle and on charge collection efficiency. A big improvement in resolution, with respect to a simple digital read-out of the pixels, can be achieved by considering the charge collected by each pixel that constitutes a given cluster. In this case, the position calculated by digital read-out can be corrected by a term based on the *charge sharing* among the pixels composing the cluster. A cal-

ibration is therefore needed, in order to evaluate the weight of the correction. All these aspects where analyzed by using both cosmic ray data and simulated cosmic ray events. The calibration procedure that was developed on simulated collisions has been applied for the first time on real data. A set of calibration constants covering a wide range of particle incident angles and cluster sizes has been derived. The charge sharing algorithm was compared to the digital read-out by using simulated data and the resolution was improved up to 50% in the precise R-Φ direction and up to 25% along the beam axis direction. A similar improvement has also been observed on the distribution of residual resolution in real data, even if the relative improvement is smaller, since residual resolution is dominated by track extrapolation uncertainty and by detector misalignments. In this case, the major impact was registered by considering clusters composed by two row or two columns of pixels, where an improvement of 8% along the precise row direction and 6% along the column direction is seen. The study of the resolution of the Pixel Detector also made possible to determine the resolution as a function of the incident angle and of the cluster size. For an incident angle ϕ_i between -20° and 20° the resolution in the precise direction varies between 5 and 12 μm, depending on the incident angle, when using the charge sharing algorithm. In the beam axis direction, instead, a resolution between 80 and 115 μm was registered for $|\eta_i| \in [-1.5; 1.5]$.

The global performances of the tracking system are reported in Chapter 5. Cosmic ray tracks were selected, in order to consider only tracks that traverse the entire Inner Detector. Furthermore, tracks that traversed the beam pipe were used and a *splitting* algorithm was applied in order to divide each track in an *upper* part and a *lower* part, each one resembling a typical collision track. This procedure also gave the possibility to measure the resolution in each track parameter by comparing the values estimated for each split track. Several effects were estimated using this method. The multiple scattering contribution was studied, as well as the dependence of resolution on the distance of the track from beam axis. Finally, systematic errors were searched for and evidenced by analyzing the resolution as a function of the azimuthal angle. The nominal resolution in the transverse impact parameter is expected to be between 7–14 μm for high-momentum tracks stemming from the nominal interaction point, depending on the polar angle of the track. Cosmic ray tracks showed, at the end of the commissioning activity, a resolution of 18 μm in the impact parameter, when considering tracks with $p_{\mathrm{T}} > 5$ GeV and $d_0 < 20$ mm. The discrepancy between the measured values and the design ones for collisions was estimated to originate from two different effects: residual misalignment of detector elements and spatial distribution of the tracks. The two effects were disentangled by considering a simulation of cosmic rays crossing the ATLAS detector. In this case the discrepancy seen with respect to collision data is entirely due to the spatial distribution of tracks, while the difference with respect to real data can be ascribed to detector misalignments. By comparing simulated and real data, in the case of d_0 resolution, a remaining difference between 20% and 30% has been measured, due to residual misalignments among detector modules.

The analyses reported in this thesis have evidenced the optimal performances of the ATLAS Inner Detector tracking system on cosmic ray data. The resolution of the Pixel Detector sub-system has been optimized and extensively studied. The resolution in the impact parameter and several other variables

have been measured. Few systematic effects due to weak mode deformations of the Inner Detector sub-systems have been spotted out. The ATLAS tracking system can be considered commissioned and ready to profit from collision data. In order to reach nominal performance in the full system, small refinements will be necessary to remove weak mode deformations effect. Further improvements in the resolution of track parameters will be possible by an accurate calibration of the error associated to each spatial measurement.

The work started during this thesis will be completed by analyzing the impact parameter resolution achievable with collision tracks. The experience achieved in these studies will be very valuable in the study of top quark properties, in particular when applying b-tagging algorithms to select a sample of top pair events, in order to measure the top pair production cross-section.

Bibliography

[1] L. Evans and P. Bryant (editors), *LHC Machine*, Journal of Instrumentation **3** (2008) no. 08, S08001.

[2] The ALICE Collaboration, *The ALICE experiment at the CERN LHC*, Journal of Instrumentation **3** (2008) no. 08, S08002.

[3] The LHCb Collaboration, *The LHCb Detector at the LHC*, Journal of Instrumentation **3** (2008) no. 08, S08005.

[4] The ATLAS collaboration, *The ATLAS Experiment at the CERN Large Hadron Collider*, Journal of Instrumentation **3** (2008) no. 08, S08003.

[5] The CMS Collaboration, *The CMS experiment at the CERN LHC*, Journal of Instrumentation **3** (2008) no. 08, S08004.

[6] The ATLAS collaboration, *The ATLAS Experiment web page*, `http://atlas.ch/`, November, 2009.

[7] *The CERN web page*, `http://cern.ch/`, November, 2009.

[8] *LHC commissioning web page*, `http://lhc-commissioning.web.cern.ch/lhc-commissioning/`, November, 2009.

[9] The ATLAS collaboration, *Expected Performance of the ATLAS Experiment - Detector, Trigger and Physics*. CERN-OPEN-2008-020. `arXiv:0901.0512 [hep-ex]`.

[10] *The TEVATRON web page*, `http://www-bdnew.fnal.gov/tevatron/`, November, 2009.

[11] J. Campbell, J. Huston, and W. Stirling, *Hard Interactions of Quarks and Gluons: a Primer for LHC Physics*, Reports on Progress in Physics **70** (2007) no. 1, 89–193.

[12] ALEPH Collaboration, DELPHI Collaboration, L3 Collaboration, OPAL Collaboration and The LEP Working Group for Higgs Boson Searches, *Search for the Standard Model Higgs boson at LEP*, Physics Letters B **565** (2003) 61 – 75.

[13] ALEPH Collaboration, DELPHI Collaboration, L3 Collaboration, OPAL Collaboration and The LEP Working Group for Higgs Boson Searches, *Precision Electroweak Measurements and Constraints on the Standard Model*, CERN-PH-EP/2007-039 , `arXiv:0712.0929 [hep-ex]`.

[14] L. Maiani, G. Parisi, and R. Petronzio, *Bounds on the number and masses of quarks and leptons*, Nuclear Physics B **136** (1978) no. 1, 115 – 124.

[15] N. Cabibbo, L. Maiani, G. Parisi, and R. Petronzio, *Bounds on the fermions and Higgs boson masses in grand unified theories*, Nuclear Physics B **158** (1979) no. 2-3, 295 – 305.

[16] R. Dashen and H. Neuberger, *How to Get an Upper Bound on the Higgs Mass*, Phys. Rev. Lett. **50** (Jun, 1983) 1897–1900.

[17] D. J. E. Callaway, *Non-triviality of gauge theories with elementary scalars and upper bounds on Higgs masses*, Nuclear Physics B **233** (1984) no. 2, 189 – 203.

[18] M. A. B. Bég, C. Panagiotakopoulos, and A. Sirlin, *Mass of the Higgs Boson in the Canonical Realization of the Salam-Weinberg Theory*, Phys. Rev. Lett. **52** (Mar, 1984) 883–886.

[19] B. Grzadkowski and M. Lindner, *Stability of triviality mass bounds in the standard model*, Physics Letters B **178** (1986) no. 1, 81 – 83.

[20] M. Lindner, *Implications of triviality for the standard model*, Zeitschrift für Physik C Particles and Fields **31** (june, 1986) 295–300.

[21] G. Altarelli and G. Isidori, *Lower limit on the Higgs mass in the standard model: An update*, Physics Letters B **337** (1994) no. 1-2, 141 – 144.

[22] J. A. Casas, J. R. Espinosa, and M. Quirós, *Improved Higgs mass stability bound in the standard model and implications for supersymmetry*, Physics Letters B **342** (1995) no. 1-4, 171 – 179.

[23] J. A. Casas, J. R. Espinosa, and M. Quirós, *Standard model stability bounds for new physics within LHC reach*, Physics Letters B **382** (1996) no. 4, 374 – 382.

[24] T. Hambye and K. Riesselmann, *Matching conditions and Higgs boson mass upper bounds reexamined*, Phys. Rev. D **55** (Jun, 1997) 7255–7262.

[25] K. Yorita, *Standard Model Higgs Searches at the Tevatron (Low Mass: $M_H \sim 140$ GeV)*, 2008. `http://indico.in2p3.fr/conferenceDisplay.py?confId=420`. Talk given at the XLIII Rencontres de Moriond, La Thuile, March 1-8, 2008.

[26] L. Zivkovic, *Search for the Standard Model Higgs Boson at High Mass at the Tevatron*, 2008. `http://indico.in2p3.fr/conferenceDisplay.py?confId=420`. Talk given at the XLIII Rencontres de Moriond, La Thuile, March 1-8, 2008.

[27] CDF Collaboration, *Observation of Top Quark Production in $p\bar{p}$ Collisions with the Collider Detector at Fermilab*, Phys. Rev. Lett. **74** (Apr, 1995) 2626–2631.

[28] F. Abe et al., *Evidence for top quark production in $p\bar{p}$ collisions at $\sqrt{s} = 1.8$ TeV*, Phys. Rev. D **50** (Sep, 1994) 2966–3026.

[29] F. Abe et al., *Evidence for top quark production in $p\bar{p}$ collisions at $\sqrt{s} = 1.8$ TeV*, Phys. Rev. Lett. **73** (Jul, 1994) 225–231.

[30] DØ Collaboration, *Observation of the Top Quark*, Phys. Rev. Lett. **74** (Apr, 1995) 2632–2637.

[31] The ATLAS collaboration, *Prospects for the Top Pair Production Cross-section at $\sqrt{s}$ = 10 TeV in the Single Lepton Channel in ATLAS*, ATL-PHYS-PUB-2009-087 ,

http://cdsweb.cern.ch/record/1200436.

[32] The ATLAS collaboration, *Prospects for measuring top pair production in the dilepton channel with early ATLAS data at* $\sqrt{s}$*=10 TeV*, ATL-PHYS-PUB-2009-086 , http://cdsweb.cern.ch/record/1200287.

[33] The ATLAS collaboration, *Prospects for Supersymmetry and Univeral Extra Dimensions discovery based on inclusive searches at a 10 TeV centre-of-mass energy with the ATLAS detector*, ATL-PHYS-PUB-2009-084 , http://cdsweb.cern.ch/record/1200151.

[34] U. De Sanctis, *Supersymmetry discovery potential in the 2 leptons channel with ATLAS.* PhD thesis, Università degli Studi di Milano, 2008. http://cdsweb.cern.ch/record/1159133.

[35] S. Montesano, *Ricerca di particelle supersimmetriche nell'ambito dell'esperimento ATLAS*, Master's thesis, Università degli Studi di Milano, 2005.

[36] U. D. Sanctis, T. Lari, S. Montesano, and C. Troncon, *Perspectives for the detection and measurement of Supersymmetry in the focus point region of mSUGRA models with the ATLAS detector at LHC*, The European Physical Journal C - Particles and Fields **52** (November, 2007) 743–758.

[37] The ATLAS collaboration, *Expected Performance of the ATLAS Experiment - Detector, Trigger and Physics*, ch. Dilepton Resonances at High Mass. CERN-OPEN-2008-020, 2008. arXiv:0901.0512 [hep-ex].

[38] The ATLAS collaboration, *Expected Performance of the ATLAS Experiment - Detector, Trigger and Physics*, ch. Lepton plus Missing Transverse Energy Signals at High Mass. CERN-OPEN-2008-020, 2008. arXiv:0901.0512 [hep-ex].

[39] The ATLAS collaboration, *Expected Performance of the ATLAS Experiment - Detector, Trigger and Physics*, ch. Vector Boson Scattering at High Mass. CERN-OPEN-2008-020, 2008. arXiv:0901.0512 [hep-ex].

[40] The ATLAS collaboration, *Expected Performance of the ATLAS Experiment - Detector, Trigger and Physics*, ch. Discovery Reach for Black Hole Production. CERN-OPEN-2008-020, 2008. arXiv:0901.0512 [hep-ex].

[41] A. Trzupek, *Heavy Ion Physics with the ATLAS Detector at the LHC*, in *The 2009 Europhysics Conference on High Energy Physics, Krakow, 16-22 July 2009*. ATL-PHYS-PROC-2009-090. http://cdsweb.cern.ch/record/1206231.

[42] S. Armstrong et al., *Architecture of the ATLAS High Level Trigger Event Selection Software*, Nuclear Instruments and Methods in Physics Research Section A: Accelerators, Spectrometers, Detectors and Associated Equipment **518** (2004) no. 1-2, 537 – 541.

[43] F. Viegas, R. Hawkings, and G. Dimitrov, *Relational databases for conditions data and event selection in ATLAS*, Journal of Physics: Conference Series **119** (2008) no. 4, 042032 (10pp).

[44] The ATLAS collaboration, *ATLAS computing: Technical Design Report*.

CERN-LHCC-2005-022. http://cdsweb.cern.ch/record/837738.

[45] G. Barrand et al., *GAUDI – A software architecture and framework for building HEP data processing applications*, Computer Physics Communications **140** (2001) no. 1-2, 45 – 55.

[46] S. Agostinelli and et al., *G4–a simulation toolkit*, Nuclear Instruments and Methods in Physics Research Section A: Accelerators, Spectrometers, Detectors and Associated Equipment **506** (2003) no. 3, 250 – 303.

[47] J. Allison and et al., *Geant4 developments and applications*, Nuclear Science, IEEE Transaction **53** (Feb., 2006) 270 – 278.

[48] T. Sjöstrand, S. Mrenna, and P. Skands, *PYTHIA 6.4 physics and manual*, Journal of High Energy Physics **2006** (2006) no. 05, 026.

[49] M. Smizanska, S. P. Baranov, J. Hrivnác, and E. Kneringer, *Overview of Monte Carlo simulations for ATLAS B-physics in the period 1996-1999*, ATL-PHYS-2000-025 , http://cdsweb.cern.ch/record/684060.

[50] C Anastopoulos et al., *Physics analysis tools for beauty physics in ATLAS*, Journal of Physics: Conference Series **119** (2008) no. 3, 032003 (7pp).

[51] G. Marchesini et al., *HERWIG 5.1 - a Monte Carlo event generator for simulating hadron emission reactions with interfering gluons*, Computer Physics Communications **67** (1992) no. 3, 465 – 508.

[52] G. Corcella et al., *HERWIG 6: an event generator for hadron emission reactions with interfering gluons (including supersymmetric processes)*, Journal of High Energy Physics **2001** (2001) no. 01, 010–010.

[53] G. Corcella et al., *HERWIG 6.5 Release Note.*, tech. rep., CERN-TH-2002-270. arXiv:0210213 [hep-ex].

[54] Tanju Gleisberg et al., *SHERPA 1.α, a proof-of-concept version*, Journal of High Energy Physics **2004** (2004) no. 02, 056–056.

[55] M. Gyulassy and X.-N. Wang, *HIJING 1.0: A Monte Carlo program for parton and particle production in high energy hadronic and nuclear collisions*, Computer Physics Communications **83** (1994) no. 2-3, 307 – 331.

[56] M. L. Mangano et al., *ALPGEN, a generator for hard multiparton processes in hadronic collisions*, Journal of High Energy Physics **2003** (2003) no. 07, 001–001.

[57] S. Frixione, P. Nason, and B. R. Webber, *Matching NLO QCD and parton showers in heavy flavour production*, Journal of High Energy Physics **2003** (2003) no. 08, 007–007.

[58] B. P. Kersevan and E. Richter-Was, *The Monte Carlo Event Generator AcerMC version 1.0 with interfaces to PYTHIA 6.2 and HERWIG 6.3*, Computer Physics Communications **149** (2003) no. 3, 142 – 194.

[59] S. Jadach, J. H. Kühn, and Z. Was, *TAUOLA - a library of Monte Carlo programs to simulate decays of polarized τ leptons*, Computer Physics Communications **64** (1991) no. 2, 275 – 299.

[60] E. Barberio, B. van Eijk, and Z. Was, *Photos – a universal Monte Carlo for QED radiative corrections in decays*, Computer Physics Communications **66** (1991) no. 1, 115 – 128.

[61] D. J. Lange, *The EvtGen particle decay simulation package*, Nuclear Instruments and Methods in Physics Research Section A: Accelerators,Spectrometers,Detectors and Associated Equipment **462** (2001) no. 1-2, 152 – 155.

[62] H. Baer, F. E. Paige, S. D. Protopescu, and X. Tata, *ISAJET 7.69: A Monte Carlo Event Generator for pp, $\bar{p}p$, and $e^{=}e^{-}$ Reactions*, `arXiv:0312045v1 [hep-ph]`.

[63] T. Sjöstrand, S. Mrenna, and P. Skands, *A brief introduction to PYTHIA 8.1*, Computer Physics Communications **178** (2008) no. 11, 852–867.

[64] M. Bähr et al., *Herwig++ physics and manual*, Eur. Phys. J. C **58** (dec, 2008) 639–707.

[65] T. Stelzer and W. F. Long, *Automatic generation of tree level helicity amplitudes*, Computer Physics Communications **81** (1994) no. 3, 357 – 371.

[66] C. M. Harris, P. Richardson, and B. R. Webber, *CHARYBDIS: a black hole event generator*, Journal of High Energy Physics **2003** (2003) no. 08, 033–033.

[67] The ATLAS collaboration, *ATLAS inner detector: Technical design report. Vol. 1*. CERN-LHCC-97-16. `http://atlas.web.cern.ch/Atlas/GROUPS/INNER_DETECTOR/TDR/tdr.html`.

[68] The ATLAS collaboration, *ATLAS inner detector: Technical design report. Vol. 2*. CERN-LHCC-97-17. `http://atlas.web.cern.ch/Atlas/GROUPS/INNER_DETECTOR/TDR/tdr.html`.

[69] P. A. Coe, D. F. Howell, and R. B. Nickerson, *Frequency scanning interferometry in ATLAS: remote, multiple, simultaneous and precise distance measurements in a hostile environment*, Measurement Science and Technology **15** (2004) no. 11, 2175–2187.

[70] G. Aad et al., *ATLAS pixel detector electronics and sensors*, Journal of Instrumentation **3** (2008) no. 07, P07007.

[71] D. Attree et al., *The evaporative cooling system for the ATLAS inner detector*, Journal of Instrumentation **3** (2008) no. 07, P07003.

[72] G. Lindström et al., *Radiation hard silicon detectors–developments by the RD48 (ROSE) collaboration*, Nuclear Instruments and Methods in Physics Research Section A: Accelerators, Spectrometers, Detectors and Associated Equipment **466** (2001) no. 2, 308 – 326.

[73] M. S. Alam et al., *The ATLAS silicon pixel sensors*, Nuclear Instruments and Methods in Physics Research Section A: Accelerators, Spectrometers, Detectors and Associated Equipment **456** (2001) no. 3, 217 – 232.

[74] C. Gemme et al., *Study of indium bumps for the ATLAS pixel detector*, Nuclear Instruments and Methods in Physics Research Section A: Accelerators, Spectrometers, Detectors and Associated Equipment **465** (2001) no. 1, 200 – 203.

[75] G. C. J. Wolf and H. Reichl, *Lead/Tin (95/5%) solder bumps for flip chip applications based on Ti:W(N)/Au/Cu underbump metallisation*, in *Proceedings of the Fifth International TAB/Advanced Packaging Symposium ITAP*, p. 141. San Jose USA, 1993.

[76] O. Ehrmann et al., *A bumping technology for reduced pitch*, in *Proceedings of the Second International TAB Symposium*, p. 41. San Jose USA, 1990.

[77] J. Wolf, *PbSn60 solder bumping by electroplating, Pixel 2000 Conference*, `http://www.ge.infn.it/Pix2000/slides/wolf.pdf.`, Genova, 2000.

[78] Ivan Peric et al., *The FEI3 readout chip for the ATLAS pixel detector*, Nuclear Instruments and Methods in Physics Research Section A: Accelerators, Spectrometers, Detectors and Associated Equipment **565** (2006) no. 1, 178 – 187. Proceedings of the International Workshop on Semiconductor Pixel Detectors for Particles and Imaging - PIXEL 2005.

[79] R. Beccherle et al., *MCC: the Module Controller Chip for the ATLAS Pixel Detector*, Nuclear Instruments and Methods in Physics Research Section A: Accelerators, Spectrometers, Detectors and Associated Equipment **492** (2002) no. 1-2, 117 – 133.

[80] A Abdesselam et al., *The barrel modules of the ATLAS semiconductor tracker*, Nuclear Instruments and Methods in Physics Research Section A: Accelerators, Spectrometers, Detectors and Associated Equipment **568** (2006) no. 2, 642 – 671.

[81] A. Ahmad et al., *The silicon microstrip sensors of the ATLAS semiconductor tracker*, Nuclear Instruments and Methods in Physics Research Section A: Accelerators, Spectrometers, Detectors and Associated Equipment **578** (2007) no. 1, 98 – 118.

[82] A Abdesselam et al., *The ATLAS semiconductor tracker end-cap module*, Nuclear Instruments and Methods in Physics Research Section A: Accelerators, Spectrometers, Detectors and Associated Equipment **575** (2007) no. 3, 353 – 389.

[83] F. Campabadal et al., *Design and performance of the ABCD3TA ASIC for readout of silicon strip detectors in the ATLAS semiconductor tracker*, Nuclear Instruments and Methods in Physics Research Section A: Accelerators, Spectrometers, Detectors and Associated Equipment **552** (2005) no. 3, 292 – 328.

[84] A Abdesselam et al., *The optical links of the ATLAS SemiConductor Tracker*, Journal of Instrumentation **2** (2007) no. 09, P09003.

[85] A Abdesselam et al., *The data acquisition and calibration system for the ATLAS Semiconductor Tracker*, Journal of Instrumentation **3** (2008) no. 01, P01003.

[86] The ATLAS TRT collaboration, *The ATLAS TRT Barrel Detector*, Journal of Instrumentation **3** (2008) no. 02, P02014.

[87] The ATLAS TRT collaboration, *The ATLAS TRT end-cap detectors*, Journal of Instrumentation **3** (2008) no. 10, P10003.

[88] E. Abat and et al., *The ATLAS Transition Radiation Tracker (TRT) proportional drift tube: design and performance*, Journal of Instrumentation **3** (2008) no. 02, P02013.

[89] The ATLAS TRT collaboration, *The ATLAS TRT electronics*, Journal of Instrumentation **3** (2008) no. 06, P06007.

[90] C. Amsler et al. (Particle Data Group), *The Review of Particle Physics*. Physics Letters B667, 1, 2008. http://pdg.lbl.gov.

[91] The ATLAS collaboration, *Expected Performance of the ATLAS Experiment - Detector, Trigger and Physics*, ch. *b*-Tagging Performance. CERN-OPEN-2008-020. arXiv:0901.0512 [hep-ex].

[92] The ATLAS collaboration, *Expected Performance of the ATLAS Experiment - Detector, Trigger and Physics*, ch. Vertex reconstruction for *b*-Tagging. CERN-OPEN-2008-020. arXiv:0901.0512 [hep-ex].

[93] The ATLAS collaboration, *Expected Performance of the ATLAS Experiment - Detector, Trigger and Physics*, ch. Effects of Misalignment on *b*-Tagging. CERN-OPEN-2008-020. arXiv:0901.0512 [hep-ex].

[94] The ATLAS collaboration, *Expected Performance of the ATLAS Experiment - Detector, Trigger and Physics*, ch. Determination of Top Quark Pair Production Cross-Section. CERN-OPEN-2008-020. arXiv:0901.0512 [hep-ex].

[95] C. Amsler et al. (Particle Data Group), *The Review of Particle Physics*, ch. Cosmic rays. Physics Letters B667, 1, 2008. http://pdg.lbl.gov.

[96] C. Amsler et al. (Particle Data Group), *The Review of Particle Physics*, ch. Passage of particles through matter. Physics Letters B667, 1, 2008. http://pdg.lbl.gov.

[97] A. Dar, *Atmospheric Neutrinos, Astrophysical Neutrons, and Proton-Decay Experiments*, Phys. Rev. Lett. **51** (Jul, 1983) 227–230.

[98] H. Bichsel, *Straggling in thin silicon detectors*, Rev. Mod. Phys. **60** (Jul, 1988) 663–699.

[99] V. Radeka, *Low Noise Techniques in Detectors*, Annual Review of Nuclear and Particle Science **38** (dec, 1988) 217–277.

[100] R. Pehl, F. Goulding, D. Landis, and M. Lenzlinger, *Accurate determination of the ionization energy in semiconductor detectors*, Nuclear Instruments and Methods **59** (1968) no. 1, 45 – 55.

[101] R. D. Ryan, *Precision Measurements of the Ionization Energy and Its Temperature Variation in High Purity Silicon Radiation Detectors*, Nuclear Science, IEEE Transactions on **20** (Feb., 1973) 473–480.

[102] P. Christmas, *Average energy required to produce an ion pair : ICRU Report 31, 1979, ICRU*

Publications, PO Box 30165, Washington, DC 20014, U.S.A. 52 pp. 5.25., Radiation Physics and Chemistry (1977) **16** (1980) no. 6, 493 – 493.

[103] F. Scholze et al., *Determination of the electron-hole pair creation energy for semiconductors from the spectral responsivity of photodiodes*, Nuclear Instruments and Methods in Physics Research Section A: Accelerators, Spectrometers, Detectors and Associated Equipment **439** (2000) no. 2-3, 208 – 215.

[104] C. Amsler et al. (Particle Data Group), *The Review of Particle Physics*, ch. Particle Detectors. Physics Letters B667, 1, 2008. http://pdg.lbl.gov.

[105] T. Lari, *Study of silicon pixel sensors for the ATLAS detector*. PhD thesis, Università degli Studi di Milano, 2001. http://cdsweb.cern.ch/record/531625.

[106] W. Shockley, *Electrons and Holes in Semiconductors*. D. Van Nostrand Company, Inc., New York, USA, 1950.

[107] S. M. Sze, *Physics of Semiconductor Devices*. Wiley-Interscience, 2nd ed., 1981.

[108] C. Jacoboni, C. Canali, G. Ottaviani, and A. Alberigi Quaranta, *A review of some charge transport properties of silicon*, Solid-State Electronics **20** (1977) no. 2, 77 – 89.

[109] G. Persky and D. J. Bartelink, *High-Field Diffusivity of Electrons in Silicon*, Journal of Applied Physics **42** (1971) no. 11, 4414–4421.

[110] L. Dell'Asta, *Simulazione con Geant4 del rivelatore a pixel di ATLAS*, Master's thesis, Università degli Studi di Milano, 2007.

[111] F. De Lorenzi, *Timing characteristics of the ATLAS pixel detector*, Master's thesis, Università degli Studi di Milano, 2007.

[112] A. Arelli-Maffioli, *Studio di un algoritmo lineare di ricostruzione analogica della posizione per il rivelatore a pixel di ATLAS.* Master's thesis, Università degli Studi di Milano, 2007. http://cdsweb.cern.ch/record/1092932.

[113] M. Aleppo, *A measurement of Lorentz angle of radiation-hard pixel sensors*, Nucl. Instrum. Meth. **A465** (2000) 108–111.

[114] A. Andreazza, *Progresses on the ATLAS pixel detector*, Nucl. Instrum. Meth. **A461** (2001) 168–171.

[115] I. Gorelov et al., *A measurement of Lorentz angle and spatial resolution of radiation hard silicon pixel sensors*, Nuclear Instruments and Methods in Physics Research Section A: Accelerators, Spectrometers, Detectors and Associated Equipment **481** (2002) 204–221.

[116] F. Ragusa, *Recent developments in the ATLAS pixel detector*, Nuclear Instruments and Methods in Physics Research Section A: Accelerators, Spectrometers, Detectors and Associated Equipment **447** (2000) no. 1-2, 184 – 193.

[117] C. Troncon, *Detailed studies of the ATLAS pixel detectors*, IEEE Trans. Nucl. Sci. **47** (2000)

737–744.

[118] A. Andreazza, *Performance of ATLAS pixel detector prototype modules*, Nucl. Instrum. Meth. **A513** (2003) 103–106.

[119] T. Lari, *Measurements of spatial resolution of ATLAS pixel detectors*, Nucl. Instrum. Meth. **A465** (2000) 112–114.

[120] The ATLAS collaboration, *Expected Performance of the ATLAS Experiment - Detector, Trigger and Physics*, ch. The Expected Performance of the Inner Detector. CERN-OPEN-2008-020. arXiv:0901.0512 [hep-ex].

[121] T. Akesson et al., *ATLAS Tracking Event Data Model*, ATL-SOFT-PUB-2006-004 , http://cdsweb.cern.ch/record/973401.

[122] T. G. Cornelissen et al., *Updates of the ATLAS Tracking Event Data Model (Release 13)*, ATL-SOFT-PUB-2007-003 , http://cdsweb.cern.ch/record/1038095.

[123] F. Ragusa and L. Rolandi, *Tracking at LHC*, New Journal of Physics **9** (2007) 336.

[124] V. L. Highland, *Some practical remarks on multiple scattering*, Nuclear Instruments and Methods **129** (1975) no. 2, 497 – 499.
V.L. Highland, *Erratum to some practical remarks on multiple scattering*, Nuclear Instruments and Methods 161 (1979), p. 171.

[125] G. Molière, *Theorie der Streuung schneller geladener Teichen II: Mehrfach- und Vielfachstreuung,*, Z. Naturforsch. **3a** (1948) 78.

[126] R. Gluckstern, *Uncertainties in track momentum and direction, due to multiple scattering and measurement errors*, Nuclear Instruments and Methods **24** (1963) 381 – 389.

[127] A. S. Schwarz, *Heavy flavour physics at colliders with silicon strip vertex detectors*, Physics Reports **238** (1994) no. 1-2, 1 – 133.

[128] A. Salzburger, *The ATLAS Track Extrapolation Package*, ATL-SOFT-PUB-2007-005 , http://cdsweb.cern.ch/record/1038100.

[129] O. Brandt, *The Alignment of the ATLAS Silicon Tracker*, arXiv:0808.0204 [physics.ins-det].

[130] P. Brückman de Renstrom, *Proceedings of the first LHC Detector Alignment Workshop*, ch. Alignment strategy for the Inner Detector of ATLAS. CERN 2007-004. http://cdsweb.cern.ch/record/970621.

[131] T. Golling, *Alignment of the Silicon Tracking Detector using Survey Constraints*, ATL-INDET-PUB-2006-001 , http://cdsweb.cern.ch/record/941076.

[132] F. Heinemann, *Track Based Alignment of the ATLAS Silicon Detectors with the Robust Alignment Algorithm*, ATL-INDET-PUB-2007-011 , arXiv:0710.1166 [physics.ins-det].

[133] P. Brückman, A. Hicheur, and S. J. Haywood, *Global chi2 approach to the Alignment of the ATLAS Silicon Tracking Detectors*, ATL-INDET-PUB-2005-002 , http://cdsweb.cern.ch/record/835270.

[134] R. Frühwirth, *Application of Kalman filtering to track and vertex fitting*, Nuclear Instruments and Methods in Physics Research Section A: Accelerators, Spectrometers, Detectors and Associated Equipment **262** (1987) no. 2-3, 444 – 450.

[135] V. Kartvelishvili, *Electron bremsstrahlung recovery in ATLAS*, Nuclear Physics B - Proceedings Supplements **172** (2007) 208 – 211. Proceedings of the 10th Topical Seminar on Innovative Particle and Radiation Detectors.

[136] A. Strandlie and J. Wroldsen, *Treatment of non-Gaussian tails of multiple Coulomb scattering in track fitting with a Gaussian-sum filter*, Nuclear Instruments and Methods in Physics Research Section A: Accelerators, Spectrometers, Detectors and Associated Equipment **559** (2006) no. 1, 158 – 161. Proceedings of the X International Workshop on Advanced Computing and Analysis Techniques in Physics Research - ACAT 05.

[137] S. Fleischmann, *Track Reconstruction in the ATLAS Experiment: The Deterministic Annealing Filter.* PhD thesis, Bergische Univ. Wuppertal, 2006. http://cdsweb.cern.ch/record/1014533.

[138] R. Frühwirth and A. Strandlie, *Track fitting with ambiguities and noise: A study of elastic tracking and nonlinear filters*, Computer Physics Communications **120** (1999) no. 2-3, 197 – 214.

[139] T. G. Cornelissen, *Track Fitting in the ATLAS Experiment.* PhD thesis, Univ. Amsterdam, 2006. http://cdsweb.cern.ch/record/1005181.

[140] T. G. Cornelissen et al., *Concepts, Design and Implementation of the ATLAS New Tracking (NEWT)*, ATL-SOFT-PUB-2007-007 , http://cdsweb.cern.ch/record/1020106.

[141] R. O. Duda and P. E. Hart, *Use of the Hough transformation to detect lines and curves in pictures*, Commun. ACM **15** (1972) no. 1, 11–15.

[142] T. G. Cornelissen et al., *Single Track Performance of the Inner Detector New Track Reconstruction (NEWT)*, ATL-INDET-PUB-2008-002 , http://cdsweb.cern.ch/record/1092934.

Errata in printed version

- In Figures 4.19(a), 4.19(c), , 4.19(d), 4.20(a), 4.20(c), 4.21(b), 4.21(c), the distribution drawn with blue triangles refers to the "*digital position*" and not to the "*center of the cluster*" as written in the legend.
- Figure 5.43(b) has a missing absolute value in the y axis label. The label should be "$p \times \Delta(|q/p|)$".
- Eq. 5.11 should be:

$$\chi^2 = \sum_{i=1}^{N} \frac{(z_i - z_0 - R_i \cot\theta)^2}{\sigma_i^2}. \tag{5.55}$$

- Eq. 5.15 should be:

$$\chi^2 = \sum_{i=1}^{N} \frac{(y_i - a - bx_i - cx_i)^2}{\sigma_i^2}, \tag{5.56}$$